ECAP-2013-033

THE ANTARES NEUTRINO TELESCOPE AND CONSTRAINTS FOR NON-UNIVERSAL SUPERSYMMETRIC MODELS FROM RECENT EXPERIMENTAL RESULTS

DAS NEUTRINO TELESKOP ANTARES UND EINSCHRÄNKUNGEN NICHT-UNIVERSELLER SUPERSYMMETRISCHER MODELLE MIT EXPERIMENTELLEN ERGEBNISSEN

Der Naturwissenschaftlichen Fakultät
der Friedrich-Alexander-Univeristät
Erlangen-Nürnberg
zur
Erlangung des Doktorgrades Dr. rer. nat.

vorgelegt von
Andreas Volker Spies
aus Sulzbach-Rosenberg

Als Dissertation genehmigt
von der Naturwissenschaftlichen Fakultät
der Friedrich-Alexander Universität Erlangen-Nürnberg

Tag der mündlichen Prüfung: 27.02.2014

Vorsitzende/r des Promotionsorgans: Prof. Dr. Johannes Barth

Gutachter/in: Prof. Dr. Gisela Anton
Prof. Dr. Ulrich Katz

Abstract

The ANTARES neutrino telescope was built at a depth of ~ 2500 m in the Mediterranean Sea near Toulon in the south of France. ANTARES searches for neutrinos originating from annihilating dark matter particles in the Sun. In order to identify those neutrinos, a high angular resolution for the expected energies ($\lesssim 1$ TeV) is necessary. With ANTARES, a high angular resolution can only be achieved with a sophisticated position calibration system of the detection units. The existing positioning calibration algorithm (alignment) was improved, such that more data with an accurate information about the detection units' position is available for subsequent processing. The improved algorithm lead to a significant increase of available alignment information compared to the previous algorithm. Further, an error calculation on the detection units' position and orientation was implemented, in order to improve the estimations of uncertainties for a given neutrino event.

In the second part of this work non-universal supersymmetric extensions of the standard model of particle physics were investigated. The well studied constrained Minimal Supersymmetric Standard Model (cMSSM) was used as a reference model. By introducing a non-universal Higgs (NUHM) or gauge sector (NUGM), more general models were constructed and their phenomenological implications were discussed. Recent experimental results from direct as well as indirect dark matter search experiments were applied to the model's parameter space. Further, the discovery of a Higgs boson at the LHC last year was taken into account. A χ^2 analysis was performed to test the compatibility between model predictions and experimental measurements. Included observables were the neutralino relic density Ωh^2, the Higgs-boson mass m_h and several flavor observables, such as $\mathrm{BR}(B \to X_\mathrm{s}\gamma)$. It was found, that the least agreement between observations and predictions is given in the cMSSM. A better agreement is given in the NUHM and NUGM scenario. Both scenarios were compatible with each other. Finally, favored regions for dark matter search observables were derived. These regions are not yet excluded experimentally, but will be tested in the future.

Zusammenfassung

Das Neutrino Teleskop ANTARES wurde im Mittelmeer in einer Tiefe von ca. 2500 m gebaut. Es befindet sich vor der südfranzösischen Küste in Toulon. ANTARES sucht nach Neutrinos aus annihilierenden dunkle Materie Teilchen in der Sonne. Zur Identifikation dieser Neutrinos, ist eine akurate Winkelauflösung im erwarteten Energiebereich ($\lesssim 1$ TeV) erforderlich. Dies ist nur durch eine leistungsfähige Positionskalibration der Detektoreinheiten zu erreichen. Der bestehende Algorithmus zur Ortsbestimmung der Detektorelemente (alignment) wurde verbessert. Dadurch wurde eine erhöhte Alignment-Effizienz erzielt, d.h. mehr Daten mit akurater Ortsinformation stehen für die Weiterprozessierung zur Verfügung. Der verbesserte Algorithmus führte zu einer signifikanten Erhöhung verfügbarer Alignmentinformation, verglichen mit früheren Versionen. Darüber hinaus wurde die Fehlerrechnung mit Bezug auf die Stockwerksposition und -ausrichtung implementiert, um eine Abschätzung der Unsicherheiten eines Neutrino Ereignisses zu verbessern.

Im zweiten Teil dieser Arbeit wurden supersymmetrische Erweiterungen des Standard Models der Teilchenphysik diskutiert. Das am häufigsten untersuchte constrained Minimal Supersymmetric Standard Model (cMSSM) diente dabei als Referenz-Model. Verallgemeinerte Modelle wurden durch Hinzufügen nicht universeller supersymmetrischer Higgs- (NUHM) oder Eichsektoren (NUGM) konstruiert und deren phänomenologische Auswirkungen untersucht. In der Analyse wurden aktuelle experimentelle Ergebnisse der direkten und indirekten Suche nach Dunkler Materie berücksichtigt. Die Detektion des Higgs-Bosons am Large Hadron Collider (LHC) wurde in die Diskussion ebenfalls mit einbezogen. Die Verträglichkeit zwischen Modelvorhersagen und experimentellen Messungen wurde mit Hilfe einer χ^2-Analyse überprüft. Nicht-universelle Modelle (NUHM und NUGM) erzielten vergleichbare Ergebnisse und weisen ein höheres Mass an Verträglichkeit zwischen Vorhersage und Messung auf, als das cMSSM. Abschließend wurden bevorzugte Regionen für Messgrößen zur Suche nach dunkler Materie abgeleitet. Derzeit sind diese Regionen nicht ausgeschlossen, werden jedoch in naher Zukunft experimentell zugänglich sein.

Contents

List of Figures

List of Tables

Dedication

This thesis is dedicated to my wife Franziska Spies.

Acknowledgments

I would like to thank my supervisors G. Anton and U. Katz for supporting this work and offering me this excellent opportunity to contribute to the research in the field of astroparticle physics. Further, I would like to thank J. Hössl, T. Eberl, K. Graf and A. Kappes for various fruitful discussions about calibration issues, dark matter related topics, or any other concerns. I would like to thank the group members, K. Roensch, S. Wagner, K. Geyer, F. Folger and R. Richter for the motivating and inspiring working climate during the last years. Especially, I want to thank my wife, Franziska Spies, supporting me at any time. Last but not least I want to thank my parents, offering me the possibility to focus on my studies at any time and deepen my knowledge during my doctoral thesis.

1

Introduction

"It doesn't matter how beautiful your theory is, it doesn't matter how smart you are. If it doesn't agree with experiment, it's wrong."
Richard P. Feynman

Today's astronomy not only consists of the optical observation of photons coming from astronomical objects, such as stars, galaxies, or remnants of exploded stars. Experimental methods go far beyond observations with optical telescopes. Neutrinos, a particle species in the standard model of particle physics (SM), are excellent candidates to observe astrophysical objects. It is believed that hadronic charged particles are produced and accelerated to highest energies in objects like active galactic nuclei (AGN), or supernova remnants. As secondary products, high energetic neutrinos result. In contrast to other messenger particles like protons or electrons, neutrinos are electrical neutral. This means, they do not interact with intergalactic magnetic fields and propagate undeflected from their origin to observatories located on Earth. Photons, electrical neutral as well, offer this property, too, but have the disadvantage, that the Universe is opaque for photons with energies higher than 100 TeV and distances larger than the galactic scale.

Neutrinos can not only give information about acceleration mechanisms taking place in astrophysical objects, they may give a hint on the nature of dark matter (DM). Several observations, e.g. rotation velocities of stars in galaxies or the temperature fluctuations of the cosmic microwave background (CMB), show the evidence for the existence of dark matter. From the CMB the composition of the Universe can be derived. It follows, that only 4.6% of the energy density in today's Universe account for ordinary baryonic matter, such as atoms. 71.4% account for an unknown component, the so-called dark energy. The remaining 24% are made up by dark matter. Up to now, no explanation of the nature of dark matter has been found. Although several attempts to explain experimental measurements exist, reaching from modifying Newtonian dynamics (MOND) or the assumption that general relativity behaves differently at different length scales, the most common approach is the introduction of new particle species that account for dark matter. The standard model of particle physics (SM) does not provide such a candidate and theories beyond the SM are

necessary. Famous examples are higher dimensional theories, such as Kaluza-Klein excitations of SM particles into a compactified extra dimension, or supersymmetric extensions (SUSY) of the SM that connect fermionic with bosonic degrees of freedom. In that way, each SM particle gets a SUSY partner differing in spin by unit 1/2. Both theories provide excellent dark matter particle candidates. They are weakly interacting and massive and called WIMPs (weakly interacting massive particles). Assuming a parity quantum number to be conserved, the lightest of those WIMPs is stable. These lightest WIMPs are called LKP (lightest Kaluza-Klein Particle) or LSP (lightest SUSY particle) and provide a dark matter particle candidate.

Several experimental methods exist, to detect dark matter particles. They can be classified into three categories. First, DM particles may be produced at colliders, like the LHC. Ordinary, charged SM particles are accelerated to high energies and are brought to collision. Possibly, particles related to physics beyond the SM, e.g., SUSY dark matter particles, are produced and may be detected. Secondly, DM particles can be searched for directly, where they scatter off atomic nuclei and the recoil energy of atomic nuclei is measured. Last but not least, DM particles may be detected indirectly. Both, the LKP or the LSP can annihilate pairwise and annihilation products, e.g., electrons, photons, neutrinos, may be detected by indirect detection experiments, e.g., H.E.S.S. (in the case of photons) or ANTARES/IceCube (in the case of neutrinos).

This work is organized as follows. In Section 2 the ANTARES neutrino telescope and its principle of detection is introduced. Section 3 is dedicated to the positioning calibration, that is necessary to provide the subsequent track reconstruction with a spatial resolution of the ANTARES detection units of high precision. In Section 4, a particle physics description of dark matter, especially SUSY dark matter is given. Further, the different detection techniques are explained in detail. Different SUSY models, that were investigated in this work are discussed in Section 5. Subsequently, their analysis with respect to recent results from direct and indirect detection experiments and the Higgs boson as well as a χ^2 analysis are explained in Section 6. In Section 7, the conclusion of this work is presented.

2

The ANTARES Neutrino Telescope

2.1 Principle of Detection

The neutrino telescope ANTARES (**A**stronomy with a **N**eutrino **T**elescope in **A**byss Environmental **RES**earch) is based on the principle of detection of Cerenkov light. It is emitted by charged particles that move faster than the speed of light in the surrounding medium. Muon neutrinos interact in or in the vicinity of the detector with a nucleon of the medium via deep inelastic lepton hadron scattering (Figure 2.1). Either a muon is produced (charged current) or a neutrino without changing its charge (neutral current). Both interactions are accompanied by a hadronic shower.

Figure 2.1: Charge current interaction (left) via exchange of the charged $W^\pm$ boson producing a muon $\mu^\pm$ and a hadronic shower. Respectively, a neutral current interaction (right) via exchange of the neutral Z boson and a hadronic shower.

The produced muons emit light at the Cerenkov angle, θ_C, given by $\cos(\theta_C) = (n\beta)^{-1}$. $n = 1.34$ is the refractive index of seawater and $\beta = v_{\text{muon}}/c_{\text{vac}}$ is the velocity. From the time when emitted Cerenkov photons hit the detection units and from their position the direction of the muon is reconstructed. The mean kinematic angle $\langle\phi\rangle$ between the original muon neutrino and the produced muon is given by Aslanidis et al. 1999.

$$\langle\phi_{\nu_\mu\to\mu}\rangle = \frac{0.7^\circ}{(E_{\nu_\mu}/TeV)^{0.6}} \tag{2.1}$$

Thus, at high energies the direction and the origin of the neutrino can be derived with reasonable precision.

2.2 Layout of the Detector

The ANTARES neutrino telescope was build in a mooring depth of $\sim$ 2.5 km in the Mediterranean Sea, near Toulon in the south of France.

ANTARES consists of twelve detection lines with a spatial distance of about 70 m (Figure 2.2). Each line is roughly 500 m long and fixed at the sea bed with a dead weight (bottom string socket BSS). On top a buoy is fixed to keep the line vertical. As the lines are deployed in water they move to a certain extend with the sea current around the anchoring point. Each line carries 25 storeys (Figure 2.3) connected with electro-mechanical cables. These cables provide the infrastructure for data transfer and the mechanical structure. The first storey (from bottom to top) is mounted at a height of 100 m. The remaining storeys are distributed equidistant along the line with a distance of 14.5 m. Each of the storeys is equipped with three optical modules (OM) that are glass spheres mounted in a plane with 120° angular spacing. Each OM houses a 10" photomultiplier tube (PMT). The PMTs' axes are directed 45° downwards to be most sensitive for upward going muons (signal events). For timing and position calibration, every fifth storey houses a LED beacon and a hydrophone, respectively. Each storey carries a titanium cylinder, the so-called local control module (LCM). It contains the electronics of the storey. Five storeys are grouped together to so-called sectors. The second storey of each sector (from bottom up) carries the master local control module (MLCM) that collects the date from the corresponding sector. The BSS of each line houses the string control module (SCM) which collects the data from corresponding MLCMs of the line. The SCMs are connected with an electro-optical cable with the junction box (JB). The JB itself is connected with the shore station in La Seyne sur Mer in France.

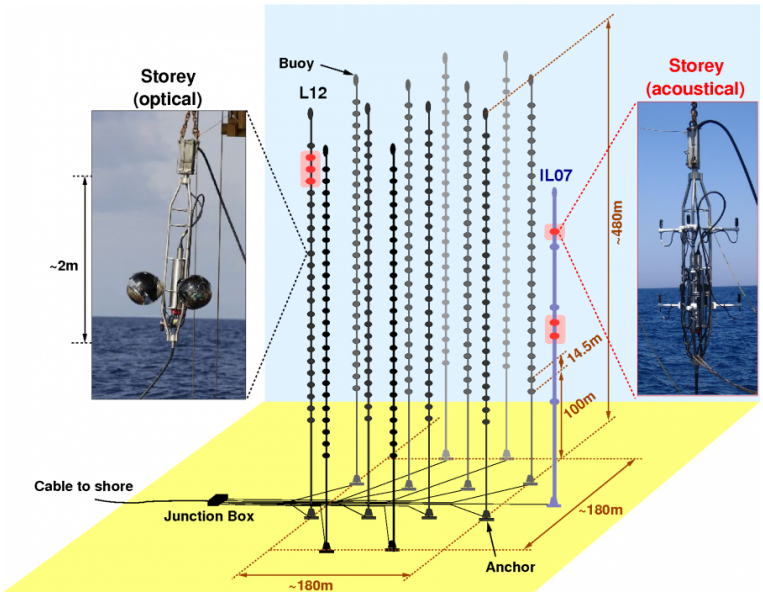

Figure 2.2: Schematic view of ANTARES

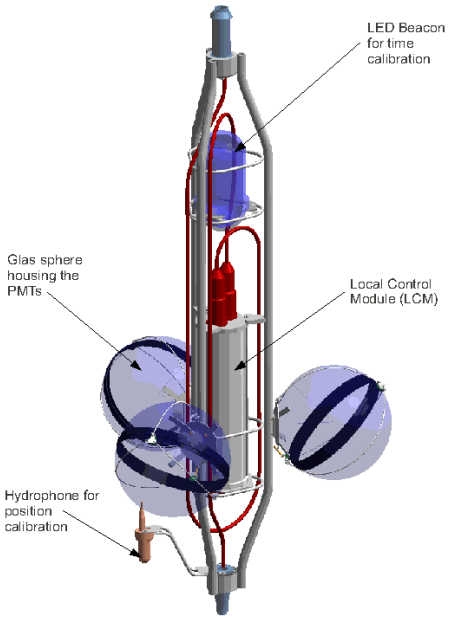

Figure 2.3: Storey of ANTARES: a titanium frame carries the LCM and OMs. At the bottom of some storeys a hydrophone for position calibration and a LED beacon on top for time calibration is installed.

The uppermost sector of line 12 is replaced by an acoustic sector. There, instead of OMs, hydrophones for the acoustic detection of neutrinos have been mounted. Additionally to these twelve lines, an instrumentation line (IL) was deployed. There, three more storeys for acoustic neutrino detection are mounted, as well as an prototype optical module for the future KM3NeT neutrino telescope. Further, an Acoustic Doppler Current Profiler (ADCP) for measuring the sea current, salinity and the speed of sound is installed.

3

The Positioning Calibration of ANTARES

As mentioned in the previous Chapter, the ANTARES detector lines are only fixed on the sea bed. Thus, they are free to be deflected from the vertical or rotate with the sea current. For a precise reconstruction of muon tracks, with respect to its direction, it is mandatory to determine the position and orientation of each OM accurately. The method how the position of the detection units is determined is part of this chapter.

3.1 The Acoustic Positioning System

First, the anchor position of each ANTARES detector line has to be determined. Therefor, each BSS is equipped with acoustic transponders to determine the position via triangulation. Further, five reference transponders are embedded on the sea floor in the vicinity of ANTARES, whose positions were determined with an accuracy better than 1 m before the first ANTARES detector element was deployed. To avoid acoustic interferences, additionally an acoustic module is operated 15 - 20 m below the sea surface. By measuring the acoustic travel times between the BSSs, the acoustic module on the ship and the reference transponders the anchor position of the ANTARES lines is determined with a spatial error less than 1 m.

The absolute orientation of the ANTARES detector relative to the sky is determined using the absolute BSS positions and their positions relative to each other. Relative BSS positions are determined with a so-called High Frequency Long Baseline Positioning System (HFLBL) developed by the company GENISEA/ECA [1] (Figure 3.1).
The HFLBL transponders on the BSS are mounted with a lever arm of 0.29 m, so its orientation has to be determined with a compass with accuracy of about 5° from a submarine used during the deployment of the line. Using both, absolute and relative BSS positions, the absolute orientation of the detector is determined within an uncertainty of 0.13° in the horizontal plane and 0.06° in the vertical direction (Adrian-Martinez et al. 2012).

The acoustic modules mounted on the BSS are receiver as well as emitter (RxTx module

[1] formerly GENISEA now ECA http://www.eca.fr

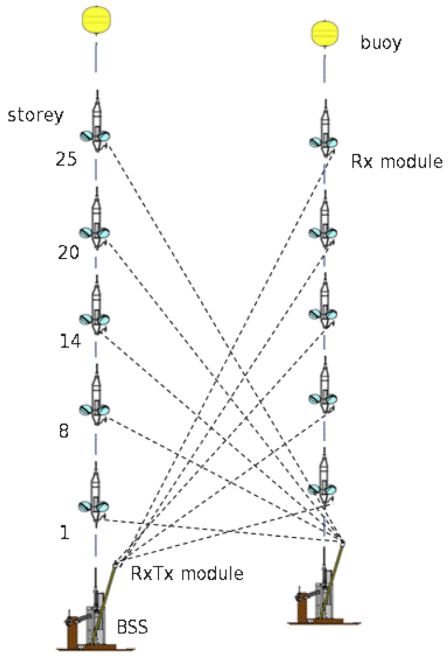

Figure 3.1: Scheme of the acoustic High Frequency Long Baseline Positioning System (HFLBL) for the determination of the relative positions of the ANTARES detector units. Picture from Adrian-Martinez et al. 2012.

in Figure 3.1). Storeys 1, 8, 14, 20 and 25 on each line are equipped with an acoustic receiver (Rx module). The positions of these five storeys are determined via acoustic triangulation by sending acoustic signals in a programmable successive periodic cycle, so-called TimeStamp (every six (2007/01-2008/04) or two (2008/04 - present) minutes). Then, the obtained positions are put into the data-base for further processing. To reduce noise the sliding average is taken over time periods of 20 minutes. Values that show a strong deviation from the average are removed.

3.2 The Compass-Tiltmeter System

To get the orientation of the ANTARES storeys they are equipped with a commercial so called TCM2 board, manufactured by PNI Sensor Corporation [2]. Additionally, a compass module is mounted on each storey. The TCM2 board measures the storey's inclination based on the principle of the movement of a fluid with respect to the horizontal in two perpendicular axes, called pitch and roll. The accuracy (resolution) of the TCM2 is 0.2° (0.1°). The compass module measures the Earth magnetic field components $\vec{B} = (B_x, B_y, B_z)$ to determine the horizontal orientation of the storey. To calculate the heading of the storey, two correction terms are necessary. The first, $\Delta h_{m/g} = 0.57°$, corrects the difference between magnetic and geographic north pole. The azimuth angle or the distance between two points is much easier to estimate in a grid coordinate system compared to the usual spherical angles latitude and longitude. For this reason, ANTARES uses the so-called Universal Transverse Mercator grid (UTM) for the positioning of the lines and OMs. Thus, a second correction

[2] http://www.pnicorp.com

factor for the UTM northing coordinate and the geographic north, $\Delta h_{\mathrm{UTM}} = 1.93°$, is necessary. Further, an annual correction factor of $+0.12°$ has to be applied that accounts for the movement of the magnetic north pole.

In total, the heading h of an ANTARES storey is given by

$$h = \arctan\left(\frac{B_x}{B_y}\right) + \Delta h_{m/g} + \Delta h_{\mathrm{UTM}} \tag{3.1}$$

The vertical component B_z of the Earth magnetic field is neglected in Equation 3.1, as typical storey inclinations are smaller than 1°.

Compass calibration

The Earth magnetic field at the ANTARES detector is 24 μT in the horizontal plane. The measured values of B_x and B_y should result in a circle in the $B_y - B_x$ plane (dashed circle in Figure 3.2) for the rotation of an ANTARES storey around the line axis.

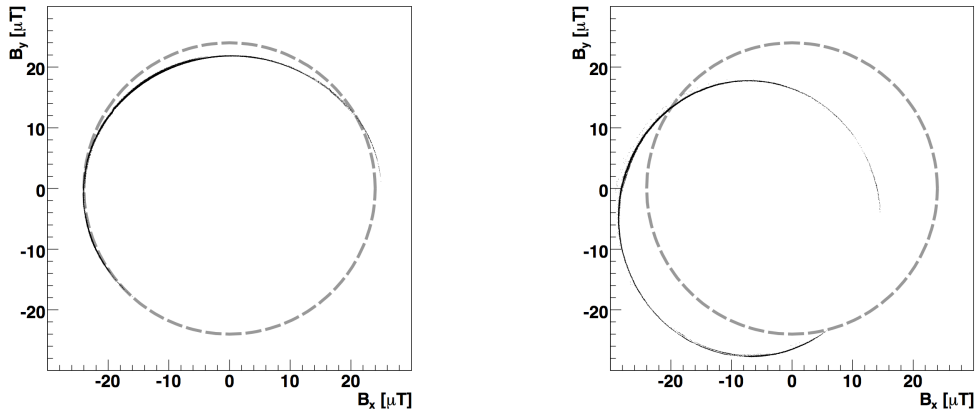

Figure 3.2: Measured B_x and B_y components of the Earth magnetic field (black circle) for the time period 11/2010 - 12/2010. Expected values are shown as dashed gray circle.

Internal magnetic fields from electronic devices inside the LCM may lead to a shift of the circle in a certain direction. These fields are fixed to the local frame of the LCM and can be cured by adding an offset to the B-field components. Eccentric or distorted circles are caused by miscalibration of the compass devices. In such cases a scaling factor $c_{x,y}$ has to be applied. The corrected B-field components are then given by Adrian-Martinez et al. 2012

$$B_{x,y}^{\mathrm{corr}} = c_{x,y}\left(B_{x,y} - B_{x,y}^{\mathrm{off}}\right) \tag{3.2}$$

The corrected value of the magnetic field $B_{x,y}^{\mathrm{corr}}$ is used to calculate the heading of the ANTARES storeys. The compass calibration is done *in situ* as anthropogenic magnetic fields are absent in the deep sea.

Tiltmeter calibration
As the tiltmeter's measurements are based on the movement of a fluid, it is very important to know how the TCM2 card is mounted on the storey. Both, orientation of the TCM2 as well as offsets of pitch and roll were measured in the laboratory, before line deployment. Further, pitch and roll are calibrated *in situ*. Over a certain period of time, pitch and roll are expected to vary around the offsets measured in the laboratory. Changing the sea current's direction leads to a different orientation between the tiltmeters and the inclination of a storey. Exemplary, the variation in time for pitch and roll is shown in Figure 3.3 for line 12 storey 9 for a period of two months from November 2010 to December 2010

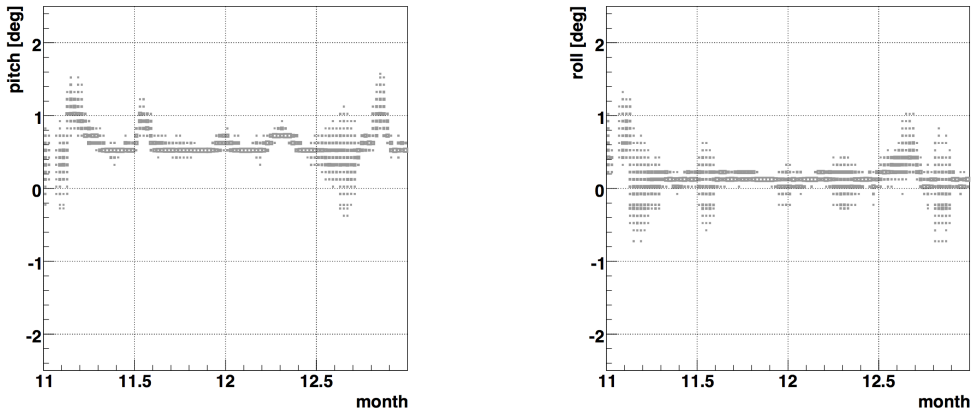

Figure 3.3: Measured pitch (left) and roll (right) values for line 12 storey 9 for 2010/Nov - 2010/Dec.

3.3 The Line Shape Model

Only for storeys that are equipped with a hydrophone the position can be determined via triangulation. In order to get the position of storeys without hydrophone a mechanical model was developed based on the principles of flow resistance, R, in the sea current and buoyancy, B. The zenith angle, θ, of the i-th detector element (i.e., the storey's inclination) is determined by Adrian-Martinez et al. 2012

$$\tan(\theta_i) = \frac{\sum_{j=i}^{N} R_j}{\sum_{j=i}^{N} B_j} \tag{3.3}$$

where B_j is the difference between buoyancy and the weight in air of detector element j. The flow resistance R_j is given by $R_j = \frac{1}{2}\rho c_{w,j} A_j v^2$ where A_j is the cross-section of detector element j perpendicular to the sea current with velocity v. $c_{w,j}$ is the drag coefficient and ρ is the density of sea water.

From the zenith angle $\tan(\theta_i)$ the slope of the line at detector element i can be calculated

according to

$$\tan(\theta) = \frac{dr(z)}{dz} = \frac{R(z)}{B(z)} \tag{3.4}$$

where $r(z)$ is the radial elongation of the line at height z and $R(z)$ and $B(z)$ are continuous functions, that follow from smearing out the flow resistance, R_j, and buoyancy, B_j, over the total length of the line (Adrian-Martinez et al. 2012).

Integration of Equation 3.4 gives the radial displacement, $r(z)$, according to

$$r(z) = \int_0^z dz' \frac{R(z')}{B(z')} = \left[\frac{b}{c}z - \frac{ad-bc}{d^2} ln(1 - \frac{d}{c}z)\right] v^2 \tag{3.5}$$

where the coefficients a, b, c and d are given by

$$\begin{aligned} a &= 25\,(R_{\text{storey}} + R_{\text{cable12m}}) + R_{\text{cable100m}} + R_{\text{buoy}} \\ b &= \frac{1}{h}\,(25\,(R_{\text{storey}} + R_{\text{cable12m}}) + R_{\text{cable100m}}) \\ c &= 25\,(B_{\text{storey}} + B_{\text{cable12m}}) + B_{\text{cable100m}} + B_{\text{buoy}} \\ d &= \frac{1}{h}\,(25\,(B_{\text{storey}} + B_{\text{cable12m}}) + B_{\text{cable100m}}) \end{aligned} \tag{3.6}$$

h is the height of the line. The flow resistance R_j and buoyancy B_j of the corresponding detector unit j were measured in the laboratory and are given by Adrian-Martinez et al. 2012

$$\begin{aligned} R_{\text{storey}} &= 383.8\ \text{Ns}^2/\text{m}^2 \\ R_{\text{cable12m}} &= 222\ \text{Ns}^2/\text{m}^2 \\ R_{\text{cable100m}} &= 1850\ \text{Ns}^2/\text{m}^2 \\ R_{\text{buoy}} &= 453\ \text{Ns}^2/\text{m}^2 \\ B_{\text{storey}} &= 265.6\ \text{N} \\ B_{\text{cable12m}} &= -52.9\ \text{N} \\ B_{\text{cable100m}} &= -440\ \text{N} \\ B_{\text{buoy}} &= \approx 7\ \text{kN} \end{aligned}$$

In Figure 3.4, the elongation of a line depending on the sea current velocity, v_{sea}, is shown. The elongations are plotted for $v_{\text{sea}} = 0, 5, 10, 15, 20$ and 25 cm/s.

For small velocities ($\lesssim 5$ cm/s) the elongation of the line for storey 25 is approximately 1 m, increasing up to ~ 25 m for velocities ~ 25 cm/s.

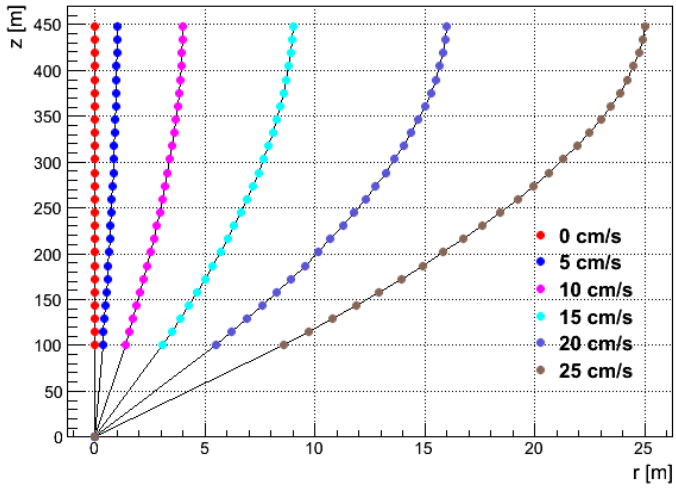

Figure 3.4: Radial elongation of an ANTARES line depending on the height, z, and the velocity of the sea current, v_{sea}, for $v_{\text{sea}} = 0$ (red), 5 (blue), 10 (magenta), 15 (turquoise), 20 (purple) and 25 cm/s (faint brown). The height is measured from the sea bed. For presentation purposes lines appear with a different length.

3.4 Detector Alignment

The hydrophone positions are determined for time intervals of two minutes. This is done offline by the ANTARES group in Marseilles. The triangulated positions are written to a data-base. Also, the data for pitch and roll, as well as the heading are available in the data-base for the same time interval. The positions are fitted to the line shape model introduced in the previous subsection.

The line shape formula 3.5 is used to perform a χ^2 fit to the five triangulated hydrophone positions of each line with the sea current velocity v as free parameter. Practically, the sea current velocity v in Equations 3.4 and 3.5 is decomposed into its components in x- and y-direction, v_x and v_y. Simultaneously, the inclination of each storey is obtained from Equation 3.4. Having fit v_x and v_y additionally the line's azimuth angle (direction of inclination) ϕ_{Line} is given by

$$\tan\phi_{\text{Line}} = \frac{v_y}{v_x} \tag{3.7}$$

The fitted velocity for lines 1,7 and 12 and their azimuth angles are shown in Figure 3.5 for the year 2010.

The fitting procedure takes into account Gaussian errors for the uncertainties on hydrophone positions (5 cm), heading (1 degree) and pitch and roll (both 0.2 degrees).

To achieve an accuracy sufficient for the storey's position and orientation it is required that at least one hydrophone and ten tiltmeters per line are working. If this was not the

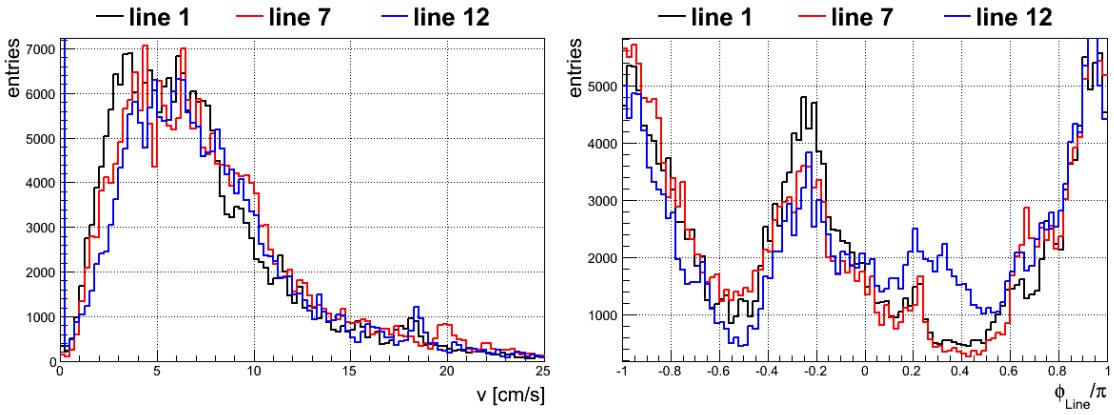

Figure 3.5: Fitted sea current velocity v^{fit} and the fitted line azimuth $\phi^{\text{fit}}_{\text{Line}}/\pi$ for line 1 (black), 7 (red) and 12 (blue) in the year 2010.

case, no detector alignment for the whole detector was written to the data-base for earlier versions of the alignment algorithm. This can be the case during the first minutes after starting the data acquisition, or if there are communication problems of the detector electronics with the corresponding read out procedures installed directly at the detector or at the shore station.

Under the assumption that the sea current doesn't change drastically over short periods and distances between certain lines this "missing alignment problem" is avoided by the following procedure, that was implemented in the scope of this work: the average velocity of the sea current from all lines used in the fit is calculated according to

$$\langle v \rangle = \frac{1}{n_{\text{fit}}} \sum_{i=1}^{n_{\text{fit}}} v_i^{\text{fit}} \tag{3.8}$$

where n_{fit} is the number of lines that could be fit and v_i^{fit} is the corresponding velocity of line i that was fit. The mean velocity $\langle v \rangle$ is applied to the line shape formula (Eq. 3.5) and the storey positions of lines that couldn't be fit is calculated with $\langle v \rangle$.

The time evolution of the sea current velocity is shown on the left hand side of Figure 3.6. Presented is the period of one day (2008/01/10). For the same day the deviation of the velocity obtained for the individual lines from the average velocity of all lines is shown on the right hand side.

Although the fitted sea current velocities can differ up to 0.8 cm/s between certain lines at a given time, this difference remains almost constant over the period of one day, e.g line 7 (turquoise data points in Figure 3.6) shows the largest fitted sea current velocities. This directly translates into the residuals, $v - \langle v \rangle$, of the fitted sea current velocities. They are grouped around zero. Nevertheless, the maximum residual is ± 0.5 cm/s. This justifies the approximation to apply an averaged velocity to lines where an insufficient amount of hydrophone and/or tiltmeter data is available.

The new alignment algorithm leads to a significant increase of the amount of available

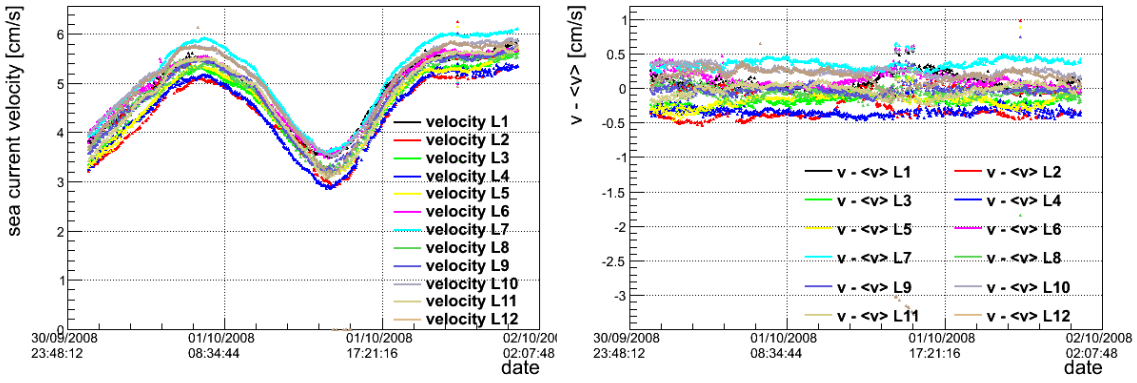

Figure 3.6: Evolution of the lines velocities for day 2008/01/10 on the left hand side. Right hand side: residual $v - \langle v \rangle$ of the fitted sea current velocity for each line for the same day.

alignment data in the year 2009 of ∼42% (Figure 3.7). In 2007 ∼27% more data is available and ∼4% in 2008 (two months in 2008, the detector was not operational and the change from six minute periods to two minute periods took place[1]). From January of 2007 until the end of March of 2008 alignment TimeStamps covered a time period of six minutes. Unless the change from six to two minutes was already in March, the old alignment algorithm used the six minute TimeStamp until the end of May. If the detector is read out more often it is far more likely that some problems occur during the read out and no hydrophone and/or tiltmeter data is available leading to missing alignment. The other way round, if TimeStamps span over a bigger period of time it is far more likely that the detector read out problems vanish. Further, in 2008 there was a two months shut down of the detector due to technical problems. These are the reasons why the year 2008 only shows a small deviation in the amount of available alignment data.

3.5 Error Estimation of the Alignment Procedure

In earlier versions of the alignment algorithm no error on the storey's position and orientation was calculated. These errors are crucial to estimate uncertainties of subsequent track reconstruction algorithms. In the scope of this work a Gaussian error propagation was implemented. From alignment version v:0.994 onwards, the errors are calculated for every aligned TimeStamp and are written to the data-base.

The error estimation is part of this section. As already mentioned in the previous section, the only free parameter of the fitting procedure is the sea current velocity in x and y direction. Remembering the lineshape formula 3.5

$$r(z) = \left[\frac{b}{c}z - \frac{ad - bc}{d^2} ln(1 - \frac{d}{c}z)\right] v^2 \tag{3.9}$$

[1]The hydrophone positions, used for fitting the line shape formula (Eq. 3.5), are determined via sending acoustic signals in a programmable periodic cycle, so-called TimeStamps

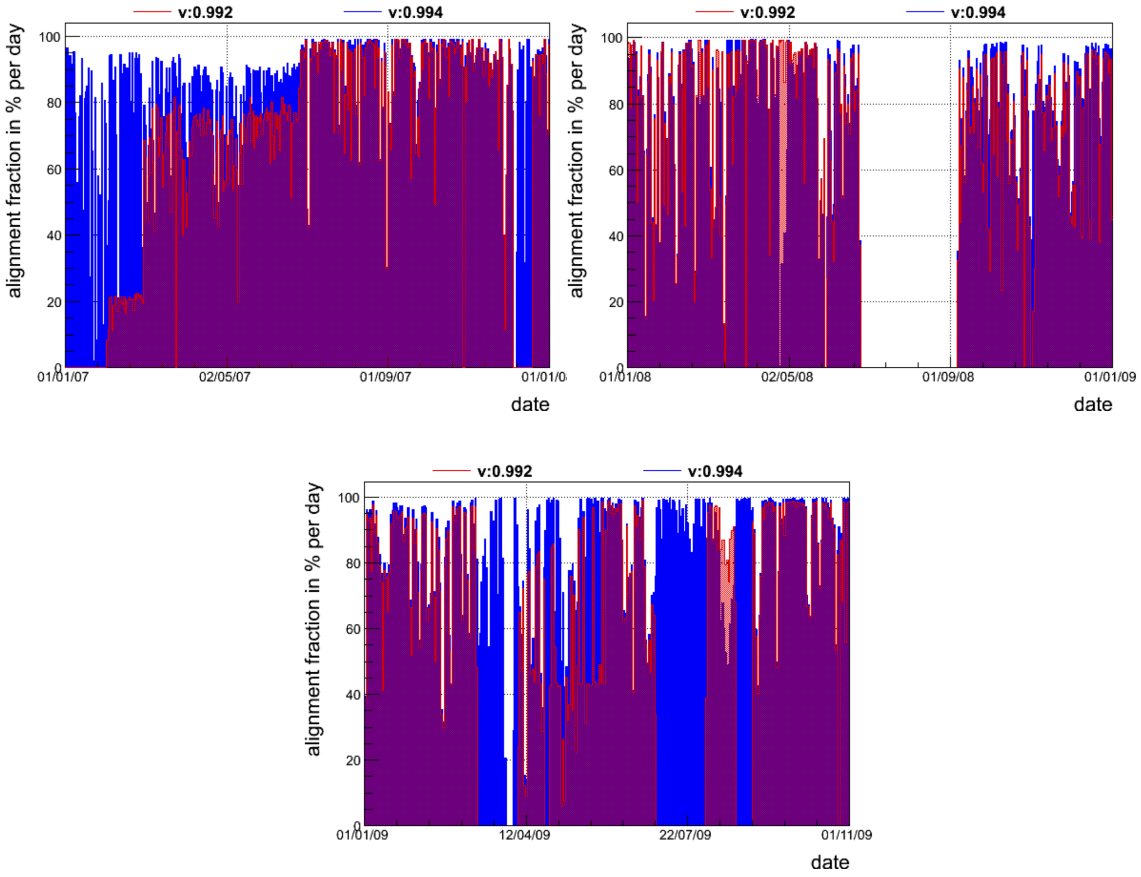

Figure 3.7: Alignment coverage per day normalized to the maximum alignment coverage that can be achieved; colors: blue: alignment algorithm version v:0.994, red: alignment algorithm version v:0.992; shown are the differences for years 2007 (upper left), 2008 (upper right) and 2009 (bottom center) until October.

where $v^2 = v_x^2 + v_y^2$. The storey's horizontal position (x, y) is connected to the line's azimuth angle

$$\phi_{\text{Line}} = \arctan(v_y/v_x) \tag{3.10}$$

according to

$$\begin{aligned} x(v_x, v_y) &= r(z) \cdot \cos\phi_{\text{Line}} \\ y(v_x, v_y) &= r(z) \cdot \sin\phi_{\text{Line}} \end{aligned} \tag{3.11}$$

Spatial Errors

The spatial errors on the storey's x and y position, Δx and Δy are calculated according to

$$\Delta x = \sqrt{\left(\frac{\partial x(v_x, v_y)}{\partial v_x} \cdot \Delta v_x\right)^2 + \left(\frac{\partial x(v_x, v_y)}{\partial v_y} \cdot \Delta v_y\right)^2}$$
$$\Delta y = \sqrt{\left(\frac{\partial y(v_x, v_y)}{\partial v_x} \cdot \Delta v_x\right)^2 + \left(\frac{\partial y(v_x, v_y)}{\partial v_y} \cdot \Delta v_y\right)^2} \tag{3.12}$$

where $\Delta v_{x,y}$ are errors on the sea current velocity resulting from the χ^2 fit. $(\partial x, y/\partial v_{x,y})$ are the derivatives of Equations 3.11.

Error for Pitch and Roll

Pitch p and Roll r of a given storey depend on the storey's azimuth angle φ_{storey} and its zenith angle $\vartheta_{\text{storey}}$ and are given by

$$\begin{aligned} p(\varphi_{\text{storey}}, \vartheta_{\text{storey}}) &= \left|\arctan\left(\sqrt{\frac{\tan^2\vartheta_{\text{storey}}}{1+\tan^2\varphi_{\text{storey}}}}\right)\right| \\ r(\varphi_{\text{storey}}, \vartheta_{\text{storey}}) &= \left|\arctan\left(\tan\varphi_{\text{storey}} \cdot \sqrt{\frac{\tan^2\vartheta_{\text{storey}}}{1+\tan^2\varphi_{\text{storey}}}}\right)\right| \end{aligned} \tag{3.13}$$

The errors for p and r are then calculated according to

$$\Delta p,r = \sqrt{\left(\frac{\partial p,r}{\partial \varphi_{\text{storey}}} \cdot \Delta\varphi_{\text{storey}}\right)^2 + \left(\frac{\partial p,r}{\partial \vartheta_{\text{storey}}} \cdot \Delta\vartheta_{\text{storey}}\right)^2} \tag{3.14}$$

$\Delta\varphi_{\text{storey}}$ and $\Delta\vartheta_{\text{storey}}$ are errors on the storey's zenith and azimuth angle (for calculation see Eq. 3.18). φ_{storey} and $\vartheta_{\text{storey}}$ are defined by

$$\begin{aligned} \tan(\vartheta_{\text{storey}}) &= \tan(\arccos(dz)) \\ \tan(\varphi_{\text{storey}}) &= \tan\left(\arctan\left(\frac{dy}{dx}\right) - \pi + h\right) \end{aligned} \tag{3.15}$$

where h is the heading given by Equation 3.1. dz, dy and dx are the derivatives of the lineshape formula 3.5 with respect to x,y and z position. The derivatives are given by

$$\begin{aligned} dx &= \cos\phi_{\text{Line}} \cdot dr \\ dy &= \sin\phi_{\text{Line}} \cdot dr \\ dz &= \sqrt{1 - dx^2 - dy^2}. \end{aligned} \tag{3.16}$$

dr is the derivative of the line shape formula 3.5 with respect to the z- position. The error

on the line's azimuth angle is calculated by

$$\Delta\phi_{\text{Line}} = \sqrt{\left(\frac{\partial\phi_{\text{Line}}}{\partial v_y}\cdot\Delta v_y\right)^2 + \left(\frac{\partial\phi_{\text{Line}}}{\partial v_x}\cdot\Delta v_x\right)^2} \tag{3.17}$$

With the above Equations the errors of the storey's azimuth, φ_{storey}, and zenith angle, $\vartheta_{\text{storey}}$, are calculated according to

$$\begin{aligned}\Delta\vartheta_{\text{storey}} &= \frac{d\vartheta_{\text{storey}}}{d(dz)}\cdot\Delta(dz) \qquad (3.18)\\ \Delta\varphi_{\text{storey}} &= \sqrt{\left(\frac{\partial\varphi_{\text{storey}}}{\partial(dy)}\cdot\Delta(dy)\right)^2 + \left(\frac{\partial\varphi_{\text{storey}}}{\partial(dx)}\cdot\Delta(dx)\right)^2 + \left(\frac{\partial\varphi_{\text{storey}}}{\partial h}\cdot\Delta h\right)^2}\end{aligned}$$

where the uncertainty on the heading is assumed to be 1° (given by the manufacturer of the compass device). Plugging all above formulae together the uncertainties on the storey's position are calculated for each alignment cycle and are written to the data-base. Exemplary the errors on the storey's x and y position are shown for April of 2010 (Figure 3.8).

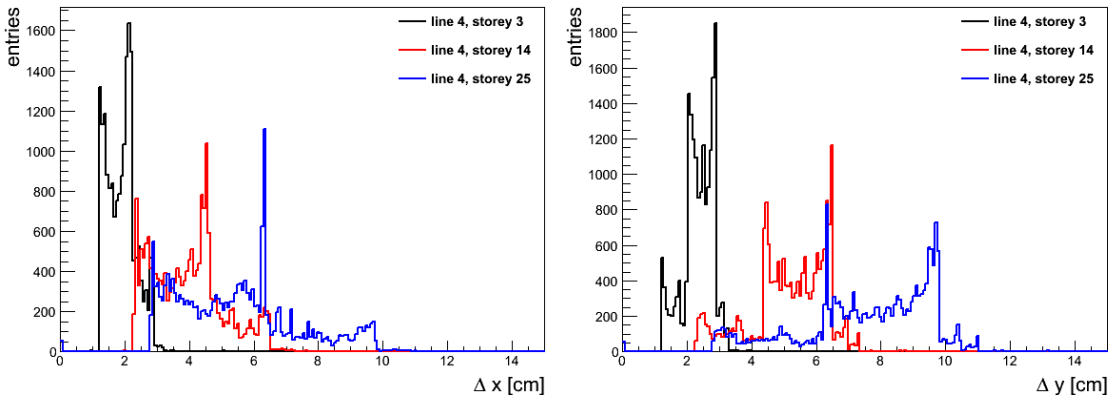

Figure 3.8: Calculated error on the storey's x (left) and y position (right) plotted on the x-axis. Shown are storeys 3 (black line), 14 (red line) and 25 (blue line) for April 2010.

As expected, errors on higher storeys are the biggest ($\lesssim$ 15 cm), whereas uncertainties on lower storeys are smaller. Further, errors in y-direction exceed errors in x-direction, as the sea current's preferred direction was the y-direction during this period.

After providing the track reconstruction with storey positions with an uncertainty better than 15 cm, in the second part of my thesis I will focus on the search for supersymmetric Dark Matter (DM).

4

Dark Matter

4.1 Need for Dark Matter

In this Section a selection of observational hints and evidences for the existence of dark matter are introduced. Further, the theoretical background of supersymmetric extension of the standard model of particle physics is explained. Amongst other things, supersymmetry provides a plausible particle candidate to explain dark matter.

4.1.1 Galaxy Rotation Curves

From the measurement of rotation curves of spiral galaxies their mass can be determined. They are measured via Doppler shifts of spectral lines. From Keplerian dynamics, the rotation velocity is expected to decrease with increasing distance from the center of the galaxy. Against this expectation, the rotation curve for a typical galaxy increases linearly with the distance for the inner part of the galaxy and saturates for the outer part of the galaxy (Figure 4.1). Many galaxies that show this behavior were found (Persic et al. 1996).

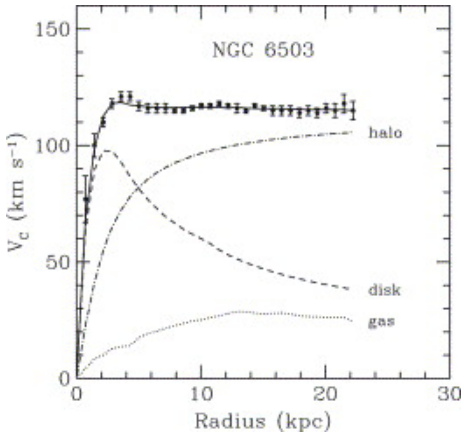

Figure 4.1: Rotation curve of galaxy NGC 6503. Full circles are measured data. The dotted line represents the contribution from gas, the dashed line the contribution from the disc of the galaxy. The dash-dotted line is the contribution from an assumed dark matter halo. Picture from Bertone et al. 2005

This behavior indicates an additional component of non luminous mass and can be explained under the assumption that galaxies are surrounded by a halo of dark matter.

4.1.2 Cosmic Microwave Background

Due to the high energy density in the early Universe, atoms only existed in an ionized state. Photon absorption and emission processes were in the state of equilibrium and the early Universe was opaque for photons. With the expansion of the Universe it cooled down and ionized atoms recombined with electrons and created the first atoms. At that time ($\sim$ 380 000 years after the Big Bang), the Universe became transparent for photons known as cosmic microwave background. It was discovered by Penzias & Wilson 1965.

The cosmic microwave background is a perfect black body with a temperature of ~ 2.7 K. Satellite missions like COBE [1] or WMAP [2] have investigated the temperature fluctuations of the CMB (Figure 4.2).

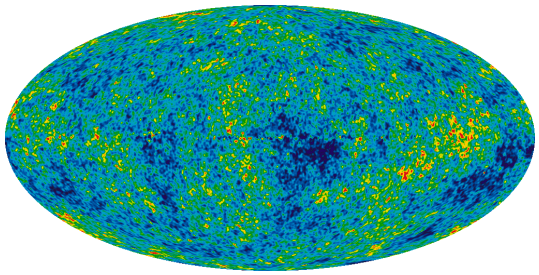

Figure 4.2: Sky map of temperature fluctuations of the Cosmic Microwave Background measured by WMAP. Picture taken from http://map.gsfc.nasa.gov.

Red spots in Figure 4.2 are $2.0 \cdot 10^{-4}$ K hotter than blue spots. These temperature fluctuations originate from primordial curvature fluctuations during inflation and determine the composition of the early universe (Challinor 2006). The temperature fluctuations were expanded into a multipole series (Figure 4.3).

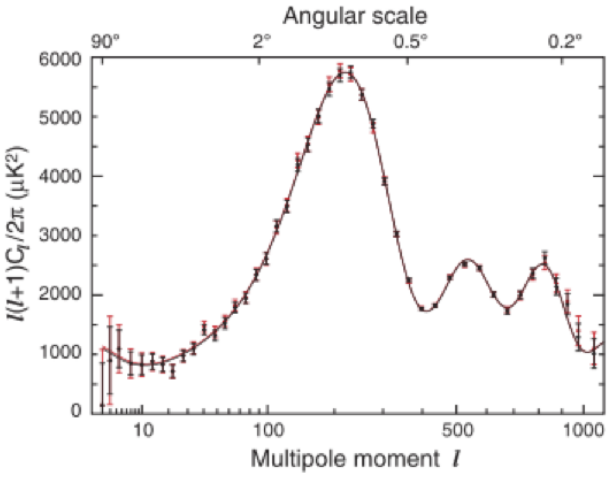

Figure 4.3: Multipole expansion of the temperature fluctuations shown in Figure 4.2. Picture from Hinshaw et al. 2012

From Figure 4.3 cosmological parameters can be derived. The first three peaks are acoustic peaks whose positions depend on the matter density Ω_m and baryon density Ω_b (Challinor 2006). The total energy density of today's universe is composed of 4.6% ordinary, baryonic

[1] http://lambda.gsfc.nasa.gov/product/cobe
[2] http://map.gsfc.nasa.gov

matter, 71.4% dark energy and 24% dark matter (Komatsu et al. 2010). At the time, when this work was written, new results from the Planck[1] mission were released. The new value for the cold dark matter relic density was found to be $\Omega h^2 = 0.1196 \pm 0.0031$ (Ade et al. 2013). Consequently, the Universe's composition changed and 4.9% are made up by ordinary matter, 26.8% account for dark matter and 68.3% account for dark energy. The new Planck results couldn't be considered in this work anymore.

4.2 Supersymmetric Dark Matter

4.2.1 Motivation

All interactions that appear in our universe can be described by four fundamental forces. That are gravitation, strong, weak and electromagnetic interaction. Except gravitation, the latter are theoretically described by quantum field theories based on the principle of gauge invariance. That are the gauge groups $SU(3)$ for strong interactions, $SU(2)$ for weak and $U(1)$ for electromagnetic interactions. They can be unified to the standard model of particle physics (SM), described by the gauge group $SU(3)_C \times SU(2)_L \times U(1)_Y$. The SM is one of the most accurate theories in physics today. It is extremely predictive, see e.g. the prediction of the existence of $W^{\pm}$ and Z bosons, the gauge bosons of the weak interaction. Moreover, it is one of the most accurate models that exist. Nevertheless there are still some unsolved problems, e.g. how to break the electroweak symmetry (EWSB), no natural dark matter candidate, no exact unification of the gauge couplings and a few more. EWSB is assumed to be mediated via the Higgs boson. In 2012, a new scalar boson was discovered which is a Higgs boson (The CMS Collaboration 2013,The ATLAS Collaboration 2012a). Hence, the only particle that can have a non zero vacuum expectation value (vev) and therefore, break electroweak symmetry must be scalar, the Higgs must also be a scalar. Unfortunately, it can obtain large radiative corrections due to renormalization effects that lead to quadratic divergences

$$\delta M_H^2 \propto g^2 \int^{\Lambda} \frac{d^4k}{(2\pi)^4} \frac{1}{k^2} \sim g^2 \Lambda^2 \tag{4.1}$$

where Λ is the cut-off scale of the theory. Therefore, the SM is only valid up to that scale. g is the coupling constant related to the coupling to the Higgs boson and k is the momentum of the boson in the loop of the 'self-energy' diagram. With radiative corrections of equation (4.1) it is not possible to obtain a Higgs boson with mass $\sim$ 125 GeV/c^2 (The CMS Collaboration 2013,The ATLAS Collaboration 2012a) unless one introduces an unnatural fine tuning of parameters, order-by-order in perturbation theory.

Now, the basic idea of supersymmetry is to connect bosonic degrees of freedom with the fermionic ones by introducing the generator Q of supersymmetric transformations that acts on a fermion f and boson b according to

$$\bar{Q}|b_{\mathrm{S}}\rangle = |f\rangle \text{ and } \bar{Q}|f\rangle = |b_{\mathrm{V}}\rangle \text{ and } Q|f\rangle = |b_{\mathrm{S}}\rangle. \tag{4.2}$$

[1] http://sci.esa.int/planck/

According to Equation (4.2) Q transforms a fermion, f into a boson, b and vice versa. The subscripts S and V denote scalar and vector bosons, respectively. Moreover, Q only acts on the spin of the particle and not on its mass. If supersymmetry is realized in nature every SM fermion must have a scalar partner with equal mass as well as every SM boson must have a fermionic partner with equal mass. In that way, the quadratic divergences of equation (4.1) are avoided because boson and fermion loop corrections have opposite sign and cancel each other, i.e.

$$\delta M_H^2 \sim g^2\Lambda^2|_{boson} - g^2\Lambda^2|_{fermion} = 0. \tag{4.3}$$

In this manner a light Higgs boson with $M_H \sim \mathcal{O}(M_W)$ can be obtained.

In the following sections the framework of the **M**inimal **S**upersymmetric **S**tandard **M**odel (MSSM) is explained as well as the mechanism how to break supersymmetry (SUSY). The SUSY generator Q only acts on the spin (helicity) of a given state and not on its mass. Thus, standard model particles and their supersymmetric partners are degenerate in mass. As no SUSY particles are discovered with equal mass to their standard model partners, SUSY must be broken.

4.2.2 Minimal Supersymmetric Standard Model

In the minimal supersymmetric extension of the standard model, every SM particle has exactly one superpartner. The MSSM has the same gauge group as the SM, namely $SU(3)_C \times SU(2)_L \times U(1)_Y$. Every SM spin-1 particle makes up a vector multiplet with its supersymmetric spin-1/2 particle. Like in the SM 3 generations quarks and leptons with spin 1/2 exist that are grouped to chiral superfields with their scalar supersymmetric partners, the squarks and sleptons ($\tilde{Q}$,$\tilde{u}_R$,$\tilde{d}_R$,$\tilde{L}$,$\tilde{l}_R$). In contrast to the SM, there are two Higgs fields, $\tilde{H}_1 = (\tilde{H}_1^0, \tilde{H}_1^-)$ and $\tilde{H}_2 = (\tilde{H}_2^+, \tilde{H}_2^0)$. The scalar components of $\tilde{H}_1^0$ and $\tilde{H}_2^0$ get a non-zero vacuum expectation value (vev) and break down the electroweak symmetry $SU(2) \times U(1)$. For chirality reasons $\tilde{H}_1^0$ can only generate masses of down-type quarks and charged leptons, whereas $\tilde{H}_2^0$ only generates the masses of up-type quarks (neutrinos are regarded as massless). The gauge symmetry of the SM is free from anomalies, so the MSSM also must be anomaly free. Therefore, an even number of Higgs fields is required. To achieve a good agreement with the experimental measured value of the weak mixing angle $\sin(\Theta_W) = 0.231$ two Higgs fields are necessary (Weinberg 2005,Acciari et al. 1998).

The fields $\tilde{H}_1$ and $\tilde{H}_2$ have eight degrees of freedom (DoF). Three of them are 'eaten' by the weak gauge bosons $W^\pm$ and Z_0. The five remaining DoFs resemble the five Higgs particles. Two of them are CP-even (H_1^0, H_2^0), one is CP-odd (A, often called pseudo scalar) and two are charged $H^\pm$. The particle content of the MSSM is shown in Table (4.1)

The interaction eigenstates of the wino, $\tilde{W}^\pm$, the two charged higgsinos, $\tilde{H}_1^-$ and $\tilde{H}_2^+$, carry the same quantum numbers and therefore mix to generate the mass eigenstates of two charginos $\chi_{1,2}^\pm$. The same holds for the bino $\tilde{B}$, the wino $\tilde{W}^3$ and the higgsinos $\tilde{H}_1^0$ and $\tilde{H}_2^0$ that mix and give the mass eigenstates of four neutralinos $\chi_{1,2,3,4}^0$.

Additionally, the so-called R-parity is introduced (Farrar & Fayet 1978). It is given by

$$R = (-1)^{2S+3B+L} \tag{4.4}$$

Supersymmetric Particles				**Standard Model Partner**	
Interaction Eigenstates		Mass Eigenstates		**+ scalar Higgs sector**	
Symbol	Name	Symbol	Name	Symbol	Name
$\tilde{q}_R$, $\tilde{q}_L$	Squark	$\tilde{q}_1$, $\tilde{q}_2$	Squark	$q = u,d,c,s,t,b$	Quark
$\tilde{l}_R$, $\tilde{l}_L$	Slepton	$\tilde{l}_1$, $\tilde{l}_2$	Slepton	$l = e,\mu,\tau$	Lepton
$\tilde{\nu}$	Sneutrino	$\tilde{\nu}$	Sneutrino	$\nu = \nu_e,\nu_\mu,\nu_\tau$	Neutrino
$\tilde{g}$	Gluino	$\tilde{g}$	Gluino	g	Gluon
$\tilde{W}^{\pm}$	Wino			$W^{\pm}$	W boson
$\tilde{H}_1^-$	Higgsino	$\chi^{\pm}_{1,2}$	Chargino	H^-	Higgs boson
$\tilde{H}_2^+$	Higgsino			H^+	Higgs boson
$\tilde{B}$	Bino			B	B boson
$\tilde{W}^3$	Wino			W^3	W boson
$\tilde{H}_1^0$	Higgsino	$\chi^0_{1,2,3,4}$	Neutralino	H_1^0	Higgs boson
$\tilde{H}_2^0$	Higgsino			H_2^0	Higgs boson

Table 4.1: Particle Content of the MSSM

where S is the spin of the particle, B and L are baryon and lepton numbers. Supersymmetric particles have $R = -1$, whereas ordinary particles have $R = 1$. If R-parity is conserved, SUSY particles can only be produced pair wise and the lightest supersymmetric particle (LSP) is stable. This makes it an excellent dark matter candidate. For the sake of completeness it should be mentioned that R-parity is not a supersymmetric issue. Grand unified theories (GUTs) suffer from the possibility of proton decays (see Figure 4.4).

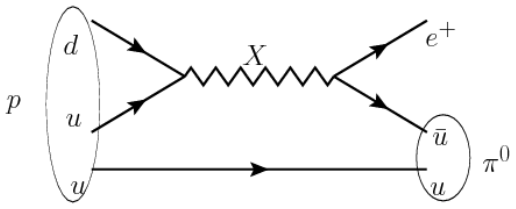

Figure 4.4: Proton decay $p \to e^+\pi^0$.

This is in conflict with experimental measurements giving a proton lifetime longer than $6.6 \cdot 10^{33}$ years (Nishino et al. 2009).

Soft Supersymmetry Breaking

The MSSM is defined by a minimal set of parameters that break SUSY "softly", i.e. only logarithmic divergences appear. Therefore, a superpotential is introduced that satisfies gauge invariance, renormalization and R-parity. Its scalar part, V_{soft}, responsible for soft SUSY breaking can be written as

$$
\begin{aligned}
V_{\text{soft}} &= \epsilon_{ij}\left(\tilde{\mathbf{e}}_R^*\mathbf{A}_E\mathbf{Y}_E\tilde{\mathbf{l}}_L^i H_1^j + \tilde{\mathbf{d}}_R^*\mathbf{A}_D\mathbf{Y}_D\tilde{\mathbf{q}}_L^i H_1^j - \tilde{\mathbf{u}}_R^*\mathbf{A}_U\mathbf{Y}_U\tilde{\mathbf{q}}_L^i H_2^j\right) \\
&+ H_1^{i*}m_1^2 H_1^i + H_2^{i*}m_2^2 H_2^i - \epsilon_{ij}(B\mu H_1^i H_2^j + h.c.) \\
&+ \tilde{\mathbf{q}}_L^{i*}\mathbf{M}_Q^2\tilde{\mathbf{q}}_L^i + \tilde{\mathbf{l}}_L^{i*}\mathbf{M}_L^2\tilde{\mathbf{l}}_L^i + \tilde{\mathbf{u}}_R^*\mathbf{M}_U^2\tilde{\mathbf{u}}_R + \tilde{\mathbf{d}}_R^*\mathbf{M}_D^2\tilde{\mathbf{d}}_R + \tilde{\mathbf{e}}_R^*\mathbf{M}_E^2\tilde{\mathbf{e}}_R \\
&+ \frac{1}{2}M_1\tilde{B}\tilde{B} + \frac{1}{2}M_2\left(\tilde{W}^3\tilde{W}^3 + 2\tilde{W}^+\tilde{W}^-\right) + \frac{1}{2}M_3\tilde{g}\tilde{g}
\end{aligned}
\tag{4.5}
$$

$\mathbf{A}_{E,D,U}$ corresponds to the trilinear couplings that appear in diagrams like figure 4.5. $M_{1,2,3}$ are the gaugino mass parameters. μ is the higgsino mass parameter and $m_{1,2}$ are the ones for Higgs mass. "Tilde" assigns the scalar components of the superfields. B is the bilinear coupling between the two Higgs fields H_1 and H_2.

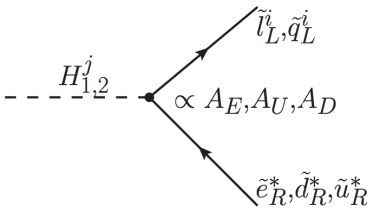

Figure 4.5: Feynman diagram for trilinear coupling A appearing in scalar superpotential Equation 4.5.

Electroweak Symmetry Breaking

Electroweak symmetry breaking in the MSSM is done via the so-called super-Higgs-mechanism. It is analogous to the Higgs mechanism in the SM. The two Higgs fields of the MSSM acquire a non-zero vev

$$
\langle H_1\rangle = \begin{pmatrix} \frac{v_1}{\sqrt{2}} \\ 0 \end{pmatrix} \qquad \langle H_2\rangle = \begin{pmatrix} 0 \\ \frac{v_2}{\sqrt{2}} \end{pmatrix}. \tag{4.6}
$$

The mass of the W-boson in the SM is related to the vevs v_1 and v_2 according to

$$
m_W^2 = \frac{1}{2}g^2\left(v_1^2 + v_2^2\right). \tag{4.7}
$$

Simultaneously, the Z-boson mass obeys equation

$$
m_Z^2 = \frac{1}{2}\left(g^2 + g'^2\right)\left(v_1^2 + v_2^2\right) \tag{4.8}
$$

where g and g' are the gauge coupling constants of $SU(2)$ and $U(1)$, respectively. The ratio of the two Higgs vevs is defined as

$$
\tan(\beta) \equiv \frac{v_2}{v_1}. \tag{4.9}
$$

The electroweak symmetry should be broken at low energies. This requirement results in two minimization conditions for the Higgs potential, V_{Higgs} (Djouadi et al. 1999)

$$
\begin{aligned}
V_{Higgs} &= \left(m_{H_1}^2+\mu^2\right)|H_1|^2+\left(m_{H_2}^2+\mu^2\right)|H_2|^2+B\mu(H_2H_1+h.c.)\\
&+ \frac{g'^2+g^2}{2}(H_1^\dagger H_1-H_2^\dagger H_2)^2+\frac{g^2}{2}(H_1^\dagger H_2)(H_2^\dagger H_1). \qquad (4.10)
\end{aligned}
$$

From the minimization conditions $\frac{\partial V_{Higgs}}{\partial H_2^0}=\frac{\partial V_{Higgs}}{\partial H_1^0}=0$ for μ^2 and $B\mu$ follows

$$
\begin{aligned}
\mu^2 &= \frac{1}{2}\left[\tan(2\beta)(m_{H_2}^2\tan\beta-m_{H_1}^2 cot\beta)-m_Z^2\right],\\
B\mu &= \frac{1}{2}\sin(2\beta)\left[m_{H_2}^2+m_{H_1}^2+2\mu^2\right]. \qquad (4.11)
\end{aligned}
$$

Consistent breaking of the electroweak symmetry can only be achieved if $\mu^2>0$. The sign of μ remains undetermined. Free parameters of the Higgs sector are the masses m_1 and m_2 and B of equation (4.5) (Gunion et al. 1990). The above minimization conditions reduce them to two independent parameters, $\tan(\beta)$ and m_A the mass of the pseudo scalar Higgs Boson A (often also assigned H_3^0).

4.2.3 Mass Spectrum of the MSSM

Neutralinos

The mass matrix $\mathcal{M}_\chi$ of the neutralino in the base of gauge eigenstates $(\tilde{B},\tilde{W}^3,\tilde{H}_1^0,\tilde{H}_2^0)$ is given by Martin 2011

$$
\mathcal{M}_\chi=\begin{pmatrix}
M_1 & 0 & -\frac{g'v_1}{\sqrt{2}} & +\frac{g'v_2}{\sqrt{2}}\\
0 & M_2 & +\frac{gv_1}{\sqrt{2}} & -\frac{gv_2}{\sqrt{2}}\\
-\frac{g'v_1}{\sqrt{2}} & +\frac{gv_1}{\sqrt{2}} & \delta_{33} & -\mu\\
\frac{g'v_2}{\sqrt{2}} & -\frac{gv_2}{\sqrt{2}} & -\mu & \delta_{44}
\end{pmatrix}. \qquad (4.12)
$$

δ_{33} and δ_{44} are loop corrections that could play an important role when calculating the relic density of the neutralinos (see Section 4.3.1). Diagonalizing $\mathcal{M}_\chi$ of Equation 4.12 gives the neutralino mass eigenstates

$$
\chi_i^0=N_{i1}\tilde{B}+N_{i2}\tilde{W}^3+N_{i3}\tilde{H}_1^0+N_{i4}\tilde{H}_2^0 \quad i=1,2,3,4 \qquad (4.13)
$$

where N is the unitary matrix that diagonalizes $\mathcal{M}_\chi$.

Charginos

Analogue to the neutralinos, $\tilde{W}^\pm$ and $\tilde{H}_{1,2}^\pm$ mix to charginos. The mass matrix is then given

by

$$\mathcal{M}_{\chi^\pm} = \begin{pmatrix} 0 & 0 & M_2 & gv_1 \\ 0 & 0 & gv_2 & \mu \\ M_2 & gv_2 & 0 & 0 \\ gv_1 & \mu & 0 & 0 \end{pmatrix}. \tag{4.14}$$

Diagonalizing $\mathcal{M}_{\chi^\pm}$ leads to the chargino mass eigenstates given by

$$\begin{aligned} \tilde{\chi}_i^- &= U_{i1}\tilde{W}^- + U_{i2}\tilde{H}_1^- \quad i = 1,2 \\ \tilde{\chi}_i^+ &= V_{i1}\tilde{W}^+ + V_{i2}\tilde{H}_2^+ \quad i = 3,4 \end{aligned} \tag{4.15}$$

where U and V are unitary matrices that diagonalize $\mathcal{M}_{\chi^\pm}$.

Sfermions
In the base of the interaction eigenstates $(\tilde{f}_L, \tilde{f}_R)$ the mass matrix for sfermions is given by (see e.g. Ref. Djouadi et al. 2007)

$$\mathcal{M}_{\tilde{f}}^2 = \begin{pmatrix} m_{\tilde{f}_L}^2 + (I_{3f} - q_f \sin^2\Theta_W) m_Z^2 \cos 2\beta + m_f^2 & m_f(A_f - \mu\cot\beta) \\ m_f(A_f - \mu\cot\beta) & m_{\tilde{f}_R}^2 - q_f \sin^2\Theta_W m_Z^2 \cos 2\beta + m_f^2 \end{pmatrix}. \tag{4.16}$$

I_{3f} represents the z-component of the weak isospin, Θ_W is the weak mixing angle and q_f the charge of the corresponding fermion with mass m_f. A_f are the trilinear couplings for sfermions of species $\tilde{f}$ with mass $m_{\tilde{f}}$. μ is again the Higgs mass parameter. By diagonalizing $\mathcal{M}_{\tilde{f}}^2$ in Equation 4.16 the mass eigenstates $(\tilde{f}_1, \tilde{f}_2)$ are obtained. The squared mass of a sfermion of species $\tilde{f}$ is then given by

$$m_{\tilde{f}_{1,2}}^2 = m_f^2 + \frac{1}{2}\left[m_{\tilde{f}_L}^2 + m_{\tilde{f}_R}^2 \mp \sqrt{\left(m_{\tilde{f}_L}^2 + m_{\tilde{f}_R}^2\right)^2 + 4m_f^2(A_f - \mu\cot\beta)^2} \right]. \tag{4.17}$$

4.3 Relic Density and Neutralino Capture

4.3.1 Relic Density

In the early Universe matter was in equilibrium, i.e. existing particles annihilate with each other, or decay and are produced again. With the expansion of the Universe, it cools down. In equilibrium the number density of WIMPs n_{WIMP} is given by

$$n_{\text{WIMP}} \propto e^{-\frac{m_{\text{WIMP}} \cdot c^2}{kT_{\text{Universe}}}}. \tag{4.18}$$

With decreasing temperature, also the number density of WIMPs decreases. At some point the population of WIMPs gets depleted too much and the probability of one WIMP

annihilating with another becomes small. A substantial number of WIMPs is left over called relic density Ω_{WIMP}. This mechanism is also known as "freeze out". The temporal evolution of the number density n_{WIMP} is described by the Boltzmann Equation (exact calculation see Edsjö 1997 and references therein)

$$\frac{dn}{dt} = -3Hn - \langle \sigma_A v \rangle \left(n^2 - n_{eq}^2 \right) \tag{4.19}$$

where H is the Hubble constant responsible for the expansion of the Universe. $\langle \sigma_A v \rangle$ is the thermally averaged WIMP annihilation cross-section times the velocity of the WIMP and n_{eq} is the number density of the WIMP in thermal equilibrium. The WIMPs relic density is then given by

$$\Omega_{\mathrm{WIMP}} = \frac{m_{\mathrm{WIMP}} \cdot n_{\mathrm{WIMP}}}{\rho_{\mathrm{crit}}} \tag{4.20}$$

where ρ_{crit} is the critical density, where $\Omega = \rho/\rho_{\mathrm{crit}} = 1$. In the following focus is set on the neutralino as WIMP.

4.3.2 Neutralino Capture

Neutralinos propagate through interstellar media and loose energy via scattering processes. If they have lost sufficiently energy they can be gravitationally trapped inside massive bodies, e.g. the Sun or the Earth. The temporal evolution of the neutralino number density N_χ is given by

$$\frac{dN_\chi}{dt} = C - C_A N_\chi^2 - C_E N_\chi \tag{4.21}$$

where C describes the neutralino capture itself. The second term is twice the annihilation rate Γ_A as pairs of neutralinos annihilate. The last term describes the evaporation of neutralinos and can be neglected for neutralinos with mass above 5 GeV (Griest & Seckel 1987,Gould 1987). Solving Equation 4.21 with respect to the annihilation rate Γ_A results in

$$\Gamma_A = \frac{1}{2} C \tanh^2 \left(\frac{t}{\tau} \right) \tag{4.22}$$

where τ is the time until equilibrium between capture and annihilation is reached. If $t \gg \tau$ (e.g. $t_{\text{solar system}} \gg \tau$) the annihilation rate is no longer determined by the annihilation cross-section but solely determined by the capture rate C. In this case, the annihilation rate is at its maximum and a maximum yield of annihilation products will result. Indirect detection experiments, which are part of the discussion in the next subsection, benefit from this maximum annihilation rate.

The capture rate in the Sun C_{Sun} for a neutralino with mass m_χ is given by Gould 1991

$$C_{\mathrm{Sun}} = 3.35 \mathrm{s}^{-1} \frac{\rho_0}{0.3 \text{ GeV cm}^{-3}} \left(\frac{270 \text{ km/s}}{\bar{v}} \right)^3 \frac{\sigma_H^{sd} + \sigma_H^{si} + 0.07 \sigma_{He}^{si}}{10^{-6} \text{ pb}} \frac{100 \text{ GeV}}{m_\chi}. \tag{4.23}$$

ρ_0 is the expected dark matter density of neutralinos at the Sun's position (local dark matter density) and is given by $\rho_0 = 0.3$ GeV/cm^3 (Nakamura et al. 2011). $\bar{v} = \sqrt{\langle v^2 \rangle}$ is the velocity dispersion of the neutralino. σ_H^{sd}, σ_H^{si} and σ_{He}^{si} are the elastic neutralino scattering cross-sections for spin-dependent and spin-independent scattering on hydrogen atoms and spin-independent elastic scattering on helium atoms, respectively.

4.4 Search for Dark Matter

In this section the different experimental methods for the detection of a dark matter particle are introduced. This work concentrates on two classes of dark matter search experiments. On the one hand, there is the direct search where dark matter particles scatter off atomic nuclei. On the other hand, indirect detection methods search for self annihilation products of dark matter particles. Last but not least, dark matter particles can be produced by colliding standard model particles. The three principles can be illustrated as in Figure 4.6.

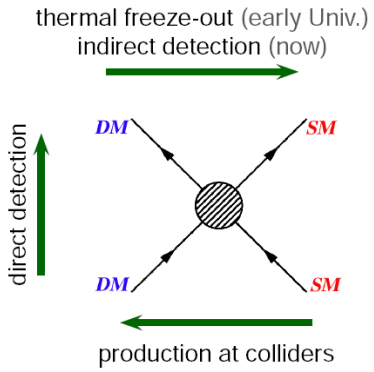

Figure 4.6: Different dark matter search strategies. From right to the left: two colliding standard model particles may produce dark matter particles (production of dark matter); from bottom to the top: dark matter particles scatter off a standard model particle (direct detection); from left to the right: two annihilating dark matter particles produce standard model particles (indirect detection). Picture taken from http://www.mpi-hd.mpg.de.

4.4.1 Direct Search

Each experiment dedicated to the direct search for dark matter follows the same principles. Every galaxy is assumed to be surrounded by a halo consisting of dark matter particles. As the Earth passes through this halo and therefore, through dark matter particles, they can interact with ordinary matter by scattering off atomic nuclei and transferring energy to them. This recoil energy may be detected. The difference between different direct detection experiments is the method of measuring the recoil energy and the target material used in the detector. For example, the XENON experiment uses ionization and scintillation methods when measuring the recoil energy. The different detection techniques of the different experiments are illustrated in Figure 4.7.

The differential recoil energy spectrum per unit mass is given by (Armengaud 2010)

$$\frac{dR}{dE_r} = \frac{\sigma_0 \rho_0}{2 m_{DM} m_{\mathrm{red}}^2} F^2(q) \int_{v_{\min}}^{\infty} dv \frac{f(v)}{v} \tag{4.24}$$

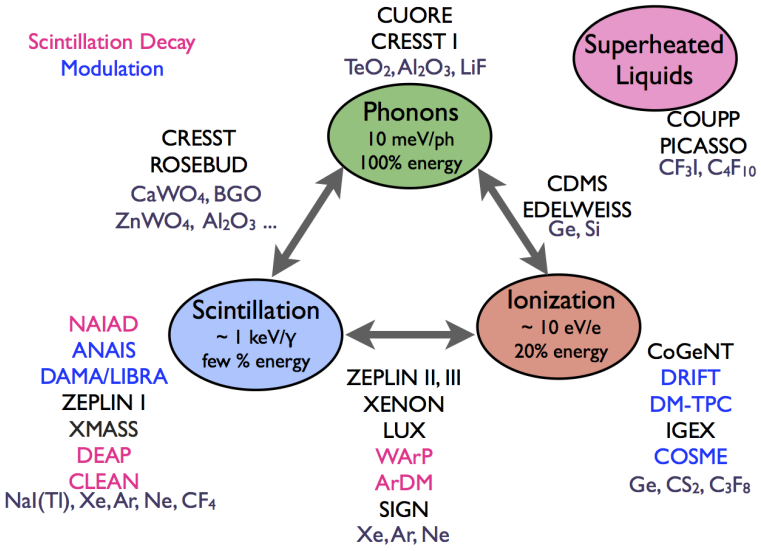

Figure 4.7: Different detection techniques of the different direct detection dark matter search experiments. Picture taken from Saab 2012.

where ρ_0 is the local dark matter density. σ_0 denotes the elastic scattering cross-section between the dark matter particle and the target nucleus. m_{red} is the reduced mass of the dark matter particle with mass m_{DM} and the nucleus with mass m_N where $m_{\text{red}} = \frac{m_{DM} m_N}{m_{DM}+m_N}$. $F^2(q)$ is the nuclear form factor at a momentum transfer q. $f(v)$ is the velocity distribution of dark matter particles in the halo, which is usually assumed to follow a Maxwellian distribution.

Scalar (spin-independent) cross-section:
The differential cross-section for scalar (spin-independent) interactions is given by (Jungmann et al. 1996)

$$\frac{d\sigma}{d|q|^2} = \frac{\sigma_0}{4m_{\text{red}}^2 v^2} F^2(q) = [Z f_p + (A-Z) f_n]^2 \frac{F^2(q)}{\pi v^2} \tag{4.25}$$

where f_p and f_n denote the coupling of the dark matter particle to the proton and neutron, respectively. From Equation 4.25 the spin-independent cross-section, σ_0 can be derived as

$$\sigma_0 = \frac{4m_{\text{red}}^2}{\pi} [Z f_p + (A-Z) f_n]^2 . \tag{4.26}$$

By measuring the differential recoil energy spectrum of Equation 4.24 the spin-independent cross-section, σ_0, is obtained. In most cases $f_p \sim f_n$ holds. Therefore, σ_0 is proportional to the squared mass number of the nucleus. Of course, also spin-dependent interactions exist. For mass numbers $A \geq 20$ the scalar interaction dominates and spin-dependent interactions can be neglected, following Jungman et al.

Results from different direct detection experiments were used in this work. The corresponding limits are shown in Figure 4.8.

Currently the best limit is given by the XENON 100 collaboration. Therefore, this work focuses on this limit. In the following the XENON detector shall be explained. Its detection

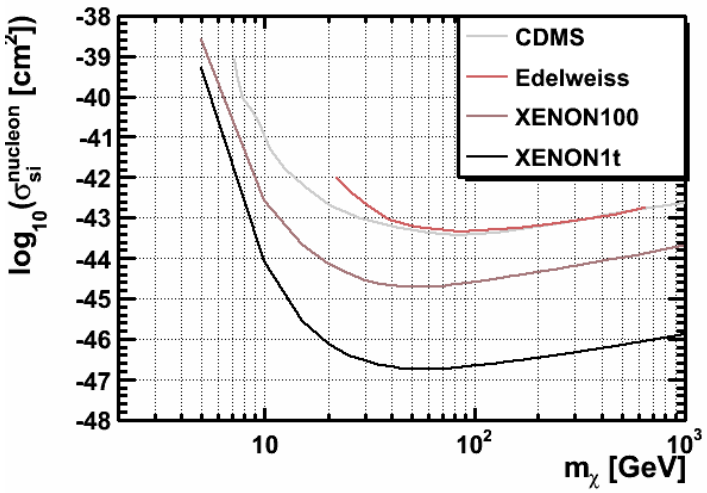

Figure 4.8: Limits on the spin-independent WIMP-nucleon cross-section from different direct detection experiments CDMS (Ahmed et al. 2010), Edelweiss (Armengaud et al. 2011), XENON 100 (April et al. 2012a) and expected sensitivity of XENON 1T (April et al. 2012b).

principle is shown in Figure 4.9.

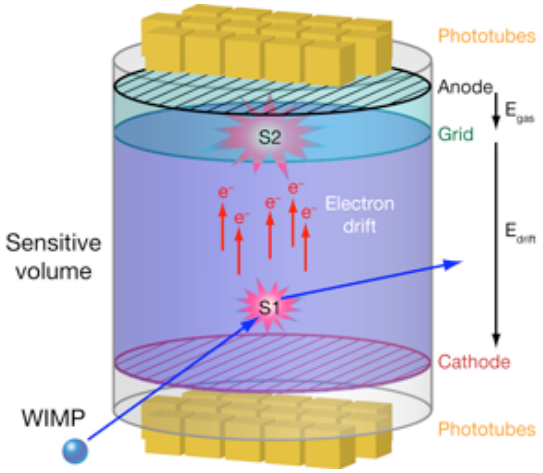

Figure 4.9: Principle of detection for direct dark matter search experiments, exemplary shown for the XENON 100 detector.

Dark matter particles (WIMP) scatter off atomic nuclei in liquid xenon. This creates primary scintillation light (S1). It is detected via photomultipliers located on top and bottom of the detector. The interaction also ionizes the liquid xenon and releases electrons. Due to the applied electric field (E_{drift}), the electrons drift towards the xenon gas phase, where secondary scintillation light (S2) is produced by electrons colliding with xenon atoms. The ratio of signals S2/S1 discriminates nuclear recoils from electron recoils where photons

are scattered off electrons, i.e. $(\mathrm{S2/S1})_{\mathrm{nuclear}} \ll (\mathrm{S2/S1})_{\mathrm{photon}}$.

Axial-vector (spin-dependent) cross-section:
Although, scalar interactions dominate for mass numbers $A > 20$, the spin-dependent WIMP nucleon cross-section is discussed in this paragraph. The differential spin-dependent cross-section is given by (for detailed calculation see Jungmann et al.)

$$\frac{d\sigma}{d|q|^2} = \frac{\sigma_0}{4m_{\mathrm{red}}^2 v^2} F^2(q) = \frac{8}{\pi v^2} \Lambda^2 G_F^2 J(J+1) \frac{S(q)}{S(0)} \tag{4.27}$$

m_{red} again is the reduced mass of the nucleon WIMP system and v is the WIMP velocity relative to the target nucleus. The quantity $S(q)$ comes from nuclear matrix element calculations. G_F is the Fermi constant and J is the total angular momentum of the nucleus. The ratio $S(q)/S(0)$ can be identified with the form factor $F(q)^2$. Λ reflects the nuclear calculation of the spin content of protons and neutrons contained in the nucleus. Comparing the left and right hand side of Equation 4.27 the spin dependent WIMP nucleon cross-section can be derived as

$$\sigma_0 = \frac{32}{\pi} m_{\mathrm{red}}^2 \Lambda^2 G_F^2 J(J+1) \tag{4.28}$$

Like in the case of the spin-independent cross-section, the measured recoil energy spectrum reveals the spin-dependent WIMP nucleon cross-section. Experimental limits on the spin-dependent WIMP proton cross-section are presented in Figure 4.10.

It reveals, that limits coming from indirect detection experiments, i.e. neutrino telescopes ANTARES, Baksan and IceCube, are the most constraining ones. In this work, their limits are used for constraining the parameter space of the investigated supersymmetric models. The detection principles of neutrino telescopes is explained in the following subsection.

4.4.2 Indirect Search

In principle, all indirect dark matter searches are based on the search for annihilation products of two dark matter particles, e.g. neutrinos, photons, or antiprotons. Although, each of these channels is worth being investigated, this work focuses on neutrinos from annihilating dark matter. Dark matter particles propagate through the galactic dark matter halo. If the dark matter particle is on an orbit through a massive body, e.g. the Sun or the Earth, it may scatter off nuclei therein, down to velocities smaller than the escape velocity. The dark matter particles get gravitationally trapped and accumulate in the corresponding object. Two dark matter particles can then annihilate into standard model particles, e.g. quarks, Higgs or weak interaction bosons. Most of them decay or are absorbed on very short time scales, so that they can not escape. Nevertheless, neutrinos result from decaying intermediate annihilation products and escape. They may propagate to the Earth, where they can be detected with neutrino telescopes like IceCube or ANTARES. The principle of indirect detection with neutrino telescopes is illustrated in Figure 4.11

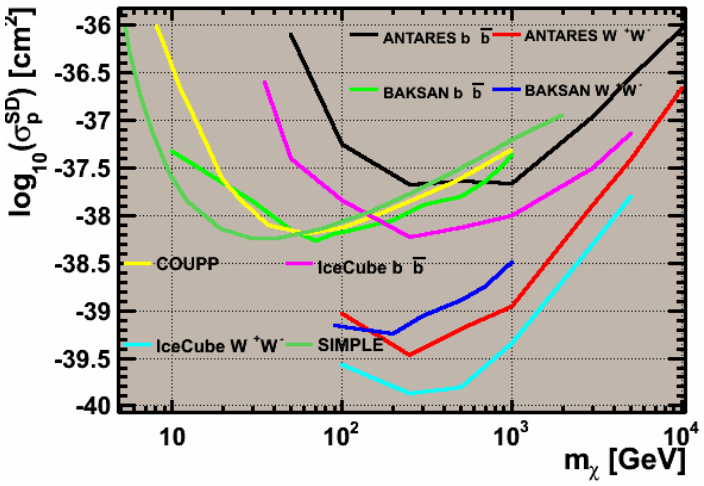

Figure 4.10: Experimental limits on the spin-dependent WIMP-nucleon cross-section; black line: ANTARES limit at 90% C.L. for annihilation channel W^+W^-, red line: ANTARES limit at 90% C.L. for annihilation channel $b\bar{b}$ (Adrian-Martinez et al. 2012); magenta line: IceCube limit at 90% C.L. for $b\bar{b}$, turquoise line: IceCube limit at 90% C.L. for annihilation channel W^+W^- (Aartsen et al. 2013), light green line: Baksan limit at 90% C.L. for $b\bar{b}$, blue line: Baksan limit at 90% C.L. for annihilation channel W^+W^- (Boliev et al. 2013), yellow line: COUPP limit at 90% C.L. (Behnke et al. 2012), dark green line: SIMPLE limit at 90% C.L. (Felizardo et al. 2012).

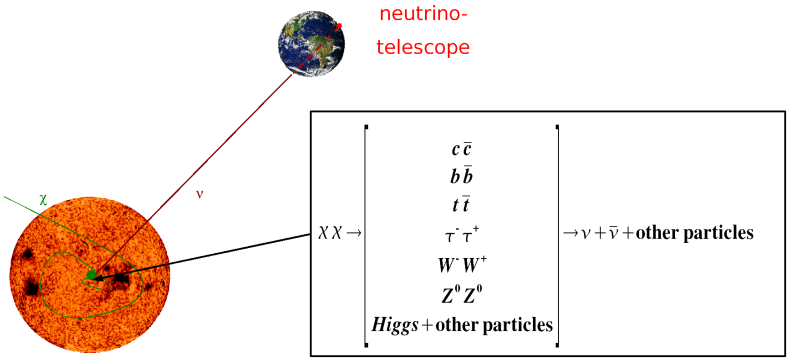

Figure 4.11: Indirect detection of dark matter using neutrino telescopes

Arriving at the Earth, neutrinos can interact amongst others via charged current interactions (deep inelastic lepton-nucleon scattering) in the vicinity of the detector and for muon neutrinos a charged muon is produced. This muon moves faster than the speed of light in the surrounding medium (e.g. ice or water) and emits Cerenkov light. This light can be detected with photomultipliers. By measuring the arrival time and position of the emitted

Cerenkov photons, the direction and energy of the neutrino can be reconstructed.

In this work, the two neutrino telescopes IceCube and ANTARES are considered. The first is located on the South Pole. 86 strings with photomultipliers for the detection of the emitted Cerenkov light are deployed in ice at a depth of $\sim$ 2500 m. The second was already introduced in detail in the Section 2 and 3. In Figure 4.12 a schematic layout of both experiments is shown.

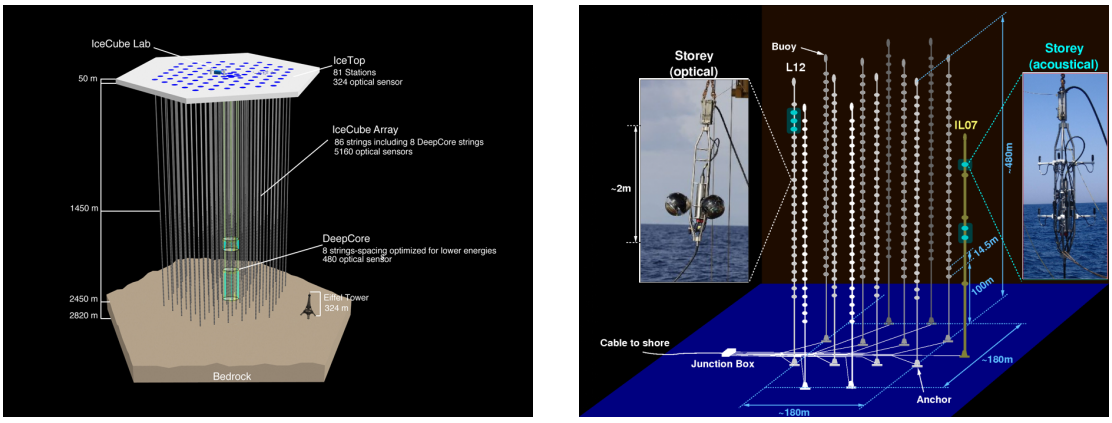

Figure 4.12: The IceCube detector (left) with its low energy extension Deep Core and the ANTARES detector (right)

The current limits on the muon (neutrino) flux for dark matter annihilating in the Sun from IceCube and ANTARES are shown in Figure 4.13. These limits assume an exclusive annihilation channel, either W^+W^-, $b\bar{b}$ or $\tau^+\tau^-$ as benchmark channels.

From the observed muon flux (or the observed limit) the spin-independent and spin-dependent WIMP nucleon cross-section can be calculated. Assuming one WIMP annihilation channel to be dominant, which is done when calculating the limits of Figure 4.13, according to Wikström & Edsjö 2009 the observed muon flux $\phi_\mu^{\rm obs}$ can be written as

$$\phi_\mu^{\rm obs} = \eta_f(m_\chi)\Gamma_A \tag{4.29}$$

where Γ_A is the annihilation rate and the function η_f depends on the WIMP mass, m_χ. If either the spin-independent or the spin-dependent interaction is dominant their cross-sections can be expressed in terms of the annihilation rate Γ_A

$$\begin{aligned} \sigma^{\rm SI} &= \lambda^{\rm SI}(m_\chi)\Gamma_A, \\ \sigma^{\rm SD} &= \lambda^{\rm SD}(m_\chi)\Gamma_A. \end{aligned} \tag{4.30}$$

Combining Equations 4.29 and 4.30 the WIMP nucleon cross-section can be calculated from the muon flux according to

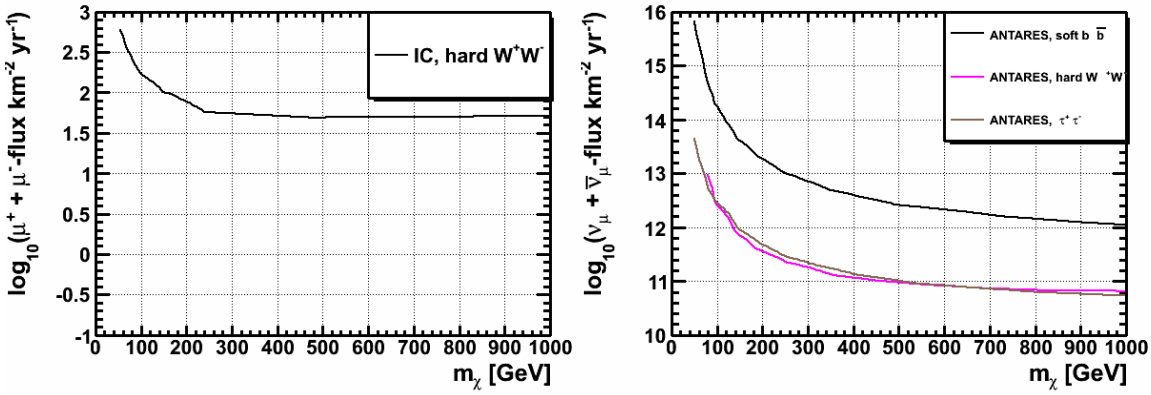

Figure 4.13: Limit on the muon flux from dark matter annihilations in the Sun from the IceCube collaboration (left) for 100% annihilation in the channel W^+W^- (The IceCube Collaboration 2011); ANTARES limits (right) on the muon neutrino flux for annihilation channels W^+W^- (brown line), $b\bar{b}$ (black line) and $\tau^+\tau^-$ (magenta line) (Adrian-Martinez et al. 2012).

$$\begin{aligned} \sigma^{\mathrm{SI}} &= \kappa^{SI}\phi_\mu \\ \sigma^{\mathrm{SD}} &= \kappa^{SD}\phi_\mu \end{aligned} \tag{4.31}$$

The conversion factor κ is determined from simulations. For the observed limits on the muon flux a conservative limit on the spin-independent and spin-dependent WIMP nucleon cross-section can be derived.

4.4.3 Production at Colliders

Besides looking at annihilation products of dark matter particles or scattering of dark matter particles with ordinary matter, dark matter can be produced at colliders. Standard model particles like protons (LHC), electrons and positrons (LEP) or protons and antiprotons (Tevatron) collide and potentially produce particles related to physics beyond the standard model. Amongst these, also dark matter particles may be produced. They escape the detector, as they are electrical neutral and only weakly or gravitationally interacting. The imbalance of the measured momenta leads to signatures with missing transverse energy. By reconstructing the imbalance of momenta, the mass of the dark matter particle can be determined. In Figure 4.14 an event with missing transverse energy and a single jet, recorded by the ATLAS detector at the LHC is shown.

The red line in Figure 4.14 corresponds to a reconstructed missing transverse energy of 542 GeV. The reconstructed energy of the single jet is 551 GeV.

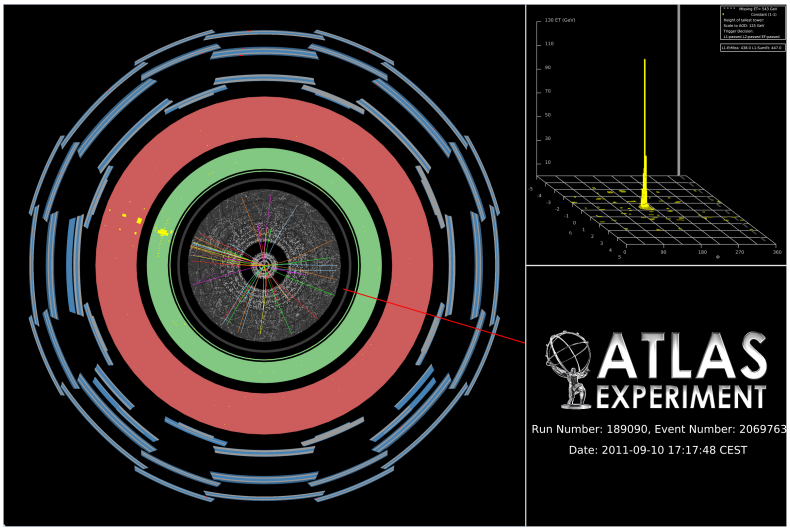

Figure 4.14: ATLAS event with missing energy (indicated by the red line) and one hadronic jet (yellow bar). Picture taken from The ATLAS Collaboration 2013

5

Supersymmetric Models

The biggest disadvantage of a supersymmetric extension of the standard model of particle physics, is its huge amount of free parameters. More than 100 additional parameters have to be treated as free parameters of the theory. On the one hand, this inevitably accompanies a loss of predictability. On the other hand, the complete parameter space of the MSSM is barely manageable with current computational technologies on a reasonable timescale. Therefore, simplifying assumptions have to be made to reduce the huge amount of free parameters. These assumptions lead to different kinds of supersymmetric models that are explained in this Chapter.

5.1 Constrained Minimal Supersymmetric Standard Model

The constrained minimal supersymmetric standard model (cMSSM) is based on the theory of supergravity. Sometimes it is also called minimal supergravity (mSugra). Supergravity performs the transition from a global supersymmetry to a local supersymmetry. To preserve supersymmetric gauge invariance, two additional fields have to be inserted, a spin-3/2 and a spin-2 particle, the gravitino and the graviton, respectively (Collins et al. 1989). Thus, requiring local gauge invariance naturally incorporates gravitation into elementary particle physics.

In the cMSSM universal boundary conditions are assumed at the scale of grand unification (GUT) (Figure 5.1), where the gauge coupling constants of SU(3), SU(2) and U(1) unify. This reduces the number of free parameters to five:

- Unified scalar masses m_0:

$$m_{\tilde{Q}} = m_{\tilde{L}} = m_{H_1} = m_{H_2} \equiv m_0, \tag{5.1}$$

- Unified gaugino masses $m_{1/2}$:

$$M_1 = M_2 = M_3 \equiv m_{1/2}, \tag{5.2}$$

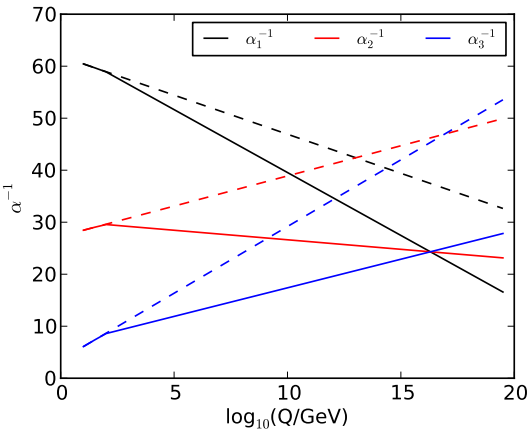

Figure 5.1: Renormalization group evolution of gauge coupling constants α^{-1} of strong (α_3^{-1}, blue), weak (α_2^{-1}, red) and electromagnetic (α_1^{-1}, black) interactions; dashed lines: standard model, solid lines: MSSM.

- Unified trilinear couplings A_0:

$$A_Q = A_L \equiv A_0. \tag{5.3}$$

Further, electroweak symmetry breaking (see previous Chapter) introduces another two parameters:

- Ratio of Higgs vacuum expectation values, $\tan\beta$,
- Sign of Higgs mass parameter of Equation 4.5, sign(μ) .

In total, the cMSSM is described by four continuous parameters, m_0, $m_{1/2}$, A_0 and $\tan\beta$ and one discrete parameter sign(μ). For the subsequent analysis they were scanned within the following ranges:

$$\begin{aligned} m_0 &\in [0, 5] \text{ TeV}, \\ m_{1/2} &\in [0, 4] \text{ TeV}, \\ A_0 &= 0, \\ \tan\beta &= 10 \text{ resp. } 45, \\ \text{sign}\mu &= +1. \end{aligned} \tag{5.4}$$

5.2 Non-universal Higgs Masses

Assuming unified scalar masses like in the cMSSM is arbitrary and not the result of any known symmetry principle (Sanjeev & Weldon 1983,Kaplunovski & Louis 1993,Choi et al. 1998). Non-universalities in the Higgs sector can arise in the framework of SUSY GUT models with SO(10) as underlying symmetry group (Baer et al. 2005). The MSSM Higgs doublets, $\tilde{H}_1$ and $\tilde{H}_2$, belong to the 10 dimensional fundamental representation while

matter fields belong to the 16 dimensional spinor representation whose mass degeneracy is guaranteed if SUSY breaking occurs above the SO(10) breaking scale. Thus, the Higgs sector is decoupled from the remaining matter sector and the cMSSM degeneracy is broken up. If the Higgs doublets, $\tilde{H}_1$ and $\tilde{H}_2$, live in the same superfield, their squared masses are equal but different from the common scalar mass m_0, i.e.

$$m_{H_1}^2 = m_{H_2}^2 \neq m_0^2. \tag{5.5}$$

In the case where $\tilde{H}_1$ and $\tilde{H}_2$ belong to different multiplets, Equation 5.5 is modified to

$$m_{H_1}^2 \neq m_{H_2}^2 \neq m_0^2. \tag{5.6}$$

The parametrization for the Higgs fields couples $\tilde{H}_1$ and $\tilde{H}_2$ to the soft scalar mass m_0 by introducing a non-universality parameter δ according to

$$m_{H_i}^2 = (1 + \delta_i)\, m_0^2 \tag{5.7}$$

where $i = 1, 2$ and $\delta_{1,2}$ parametrizes the non-universality between the scalar Higgs and scalar matter sector. When $\delta_1 = \delta_2$, Equation 5.5 is obtained, otherwise Equation 5.6. The result is a 7 dimensional parameter space with

$$\begin{aligned}
m_0 &= \text{unified mass of scalars,} \\
m_{1/2} &= \text{gaugino mass parameter,} \\
A_0 &= \text{unified trilinear couplings,} \\
\tan\beta &= \text{ratio of Higgs vacuum expectation values,} \\
\text{sign}(\mu) &= \text{sign of Higgs mass parameter } \mu \ +1 \text{ or } -1, \\
\delta_1 &= \text{non-universality parameter for } H_1, \\
\delta_2 &= \text{non-universality parameter for } H_2.
\end{aligned} \tag{5.8}$$

In the following, the case $\delta_1 = \delta_2$ will be referred to as NUHM1 scenario, while $\delta_1 \neq \delta_2$ will be labeled NUHM2 scenario. The parameter space of the non-universal Higgs scenario was analyzed for the following set of parameters

$$\begin{aligned}
m_0 &\in [0, 8] \text{ TeV}, \\
m_{1/2} &\in [0, 4] \text{ TeV}, \\
\delta_i &\in [-1, 1], \\
A_0 &= 0, \\
\tan\beta &= 10 \text{ resp. } 45, \\
\text{sign}(\mu) &= +1.
\end{aligned} \tag{5.9}$$

5.3 Non-universal Gaugino Masses

Some of the results for non-universal gaugino masses in this and the following sections were already published in Spies & Anton 2013. Thus, these sections may coincide to some extent with those in the publication. Non-universalities in the gaugino sector of the MSSM may arise from a chiral function, $f_{ab}(\phi^I)$, in the gauge kinetic part of the Lagrangian, $\mathcal{L}_{\text{gaugekin}}$ (Cremmer et al. 1982). ϕ^I is a chiral superfield and $\mathcal{L}_{\text{gaugekin}}$ is given by Huitu et al. 2000

$$\mathcal{L}_{\text{gaugekin}} = -\frac{1}{4} Re f_{ab}(\varphi^I) F^a_{\mu\nu} F^{b\mu\nu} + F^I_{a'b'} \frac{\partial f_{ab}(\varphi^I)}{\partial \varphi^I_{a'b'}} \lambda^a \lambda^b + H.c. + ... \tag{5.10}$$

where a, b are indices of the gauge generators, and λ^a is the SU(5) gaugino field. φ^I is the scalar component of ϕ^I whereas F^I is its auxiliary F-component. f_{ab} transforms as the symmetric product of two adjoint representations

$$(\mathbf{24} \otimes \mathbf{24})_{\text{symmetric}} = \mathbf{1} \oplus \mathbf{24} \oplus \mathbf{75} \oplus \mathbf{200} \tag{5.11}$$

and is given by (Huitu et al. 2000)

$$f_{ab}(\phi^I) = f_0(\phi^{\text{singlet}}) \delta_{ab} + \zeta_{\text{Mult}}(\phi^{\text{singlet}}) \frac{\phi^{\text{Mult}}_{ab}}{M_{\text{Planck}}} + \mathcal{O}((\frac{\phi^{\text{Mult}}_{ab}}{M_{\text{Planck}}})^2). \tag{5.12}$$

In the above equations Einstein's sum convention was used for indices appearing twice. f_0 and ζ_{Mult} are functions of gauge singlets ϕ^{singlet}. The index "Mult" labels possible multiplets of Eq. 5.11, that are allowed as a linear term of ϕ^{Mult} in $f_{ab}(\phi^I)$. Supersymmetry is broken by the F-components, F^I, of the chiral superfields, ϕ^I, when they acquire non-zero vacuum expectation values and thus, gaugino masses are generated. In the case of a non-singlet, these gaugino masses (M_1, M_2, M_3) are unequal, but related to each other (Ellis et al. 1985). Their relative magnitude at the scale of grand unification is given by group theoretical factors according to Amundson et al. 1996

$$\langle F_\phi \rangle_{ab} = c_a \delta_{ab} \tag{5.13}$$

with the coefficients c_a listed in Table 5.1

Representation	$M_3(M_{GUT})$	$M_2(M_{GUT})$	$M_1(M_{GUT})$
1	1	1	1
24	-2	3	1
75	-1	-3	5
200	1	2	10

Table 5.1: SU(5) mass ratios (coefficients c_a) at the GUT scale for **1**, **24**, **75** and **200** representation of SU(5)

The parametrization from Younkin & Martin 2012 was adapted and extended to include all possible representations appearing in Eq. 5.11. A mixture of singlet and non-singlet representations can be written in form of three non-universality equations for M_1, M_2 and

M_3.

$$
\begin{aligned}
M_1 &= m_{1/2}\left(\cos(\theta_1) + \sum_i a_i \sin(\theta_i)\right) \\
M_2 &= m_{1/2}\left(\cos(\theta_1) + \sum_i b_i \sin(\theta_i)\right) \\
M_3 &= m_{1/2}\left(\cos(\theta_1) + \sum_i c_i \sin(\theta_i)\right)
\end{aligned} \tag{5.14}
$$

where $i = 24, 75, 200$ labels the possible multiplets, $(a_{24}, a_{75}, a_{200}) = (1, 5, 10)$, $(b_{24}, b_{75}, b_{200}) = (3, -3, 2)$ and $(c_{24}, c_{75}, c_{200}) = (-2, -1, 1)$. θ_1 reflects the contribution of the singlet. θ_i reflects the contribution of the corresponding multiplet to the non-universality of the model. If $\theta_1 = 0$ and all $\theta_i = 0$, we obtain the cMSSM scenario, where $M_1 = M_2 = M_3 = m_{1/2}$. For $\theta_1 = \pi/2$ and all $\theta_i = \pi/2$, we have a pure $SU(5)$ non-singlet contribution reflecting the given mass ratios of Table 5.1.

In total a 9 dimensional parameter space results with

$$
\begin{aligned}
m_0 &= \text{unified mass of scalars,} \\
m_{1/2} &= \text{gaugino mass parameter,} \\
A_0 &= \text{unified trilinear couplings,} \\
\tan\beta &= \text{ratio of Higgs vacuum expectation values,} \\
\text{sign}(\mu) &= \text{sign of Higgs mass parameter } \mu \ +1 \text{ or } \ -1, \\
\theta_1 &= \text{contribution of the singlet,} \\
\theta_{24} &= \text{contribution of the 24-plet,} \\
\theta_{75} &= \text{contribution of the 75-plet,} \\
\theta_{200} &= \text{contribution of the 200-plet.}
\end{aligned} \tag{5.15}
$$

The simulations for the above parameters were carried out for

$$
\begin{aligned}
m_0 &\in [0, 5] \text{ TeV}, \\
m_{1/2} &= 600 \text{ GeV}, \\
A_0 &= -m_{1/2}, \\
\tan\beta &= 10 \text{ resp. } 45, \\
\text{sign}(\mu) &= +1, \\
\theta_j &\in [-45, 135] \text{ degree.}
\end{aligned} \tag{5.16}
$$

where $j = 1, 24, 75, 200$.

6

Analysis of Supersymmetric Models

In this Chapter the parameter space of the different supersymmetric scenarios introduced in the previous Chapter will be analyzed. Previous analysis of supersymmetric models focused on signal/detection perspectives from colliders and/or direct dark matter search experiments (see e.g., Strege et al. 2012, Gogoladze et al. 2012, Bhattacharya et al. 2011). For the first time, a complementary analysis of the models' parameter spaces with respect to direct and indirect dark matter search experiments is presented. Further, the detection of a Higgs boson with a mass of 125 GeV/c^2 (The CMS Collaboration 2013, The ATLAS Collaboration 2012a) and limits from squark and gluino masses (The ATLAS Collaboration 2012b) were taken into account. Consequently, this analysis provides one of the most complete studies of the introduced supersymmetric models.

6.1 Software Framework

This section describes the software, used for the analysis of the different SUSY scenarios. The constrained minimal supersymmetric Standard Model (cMSSM) and non-universal Higgs masses (NUHM1, NUHM2) were analyzed using the publicly available software package SuperBayeS[4](**Su**persymmetric **P**arameters **E**xtraction **R**outines for **Baye**sian **S**tatistics). It consists of the public program packages SoftSUSY (Allanach 2002) for the calculation of the supersymmetric particle spectrum. Amongst others (e.g. $(g-2)_\mu$), direct and indirect dark matter detection observables are calculated with DarkSUSY (Gondolo et al. 2004). The program FeynHiggs (Heinemeyer et al. 2000) calculates properties of the MSSM Higgs particles. B-physics decays are implemented via the program Bdecay (Roszkowski et al. 2007). For this study, SuperBayeS was extended by a further spectrum calculator SuSpect (Djouadi et al. 2007). The latter provides numerical routines, necessary to solve the relevant differential equations, but was modified to include the parametrizations of the introduced scenarios from the previous section.

The underlying algorithm for parameter space scans is based on Markov-Chain-Monte-

[4]http://www.ft.uam.es/personal/rruiz/superbayes/?page=main.html

Carlo (MCMC) simulations. An arbitrary point, $\vec{x}_0$, in an n-dimensional parameter space with probability p_0 is selected. A new point, $\vec{x}_{\rm new}$, is proposed and the corresponding calculations are performed. With the help of Bayesian techniques its probability is calculated. $\vec{x}_{\rm new}$ is accepted as new starting point if its probability $p_{\rm new}$ exceeds p_0. To avoid the Markov-Chain to be trapped at a certain point, points that result in a probability $p_{\rm new} < p_0$ will be accepted with a probability $\alpha = \min(p_{\rm new}/p_0, 1)$.

The application of the MCMC to the SUSY parameter space scan is given by the following procedure: the starting point $\vec{x}_0$ is selected. It consists of the particular free parameters of the corresponding SUSY scenario, e.g. parameters given in Equation 5.4 in the case of the cMSSM. They are passed to the SUSY spectrum calculator. If the calculated mass spectrum of SUSY particles is not rejected, e.g. by non converging renormalization group equations, tachyons, Landau poles etc., the spectrum is passed to the particular packages, especially DarkSUSY, that calculates predictions for the individual direct and indirect detection observables. The probability, $p_0(\vec{x}_0)$, under the condition that e.g., the relic density of the neutralino can be reproduced within a certain acceptance, is calculated and the predicted values of the SUSY particle spectrum, as well as indirect and direct detection observables are written to an output text file. Additionally, the SUSY spectrum is written to file using the so-called SUSY Les Houches Accord (SLHA) (Skands et al. 2004). A new point $\vec{x}_{\rm new}$ is proposed. All relevant observables are calculated and the probability $p_{\rm new}(\vec{x}_{\rm new})$ is calculated. If $p_{\rm new}(\vec{x}_{\rm new}) > p_0(\vec{x}_0)$, $\vec{x}_{\rm new}$ is accepted and the described procedure starts again. Iteratively, it is repeated until the predefined (by the user) maximum number of sampled models is achieved or if the runtime of the algorithm exceeds the time limit set by the corresponding computing cluster. The resulting SLHA file serves as input for the public package SuperIso (Mahmoudi 2009), which calculates flavor observables (see Section 6.6). SuperIso's output is written to a so-called Flavor Les Houches Accord (FLHA) (Mahmoudi 2012). The produced text files are merged with the FLHA files of SuperIso. The merged files are the base of a χ^2 analysis (see Section 6.6). Figure 6.1 graphically illustrates the sampling procedure, used in this work.

To achieve a higher efficiency, with respect to computing power, a new software framework (**N**on-**U**niversal **SU**per**SY**mmetry) was developed. NUSUSY was used to analyze the scenario with non-universal gaugino masses (NUGM). Like SuperBayeS. it serves as an interfacing routine between the SUSY spectrum calculator SuSpect (Djouadi et al. 2007) and DarkSUSY (Gondolo et al. 2004), that provides numerical routines for calculating direct and indirect detection observables. NUSUSY provides the necessary routines for sampling the SUSY parameter space points. They were chosen from a sampling algorithm that generates random numbers according to an (user-) defined distribution (e.g. uniform, normal, χ^2 etc.) in user defined intervals. To get an equal coverage of the parameter space as much as possible, a uniform distribution of the input parameters was chosen. In that way, the scenarios free parameters are drawn and subsequently passed to SuSpect. The calculated SUSY spectrum serves as input parameters for DarkSUSY to calculate the individual observables. In combination with the input parameter of the corresponding SUSY scenario as well as the SUSY spectrum, they are written to an output file. Separately, the SUSY spectrum is written to a SLHA file. The resulting SLHA files are the base for the subsequent calculation of flavor observables performed by SuperIso. Its output again is

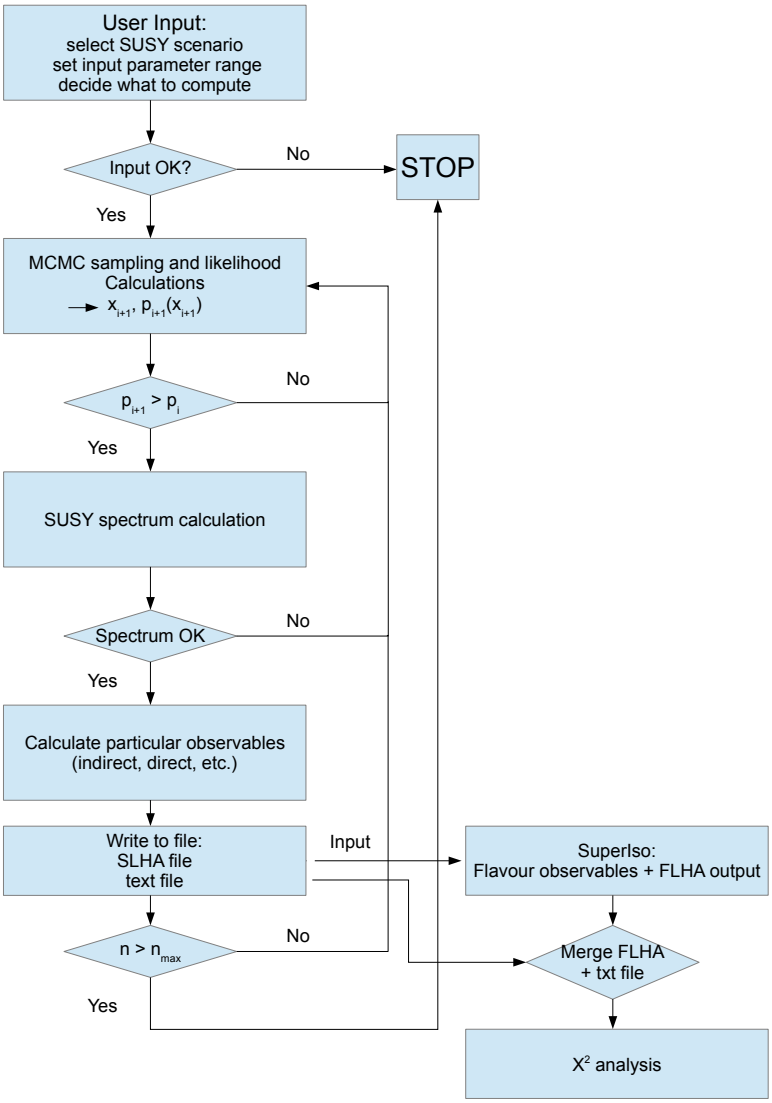

Figure 6.1: Flow-chart of the parameter space sampling procedure of SuperBayeS. SuperIso is used to calculate flavor observables such as BR($B \to X_s\gamma$). Output files from SuperIso (FLHA files) are merged with output files from SuperBayeS. The merged files are the base for a subsequent χ^2 analysis.

provided in the FLHA file. Like in the case of SuperBayeS, text files and FLHA files are merged to perform the χ^2 analysis. A flow chart, which graphically illustrates the algorithm of NUSUSY, is shown in Appendix A.1 (Figure A.1). Like in the case of SuperBayeS, the algorithm is terminated if the maximum number of sampled models is achieved, or if the runtime exceeds the given time limit.

From now on, a given point in the scenario's parameter space will be referred to as model. The class of models, e.g. cMSSM or NUHM will be named scenario. Due to the high dimensionality of the investigated scenarios, for illustration purposes some of the scenario's input parameters were fixed (Equations 5.4, 5.9 and 5.16). Throughout this Chapter, plots will be presented for $\tan\beta = 10$ on the left hand side and $\tan\beta = 45$ on the right hand side. When this is not the case, it will be mentioned in the text explicitly.

6.2 The Higgs Boson

In 2012, the LHC experiments CMS and ATLAS reported the discovery of a new boson with a mass of ~ 125 GeV/c^2 (The CMS Collaboration 2013,The ATLAS Collaboration 2012a). The new boson is most probably the long searched Higgs boson. This work is one of the first studies investigating the impact of the new detected Higgs boson on the different scenarios' parameter space. Many supersymmetric scenarios can barely achieve a Higgs boson with a mass around 125 GeV. Thus, the discovery of the Higgs boson puts severe restrictions to the scenario's parameter space.

The theoretical uncertainties on the calculation of the Higgs boson mass is $\sigma^{\text{theo}}_{\text{Higgs}} = \pm 3$ GeV (Allanach et al. 2004), while the experimental uncertainties are rather small with $\sigma^{\text{exp}}_{\text{Higgs}} = 0.4$ (stat.) $+ 0.5$ (syst.) GeV (The CMS Collaboration 2013).

cMSSM:
In the constrained minimal supersymmetric standard model, either the unified scalar masses m_0, or the unified gaugino masses $m_{1/2}$ must exceed values of 1 TeV, to achieve a Higgs boson mass, m_h, consistent with measurements. In Figure 6.2 the dependence of m_h on m_0 ($m_{1/2}$) for different values of $m_{1/2}$ (m_0) is presented.

For $m_{1/2} = 1$ TeV, m_0 must exceed at least 4.6 TeV to achieve $m_h > 122$ GeV. Increasing $m_{1/2}$ shifts m_h to higher values, e.g. for $m_{1/2} = 3$ TeV, $m_h \sim 124$ TeV for all m_0. Increasing $m_{1/2}$ leads to higher values of M_3, the gluino mass parameter of the scenario's Lagrange density. Thus, the resulting gluino and squark masses increase, raising m_h through loop contributions coming from renormalization. The influence of m_0 on m_h is less (right hand side of Figure 6.2). Only for $m_{1/2} \lesssim 1$ TeV, the contribution of m_0 is important, whereas for higher values of $m_{1/2}$ the gaugino mass contributions, i.e. M_3, dominate. Higher values of $\tan\beta$ also lead to higher m_h (Figure 6.3).

Whereas only $m_0 \geq 4$ TeV and $\tan\beta > 10$ lead to $122 < m_h < 128$ GeV for $m_{1/2} = 1$ TeV, values of $m_{1/2} \geq 2$ TeV and $\tan\beta > 8$ are sufficient to fulfill the constraint coming from the Higgs boson mass. This confirms the dominant contribution of the gaugino masses to m_h in the cMSSM scenario.

The number of models that provide a Higgs boson with a mass within the theoretical

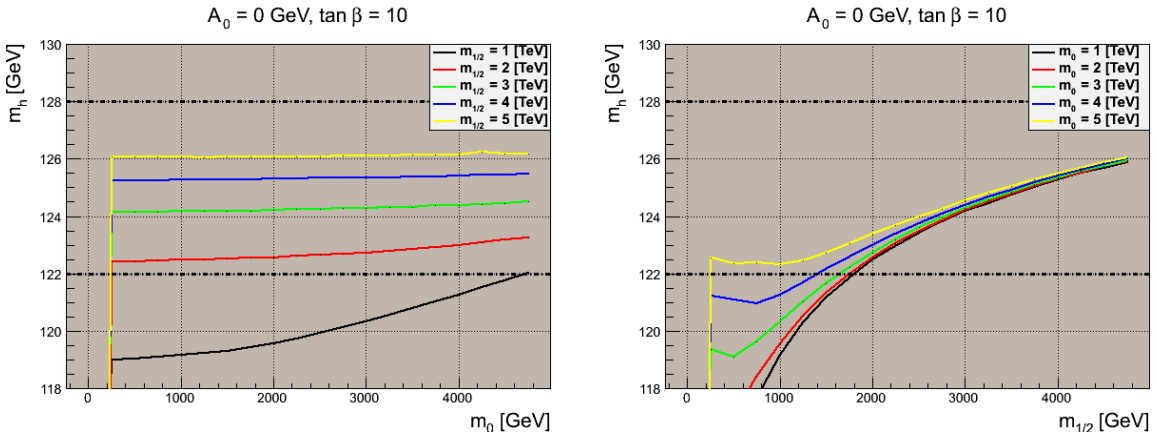

Figure 6.2: The predicted Higgs boson mass m_h is plotted versus the cMSSM input parameters m_0 (left) and $m_{1/2}$ (right). Black dash-dotted lines represent the theoretical uncertainties on m_h of $\pm$ 3 GeV. Different colors represent different values of m_0 ($m_{1/2}$) reaching from 1 to 5 TeV. A_0 was fixed to 0 GeV and $\tan\beta$ to 10.

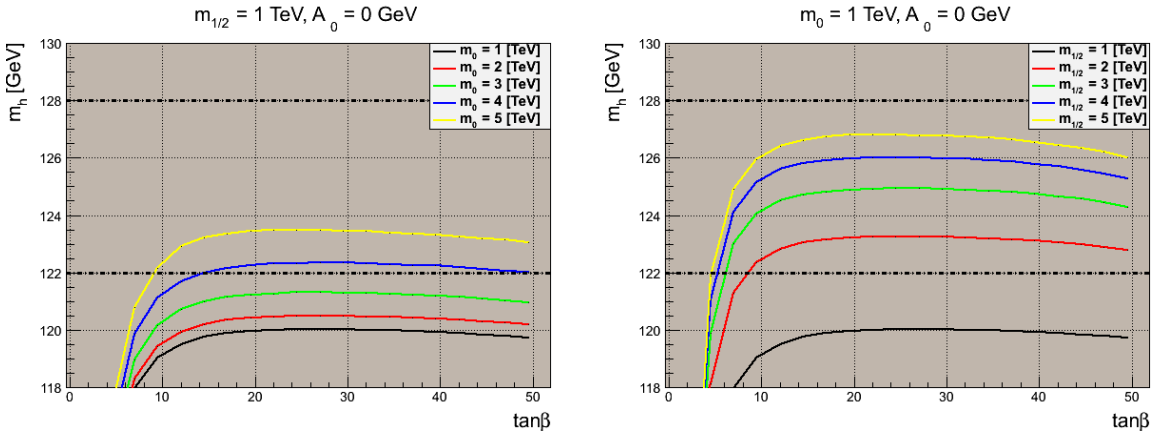

Figure 6.3: The predicted Higgs boson mass m_h is plotted versus the cMSSM $\tan\beta$ for different values of m_0 (left) and $m_{1/2}$ (right). Black dash-dotted lines represent the theoretical uncertainties on m_h of $\pm$ 3 GeV. Different colors represent different values of m_0 ($m_{1/2}$) reaching from 1 to 5 TeV. A_0 was fixed to 0 GeV and either $m_{1/2}$ (left) or m_0 (right) were fixed to 1 TeV.

error is plotted in Figure 6.4. The regions with either $m_h < 122$ GeV or $m_h > 128$ GeV are shaded in red.

In both cases ($\tan\beta = 10$ and 45), a large fraction of models do not provide a Higgs boson with the correct mass. To find the input parameters' regions that correspond to models with or without a correct Higgs boson mass, the theoretical error band around the mean values of 125 GeV was projected onto the $m_0 - m_{1/2}$ plane (Figure 6.5).

A correct mass of the Higgs boson can be achieved for $m_{1/2} \gtrsim 700$ GeV and $m_0 \gtrsim 4.5$ TeV as well as for $m_{1/2} > 1.5$ and $300 \lesssim m_0 \lesssim 1.5$ TeV for $\tan\beta = 10$. For $\tan\beta = 45$,

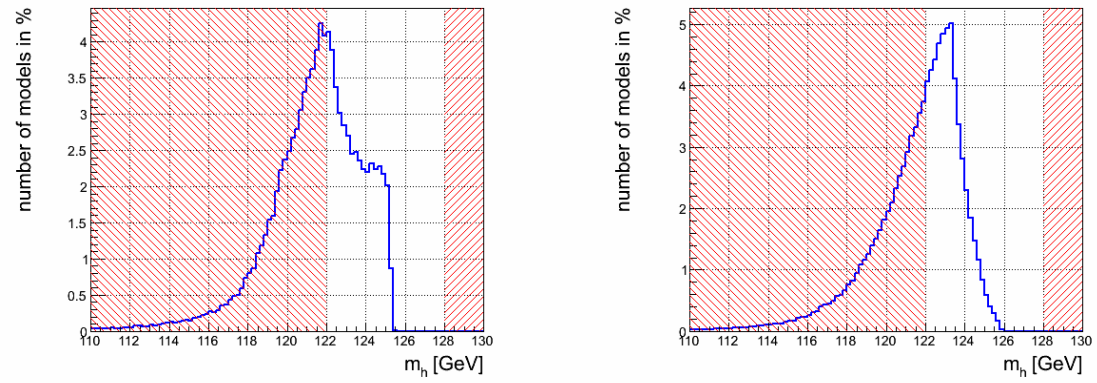

Figure 6.4: The number of models with $122 < m_h < 128$ GeV in the cMSSM scenario for $\tan\beta = 10$ (left) and $\tan\beta = 45$ (right). m_h is plotted on the x-axis, the number of models on the y-axis was normalized to the total number of simulated models. Red shaded regions are excluded regions where the calculated Higgs boson is either too light or too heavy.

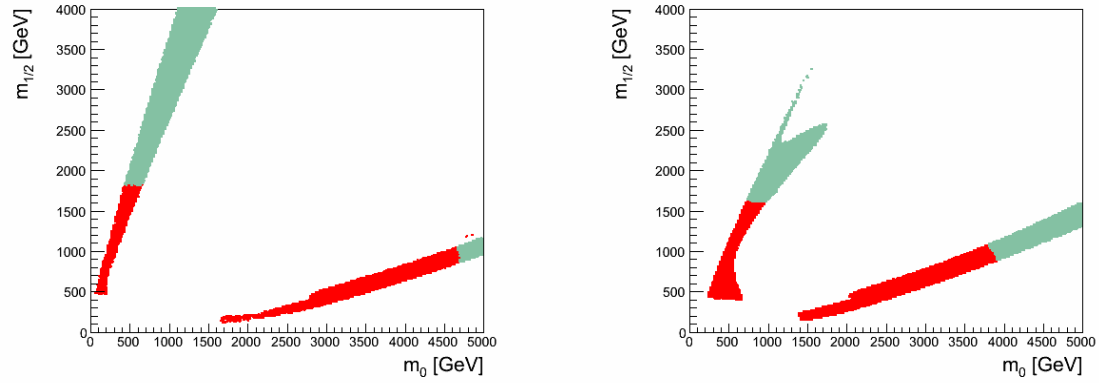

Figure 6.5: Higgs boson mass excluded regions (red) in the $m_0 - m_{1/2}$ plane. Green colored models have a Higgs boson with $122 < m_h < 128$ GeV.

regions with $122 < m_h < 128$ GeV can be found $700 \lesssim m_0 \lesssim 1.5$ TeV and $m_{1/2} > 1.5$ TeV as well as for $m_0 > 3.6$ TeV and $m_{1/2} \gtrsim 600$ GeV. Regions left blank in Figure 6.5 do not have the neutralino as LSP (small m_0 and all values of $m_{1/2}$), no radiative breaking of the electroweak symmetry ($m_0 > 1.6$ TeV and $m_{1/2} < 1$ TeV), or have a relic density larger than 1 (central region). Additionally, the excluded regions are listed in Table 6.1.

NUHM1:
In the previous paragraph it was found, that a correct Higgs-boson mass in the cMSSM can only be achieved if either m_0 or $m_{1/2}$ exceeds values of 1 TeV. Now, universal boundary conditions of the cMSSM scenario were relaxed with respect to the Higgs sector of the

$\tan\beta = 10$	$\tan\beta = 45$
$m_{1/2} < 1.8$ TeV (for $m_0 < 700$ GeV) $m_{1/2} < 1$ TeV (for $1.5 < m_0 < 4.7$ TeV)	$m_{1/2} < 1.6$ TeV (for $m_0 < 900$ GeV) $m_{1/2} < 1$ TeV (for $1.4 < m_0 < 3.9$ GeV)

Table 6.1: Regions excluded by $m_h < 122$ GeV or $m_h > 128$ GeV for input parameters m_0 and $m_{1/2}$ of the cMSSM for $\tan\beta = 10$ and 45.

MSSM. In this paragraph, the capability of achieving a Higgs boson mass consistent with measurements in the non-universal Higgs mass scenario with $m_{H_u} = m_{H_d} \neq m_0$ is part of the discussion. Remember the parametrization (Eq. 5.7) of $m_{H_{u,d}}$ given by

$$m_{H_u}^2 = m_{H_d}^2 = (1+\delta)m_0^2. \tag{6.1}$$

m_{H_u} corresponds to m_{H_2} and m_{H_d} to m_{H_1} in Eq. 5.5 and Eq. 5.6. The influence of δ on the Higgs boson mass is shown in Figure 6.6.

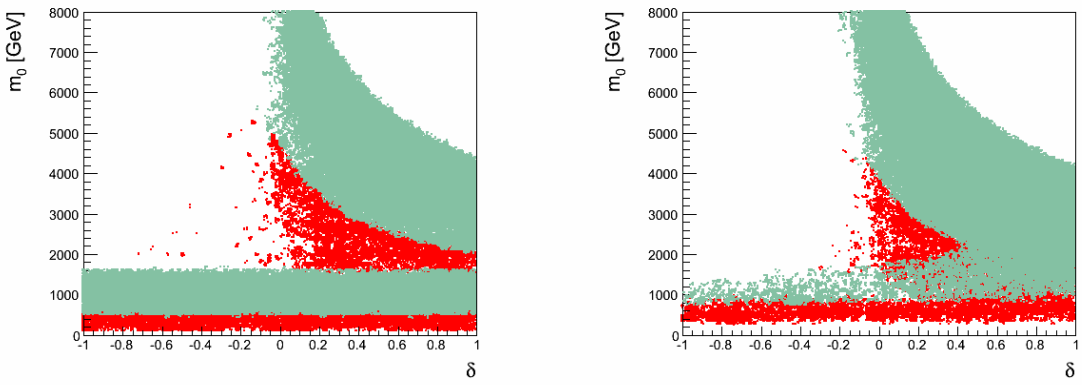

Figure 6.6: Regions in the NUHM1 parameter space excluded by the Higgs boson mass in the δ-m_0 plane. Simulation results for $\tan\beta = 10$ are shown on the left hand side, for $\tan\beta = 45$ on the right hand side. Red colored data points either have $m_h < 122$ GeV or $m_h > 128$ GeV. Green colored models fulfill the constraint $122 < m_h < 128$ GeV.

$\delta = 0$ results in the cMSSM scalar mass universality.

$$m_{\tilde{q}} = m_{\tilde{l}} = m_{H_u} = m_{H_d} \equiv m_0. \tag{6.2}$$

For small values of m_0 (~ 1 TeV) the unified gaugino mass scale $m_{1/2}$ needs to exceed $\sim$ 1.8 TeV to push the Higgs boson above 122 GeV (Figure 6.8). In that case, the gluino mass parameter M_3 exceeds values of 2 TeV and m_h is increased by loop contributions including the gluino. These models correspond to the lower green band with $0.5 < m_0 < 1.8$ TeV in figure 6.6.

Increasing m_0 and δ increases $m_{H_u} = m_{H_d}$. This leads to raising masses of the pseu-

doscalar Higgs boson m_A. m_h and m_A are connected by (Martin 2011)

$$m_h^2 = \frac{1}{2}\left(m_A^2 + m_Z^2 - \sqrt{\left(m_A^2 - m_Z^2\right)^2 + 4m_Z^2 m_A^2 \sin^2(2\beta)}\right) + \text{loop contributions} \qquad (6.3)$$

where m_Z is the mass of the Z boson. At this stage it is necessary to mention that only loop contributions can push the Higgs-boson mass above values higher than m_Z. Large contributions, coming from top (s)quark loops are necessary, and thus, a large mass for the top (s)quarks (therefore, m_0 must be large). Nevertheless, the gaugino mass scale $m_{1/2}$ needs to exceed at least 1.6 TeV and assist the common scalar mass m_0 and δ to achieve a Higgs boson with the correct mass within the error band.

From equation 6.3 it becomes clear that increasing $\tan\beta$ also increases m_h. Thus, smaller values of m_A lead to a correct Higgs boson mass. Increasing $\tan\beta$ from 10 to 45 leads to a shift of m_h of at least 1 GeV.

In Figure 6.7 the distribution of the predicted Higgs boson mass is presented where m_0, $m_{1/2}$ and δ are varied simultaneously within the parameter ranges given in Equation 5.9

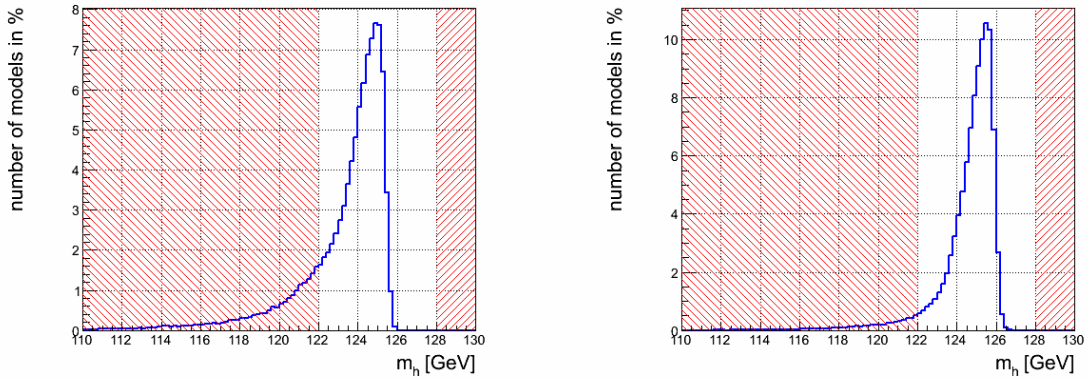

Figure 6.7: The number of models with $122 < m_h < 128$ GeV in the NUHM1 scenario for $\tan\beta = 10$ (left) and $\tan\beta = 45$ (right). m_h is plotted on the x-axis, the number of models on the y-axis was normalized to the total number of simulated models. Red shaded regions are excluded regions where the calculated Higgs boson is either too light or too heavy.

Adding a new free parameter (δ) to the theory enables numerous more models consistent with a Higgs boson within the required constraints. Thus, a large fraction of the simulated models provide a Higgs boson with a mass above 122 GeV. The corresponding parameter space is shown in Figure 6.8 for the m_0-$m_{1/2}$ plane.

Again, white regions do not have the neutralino as LSP, or a correct electroweak symmetry breaking, or have a relic density bigger than 1. Regions in the NUHM1 parameter space that are excluded by $m_h < 122$ GeV or $m_h > 128$ GeV are listed in Table 6.2

NUHM2:
In this paragraph the capability of acquiring a consistent Higgs-boson mass within the frame-

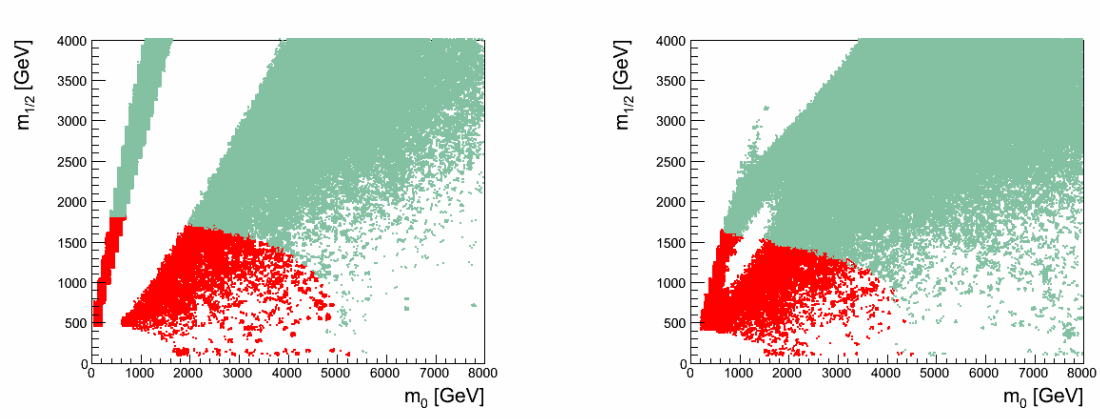

Figure 6.8: Higgs boson mass excluded regions (red) in the $m_0 - m_{1/2}$ plane for $\tan\beta = 10$ (left) and $\tan\beta = 45$ (right) for NUHM1. Green colored models have a Higgs boson with $122 < m_h < 128$ GeV.

$\tan\beta = 10$	$\tan\beta = 45$
$m_{1/2} < 1.8$ TeV (for $m_0 < 700$ GeV) $m_{1/2} < 1.6$ TeV (for $1.6 < m_0 < 4$ TeV)	$m_{1/2} < 1.6$ TeV (for $m_0 < 4.5$ TeV)

Table 6.2: Regions excluded by $m_h < 122$ GeV or $m_h > 128$ GeV for input parameters m_0, $m_{1/2}$ and m_ϕ of the NUHM1 scenario for $\tan\beta = 10$ and 45.

work of the NUHM2 scenario is investigated. In contrary to NUHM1, both squared Higgs mass parameters $m^2_{H_u}$ and $m^2_{H_d}$ are allowed to vary independently. Their parametrization is given by

$$\begin{aligned} m^2_{H_u} &= (1+\delta_{H_u})m_0^2, \\ m^2_{H_d} &= (1+\delta_{H_d})m_0^2. \end{aligned}$$

Simulations for either $\delta_{H_u} = 0$ or $\delta_{H_d} = 0$ fixed while varying the other δ had shown that the pair $(\delta_{H_u}, \delta_{H_d}) = (0.5, 1)$ is somehow optimal for achieving a correct Higgs mass. In Figure 6.9, the dependence of m_h on m_0 (x-axis) and $m_{1/2}$ (colored lines) is shown
With increasing $m_{1/2}$ the influence of m_0 on m_h decreases, whereas an increase of $m_{1/2}$ in the order of 1 TeV shifts the Higgs boson mass up by 3 GeV. Nevertheless, varying both squared Higgs masses does not lead to the possibility of both m_0 and $m_{1/2}$ being smaller than 1 TeV.

In contrast to the Figure 6.9, where δ_{H_u} and δ_{H_d} were fixed, for the following plots, they are allowed to vary within [-1,1]. m_0 was simulated in the range from 0 to 8 TeV and $m_{1/2}$ from 0 to 4 TeV. The number of models, fulfilling the constraint $122 < m_h < 128$ GeV normalized to the total number of simulated models, is shown in Figure 6.10. On the left hand side the predicted Higgs boson mass distribution is shown for $\tan\beta = 10$. On the

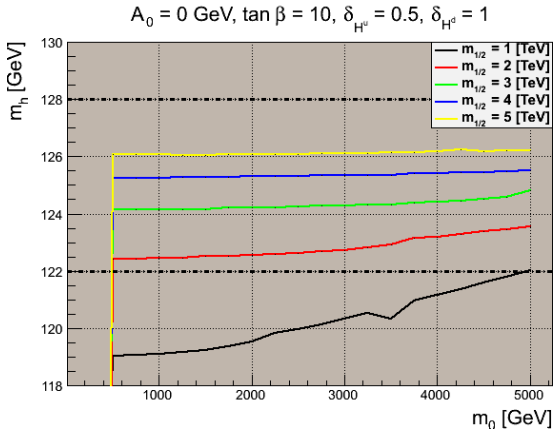

Figure 6.9: The predicted Higgs boson mass m_h plotted versus m_0 for $A_0 = 0$ GeV, $\tan\beta = 10$, $\delta_{H_u} = 0.5$ and $\delta_{H_d} = 1$. Different colors code values of $m_{1/2}$ reaching from 1 to 5 TeV.

right hand side results for $\tan\beta = 45$ are presented.

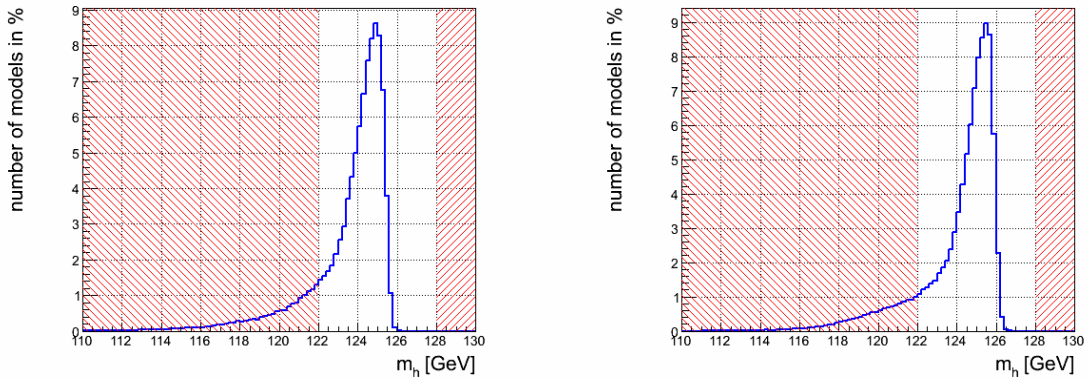

Figure 6.10: The number of models with $122 < m_h < 128$ GeV in the NUHM2 scenario for $\tan\beta = 10$ (left) and $\tan\beta = 45$ (right). $0 < m_0 < 5$ TeV, $0 < m_{1/2} < 4$ TeV, $A_0 = 0$ GeV, $\delta_{H_{u,d}}$ are varied within [-1,1]. m_h is plotted on the x-axis, the number of models on the y-axis was normalized to the total number of simulated models. Red shaded regions are excluded regions where the calculated Higgs boson is either too light or too heavy.

The corresponding regions in the parameter space, that are excluded are shown in Figure 6.11.

Non-universal Gaugino Masses (NUGM):
Last but not least, the predicted Higgs boson mass in supersymmetric scenarios with non-universal gaugino masses is discussed. The non-universal gaugino sector is assumed to arise

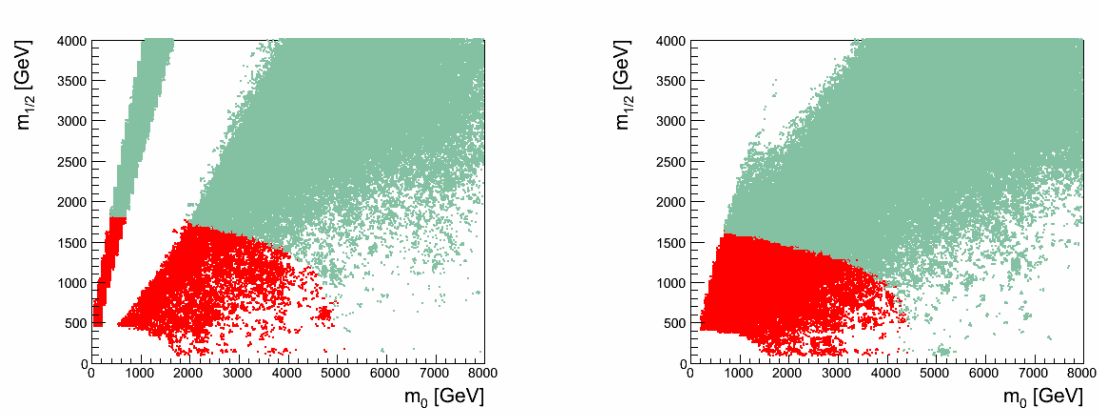

Figure 6.11: Excluded regions (red) in the $m_0 - m_{1/2}$ plane. Green colored models have a Higgs boson with $122 < m_h < 128$ GeV.

from a chiral function, f_{ab} in the gauge kinetic part of the Lagrange density of the MSSM. f_{ab} transforms as the symmetric product of two adjoint representations of the gauge group SU(5) (see. Section 5.3). A mixing between SU(5)'s singlet and non-singlets was introduced, according to Equation 5.14. Instead of varying all mixing angles of Equation 5.14, the mixing angles were unified for simplicity, such that $\theta_1 = \theta_{24} = \theta_{75} = \theta_{200} \equiv \theta$. In Appendix (A.2) plots for independently varying mixing angles are shown. With unified mixing angles, the majority of simulated models do not provide a Higgs boson with a mass of $122 < m_h < 128$ GeV (Figure 6.12). Some of the results in this paragraph were already presented in Spies & Anton 2013

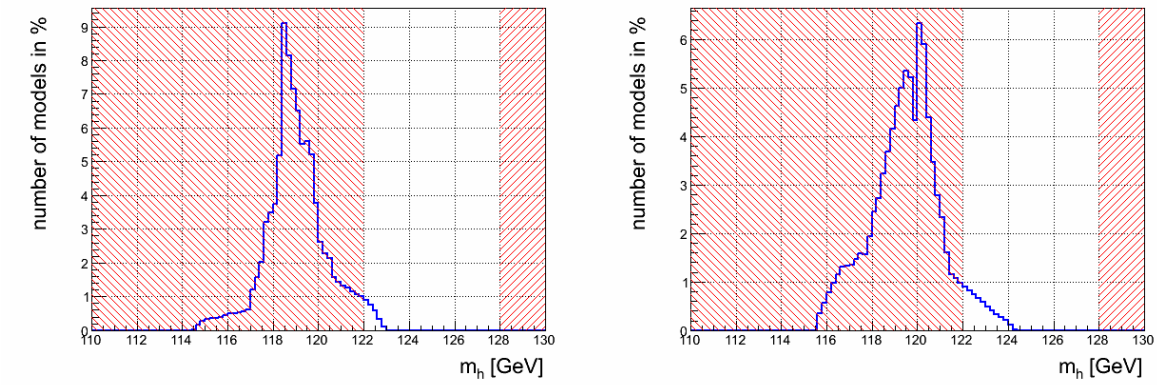

Figure 6.12: The number of models with $122 < m_h < 128$ GeV in the NUGM scenario for $\tan\beta = 10$ (left) and $\tan\beta = 45$ (right). m_h is plotted on the x-axis, the number of models on the y-axis was normalized to the total number of simulated models. Red shaded regions are excluded regions where the calculated Higgs boson is either too light or too heavy.

In Figure 6.13 the section of the θ/π-m_0 plane is highlighted where $122 < m_h < 128$ GeV

is fulfilled.

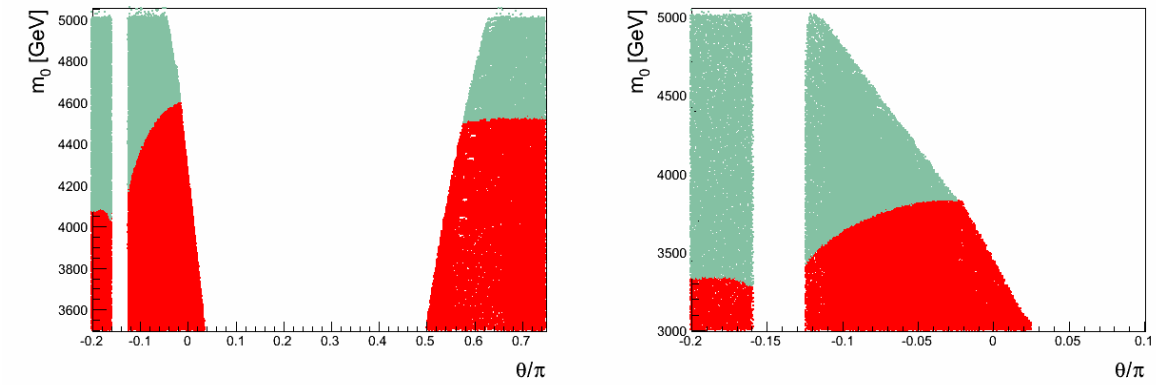

Figure 6.13: Higgs boson mass excluded regions (red) in the θ/π-m_0 plane. Green colored models have a Higgs boson with $122 < m_h < 128$ GeV.

The white region $-0.16 < \theta/\pi < -0.12$ for both $\tan\beta = 10$ and 45 is excluded by the LEP2 bound on the chargino mass (Nakamura et al. 2011). The white region $0.04 < \theta/\pi < 0.5$ for $\tan\beta = 10$ does not have a correct electroweak symmetry breaking, i.e. does not have a convergent μ from solving the renormalization group equations. This also occurs for $\theta/\pi \gtrsim 0.02$ and $\tan\beta = 45$. The excluded regions for θ/π and m_0 are summarized in Table 6.3. For the excluded values of m_0 in the intervals $-0.12 < \theta/\pi < -0.01$ ($\tan\beta = 10$) and $-0.125 < \theta/\pi < 0.025$ ($\tan\beta = 45$), a straight line approach was used leading to a slight underestimation (up to ~ 100 GeV in the middle of the θ/π intervals) of excluded values of m_0 for the given ranges of θ/π.

$\tan\beta = 10$	$\tan\beta = 45$
$m_0 < 4$ TeV (for $\theta/\pi <$ -0.16)	$m_0 < 3.3$ TeV (for $\theta/\pi <$ -0.16)
$m_0 \sim 3.64 \cdot \theta/\pi + 4.64$ TeV	$m_0 \sim 2 \cdot \theta/\pi + 3.65$ TeV
(for $-0.12 < \theta/\pi < -0.01$)	(for $-0.125 < \theta/\pi < 0.025$)
$m_0 < 4.5$ TeV (for $\theta/\pi > 0.54$)	

Table 6.3: Regions excluded by $m_h < 122$ GeV or $m_h > 128$ GeV for input parameters m_0 and θ/π of the NUGM scenario for $\tan\beta = 10$ and 45. In the second row for both columns, the boundary of the excluded region is approximated by a straight line.

To achieve a Higgs boson mass larger than 122 GeV, $|M_3|$ needs to exceed at least ~ 1 TeV for $m_0 = 5$ TeV. M_3 has to increase for decreasing m_0 (see Figure 6.14). The influence of M_1 and M_2 is negligible.

The parametrization of the gaugino masses implies for M_3.

$$M_3 = m_{1/2}\,(\cos(\theta) - 2\sin(\theta)) \tag{6.4}$$

The dependence of M_3 on the mixing angle θ, according to the parametrization of Equation

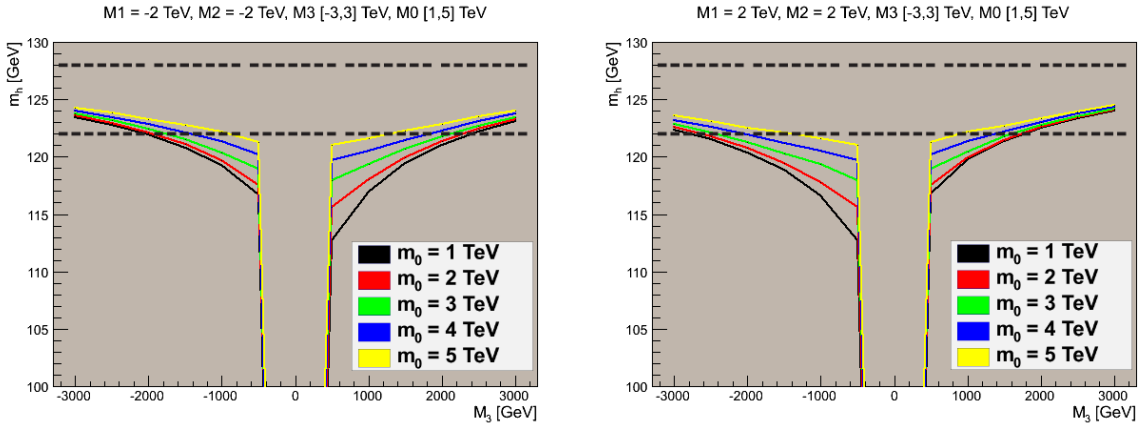

Figure 6.14: Influence of gaugino mass parameters M_1, M_2 and M_3 on the predicted Higgs boson mass, m_h, for $\tan\beta = 10$. Left: $M_1 = -2$ TeV, $M_2 = -2$ TeV, $-3 < M_3 < 3$ TeV; right: $M_1 = 2$ TeV, $M_2 = 2$ TeV, $-3 < M_3 < 3$ TeV; color coded are values for m_0 in the interval [1,5] TeV. Black dashed lines represent the uncertainty band on m_h with $122 < m_h < 128$ GeV.

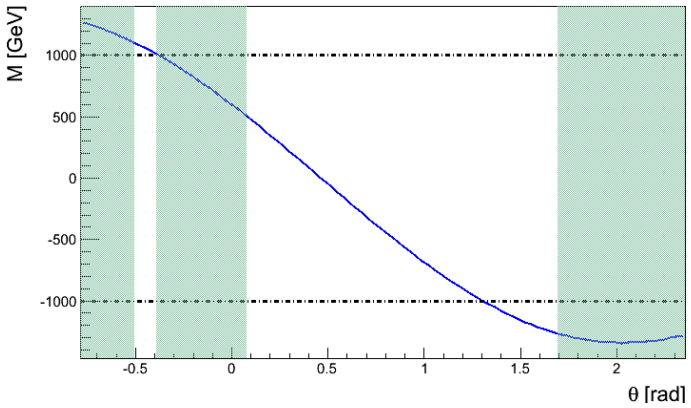

Figure 6.15: Gaugino mass parameters M_3 (blue line) plotted versus the mixing angle θ. Green shaded regions correspond to θ intervals with $122 < m_h < 128$ GeV. Black dash doted lines represent the $|M_3| = 1$ TeV.

6.4, is illustrated in Figure 6.15 (blue line). M_3 hardly exceeds 1 TeV, necessary to achieve $122 < m_h < 128$ GeV. Green colored shaded regions are the ones, that correspond to intervals for θ/π in Figure 6.13 with a correct Higgs mass for $\tan\beta = 10$ and 45. Increasing $\tan\beta$ also leads to a higher Higgs boson mass. Therefore, a consistent Higgs mass can also be achieved for smaller values of M_3 (Figure 6.15). The dependence of m_h on $\tan\beta$ is shown in Figure 6.16, for $m_0 = 4$ TeV and $\theta = -0.25$ rad which corresponds to $M_3 \sim 880$ GeV. With this choice of parameters a correct mass of the Higgs boson is achieved for $\tan\beta > 12$.

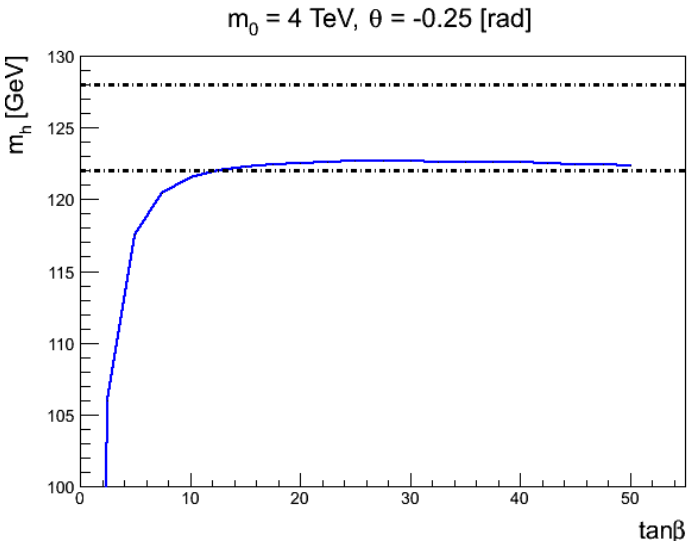

Figure 6.16: Predicted Higgs mass depending on $\tan\beta$ for $m_0 = 4$ TeV and $\theta = -0.25$ rad. Black dash doted lines represent the $122 < m_h < 128$ GeV.

Having discussed the consequences from the measured Higgs boson mass on the diverse scenarios' parameter spaces, consequences for the relic density of the neutralino will be studied in the following.

6.3 Relic Density

The previous section had revealed regions of the diverse parameter spaces, where the predicted mass of the Higgs boson is consistent with experimental measurements. In this section, the relic density of the lightest neutralino χ_1^0 is part of the discussion. Further, plots are shown for regions, where model predictions meet requirements from the Higgs-boson mass and the relic density, simultaneously. From now on, the lightest neutralino χ_1^0 is referred to as the neutralino χ. According to Hinshaw et al. 2012, the current value of the cold dark matter relic density is given by $\Omega h^2 = 0.1157 \pm 0.0023$, where h is the Hubble parameter $H_0/100$ and $H_0 = 69.33 \pm 0.88$ km/s/Mpc. In this work, the constraints on the relic density were relaxed to $\Omega h^2 = 0.11 \pm 0.02$. This accounts for the possibility, that dark matter may consist of several components and not only one particle species (relaxed lower bound). A relaxed upper bound allows R-parity violation to a certain extent and thus, allowing for decaying dark matter. Remember, the new results from Planck (Ade et al. 2013) with respect to the dark matter relic density were not taken into account in this work.

Neutralino relic density in the cMSSM:
Most regions of the cMSSM parameter space have a relic density $\Omega h^2 > 0.13$. This is caused

by the composition of the neutralino. Due to renormalization of gaugino masses, in cMSSM the lightest neutralino has a predominant bino component. Bino dominated neutralinos only annihilate via slepton exchange. Annihilation channels containing weak vector bosons and Higgs bosons are not accessible.

In Figure 6.17, regions of the cMSSM parameter space, simultaneously fulfilling relic density and Higgs mass requirements, are illustrated in the m_0-$m_{1/2}$-plane.

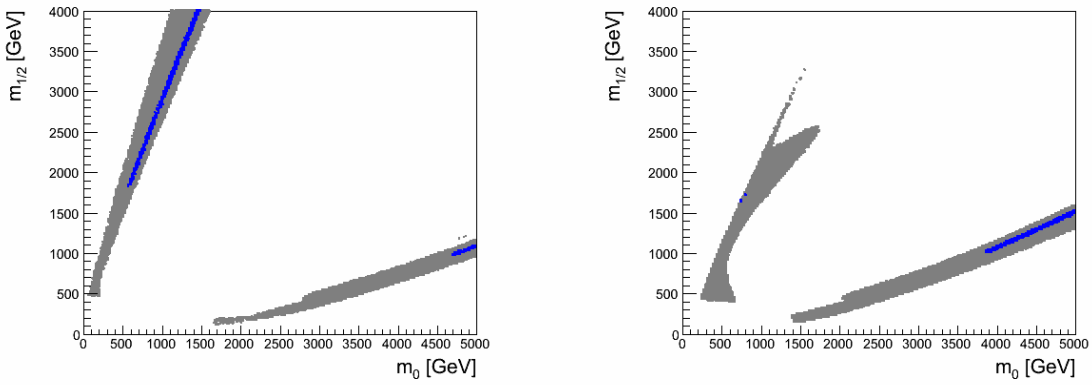

Figure 6.17: Regions in the cMSSM parameter space consistent with $122 < m_h < 128$ GeV and $0.09 < \Omega h^2 < 0.13$ (blue) for $\tan\beta = 10$ (left) and $\tan\beta = 45$ (right). Gray colored are models that are inconsistent with the Higgs mass or the relic density.

For $\tan\beta = 10$, only two small regions ($m_{1/2} > 1.6$ TeV and $500 < m_0 < 1600$ GeV as well as $m_0 > 4.6$ TeV and $m_{1/2} \sim 1$ TeV) survive. Allowed high values of $m_{1/2}$ and m_0 are driven by the Higgs mass, as for lower values m_h is too small. For $\tan\beta = 45$, models with $m_0 > 3.6$ TeV and $1 < m_{1/2} < 1.5$ TeV remain. The remaining regions in the lower right corners for both values of $\tan\beta$ are characterized by a significant higgsino component in the neutralino's composition (so-called hyperbolic branch/focus point region, HB/FP). Thus, annihilation channels including SU(2) vector bosons and Higgs bosons are accessible and help reducing the relic density. Consistent regions for small m_0 and $m_{1/2} > 1.6$ TeV, have a bino dominated neutralino. There, the tau slepton, $\tilde{\tau}$, has a mass close to that of the neutralino and coannihilations via t- and u-channel $\tilde{\tau}$ exchange reduce the value of the relic density. Nevertheless, requiring a correct mass of the Higgs boson and a correct relic density of the neutralino shrinks the allowed parameter space of the cMSSM to two thin stripes forcing either m_0 or $m_{1/2}$ to have values in the multi-TeV regime.

Regions left blank in Figure 6.17 do not have the neutralino as LSP (small m_0 and all $m_{1/2}$) or do not fulfill conditions of radiative electorweak symmetry breaking (lower right corner, small $m_{1/2} < 800$ GeV and $m_0 > 2$ TeV) or lead to a relic density larger than 1 (central bulk).

Neutralino relic density in NUHM:
While in the cMSSM few models simultaneously fulfill constraints from the Higgs boson and the relic density, models with a non-universal Higgs sector provide far more models.

The m_0-$m_{1/2}$ plane in the NUHM1 scenario is displayed in Figure 6.18.

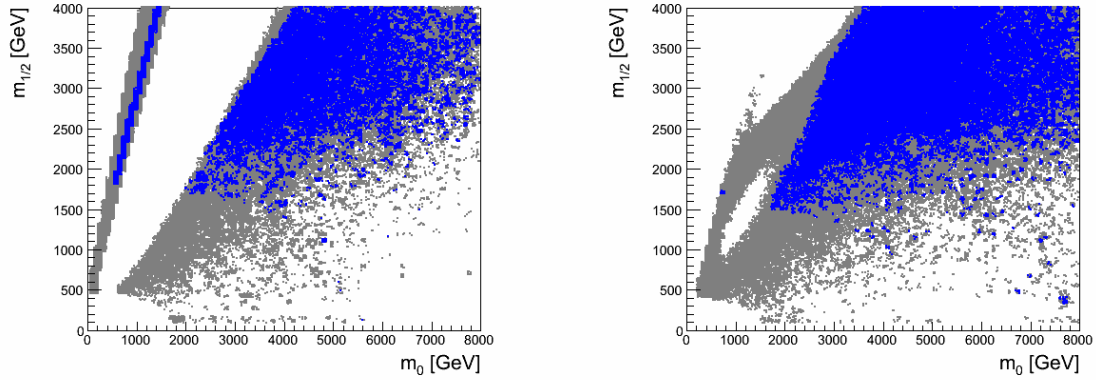

Figure 6.18: Regions in the NUHM1 parameter space consistent with $122 < m_h < 128$ GeV and $0.09 < \Omega h^2 < 0.13$ (blue) for $\tan\beta = 10$ (left) and $\tan\beta = 45$ (right). Gray colored are models that either have $\Omega h^2 < 0.09$ or $\Omega h^2 > 0.13$ or $m_h < 122$ GeV or $m_h > 128$ GeV.

As gaugino masses remain unified at the GUT scale, their masses at the scale of electroweak symmetry breaking and thus, the neutralino's composition behaves analogue to the cMSSM. The neutralino is either dominated by the bino component or a mixture between bino and higgsino. Mechanisms similar to that encountered in the cMSSM are present to achieve a relic density within the required range. For $m_0 \lesssim 1$ TeV and arbitrary values of $m_{1/2}$ the $\tilde{\tau}$ coannihilation region can be found. Blue colored models for $m_0 > 1$ TeV and $m_{1/2} \gtrsim 1.6$ TeV have a higgsino dominated neutralino and weak vector and Higgs boson annihilation channels are possible. Further, the lightest chargino $\chi_1^{\pm}$ is nearly degenerate in its mass with the neutralino. Pairs of neutralinos annihilate efficiently via t-channel chargino exchange into pairs of W bosons. This mechanism depletes the neutralino's population for $m_{1/2} < 1.6$ TeV and the relic density is too small. In addition, in this region the Higgs boson mass is not consistent with measurements.

The same mechanisms apply to NUHM2 scenario. The regions where $122 < m_h < 128$ GeV and $0.09 < \Omega h^2 < 0.13$ are fulfilled highly coincide with the regions in NUHM1, deviating on the level of a few percent. The m_0-$m_{1/2}$ plane for the NUHM2 scenario is depicted in Figure 6.19. For white regions in Figures 6.18 and 6.19 the same arguments like in the cMSSM apply.

Compared to the cMSSM reference model, in models with a non-universal Higgs sector a large part of the parameter space is consistent with the Higgs mass and the relic density, providing the neutralino as a dark matter candidate particle. Nevertheless, either m_0 or $m_{1/2}$ must exceed the TeV frontier like in the cMSSM.

Neutralino relic density in NUGM:
Some of the results in this paragraph were already published in Spies & Anton 2013. The calculated relic density in the scenario with non-universal gaugino masses, introduced in Section 5.3, is displayed in Figure 6.20.

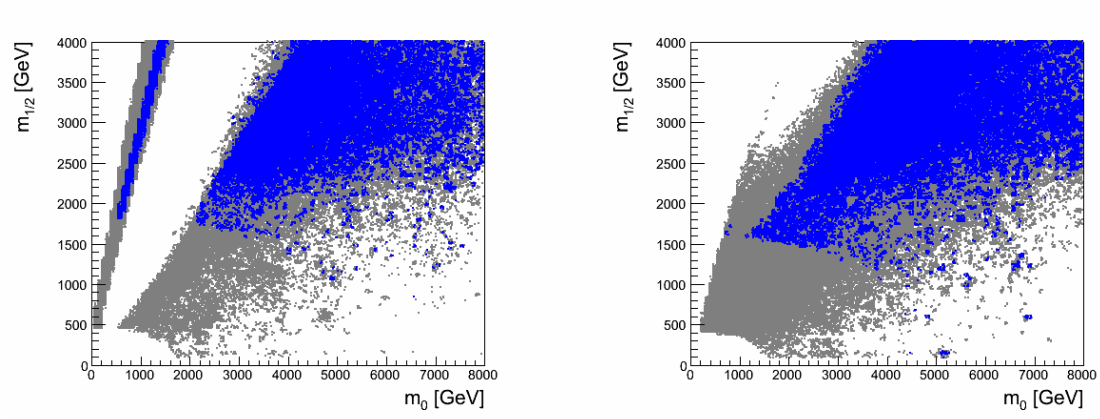

Figure 6.19: Regions in the NUHM2 parameter space consistent with $122 < m_h < 128$ GeV and $0.09 < \Omega h^2 < 0.13$ (blue) for $\tan\beta = 10$ (left) and $\tan\beta = 45$ (right). Gray colored are models that either have $\Omega h^2 < 0.09$ or $\Omega h^2 > 0.13$ or $m_h < 122$ GeV or $m_h > 128$ GeV.

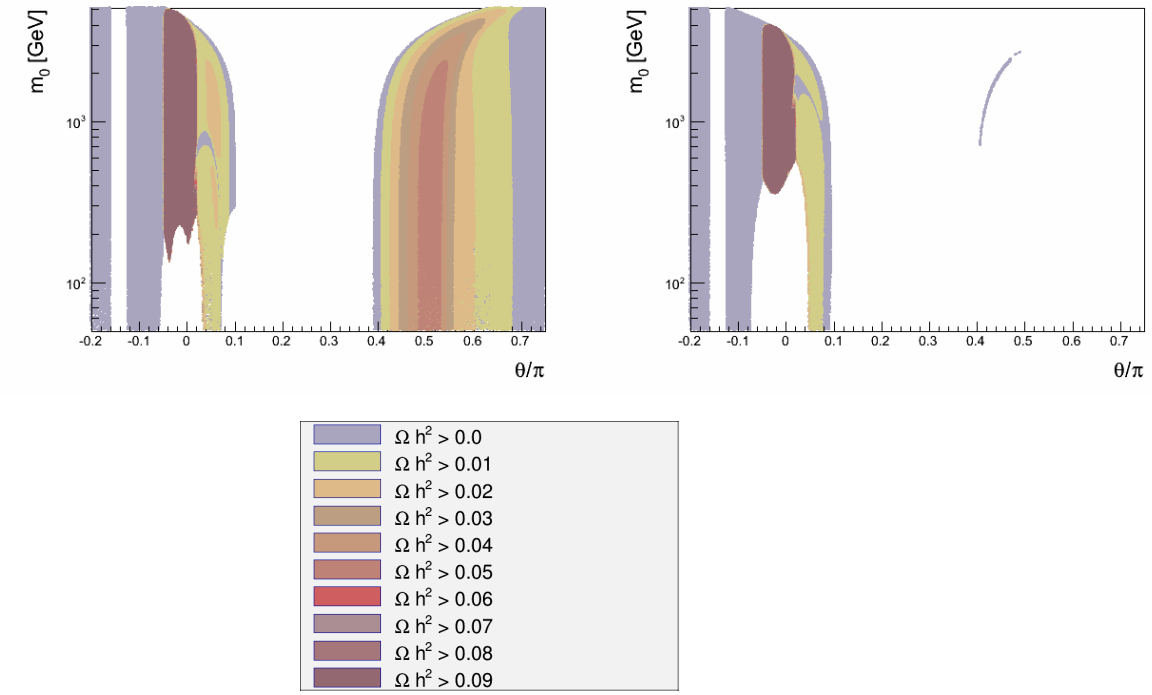

Figure 6.20: Relic density in the NUGM parameter space for $\tan\beta = 10$ (left) and $\tan\beta = 45$ (right). Colors correspond to a lower bound of the amount of dark matter in units of Ωh^2.

It was found, in contrast to the cMSSM and NUHM scenario, only a few models in the NUGM scenario fulfill the relic density requirement of $0.09 < \Omega h^2 < 0.13$. In most regions of

the NUGM parameter space the neutralino relic density is smaller than 0.09 ($\theta/\pi < -0.05$ and $\theta/\pi > 0.02$ for $\tan\beta = 10$ and 45). Thus, the relic density bounds are relaxed to $0 < \Omega h^2 < 0.13$, motivated by dark matter that may not only consist of one particle species, but a few (e.g. axions) or decaying particles in the early Universe. Treating gaugino masses independently at the GUT scale influences their values at the EWSB scale and thus, the neutralino's composition. Like in the Higgs section, the mixing angles θ_i were unified to $\theta \equiv \theta_1 = \theta_{24} = \theta_{75} = \theta_{200}$. The resulting parametrization, given by

$$\begin{aligned} M_1 &= m_{1/2}\,(\cos(\theta) + 16\sin(\theta)) \\ M_2 &= m_{1/2}\,(\cos(\theta) + 2\sin(\theta)) \\ M_3 &= m_{1/2}\,(\cos(\theta) - 2\sin(\theta)) \end{aligned} \tag{6.5}$$

leads to a neutralino mostly composed of the wino and the higgsino states. For $-0.05 \lesssim \theta/\pi \lesssim 0.05$, obviously $\sin(\theta) \sim \theta$ is given. In this region the singlet contribution (corresponds to the cMSSM) dominates and leads to a gaugino mass universality at the GUT scale. Due to renormalization, the gaugino mass ratios at the EWSB scale are $M_3{:}M_2{:}M_1 \sim 6:2:1$. The neutralino is then a pure bino state. Deviating from $-0.05 \lesssim \theta/\pi \lesssim 0.05$, implies that $|M_1(M_{\rm GUT})| \gg |M_{2,3}(M_{\rm GUT})|$ and the neutralino will be dominated by either the wino ($\theta/\pi < -0.05$ and $\theta/\pi > 0.58$) or the higgsino state ($\theta/\pi > 0.04$ and $\theta/\pi < 0.52$) or a mixture between wino and higgsino ($0.02 \lesssim \theta/\pi \lesssim 0.06$ and $0.53 \lesssim \theta/\pi \lesssim 0.56$). Unfortunately, annihilation processes for pure wino and higgsino neutralinos are very efficient and deplete the neutralino population extremly. Thus, Ωh^2 drops below 0.09. A lower value of Ωh^2 with respect to WMAP data can be accepted if the missing relic density is filled up with dark matter particles produced non-thermally, e.g. the decay of long lived particles or cosmic strings (Moroi & Randall 2000,Chung et al. 1999,Jeannerot et al. 1999). Wino or higgsino like dark matter could have been produced non-thermally, in a sense that Ωh^2 is decomposed into the sum of thermally plus non-thermally produced dark matter, $\Omega = \Omega_{\rm therm} + \Omega_{\rm nontherm}$ (see e.g. Jeannerot et al. 1999). The total relic density of cold dark matter can then be kept in agreement with observations. In Figure 6.21, regions in the θ/π-m_0 plane consistent with $122 < m_h < 128$ GeV and $0 < \Omega h^2 < 0.13$ are shown.

The parameters in the white region between $0.1 \lesssim \theta/\pi \lesssim 0.4$ for both $\tan\beta$ values do not have a correct electroweak symmetry breaking, i.e. do not have a convergent μ from solving the renormalization group equations (RGE). The region between $-0.16 \lesssim \theta/\pi \lesssim -0.12$ for both $\tan\beta$ violates the LEP2 bound on the chargino mass (Nakamura et al. 2011). The white region between $-0.07 \lesssim \theta/\pi \lesssim 0.04$ is forbidden due to tachyonic third generation sfermions ($\tan\beta = 45$), or has a Higgs potential that is unbound from below, or leads to charge and color breaking minima (see e.g. Frere et al. 1983,Alvarez et al. 1983,Derendinger & Savoy 1984,Kounnas et al. 1984), for $\tan\beta = 10$. θ/π values greater than ~ 0.4 for $\tan\beta = 45$ lead to a tachyonic pseudoscalar Higgs boson A and are excluded. For $\tan\beta = 10$, several coannihilation regions occur. For $-0.1 \lesssim \theta/\pi \lesssim 0.08$ and $m_0 \lesssim 1.5$ TeV as well as $0.54 < \theta/\pi < 0.6$ and $m_0 < 400$ GeV the tau slepton, $\tilde{\tau}$, and the tau sneutrino, $\tilde{\nu}_\tau$, are nearly degenerate with the neutralino mass. Further, the top squark, $\tilde{t}$, coannihilates with the neutralino for $0.02 \lesssim \theta/\pi \lesssim 0.08$ and $m_0 \lesssim 2$ TeV. Large parts of this coannihilation

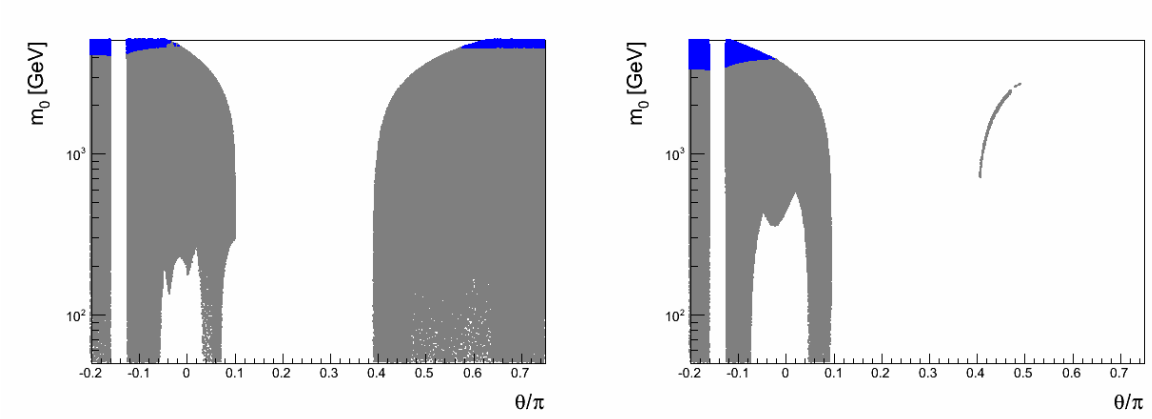

Figure 6.21: Regions in the NUGM parameter space consistent with $122 < m_h < 128$ GeV and $0 < \Omega h^2 < 0.13$ (blue) for $\tan\beta = 10$ (left) and $\tan\beta = 45$ (right). Gray colored are models that either have $\Omega h^2 > 0.13$ or $m_h < 122$ GeV or $m_h > 128$ GeV.

regions are excluded because the squarks are lighter than 1.4 TeV for $-0.05 < \theta/\pi < 0.12$ and $m_0 < 2$ TeV. Resonant annihilation regions with the pseudoscalar Higgs Boson A and the lightest Higgs boson h similar to h- and A- funnel regions of the cMSSM can be found in the vicinity of the LEP2 bound, for h, and $0.02 \lesssim \theta/\pi \lesssim 0.08$ and $m_0 < 1$ TeV for A. The latter one is excluded by squarks that are too light (The ATLAS Collaboration 2012b).

For $\tan\beta = 45$, the above regions coincide, except the $\tilde{\tau}$ and $\tilde{\nu}_\tau$ coannihilation region for $\theta/\pi \sim 0.5$, because of a tachyonic pseudoscalar Higgs boson. As for $\tan\beta = 10$, most of the coannihilation regions are excluded by squarks that are too light for $-0.04 \lesssim \theta/\pi \lesssim 0.1$ and $m_0 < 2$ TeV.

Due to the relaxed lower bound on the relic density, remaining regions of the parameter space consistent with a Higgs boson mass $122 < m_h < 128$ GeV and $\Omega h^2 < 0.13$ are highly correlated to regions where m_h achieves values within the required range. Figure 6.22 gives an enlarged viewing of allowed regions (blue colored) in Figure 6.21.

Allowing for non-universal gaugino masses enables a number of models, that simultaneously fulfill constraints from the Higgs boson as well as constraints from the relic density, where models in the cMSSM do not (imaginary vertical line at $\theta/\pi = 0$ in Figures 6.21 and Figure 6.22). Nevertheless, a high value of m_0 must be accepted, exclusively driven by the detected Higgs boson with a mass of ~ 125 GeV/c^2. Further, allowing mixing angles θ_1, θ_{24}, θ_{75} and θ_{200} to vary independently the number of consistent models is drastically enlarged. Corresponding plots can be found in the Appendix A.2.

6.4 Indirect Detection

After identifying regions of the parameter space, which are consistent with the detected Higgs boson and a correct relic density of the neutralino, current limits of selected indirect detection experiments, i.e. ANTARES and IceCube (see subsection 4.4.2), will be applied to the investigated scenarios. Special focus is set to the muon neutrino flux, ϕ_{ν_μ}, from an-

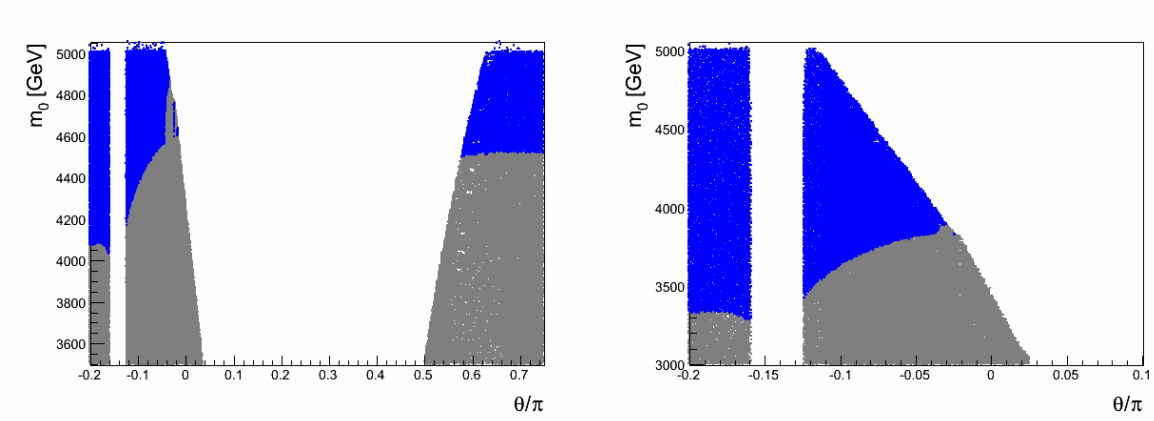

Figure 6.22: Regions in the NUGM parameter space consistent with $122 < m_h < 128$ GeV and $0 < \Omega h^2 < 0.13$ (blue) for $\tan\beta = 10$ (left) and $\tan\beta = 45$ (right). Gray colored are models that either have $\Omega h^2 > 0.13$ or $m_h < 122$ GeV or $m_h > 128$ GeV.

nihilating neutralinos in the Sun and the related muon flux, ϕ_μ (first part of this section). The measured muon flux coming from below is due to muon neutrinos which interact in charged current interactions in or close to the detector. Further, from limits on ϕ_{ν_μ}, limits on the spin-dependent neutralino proton cross-section (see subsection 4.4.1) can be derived and will be taken into account in the second part of this section.

When comparing the experimental limits presented in this Section and in Section "Direct Detection" to the model's predictions, it should be mentioned that uncertainties and approximations are contained. These uncertainties comprise the WIMP nucleon cross-section, $\sigma_{\mathrm{SI}}^{\mathrm{nucleon}}$ (section 6.5). According to Younkin & Martin 2012, uncertainties in nuclear matrix elements can reduce $\sigma_{\mathrm{SI}}^{\mathrm{nucleon}}$ by more than a factor of two. Less important are uncertainties in the local dark matter density $\rho_0 = 0.3 \pm 0.1$ GeV/cm^3 (Bovy & Tremaine 2012). It affects the capture rate of neutralinos in the Sun and also the predictability with respect to direct detection.

6.4.1 Muon Neutrino and Muon Flux from Annihilating Dark Matter

Independent from the choice of the SUSY model, the highest muon neutrino flux and thus, the highest muon flux is expected in regions of the parameter space, where the neutralino has a significant higgsino contribution. This happens if the Higgs mass parameter, μ, appearing in the scalar potential is small. Annihilation channels including Higgs bosons and vector bosons are then accessible leading to a higher yield of muon neutrinos and therefore, a higher yield of muons. Accordingly, the highest detection/exclusion capabilities of indirect dark matter search experiments are encountered in those regions. Further, a small μ is desirable as it would solve the SUSY little hierarchy problem (Younkin & Martin 2012).

All calculations in this Subsection were carried out for neutralino annihilations in the Sun.

cMSSM:
First, the resulting muon neutrino flux, ϕ_{μ_ν}, and the related muon flux, ϕ_μ, predicted by the constrained minimal supersymmetric standard model are discussed. In Figure 6.23, the integrated muon neutrino flux is plotted logarithmically versus the neutralino mass m_χ.

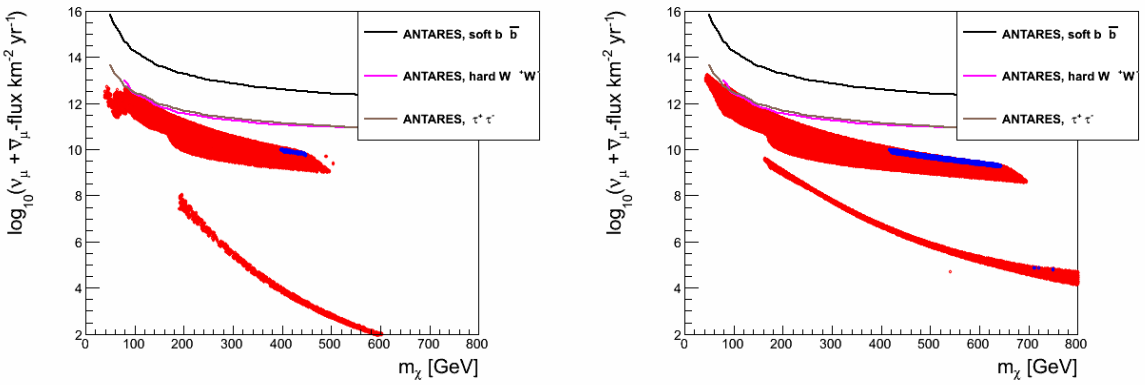

Figure 6.23: Sum of ν_μ and $\bar{\nu}_\mu$ flux from dark matter annihilation in the cMSSM, $\tan\beta = 10$ (left) and $\tan\beta = 45$ (right); colors: blue: models with $122 < m_h < 128$ GeV and $0.09 < \Omega h^2 < 0.13$ fulfilled simultaneously; red: models with $m_h < 122$ GeV or $m_h > 128$ GeV or $\Omega h^2 > 0.13$ or $\Omega h^2 < 0.09$; black line: ANTARES upper limit at 90% C.L. on $\nu_\mu + \bar{\nu}_\mu$ flux for a 100 % annihilation into $b\bar{b}$, magenta line: annihilation into W^+W^-, brown line: annihilation into $\tau^+\tau^-$ (Adrian-Martinez et al. 2012).

The neutralino mass, m_χ, must exceed ~ 400 GeV to achieve models consistent with $122 < m_h < 128$ GeV and $0.09 < \Omega h^2 < 0.13$. Those models lead to a $\nu_\mu + \bar{\nu}_\mu$ flux in the order of 10^{10} muon neutrinos plus anti muon neutrinos per km^2 and per year. From Figure 6.17 follows, that those models have either small m_0 and high $m_{1/2}$ or vice versa. The neutralino mass in that regions exceeds ~ 400 GeV.

The black, magenta and brown lines in Figure 6.23 correspond to the ANTARES limit at 90% C.L., assuming all annihilations exclusively go either into $b\bar{b}$, W^+W^-, or $\tau^+\tau^-$ (Adrian-Martinez et al. 2012). In that way, the limit is independent from the choice of SUSY model. As can be seen from Figure 6.23, ANTARES is not yet able to exclude models in the cMSSM scenario. The published ANTARES limit is based on 282.84 days of data taking. More stringent limits are expected from the analysis of further data taken with the 12 line detector configuration.

The muon flux resulting from neutrino to muon conversion in the vicinity of the detector is plotted in Figure 6.24. The black line corresponds to the muon flux limit given by the IceCube collaboration for a detector configuration of 86 strings deployed, including the low energy extension DeepCore (6 strings).

Assuming all annihilations take place via channel W^+W^- (black line in Figure 6.24, (The IceCube Collaboration 2011)), IceCube can exclude many of the models consistent with $122 < m_h < 128$ GeV and $0.09 < \Omega h^2 < 0.13$ for $\tan\beta = 10$ at 90% C.L. For $\tan\beta = 45$, more models survive the exclusion limit. The muon flux limit in Figure 6.24

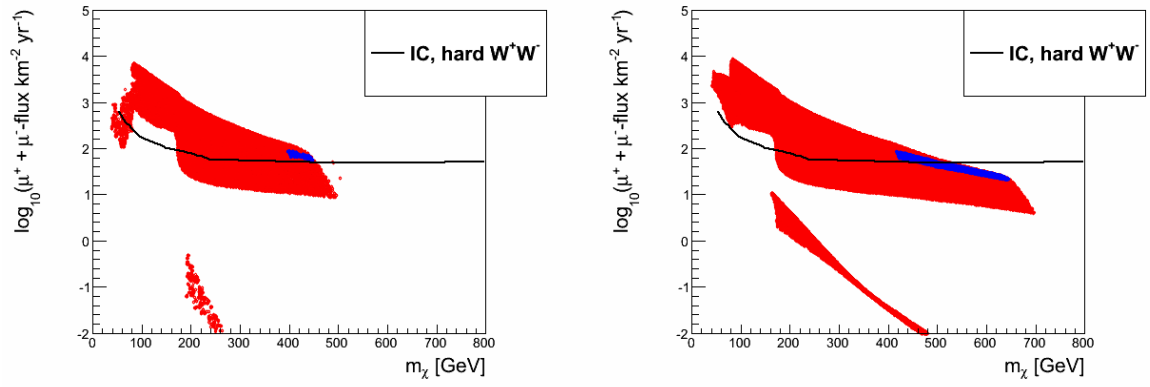

Figure 6.24: Sum of μ^+ and μ^- flux from dark matter annihilation in the cMSSM, $\tan\beta = 10$ (left) and $\tan\beta = 45$ (right); colors: blue: models with $122 < m_h < 128$ GeV and $0.09 < \Omega h^2 < 0.13$ fulfilled simultaneously; red: models with $m_h < 122$ GeV or $m_h > 128$ GeV or $\Omega h^2 > 0.13$ or $\Omega h^2 < 0.09$; black line: IceCube upper limit at 90% C.L. on $\mu^+ + \mu^-$ flux for a 100 % annihilation into W^+W^- (The IceCube Collaboration 2011).

was projected into the m_0-$m_{1/2}$ plane, to see which part of the cMSSM parameter space is excluded (Figure 6.25).

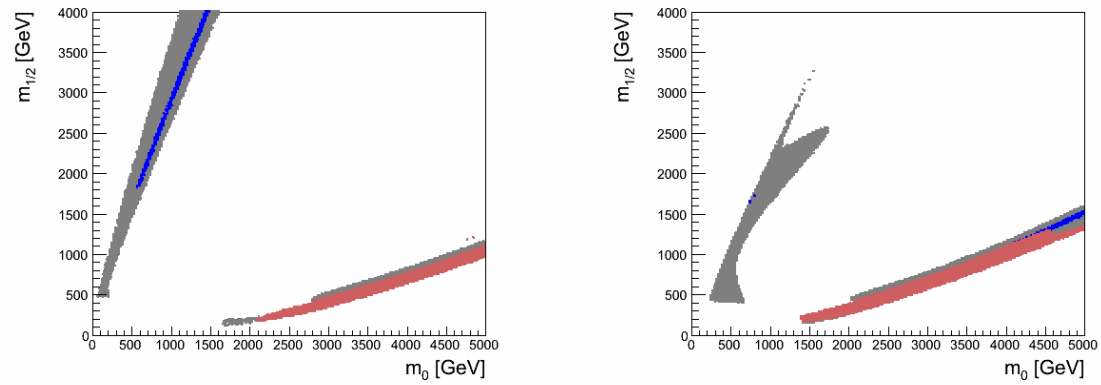

Figure 6.25: By IceCube excluded regions in the m_0-$m_{1/2}$ plane of cMSSM; colors: gray: not excluded, faint brown: excluded at 90% C.L. for annihilation channel W^+W^-, blue: not excluded models with $122 < m_h < 128$ GeV and $0.09 < \Omega h^2 < 0.13$.

The whole focus point region is excluded by IceCube for $\tan\beta = 10$, especially all models that provide a correct Higgs boson mass and a neutralino with a correct relic density. For $\tan\beta = 45$ only a few models that are conform with m_h and Ωh^2 survive the IceCube muon flux limit. The resulting μ^+-μ^- flux in the $\tilde{\tau}$ coannihilation region is smaller than $10^{-3}/km^2/yr$. Thus, models, consistent with the Higgs-boson mass and relic density in that region (see left hand side of Figure 6.25), do not appear in Figure 6.24.

NUHM:
The predicted muon neutrino and muon flux in models with a non-universal Higgs sector is shown in Figure 6.26 for the case where $\delta_{H_u} = \delta_{H_d}$ (NUHM1). Afterwards, the more general case with $\delta_{H_u} \neq \delta_{H_d}$ (NUHM2) will be discussed.

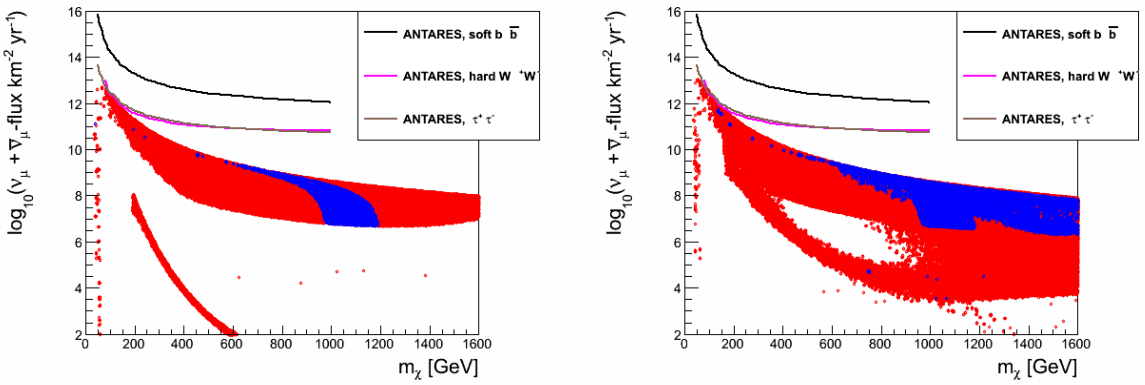

Figure 6.26: Sum of ν_μ and $\bar{\nu}_\mu$ flux from dark matter annihilation in NUHM1, $\tan\beta = 10$ (left) and $\tan\beta = 45$ (right); colors: blue: models with $122 < m_h < 128$ GeV and $0.09 < \Omega h^2 < 0.13$ fulfilled simultaneously; red: models with $m_h < 122$ GeV or $m_h > 128$ GeV or $\Omega h^2 > 0.13$ or $\Omega h^2 < 0.09$; black line: ANTARES upper limit at 90% C.L. on $\nu_\mu + \bar{\nu}_\mu$ flux for a 100 % annihilation into $b\bar{b}$, magenta line: annihilation into W^+W^-, brown line: annihilation into $\tau^+\tau^-$ (Adrian-Martinez et al. 2012).

From Figure 6.18 (in case of $\tan\beta = 10$) follows, that models consistent with m_h and Ωh^2 must exceed $m_{1/2} > 1.6$ TeV, roughly independent from m_0. In this continuous region, the neutralino has a mass of $m_\chi \gtrsim 700$ GeV (apart from a few isolated models with $m_\chi < 700$ GeV). Increasing the neutralino mass leads to smaller neutrino fluxes, as the number density of neutralinos (see Equation 4.18) decreases and thus, the number of neutralino annihilations that produce neutrinos. For $\tan\beta = 45$, values of $m_{1/2}$ can be smaller ($\gtrsim 1.5$ TeV) and therefore the mass of the neutralino is reduced to smaller values. Like in the cMSSM case, the current ANTARES limit is not yet able to exclude models in the NUHM1 scenario. Again, this will change, if more data will be analyzed in the future. Contrarily, IceCube can exclude at least a few of the models (~ 300 for $\tan\beta = 10$ and ~ 1400 for $\tan\beta = 45$) conform with m_h and Ωh^2 (Figure 6.27).

Only a slight improvement with respect to exclusion capabilities of the presented indirect dark matter searches from ANTARES and IceCube is achieved in the NUHM2 scenario, where $\delta_{H_u} \neq \delta_{H_d}$ applies. As ANTARES can not exclude any of the models consistent with $122 < m_h < 128$ GeV and $0.09 < \Omega h^2 < 0.13$ for $\tan\beta = 10$ and about 60 models for $\tan\beta = 45$, the resulting muon neutrino flux is not shown here. IceCube excludes for $\tan\beta = 10$ (left hand side of Figure 6.28) about 300 models consistent with $122 < m_h < 128$ GeV and $0.09 < \Omega h^2 < 0.13$. In the case of $\tan\beta = 45 \sim 2700$ models are excluded by IceCube.

Projecting the excluded models into the m_0-$m_{1/2}$ plane (Figure 6.29), the central gray

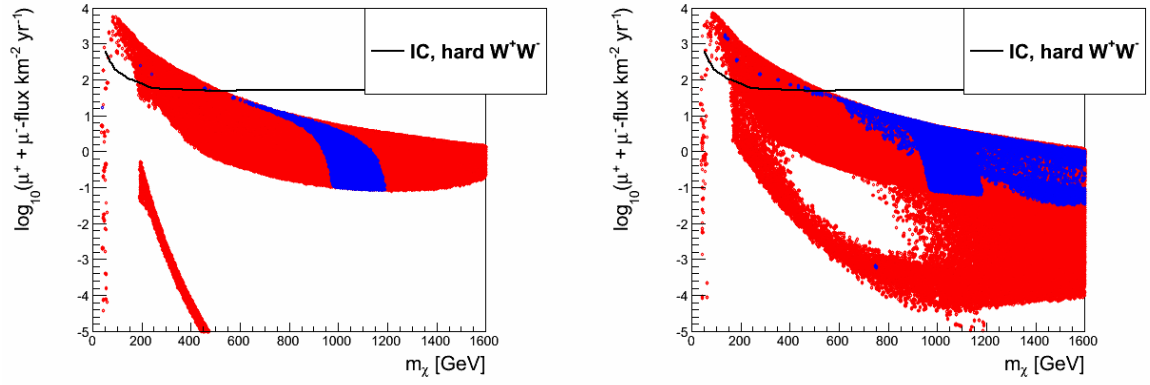

Figure 6.27: Sum of μ^+ and μ^- flux from dark matter annihilation in the NUHM1 scenario, $\tan\beta = 10$ (left) and $\tan\beta = 45$ (right); colors: blue: models with $122 < m_h < 128$ GeV and $0.09 < \Omega h^2 < 0.13$ fulfilled simultaneously; red: models with $m_h < 122$ GeV or $m_h > 128$ GeV or $\Omega h^2 > 0.13$ or $\Omega h^2 < 0.09$; black line: IceCube upper limit at 90% C.L. on $\mu^+ + \mu^-$ flux for a 100 % annihilation into W^+W^- (The IceCube Collaboration 2011).

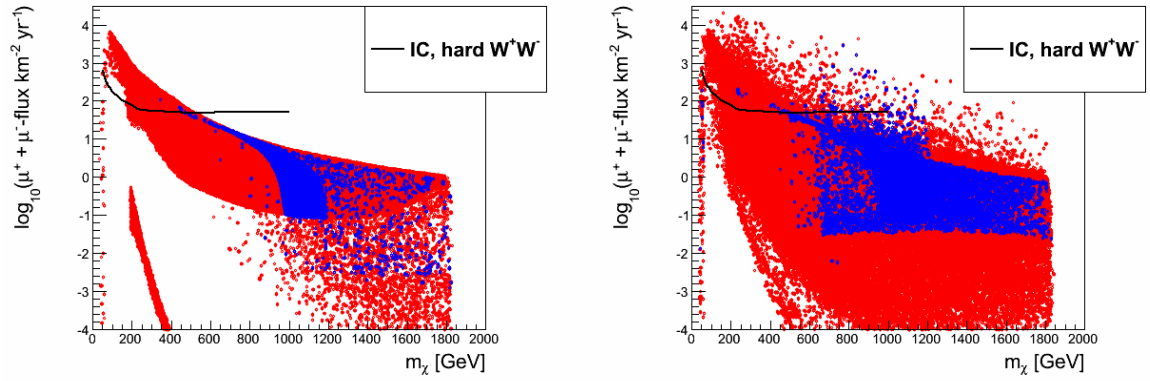

Figure 6.28: Sum of μ^+ and μ^- flux from dark matter annihilation in NUHM2, $\tan\beta = 10$ (left) and $\tan\beta = 45$ (right); colors: blue: models with $122 < m_h < 128$ GeV and $0.09 < \Omega h^2 < 0.13$ fulfilled simultaneously; red: models with $m_h < 122$ GeV or $m_h > 128$ GeV or $\Omega h^2 > 0.13$ or $\Omega h^2 < 0.09$; black line: IceCube upper limit at 90% C.L. on $\mu^+ + \mu^-$ flux for a 100 % annihilation into W^+W^- (The IceCube Collaboration 2011).

region up to $m_{1/2} \lesssim 1.5$ TeV for $\tan\beta = 10$ in both NUHM1 and NUHM2 are excluded. For $\tan\beta = 45$, the situation stays nearly the same in the NUHM1 scenario, while in NUHM2 a dip of excluded models occurs around $m_0 \sim 2.8$ TeV and $m_{1/2} \lesssim 3.5$ TeV. There, the pseudoscalar Higgs boson A has a mass $m_A \sim 2m_\chi$ and pairs of neutralinos annihilate resonantly via A exchange into pairs of fermions (A-funnel region). Thus, the resulting muon flux is enhanced and therefore accessible by the IceCube limit.

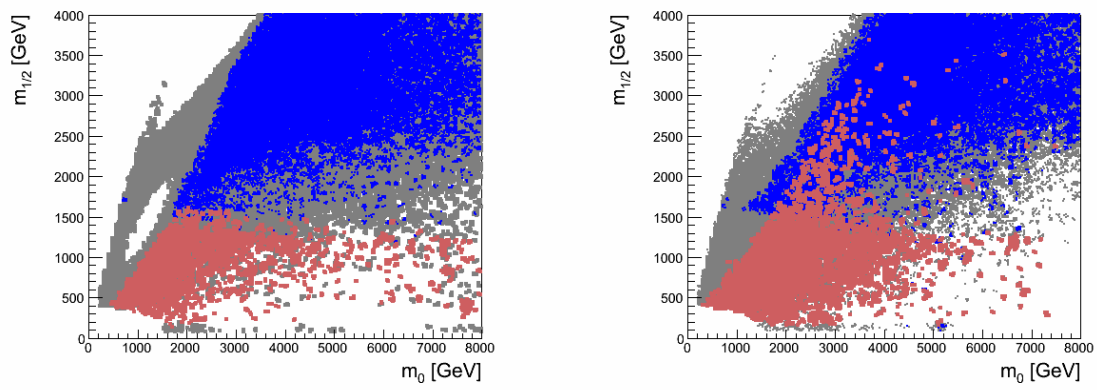

Figure 6.29: IceCube excluded regions in the m_0-$m_{1/2}$ plane of the NUHM1 (left) and NUHM2 (right) scenario for $\tan\beta = 45$. Colors: faint red: excluded by IceCube at 90% C.L. for annihilation channel W^+W^-; blue: models consistent with $122 < m_h < 128$ GeV and $0.09 < \Omega h^2 < 0.13$ (not excluded); gray: all other models

The A-funnel region is also present in NUHM1 for $\tan\beta = 45$. The given IceCube limit on the muon flux is only sensitive for neutralino masses up to ~ 500 GeV. In the corresponding region of the m_0-$m_{1/2}$ plane, where $m_\chi < 500$ GeV applies, the pseudoscalar Higgs boson, A, is too heavy, especially $m_A \gtrsim 3m_\chi$, and the A annihilation channel is forbidden kinematicaly. Further, the A-funnel region in NUHM1 is well separated from the region where $122 < m_h < 128$ GeV and $0.09 < \Omega h^2 < 0.13$ applies. Consequently, resonant annihilation via A exchange can be neglected in NUHM1 with respect to the given IceCube limit. In NUHM2, the "resonant A annihilation" region is smeared out, due to the additional degree of freedom, δ_{H_d}, allowing for a broader region where $m_A \sim 2m_\chi$ is realized.

Having studied the detection/exclusion capability of the indirect dark matter search experiments, ANTARES and IceCube, in SUSY models with non-universal scalars, in the following subsection the non-universal gaugino sector will be discussed.

NUGM:

The predicted muon neutrino and anti-muon neutrino flux is plotted versus the neutralino mass in Figure 6.30 and compared with the respective limit on the muon neutrino flux given by the ANTARES collaboration at 90% C.L. (Adrian-Martinez et al. 2012). Like in the previous chapter, some of the results presented here were already published in Spies & Anton 2013.

Like in the previous models, the ANTARES limits do not set severe constraints on the parameter space of the NUGM scenario. Only a tiny fraction of models (~ 50) can be excluded for $\tan\beta = 45$, which can be absorbed into systematic uncertainties mentioned at the beginning of this Section. Figure 6.31 shows the limit (at 90% C.L.) of the IceCube neutrino telescope (The IceCube Collaboration 2011) on the muon plus anti muon flux from neutralino annihilations. A substantial amount of models, consistent with $\Omega h^2 < 0.13$ and $122 < m_h < 128$, are not yet excluded by IceCube at 90% C.L. for $\tan\beta = 10$ as well as

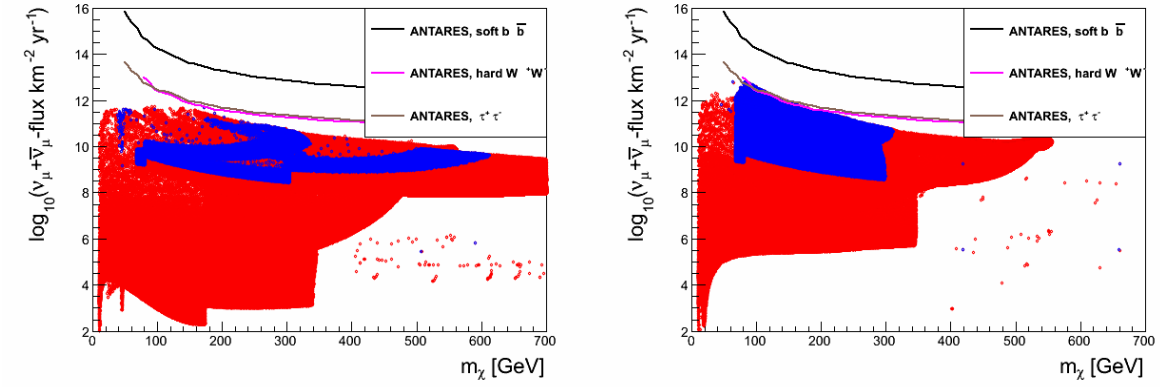

Figure 6.30: Sum of ν_μ and $\bar{\nu}_\mu$ flux the NUGM scenario, tan$\beta = 10$ (left) and tan$\beta = 45$ (right), $m_{1/2} = 600$ GeV and $A_0 = -600$ GeV; colors: blue: models with $\Omega h^2 < 0.13$ and $122 < m_h < 128 GeV$; red: all other models; black line: ANTARES upper limit at 90% C.L. on $\nu_\mu + \bar{\nu}_\mu$ flux for a 100 % annihilation into $b\bar{b}$, magenta line: annihilation into W^+W^-, brown line: annihilation into $\tau^+\tau^-$ (Adrian-Martinez et al. 2012).

tan $\beta = 45$.

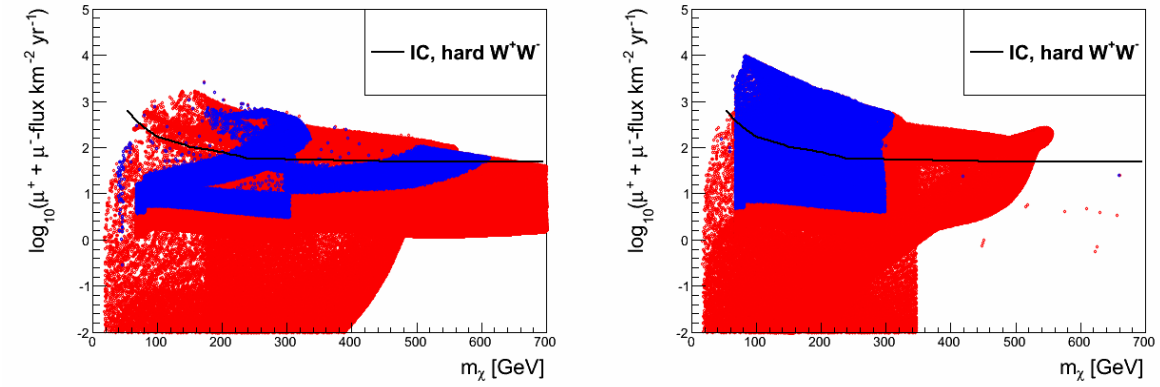

Figure 6.31: Sum of μ^+ and μ^- flux for representation $\mathbf{1} \oplus \mathbf{24} \oplus \mathbf{75} \oplus \mathbf{200}$, tan$\beta = 10$ (left) and tan$\beta = 45$ (right), $m_{1/2} = 600$ GeV and $A_0 = -600$ GeV; colors: blue: models with $\Omega h^2 < 0.13$ and $122 < m_h < 128$ GeV; red: all other models; black line: IceCube upper limit at 90% C.L. (The IceCube Collaboration 2011) on $\mu^+ + \mu^-$-flux for a 100% annihilation into W^+W^-.

The exclusion limit is projected into the $m_0 - \theta/\pi$ plane to visualize which part of the parameter space can be excluded. These regions are shown in Figure 6.32 for the annihilation channel W^+W^-.

For tan$\beta = 10$, large parts of the "high higgsino" or "small μ" regions for $0 \lesssim \theta/\pi \lesssim 0.1$ and on top ($m_0 \gtrsim 4$ TeV, $-0.2 \lesssim \theta/\pi \lesssim 0$ and $0.64 \lesssim \theta/\pi < 0.75$) are excluded assuming all

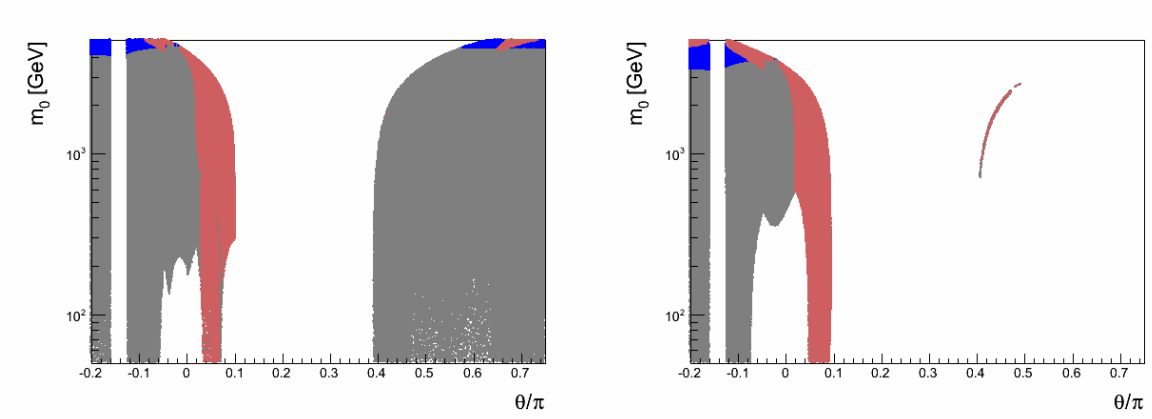

Figure 6.32: IceCube excluded models at 90% C.L. for a 100% annihilation into W^+W^- for representation $\mathbf{1} \oplus \mathbf{24} \oplus \mathbf{75} \oplus \mathbf{200}$ of SU(5) $\tan\beta = 10$ (left) and $\tan\beta = 45$ (right); gray: not excluded, faint brown: excluded, blue: models consistent with $122 < m_h < 128$ GeV and $\Omega h^2 < 0.13$ (not excluded).

annihilations go into W^+W^-. This also applies for $\tan\beta = 45$, where models with $m_0 > 3.5$ TeV and $-0.2 < \theta/\pi \lesssim 0$ are excluded as well as models with $0 \lesssim \theta/\pi < 0.1$. Also, the thin arc on the right hand side for $\tan\beta = 45$ is excluded by IceCube.

From the indirect detections point of view, the limit from the IceCube collaboration has the best power to exclude the kind of models investigated in this work.

6.4.2 Spin-Dependent Neutralino Proton Cross-section

The spin-dependent neutralino proton cross-section, $\sigma_{\mathrm{SD}}^{\mathrm{proton}}$, can be derived from the expected muon flux according to Section 4.4.2. The conversion factor κ depends on the neutralino mass, m_χ, and increases for $m_\chi \gtrsim 200$ GeV. As the muon flux limit is roughly constant for $m_\chi > 300$ GeV, $\kappa(m_\chi)$ leads to an increase of the limit on $\sigma_{\mathrm{SD}}^{\mathrm{proton}}$ for $m_\chi > 300$ GeV. The predicted cross-sections will be compared with limits from ANTARES (Adrian-Martinez et al. 2012) and IceCube (Aartsen et al. 2013) on $\sigma_{\mathrm{SD}}^{\mathrm{proton}}$. As it is common for indirect dark matter search experiments, the corresponding limits are given for two annihilation channels, i.e. $b\bar{b}$ and W^+W^-.

cMSSM:
The predicted spin-dependent neutralino proton cross-section in the cMSSM is plotted in Figure 6.33. Also shown are current experimental limits of ANTARES (gray and faint brown line) and IceCube (black and magenta line).

Due to the increase of $\kappa(m_\chi)$ for $m_\chi > 200$ GeV, neither the given ANTARES limit, nor the IceCube limit can exclude models that simultaneously provide a Higgs boson with a mass of $122 < m_h < 128$ GeV and a relic density with $0.09 < \Omega h^2 < 0.13$, for both $\tan\beta = 10$ and $\tan\beta = 45$. The corresponding plots of the excluded regions in the m_0-$m_{1/2}$ plane

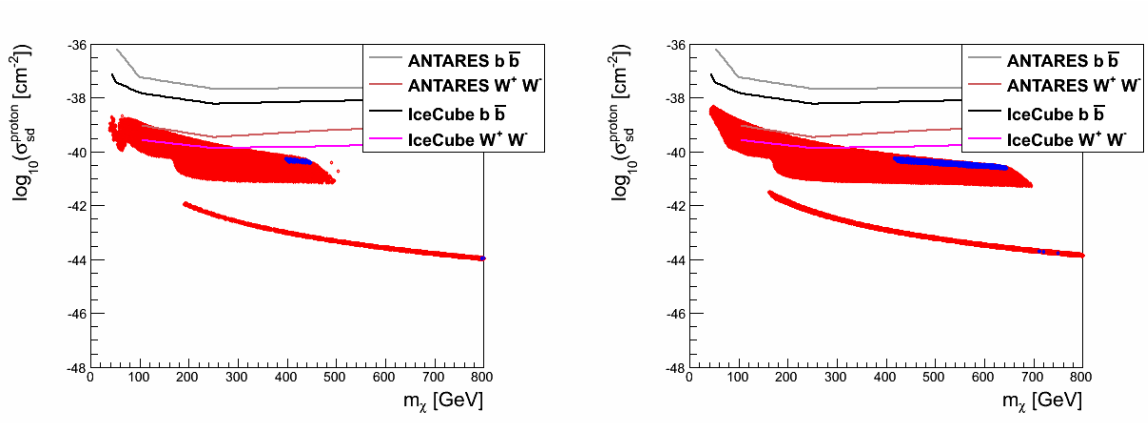

Figure 6.33: Predicted spin-dependent neutralino proton cross-section, $\sigma_{\mathrm{SD}}^{\mathrm{proton}}$, in the cMSSM scenario plotted logarithmically versus the neutralino mass m_χ for $\tan\beta = 10$ (left) and $\tan\beta = 45$ (right); colors: blue: models with $0.09 < \Omega h^2 < 0.13$ and $122 < m_h < 128$ GeV; red: all other models; gray line: ANTARES upper limit at 90% C.L. for annihilation channel $b\bar{b}$ (Adrian-Martinez et al. 2012), faint brown line: ANTARES upper limit at 90% C.L. for annihilation channel W^+W^-, black line: IceCube upper limit at 90% C.L. for channel $b\bar{b}$, magenta line: IceCube upper limit at 90% C.L. for channel W^+W^- (Aartsen et al. 2013).

can be found in the Appendix A.3.

NUHM:
Figure 6.34 shows the predicted spin-dependent neutralino proton cross-section in the NUHM1 scenario for $\tan\beta = 10$ on the left and $\tan\beta = 45$ on the right hand side. Like in the cMSSM, the current indirect dark matter search experiments ANTARES and IceCube are not yet able to put severe constraints to the scenario's parameter space, especially to regions where the predicted mass of the Higgs boson is in the range $122 < m_h < 128$ GeV at the same time fulfilling $0.09 < \Omega h^2 < 0.13$. While ANTARES can not exclude any of these models, for annihilation channel W^+W^-, IceCube excludes less than 100 of approximately 165 000 (305 000) models for $\tan\beta = 10$ (45) that fulfill the previous constraints.

Again, the corresponding excluded regions in the m_0-$m_{1/2}$ plane are shown in the Appendix A.3, for the sake of completeness. The spin-dependent neutralino proton cross-section in the more general NUHM2 model, where $m_{H_u}^2$ and $m_{H_d}^2$ were varied independently, are plotted logarithmically versus the neutralino mass in Figure 6.35

NUGM:
After having investigated the non-universal scalar sector with respect to the detection/exclusion capability of the two neutrino detectors ANTARES and IceCube, in the following the non-universal gaugino sector is part of the discussion. Figure 6.36 shows the predicted spin-dependent neutralino proton cross-section. Again, some of the results in this paragraph

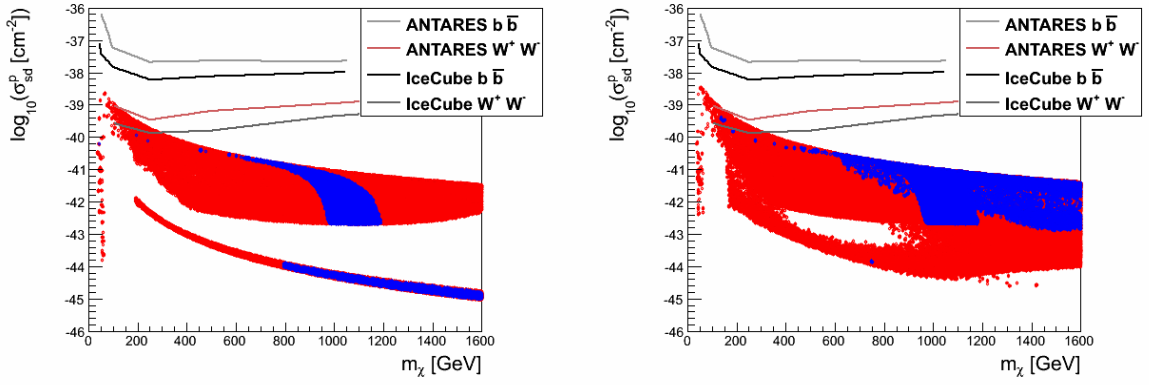

Figure 6.34: Predicted spin-dependent neutralino proton cross-section, $\sigma_{\mathrm{SD}}^{\mathrm{proton}}$, in the NUHM1 scenario plotted logarithmically versus the neutralino mass m_χ for $\tan\beta = 10$ (left) and $\tan\beta = 45$ (right); colors: blue: models with $0.09 < \Omega h^2 < 0.13$ and $122 < m_h < 128$ GeV; red: all other models; gray line: ANTARES upper limit at 90% C.L. for annihilation channel $b\bar{b}$ (Adrian-Martinez et al. 2012), faint brown line: ANTARES upper limit at 90% C.L. for annihilation channel W^+W^-, black line: IceCube upper limit at 90% C.L. for channel $b\bar{b}$, magenta line: IceCube upper limit at 90% C.L. for channel W^+W^- (Aartsen et al. 2013).

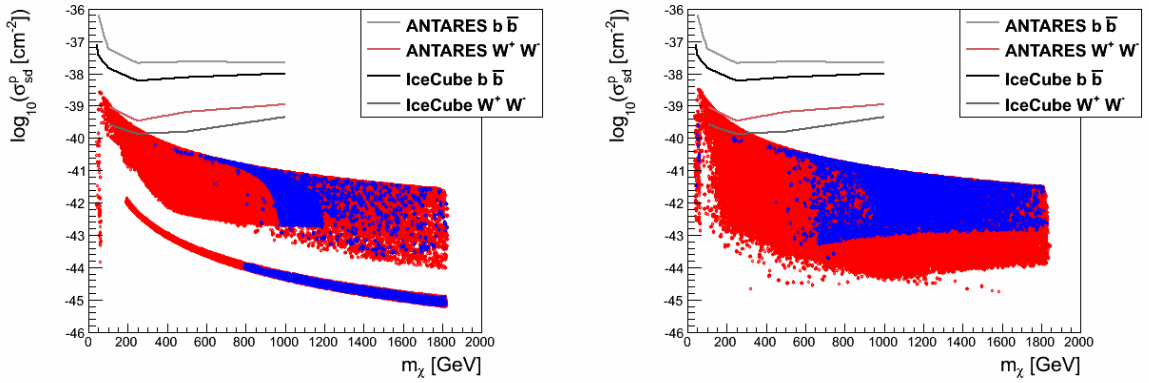

Figure 6.35: Predicted spin-dependent neutralino proton cross-section, $\sigma_{\mathrm{SD}}^{\mathrm{proton}}$, in the NUHM2 scenario plotted logarithmically versus the neutralino mass m_χ for $\tan\beta = 10$ (left) and $\tan\beta = 45$ (right); colors: blue: models with $0.09 < \Omega h^2 < 0.13$ and $122 < m_h < 128$ GeV; red: all other models; gray line: ANTARES upper limit at 90% C.L. for annihilation channel $b\bar{b}$ (Adrian-Martinez et al. 2012), faint brown line: ANTARES upper limit at 90% C.L. for annihilation channel W^+W^-, black line: IceCube upper limit at 90% C.L. for channel $b\bar{b}$, magenta line: IceCube upper limit at 90% C.L. for channel W^+W^- (Aartsen et al. 2013).

were already published in Spies & Anton 2013

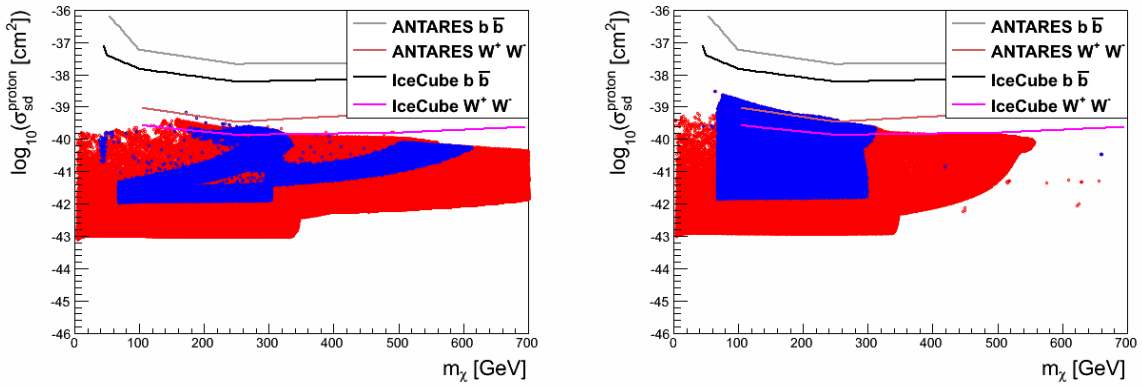

Figure 6.36: Predicted spin-dependent neutralino proton cross-section, $\sigma_{\mathrm{SD}}^{\mathrm{proton}}$, in the NUGM scenario plotted logarithmically versus the neutralino mass m_χ for $\tan\beta = 10$ (left) and $\tan\beta = 45$ (right); colors: blue: models with $0.09 < \Omega h^2 < 0.13$ and $122 < m_h < 128$ GeV; red: all other models; gray line: ANTARES upper limit at 90% C.L. for annihilation channel $b\bar{b}$ (Adrian-Martinez et al. 2012), faint brown line: ANTARES upper limit at 90% C.L. for annihilation channel W^+W^-, black line: IceCube upper limit at 90% C.L. for channel $b\bar{b}$, magenta line: IceCube upper limit at 90% C.L. for channel W^+W^- (Aartsen et al. 2013).

For $\tan\beta = 10$, IceCube already excludes models with $122 < m_h < 128$ GeV and $0.09 < \Omega h^2 < 0.13$. For $\tan\beta = 45$, both experiments ANTARES and IceCube exclude models that fulfill the Higgs and relic density constraints. The corresponding regions in the θ/π-m_0 plane are shown in Figure 6.37 for ANTARES and Figure 6.38 for IceCube.

In the cMSSM and NUHM scenario, the neutralino is dominated by either the bino and/or higgsino component. As already mentioned in Section 6.3, the parametrization of the non-universal gaugino sector leads to neutralinos, that are dominated by the wino and/or the higgsino, except for $-0.1 < \theta/\pi < 0.1$ where the neutralino is a pure bino. According to Murakami & Wells 2001, a wino and/or higgsino dominated neutralino increases scattering rates by an order of magnitude compared to a pure bino state, as scattering cross-sections are proportional to the weak coupling constant g_2^4 instead of the electromagnetic coupling constant g_1^4. Thus, both ANTARES and IceCube exclude parts of the NUGM parameter space.

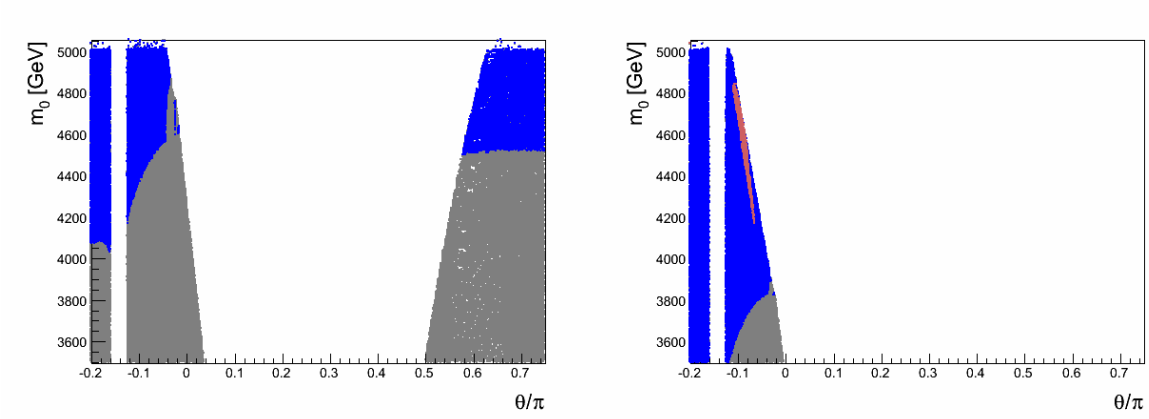

Figure 6.37: ANTARES excluded models for $\sigma_{\mathrm{SD}}^{\mathrm{proton}}$ at 90% C.L. for a 100% annihilation into W^+W^- (Adrian-Martinez et al. 2012) in NUGM for $\tan\beta = 10$ (left) and $\tan\beta = 45$ (right); gray: not excluded, faint brown: excluded, blue: models consistent with $122 < m_h < 128$ GeV and $\Omega h^2 < 0.13$.

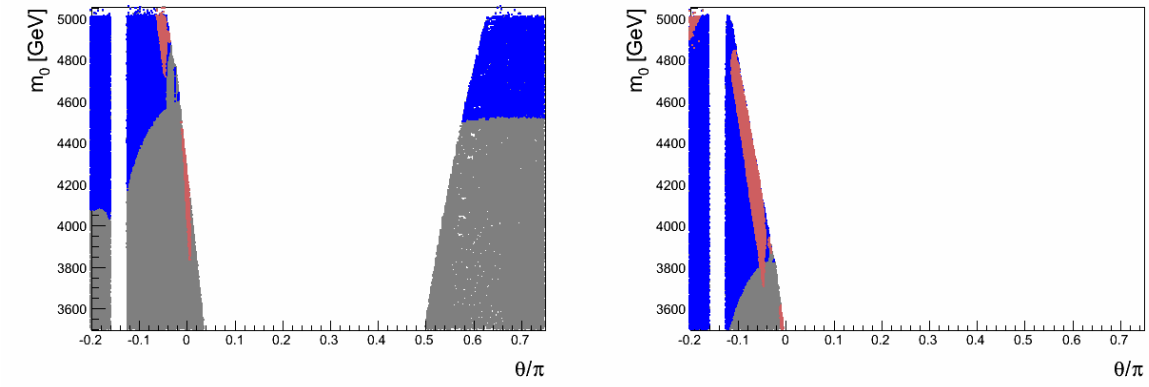

Figure 6.38: IceCube excluded models for $\sigma_{\mathrm{SD}}^{\mathrm{proton}}$ at 90% C.L. for a 100% annihilation into W^+W^- (Aartsen et al. 2013) in NUGM for $\tan\beta = 10$ (left) and $\tan\beta = 45$ (right); gray: not excluded, faint brown: excluded, blue: models consistent with $122 < m_h < 128$ GeV and $\Omega h^2 < 0.13$.

6.5 Direct Detection

A complementary experimental method for the search for dark matter are direct dark matter detection experiments. Neutralinos scatter of atomic nuclei and the recoil energy of the nucleus is measured. From the measured energy the spin-independent neutralino nucleon cross-section can be concluded (see section 4.4.1). In this section, the direct dark matter detection method is part of the discussion, i.e. the phenomenology of the introduced models is compared with the latest results given by the XENON collaboration, i.e. the current XENON 100 limit (April et al. 2012a) and exclusion/detection prospectives given by the

future extension XENON 1T (April et al. 2012b). These limits/sensitivities were selected, because they put the most stringent constraints on the scenarios' parameter spaces. Direct detection experiments are able to measure both, the spin-dependent and spin-independent neutralino nucleon cross-section. Nevertheless, for mass numbers (of the atomic nucleon) larger than 20, the spin-independent cross-section dominates. Thus, emphasis is set on the spin-independent neutralino nucleon cross-section, $\sigma_{\mathrm{SI}}^{\mathrm{nucleon}}$.

cMSSM:
Figure 6.39 shows the predicted spin-independent neutralino nucleon scattering cross-section in the cMSSM plotted versus the mass of the neutralino. Shown are limits given by the CDMS (Ahmed et al. 2010), EDELWEISS (Armengaud et al. 2011) and XENON 100 (April et al. 2012a) collaboration. Further, the predicted sensitivity of the future XENON 1T (April et al. 2012b) experiment is illustrated.

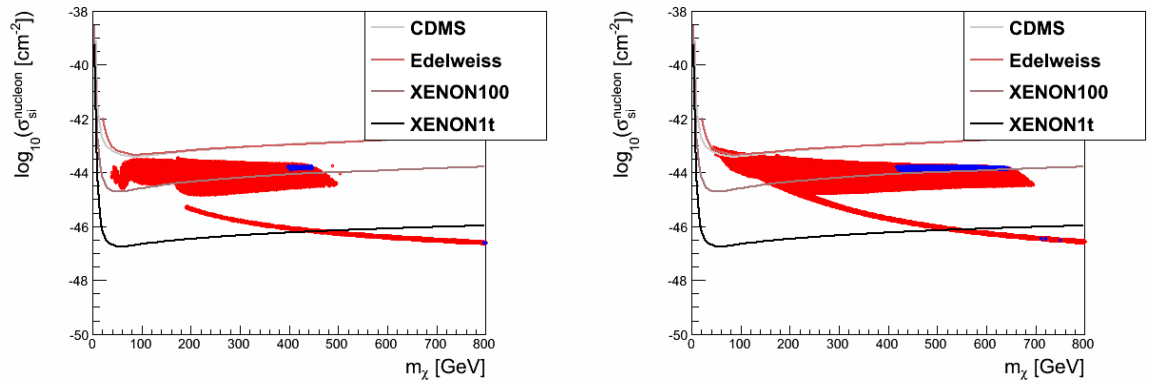

Figure 6.39: Predicted spin-independent neutralino nucleon cross-section $\sigma_{\mathrm{SI}}^{\mathrm{nucleon}}$ plotted versus the neutralino mass m_χ in the cMSSM scenario for $\tan\beta = 10$ (left) and $\tan\beta = 45$ (right); colors: blue: models consistent with $122 < m_h < 128$ GeV and $0.09 < \Omega h^2 < 0.13$, red: all other models; shown are 90% C.L. from CDMS (Ahmed et al. 2010) (gray line), EDELWEISS (Armengaud et al. 2011) (brown line), XENON 100 (April et al. 2012a) (shaded brown line) and the predicted sensitivity for XENON 1T (April et al. 2012b) (black line).

For both, $\tan\beta = 10$ and $\tan\beta = 45$, XENON 100 (brown line in Figure 6.39) excludes the whole focus point ("small μ") region of the cMSSM. Only for large values of m_χ, models consistent with m_h and Ωh^2 remain. They correspond to the $\tilde{\tau}$ coannihilation region (lower branch in Figure 6.39). Obviously, XENON 1T (black line in Figure 6.39) will be able to exclude substantially more models. Nevertheless, a few models, belonging to the $\tilde{\tau}$ coannihilation region, remain providing the neutralino as dark matter particle while simultaneously fulfilling the constraint coming from the Higgs boson mass. In Figure 6.40, excluded regions by XENON 100 are projected onto the m_0-$m_{1/2}$ plane

Not excluded models in Figure 6.40 do not appear in Figure 6.39 as they lay outside the scope of Figure 6.39, i.e. $m_\chi > 800$ GeV.

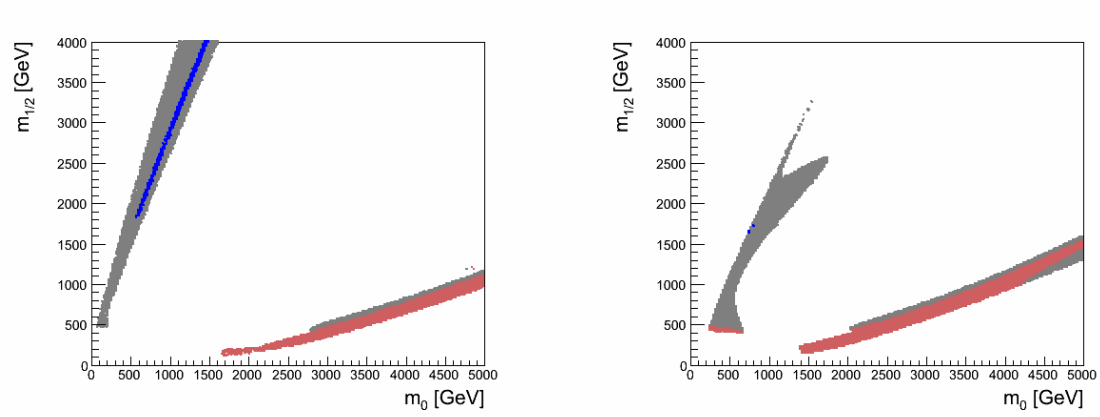

Figure 6.40: Excluded regions of the cMSSM parameter space from XENON 100, $\tan\beta = 10$ (left) and $\tan\beta = 45$ (right); colors: brown: excluded at 90% C.L., blue: models consistent with $122 < m_h < 128$ GeV and $0.09 < \Omega h^2 < 0.13$ (not excluded), gray: not excluded by XENON 100.

The current XENON 100 experiment leaves the $\tilde{\tau}$ coannihilation region of the cMSSM (small m_0 and $m_{1/2} > 1.6$ TeV) for $\tan\beta = 10$ as possible region in the parameter space, which provides a possible dark matter scenario ($0.09 < \Omega h^2 < 0.13$), at the same time providing a Higgs boson with a mass of $122 < m_h < 128$ GeV. For $\tan\beta = 45$, nearly the whole m_0-$m_{1/2}$ plane is excluded by the combination of XENON 100, Higgs mass and relic density constraints. This also applies to the future extension of XENON 100, XENON 1T. Conclusively, the cMSSM is nearly excluded at 90% C.L. by the current constraints, listed before. Of course, broadening the allowed parameter ranges of the cMSSM's input parameters or relaxing fixed values for $\tan\beta$ and A_0 would enable more models to be consistent with measurements again.

NUHM:
The current XENON 100 dark matter search experiment puts severe constraints to the cMSSM's parameter space within the parameter ranges investigated in this work. Decoupling the Higgs sector from the remaining scalar sector and relaxing the unified boundary conditions for the up- and down-type squared Higgs masses, $m^2_{H_{u,d}}$, a number of viable dark matter models survive the XENON 100 limit (Figure 6.41)

For $\tan\beta = 10$, neither XENON 100 nor XENON 1T are able to exclude all models consistent with $122 < m_h < 128$ GeV and $0.09 < \Omega h^2 < 0.13$. Interpreting the XENON 1T sensitivity as limit and providing the black line behaves like a smooth continuous function, XENON 1T would exclude the complete "small μ" region in the NUHM1 parameter space (upper branch in Figure 6.41). The remaining models, consistent with Higgs mass and relic density constraints, correspond to the $\tilde{\tau}$ coannihilation region ($m_0 \lesssim 1.1$ TeV and $m_{1/2} > 1.8$ TeV) in the m_0-$m_{1/2}$ plane of the NUHM1 scenario. Although XENON 100 excludes more models for $\tan\beta = 45$ compared to $\tan\beta = 10$, a large fraction of models, consistent with measurements of the Higgs boson mass and the relic density, provide a dark matter

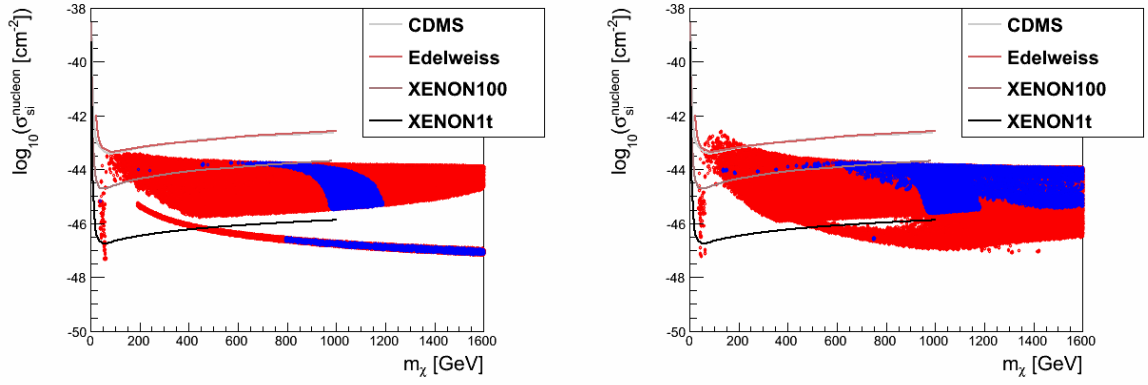

Figure 6.41: Predicted spin-independent neutralino nucleon cross-section $\sigma_{\mathrm{SI}}^{\mathrm{nucleon}}$ plotted versus the neutralino mass m_χ in the NUHM1 scenario for $\tan\beta = 10$ (left) and $\tan\beta = 45$ (right); colors: blue: models consistent with $122 < m_h < 128$ GeV and $0.09 < \Omega h^2 < 0.13$, red: all other models; shown are 90% C.L. from CDMS (Ahmed et al. 2010) (gray line), EDELWEISS (Armengaud et al. 2011) (brown line), XENON 100 (April et al. 2012a) (shaded brown line) and the predicted sensitivity for XENON 1T (April et al. 2012b) (black line).

candidate. Applying the arguments for the XENON 1T sensitivity to the case of $\tan\beta = 45$ would exclude all models fulfilling the Higgs and relic density constraints at 90% C.L, most probably. As only a few models are excluded from XENON 100, the corresponding excludable regions in the m_0-$m_{1/2}$ plane are only shown for XENON 1T (Figure 6.42).

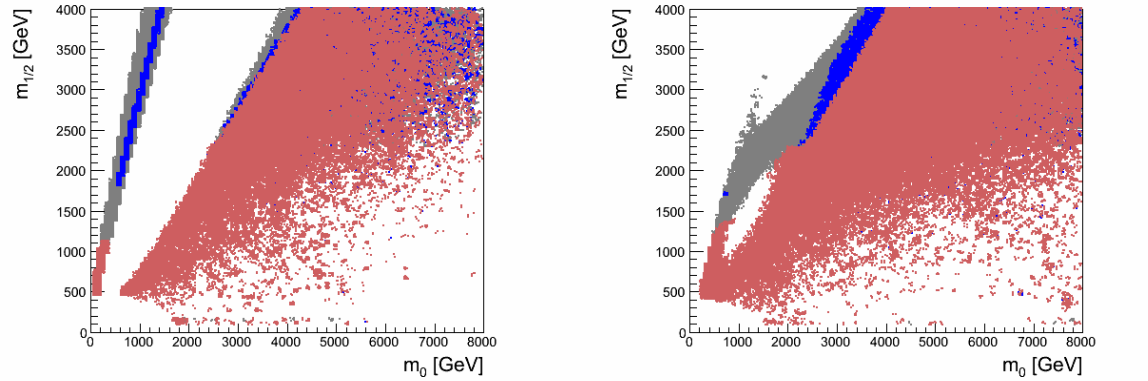

Figure 6.42: Excludable regions in the m_0-$m_{1/2}$ plane of NUHM1 from XENON 1T, $\tan\beta = 10$ (left) and $\tan\beta = 45$ (right); colors: faint red: excludable at 90% C.L., blue: models consistent with $122 < m_h < 128$ GeV and $0.09 < \Omega h^2 < 0.13$, gray: not excludable by XENON 1T.

The remaining thin blue band for $\tan\beta = 45$ accounts for the numerical implementation

of the projection of the limit lines onto the scenario's parameter space. XENON 100 and XENON 1T limits are only given up to $m_\chi \leq 1$ TeV. If $m_\chi > 1$ TeV, the corresponding models with $\sigma_{\mathrm{SI}}^{\mathrm{nucleon}}(m_\chi > 1 \text{ TeV})$ were considered as not excluded/excludable.

For $\tan\beta = 10$ and the case of $m_{H_u}^2 \neq m_{H_d}^2$ (NUHM2, Figure 6.43), the clear restricted blue regions in Figure 6.41 are smeared out (due to the additional degree of freedom) in the upper branch while for lower branch (representing the $\tilde{\tau}$ coannihilation region) remains unchanged. Therefore, XENON 100 excludes only a small fraction of the models in the "small μ" region that are consistent with Higgs mass and relic density measurements. The $\tilde{\tau}$ coannihilation region is not affected. Again, interpreting the XENON 1T sensitivity as 90% C.L. limit would exclude most of the NUHM2 focus point region (small μ), leaving the stau coannihilation region unaffected. Thus, neither XENON 100 nor the future XENON 1T can ultimately exclude the NUHM2 scenario for $\tan\beta = 10$.

For $\tan\beta = 45$, the additional degree of freedom reflecting the non-universality of $m_{H_{u,d}}^2$ smears out clear restricted regions. The current XENON 100 limit excludes more models compared to the case of $\tan\beta = 10$. Again, XENON 1T would exclude almost all models that are consistent with $122 < m_h < 128$ GeV and $0.09 < \Omega h^2 < 0.13$. The results discussed above are shown in Figure 6.43

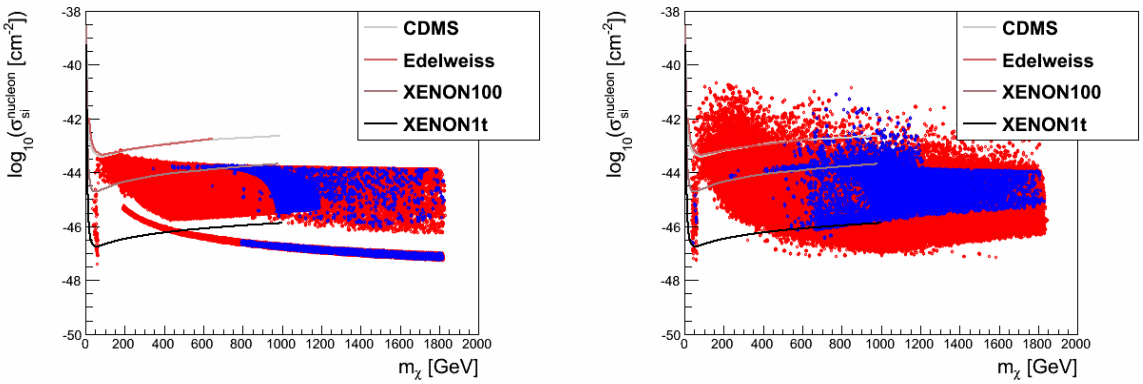

Figure 6.43: Predicted spin-independent neutralino nucleon cross-section $\sigma_{\mathrm{SI}}^{\mathrm{nucleon}}$ plotted versus the neutralino mass m_χ in the NUHM2 scenario for $\tan\beta = 10$ (left) and $\tan\beta = 45$ (right); colors: blue: models consistent with $122 < m_h < 128$ GeV and $0.09 < \Omega h^2 < 0.13$, red: all other models; shown are 90% C.L. from CDMS (Ahmed et al. 2010) (gray line), EDELWEISS (Armengaud et al. 2011) (brown line), XENON 100 (April et al. 2012a) (shaded brown line) and predicted sensitivity for XENON 1T (April et al. 2012b) (black line).

The corresponding excluded (excludable) regions in the m_0-$m_{1/2}$ plane of the NUHM2 scenario for XENON 100 (XENON 1T) stay the same compared to NUHM1 in a qualitative way, and are shown in the Appendix A.4.

NUGM:
After applying limits from direct dark matter search experiments to supersymmetric models

with a non-universal Higgs sector, a non-universal gaugino sector will be investigated in this paragraph. Some of the results in this paragraph were already published in Spies & Anton 2013. Figure 6.44 shows the predicted WIMP nucleon cross-section in the NUGM scenarios.

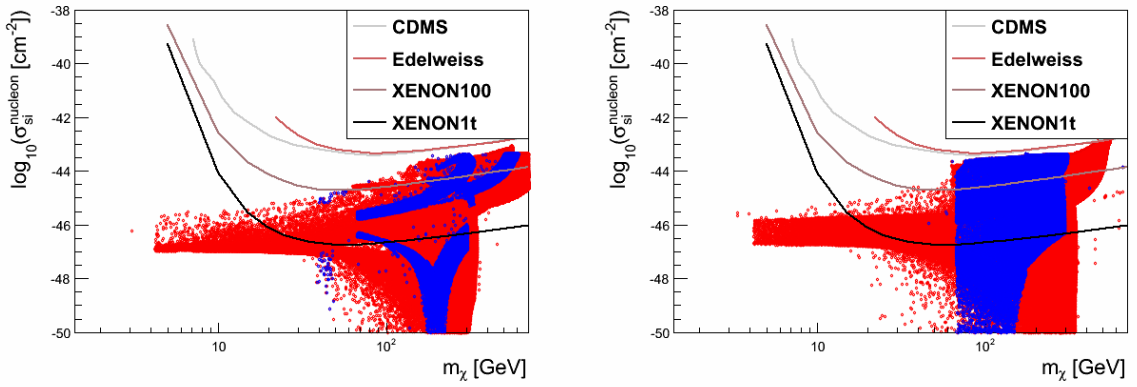

Figure 6.44: Predicted spin-independent neutralino nucleon cross-section $\sigma_{\mathrm{SI}}^{\mathrm{nucleon}}$ plotted versus the neutralino mass m_χ in the NUGM scenario for $\tan\beta = 10$ (left) and $\tan\beta = 45$ (right); colors: blue: models consistent with $122 < m_h < 128$ GeV and $0.09 < \Omega h^2 < 0.13$, red: all other models; shown are 90% C.L. from CDMS (Ahmed et al. 2010) (gray line), EDELWEISS (Armengaud et al. 2011) (brown line), XENON 100 (April et al. 2012a) (shaded brown line) and predicted sensitivity for XENON 1T (April et al. 2012b) (black line).

Clearly visible is the fact, that of all direct detection experiments shown here, only XENON 100 is able to exclude any of the simulated models. Nevertheless, a large fraction of the simulated models with a Higgs mass of $122 < m_h < 128$ GeV and $\Omega h^2 < 0.13$, are not yet excluded by direct detection experiments.

Even with the predicted sensitivity of the future extension XENON 1T (black line in Figure 6.44), a large number of models survive, that fulfill our requirements for Ωh^2 and the Higgs mass m_h. The corresponding excluded (excludable) parameter space for XENON 100 (XENON 1t) in the θ/π-m_0 plane is shown in Figures 6.45 and 6.46.

For $\tan\beta = 10$, XENON 100 excludes many of the "small μ/high higgsino" models on the right and upper edge of the left "island". The faint red band on the right "island" (excluded by XENON 100) corresponds to models where the neutralino is a mixture between wino and higgsino. In this region μ is already too high to solve fine-tuning problems, as it is the case for small μ.

For $\tan\beta = 45$, again the right and upper edge of the left "island" is excluded by XENON 100. As for the case of low $\tan\beta$, models belonging to that region, have a small μ and solve the little hierarchy problem of supersymmetry. Complementary to IceCube, no models on the thin arc on the right hand side are excluded by XENON 100.

Almost the whole cMSSM like focus point region with a small μ and a large higgsino fraction in the neutralinos composition can be tested by XENON 1T for $\tan\beta = 10$ and 45 (Figure 6.46). Only a few models for $-0.04 \lesssim \theta/\pi < 0$ and $m_0 > 4$ TeV ($\tan\beta = 10$) and

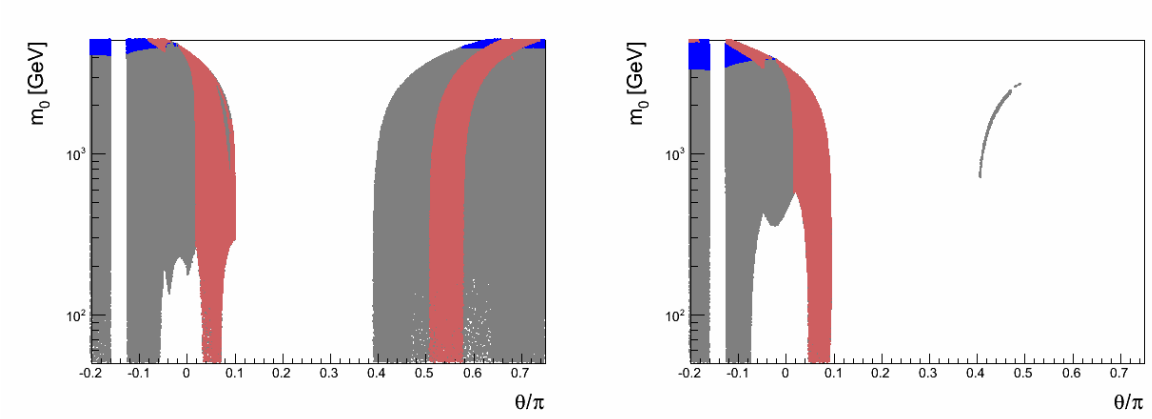

Figure 6.45: Excluded regions of the parameter space from XENON 100 for NUGM, $\tan\beta = 10$ (left) and $\tan\beta = 45$ (right); blue: $122 < m_h < 128$ GeV; gray: not excluded; faint red: excluded at 90% C.L.

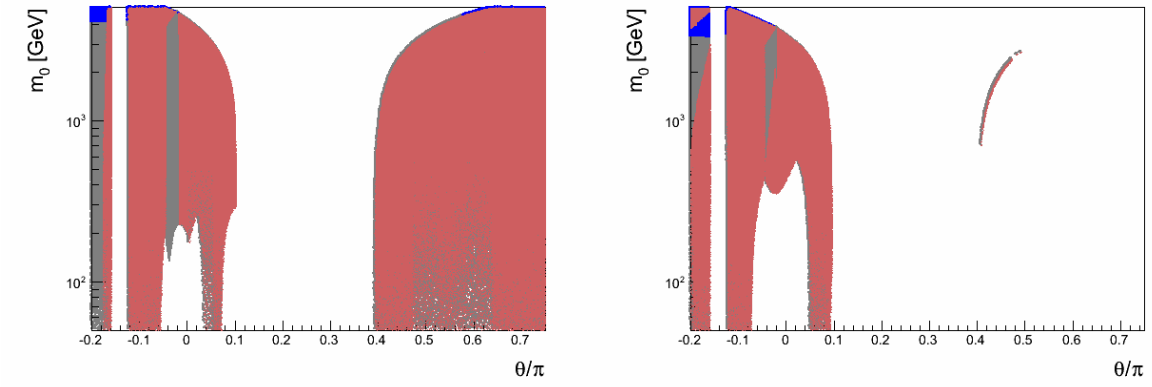

Figure 6.46: Excludable regions of the parameter space from XENON 1T for NUGM, $\tan\beta = 10$ (left) and $\tan\beta = 45$ (right); blue: $122 < m_h < 128$ GeV; gray: not excluded; faint red: excludable at 90% C.L.

$m_0 > 3.5$ TeV ($\tan\beta = 45$) may survive. In the case $\tan\beta = 10$, all models on the right "island" that fulfill $\Omega h^2 < 0.13$ and $122 < m_h < 128$ GeV would be excludable by XENON 1T. Only models with $\theta/\pi \lesssim -0.18$ still provide a consistent Higgs mass and relic density. For $\tan\beta = 45$, a triangular shaped region survives the predicted sensitivity of XENON 1T. It can be found for $m_0 > 3.4$ TeV and $\theta < -0.16$.

6.6 χ^2 Analysis

Each point in the parameter space of a scenario (cMSSM, NUHM, ...) represents a supersymmetric model. For each model, a χ^2 analysis was performed. The mass of the Higgs boson, m_h, was included, as it is mandatory for every viable SUSY extension of the SM to provide a Higgs boson with $m_h \sim 125$ GeV/c^2. Further, the relic density of the neutralino was taken into account, to provide the link between particle physics and cosmology, especially yielding a particle physics description for dark matter. Every SUSY theory must predict SM observables correctly. Therefore, the mass of the W boson, m_{W}, and the weak mixing angle, $\sin(\theta_{\mathrm{W}})$, were included in the χ^2 analysis. As a complementary tool for exploring physics beyond the SM, several flavor observables were included, such as measurements of the flavor changing neutral current, $b \to s\gamma$ ($\mathrm{BR}(B \to X_s\gamma)$). The presence of new particles as virtual states involved in processes containing only ordinary particles provide the possibility to study indirect effects of new physics.

The χ^2 value reflects a measure of agreement between the predicted and experimentally measured values of the corresponding observables. It was calculated as follows

$$\begin{aligned}\chi^2 &= \sum_i \frac{\left(\mathcal{O}_{\mathrm{exp},i} - \mathcal{O}_{\mathrm{pred},i}\right)^2}{\sigma^2_{\mathrm{exp},i}} \\ &= \chi^2(\Omega h^2) + \chi^2(m_h) + \chi^2(B \to X_s\gamma) + \chi^2(\Delta_0 \to K^*\gamma) + \chi^2(B_u \to \tau\nu_\tau) \\ &+ \chi^2(B \to D^0\tau\nu_\tau) + \chi^2\left(\frac{K \to \mu\nu}{\pi \to \mu\nu}\right) + \chi^2(R_{\mu 23}) + \chi^2(D_s \to \tau\nu_\tau) \\ &+ \chi^2(D_s \to \mu\nu_\mu) + \chi^2(M_W) + \chi^2(\sin^2\theta^W_{eff}). \end{aligned} \tag{6.6}$$

The index 'i' labels the different observables included in the χ^2 analysis. $\mathcal{O}_{\mathrm{exp},i}$ are the current experimentally measured values with the corresponding uncertainties $\sigma_{\mathrm{exp},i}$, whereas $\mathcal{O}_{\mathrm{pred},i}$ are the supersymmetric predictions coming from the simulation. Experimental constraints, used for this analysis, are the Higgs-boson mass, m_h, the neutralino relic density, Ωh^2, the decay $B \to X_s\gamma$, the isospin asymmetry, $\Delta_0(B \to K^*\gamma)$, in the decay $B \to K^*\gamma$, the leptonic decay $B_u \to \tau\nu_\tau$, the semileptonic decay $B \to D^0\tau\nu_\tau$, the ratio of the leptonic kaon decay and pion decay, $\frac{\mathrm{BR}(K\to\mu\nu)}{\mathrm{BR}(\pi\to\mu\nu)}$, the ratio $R_{\mu 23}$ proportional to CKM-matrix elements, $\frac{V_{us}(K_{l2})}{V_{us}(K_{l3})}$, of leptonic Kaon decays with two respective three leptonic final states, the leptonic decays $D_s \to l\nu_l$, where l is the final state lepton, the mass of the W-boson, M_W, and the effective weak mixing angle $\sin^2\theta^W_{eff}$. Corresponding measurements are listed in Table 6.4.

From the χ^2, calculated for each model in the corresponding scenario, the p-value was calculated. In physics it is common to claim a discovery, if the statistical significance exceeds at least 5σ, which corresponds to a p-value of 5.7×10^{-7}. Therefore, a given model in cMSSM, NUHM or NUGM will be considered as excluded if the model's p-value is smaller than 5.7×10^{-7}. The number of degrees of freedom (nDoF) is determined by the number of observables included in the χ^2 analysis (observables in Table 6.4). Thus, in this work nDoF is twelve. Consequently, models where χ^2 exceeds 52.2 are excluded ($\chi^2 = 52.2$ corresponds

Observable	**mean value**	σ_{exp}
Ωh^2	0.1123	± 0.0035 (Komatsu et al. 2010)
m_{Higgs}	125.3 GeV	(± 0.4,± 0.5) GeV (sys., stat.) (The CMS Collaboration 2013)
$\text{BR}(B \to X_s\gamma)$	3.55×10^{-4}	$(\pm 0.24, \pm 0.09) \times 10^{-4}$ (Barberio et al. 2007)
$\Delta_0(B \to K^*\gamma)$	3.1×10^{-2}	$\pm 2.3 \times 10^{-2}$ (combined (Aubert et al. 2008a Nakao et al. 2004, Nakamura et al. 2011))
$\text{BR}(B_u \to \tau\nu_\tau)$	1.64×10^{-4}	$\pm 0.34 \times 10^{-4}$ (Barberio et al. 2007)
$\text{BR}(B \to D^0\tau\nu_\tau)$	8.6×10^{-3}	$(\pm 2.4, \pm 1.1, \pm 0.6) \times 10^{-3}$ (Aubert et al. 2008b)
$\frac{\text{BR}(K\to\mu\nu)}{\text{BR}(\pi\to\mu\nu)}$	0.6358	± 0.0011 (combined (Nakamura et al. 2011, Antonelli et al. 2008))
$R_{\mu 23}$	0.999	± 0.007 (Antonelli et al. 2010)
$\text{BR}(D_s \to \tau\nu_\tau)$	5.38×10^{-2}	$\pm 0.32 \times 10^{-2}$ (Akeroyd et al. 2009)
$\text{BR}(D_s \to \mu\nu_\mu)$	5.81×10^{-3}	$\pm 0.43 \times 10^{-3}$ (Akeroyd et al. 2009)
M_W	80.385 GeV	± 0.015 GeV (Nakamura et al. 2011)
$\sin^2\theta^W_{eff}$	0.23146	± 0.00012 (Nakamura et al. 2011)

Table 6.4: Observables included in the χ^2 analysis

to a p-value of 5.7×10^{-7} for 12 DoFs), assuming the given model is realized in nature.

In contrast to investigations in the previous sections, where one or more of the scenarios' free parameters were fixed, now the parameter spaces were scanned in their complete dimensionality.

cMSSM:
As mentioned above, all parameters of the cMSSM were varied independently within the following boundaries:

$$\begin{aligned} m_0 &\in [0, 5] \text{ TeV}, \\ m_{1/2} &\in [0, 4] \text{ TeV}, \\ A_0 &\in [-3, 3] \text{ TeV}, \\ \tan\beta &\in [2, 60], \\ \text{sgn}(\mu) &= +1. \end{aligned} \tag{6.7}$$

For the parameter space scan, the χ^2 value for each model was calculated. The corresponding χ^2 distribution with respect to the above observables predicted in the cMSSM is shown in Figure 6.47. It shows a flat slope, indicating a strong disagreement between predictions of observables from Table 6.4 and their measurements, for the majority of simulated models. The resulting χ^2 value for each simulated model is plotted in the m_0-$m_{1/2}$ plane in the left hand panel of Figure 6.48. The χ^2 values are color coded, whereat red corresponds to $\chi^2 > 53$. The red and blue contours on the right hand side correspond to a compatibility within 3σ and 5σ, respectively, between predicted values of the individual observables and

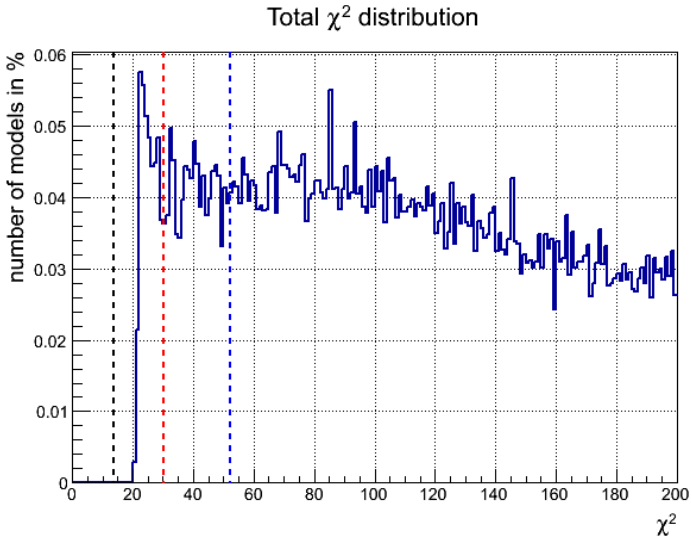

Figure 6.47: χ^2 distribution in the cMSSM, calculated according to Equation 6.6 and normalized to the total number of models. Black line: $\chi^2 = 13.8 \hat{=}$ p-value of 1σ; red line: $\chi^2 = 30.1 \hat{=}$ p-value of 3σ, blue line: $\chi^2 = 52.2 \hat{=}$ p-value of 5σ.

their measurements. The yellow and black asterisk in Figure 6.48 represents the model with the smallest χ^2 value, and thus agreeing best with experimental measurements. From this analysis follows, that almost the whole m_0-$m_{1/2}$ plane is excluded with more than 5σ (right hand side of Figure 6.48).

The position of the "best-fit" model in the m_0-$m_{1/2}$ plane is determined by the χ^2 values of the Higgs boson and the relic density. For $m_{1/2} \lesssim 1.5$ TeV, small χ^2 values for Ωh^2 are achieved, but $\chi^2(m_h)$ exceeds 15. Thus, only in the τ-coannihilation region ($m_0 \lesssim 1.6$ TeV and $m_{1/2} > 1.6$ TeV), small χ^2 values can be achieved simultaneously, for both $\chi^2(m_h)$ and $\chi^2(\Omega h^2)$. Corresponding plots are shown in Appendix A.5 (Figure A.12). The smallest χ^2 value of all simulated models is $\chi^2_{min} = 20.3$. This corresponds to a p-value of 6.2%. This means, the probability, that the observed χ^2 exceeds 20.3 by chance even if the model with χ^2_{min} is correct, is 6.2%. Predictions and measurements for the model with χ^2_{min} and observables listed in Table 6.4 are compatible within 1.87σ. The corresponding χ^2 value of each observable for the model with χ^2_{min} is shown in Figure 6.49.

The relic density and the mass of the Higgs boson are well described in the cMSSM scenario (at least in a few regions in the parameter space). Nevertheless, the predicted flavor observables deviate significantly from their measured values, leading to χ^2 of ~ 6 ($\hat{=}$ p-value of 0.014, compatible within 2.5σ) at maximum for the branching ratio BR($B_u \to \tau\nu_\tau$) and for the model with minimal χ^2. In total, high χ^2 values in the cMSSM are mostly driven by the incompatibility of predicted and measured values with respect to the flavor observables, leading to an offset of ~ 19 (see Figure 6.50). This corresponds to a p-value of 0.015 and a compatibility with measurements at the level of 2.4σ. Neglecting flavor observables leads to a smaller value of $\chi^2_{\text{min}} = 1.92$ and a p-value of 75%. Corresponding plots are shown in

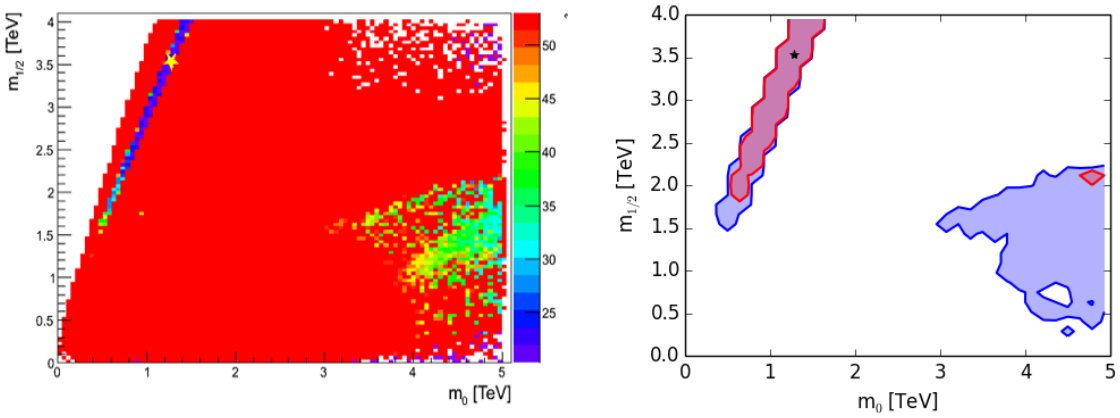

Figure 6.48: The χ^2 values of the simulated models (color coded) in the m_0-$m_{1/2}$ plane (left) and models compatible within 3σ (red contour) and 5σ (blue contour) (right). The yellow (left) and black asterisk (right) represents the "best-fit" model. Models outside the blue contour (right hand side) deviate from measurements more than 5σ and are not shown here.

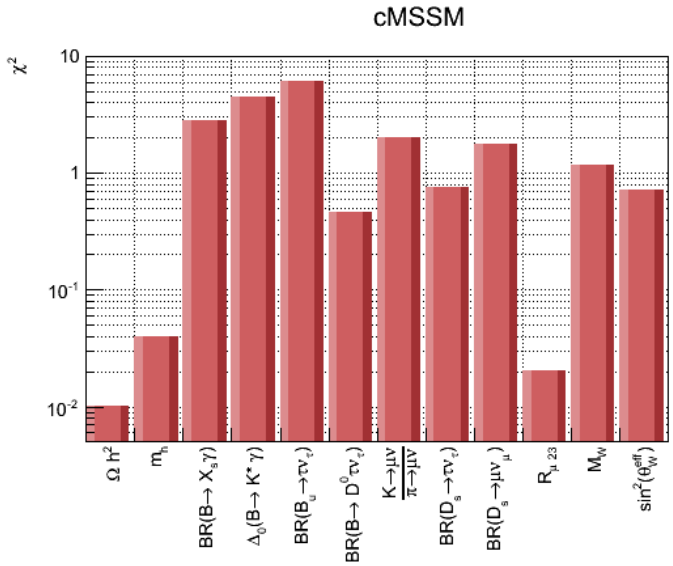

Figure 6.49: χ^2 values for the different observables of the "best-fit" model in the cMSSM.

Appendix A.6. The χ^2 distributions for each observable (including flavor observables) can be found in the Appendix A.5 (Figure A.10 and Figure A.11).

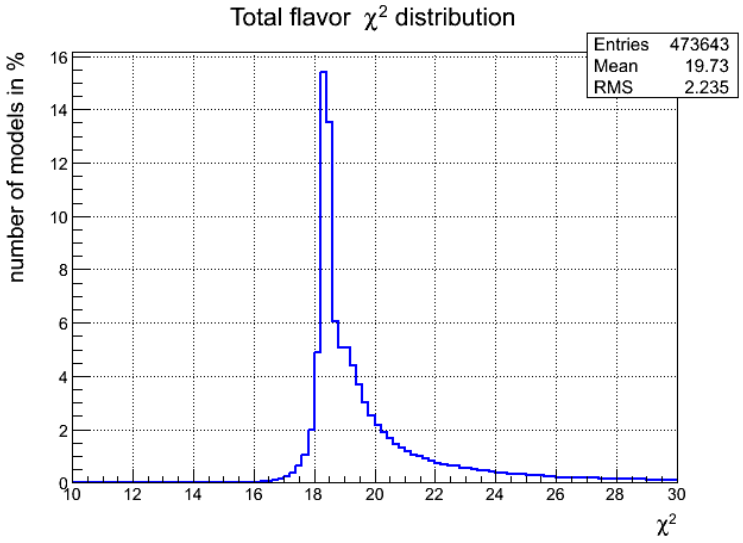

Figure 6.50: χ^2 distribution for the flavor observables in the cMSSM. The mean value of 19.7 leads to $\chi^2_{\text{total}} \geq 20.3$.

None of the current existing or future direct and indirect dark matter search experiments is able to exclude or even probe the "best-fit" model in the near future (Figure 6.51 and 6.52).

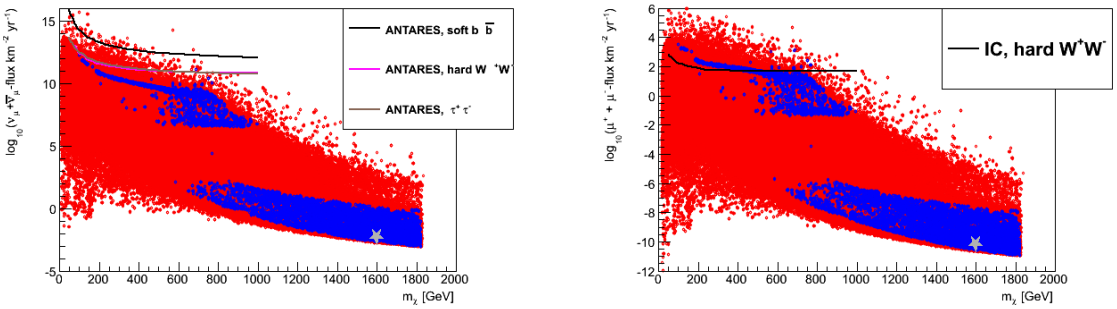

Figure 6.51: "Best-fit" model (gray asterisk) of cMSSM with respect to indirect dark matter detection observables and the given ANTARES (left) and IceCube (right) limits, assuming a 100% annihilation in either $b\bar{b}$, W^+W^-, or $\tau^+\tau^-$. Colors: blue: $122 < m_h < 128$ GeV and $0.09 < \Omega h^2 < 0.13$, red: all other models.

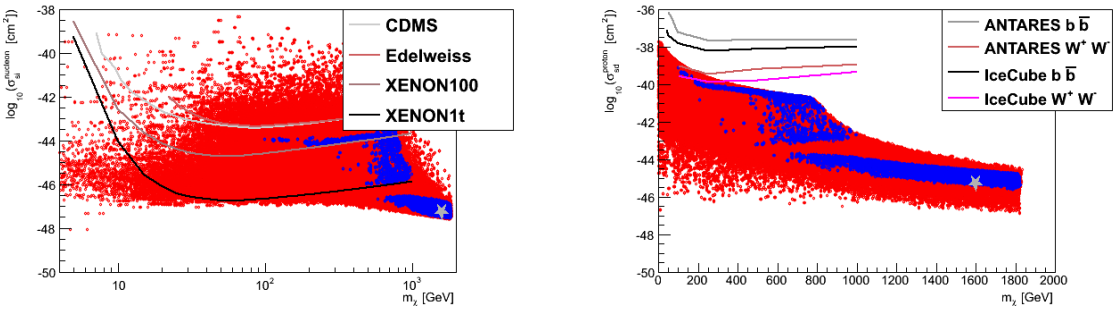

Figure 6.52: "Best-fit" model with respect to direct dark matter detection observables $\sigma_{\mathrm{SI}}^{\mathrm{nucleon}}$ (left) and $\sigma_{\mathrm{SD}}^{\mathrm{proton}}$ (right). Also shown are limits from XENON 100, CDMS, EDELWEISS and the predicted sensitivity of XENON 1T (left) as well as ANTARES and IceCube limits on $\sigma_{\mathrm{SD}}^{\mathrm{proton}}$ (right). Colors: blue: $122 < m_h < 128$ GeV and $0.09 < \Omega h^2 < 0.13$, red: all other models.

NUHM:
In this paragraph, the NUHM scenario and its compatibility with the measured values of observables listed in Table 6.4 is investigated. The complete parameter space of NUHM was scanned within the following boundaries:

$$\begin{aligned} m_0 &\in [0, 8] \text{ TeV}, \\ m_{1/2} &\in [0, 4] \text{ TeV}, \\ A_0 &\in [-3, 3] \text{ TeV}, \\ \delta_{H_u} &\in [-1, 1], \\ \delta_{H_d} &\in [-1, 1], \\ \tan\beta &\in [2, 60], \\ \mathrm{sgn}(\mu) &= +1. \end{aligned} \tag{6.8}$$

The total χ^2 distribution including the particular observables is shown in Figure 6.53 for the case of $\delta_{H_u} = \delta_{H_d}$ (left) and $\delta_{H_u} \neq \delta_{H_d}$ (right) (χ^2 distributions for the particular observables are shown in the Appendix A.5, Figure A.13 and A.14 for NUHM1, Figure A.19 and A.20 for NUHM2).

The peak of both distributions is nearly at the same position as for the cMSSM case. Nevertheless, the tails of both distributions decrease much faster than in the cMSSM, indicating a significantly better agreement of predicted and measured values of the individual observables. Further, the "best-fit" models yield a smaller χ^2_{min} of 18.83 for NUHM1 and 18.4 for NUHM2, compared to 20.3 in case of the cMSSM. This translates into p-values of 9.3% and 10% for NUHM1 and NUHM2, respectively. Consequently, predictions and

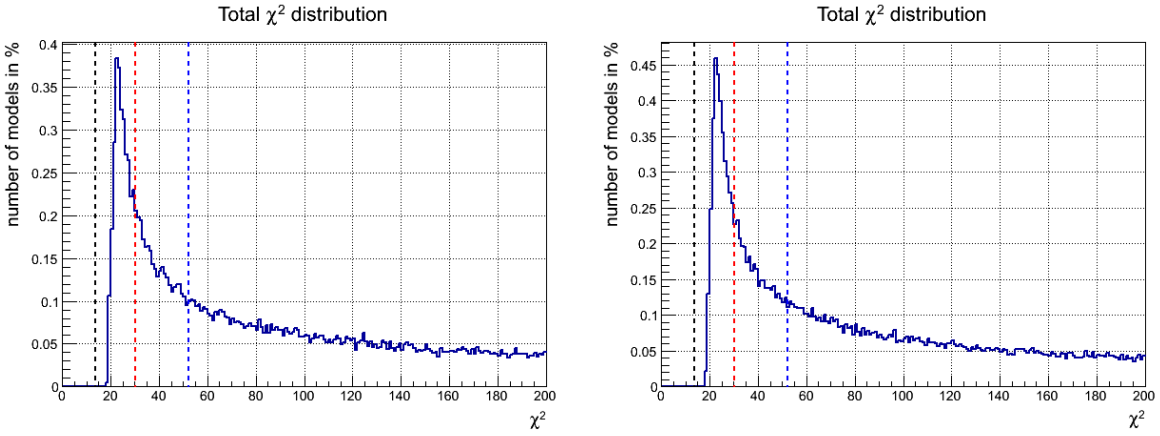

Figure 6.53: χ^2 distributions in the NUHM1 (left) and NUHM2 scenario (right) normalized to the total number of simulated models. Black line: $\chi^2 = 13.8 \hat{=}$ p-value of 1σ; red line: $\chi^2 = 30.1 \hat{=}$ p-value of 3σ, blue line: $\chi^2 = 52.2 \hat{=}$ p-value of 5σ.

measurements are compatible within 1.68σ for NUHM1 and 1.64σ for NUHM2. In Figure 6.54 the χ^2 values of the individual observables are shown for the best-fit models (NUHM1 on the left, NUHM2 on the right hand side).

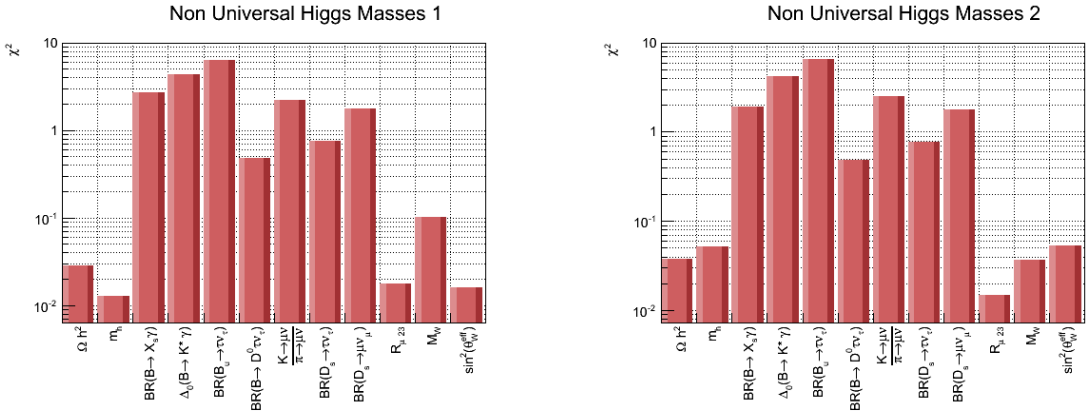

Figure 6.54: χ^2 values of the different observables for the "best-fit" model for NUHM1 (left) and NUHM2 (right).

Figure 6.55 shows the χ^2 distributions for NUHM1 (left) and NUHM2 (right) in the m_0-$m_{1/2}$ plane. Color coded are the χ^2 values for the individual models. The yellow asterisk represents the model with $\chi^2_{\text{min}} = 18.83$ (NUHM1) and $\chi^2_{\text{min}} = 18.4$ (NUHM2).
The χ^2 maps from Figure 6.55 were translated into a map, that shows the 3σ and 5σ compatibility between the models' predictions and experimental measurements (Figure 6.56)

Like in the cMSSM, the position of the "best-fit" model in the m_0-$m_{1/2}$ plane is determined by the compatibility between measurement and prediction of the Higgs-boson mass and the relic density (Appendix A.5, Figure A.15 and Figure A.22). The χ^2 values of flavor

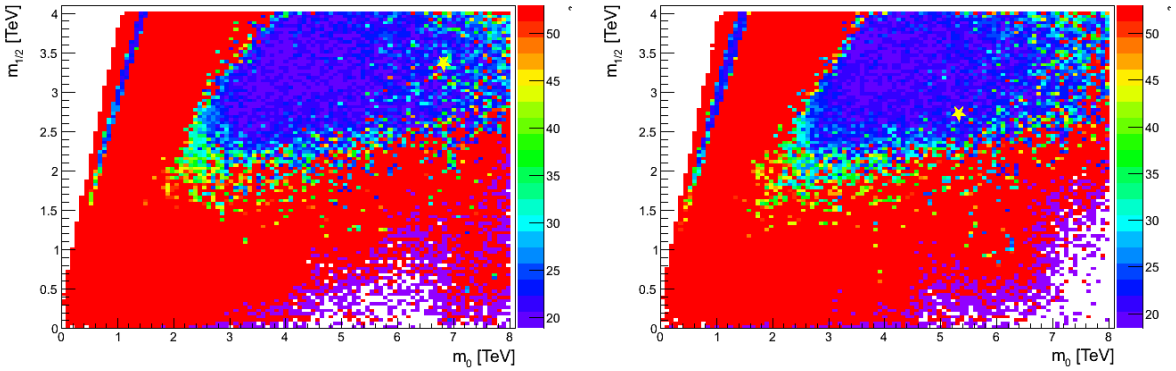

Figure 6.55: χ^2 values of the individual models color coded in the m_0-$m_{1/2}$ plane for NUHM1 (left) and NUHM2 (right). Red colored models have $\chi^2 > 53$. The yellow asterisks correspond to the "best-fit" models.

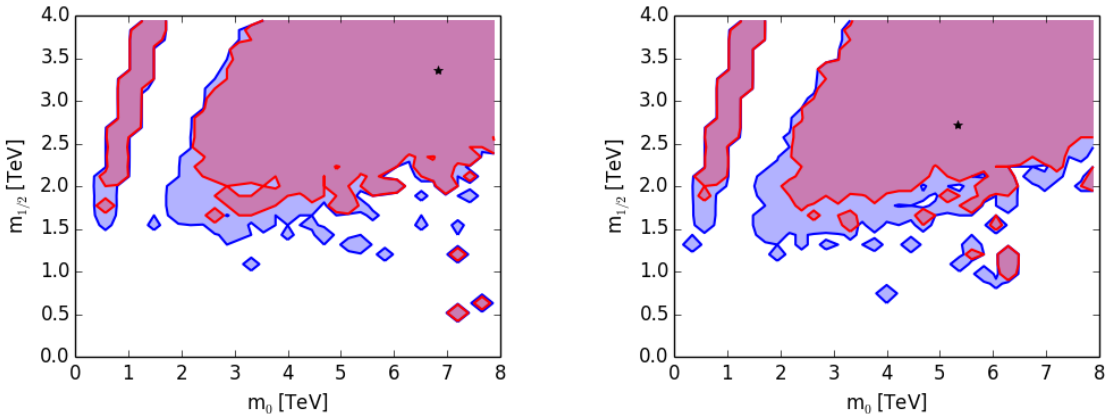

Figure 6.56: Map of compatibility regions in the m_0-$m_{1/2}$ plane for NUHM1 (left) and NUHM2 (right). Colors: red contour: compatible within 3σ; blue contour: compatible within 5σ. Black asterisks correspond to the "best-fit" models. Models outside the blue contours deviate from measurements more than 5σ and are not shown here.

observables shift χ^2 to $\chi^2 \geq 18.83$ (NUHM1) and $\chi^2 \geq 18.4$ (NUHM2). This is shown in Figure 6.57, where the distribution of the sum of χ^2 values of all flavor observables is displayed for NUHM1 (left) and NUHM2 (right).

Neglecting flavor observables leads to a smaller value of $\chi^2_{\text{min}} = 3.7 \cdot 10^{-2}$ ($1.7 \cdot 10^{-2}$) and a p-value of 99.98% (99.9964%) for NUHM1 (NUHM2). More extended regions of models, compatible with measurements within 3σ and 5σ, are found (see Appendix A.6, Figure A.33, A.34, A.35 and Figure A.36).

Further, it was found, that models in NUHM1 (Figure 6.58) with $m_{1/2} > 1.3$ TeV and $\delta > 0$ are preferred by measurements. In contrast, models with $m_{1/2} < 1.3$ TeV are excluded at the 5σ level for all values of δ, except for a small "hot spot" for $\delta \sim -0.1$ and $m_{1/2} \sim 500$

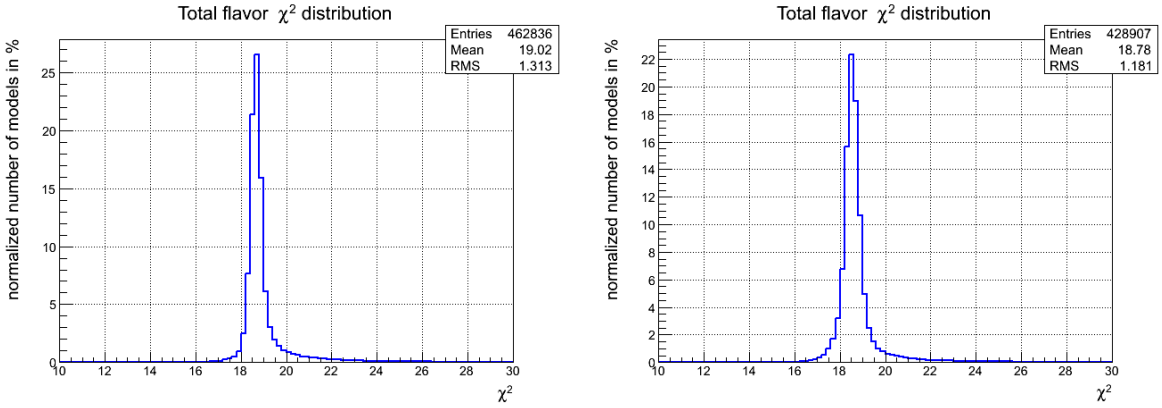

Figure 6.57: χ^2 distribution of the sum of all flavor observables for NUHM1 (left) and NUHM2 (right). The number of models is normalized to the total number of simulated models.

GeV. Moreover, extended regions for $1.4 < m_{1/2} \lesssim 2.8$ TeV and $\delta < 0$ are excluded as well. For excluded models, $\chi^2(m_h) > 8$ and $\chi^2(\Omega h^2) > 15$ applies. In combination with the χ^2 offset introduced by flavor observables, total χ^2 values are obtained, that correspond to an incompatibility worse than 5σ ($\chi^2 > 52.2$) (plots, showing the χ^2 distribution of m_h, Ωh^2 and $\sum \chi^2_{\text{flavor}}$ in different parameter space planes, are given in Appendix A.5). The same behavior was found for the δ_{H_u} parameter of the NUHM2 scenario(see Appendix A.5, Figure A.21). The second non-universality parameter, δ_{H_d}, is excluded in the simulated range from -1 to 1, for $m_{1/2} \lesssim 1.2$ TeV (Figure 6.59).

The "best-fit" model can not be tested by indirect detection experiments IceCube or ANTARES, neither for NUHM1 nor for NUHM2 (Appendix A.5, Figure A.18 and Figure A.26). Plots showing the "best-fit" model in NUHM1 and NUHM2 with respect to direct detection observables are shown in Figure 6.60. In both scenarios, none of the existing direct detection experiments is able to exclude the model with χ^2_{min}. Contrary, the future XENON 1T experiment will be able to probe the "best-fit" model at the 90% C.L. Qualitatively similar results for the spin-independent WIMP nucleon cross-section were obtained, when flavor observables were neglected. Corresponding plots are shown in Appendix A.6.

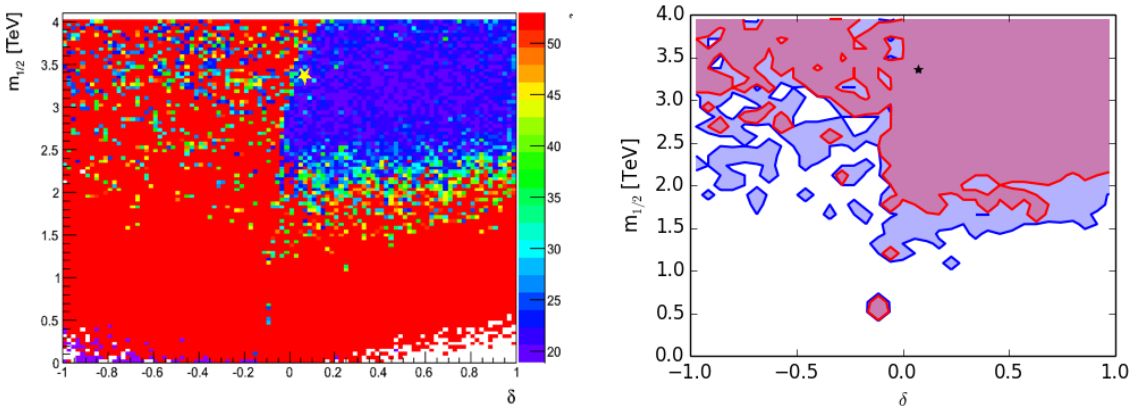

Figure 6.58: χ^2 distribution (left) and compatibility regions within 3σ and 5σ (right) in the δ-$m_{1/2}$ plane of NUHM1. χ^2 values are color coded on the left hand side. The red contour on the right hand side corresponds to a deviation less than 3σ, the blue contour corresponds to a deviation less than 5σ from experimental measurements. The yellow (left) and black asterisk (right) corresponds to the "best-fit" model. Models outside the blue contour (right hand side) deviate from measurements more than 5σ and are not shown here.

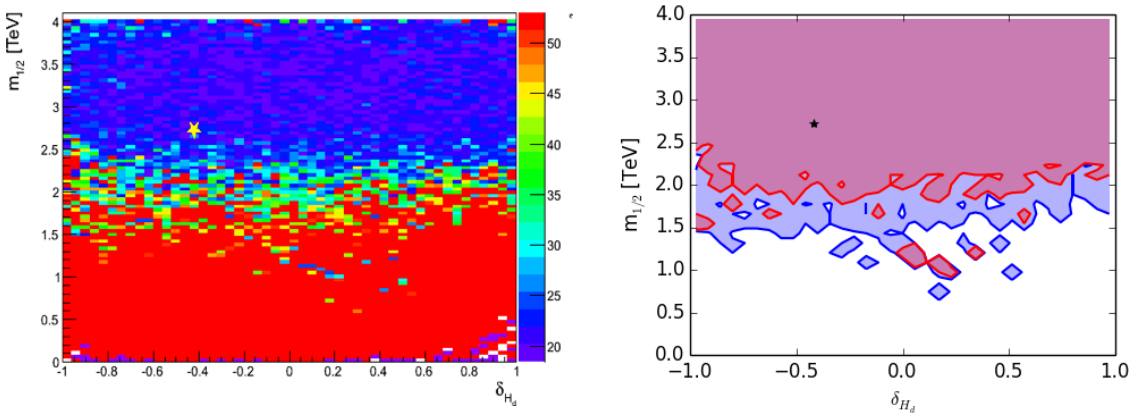

Figure 6.59: χ^2 distribution (left) and compatibility regions within 3σ and 5σ (right) in the δ_{H_d}-$m_{1/2}$ plane of NUHM2. χ^2 values are color coded on the left hand side. The red contour on the right hand side corresponds to a deviation less than 3σ, the blue contour corresponds to a deviation less than 5σ from experimental measurements. The yellow (left) and black asterisk (right) corresponds to the "best-fit" model. Models outside the blue contour (right hand side) deviate from measurements more than 5σ and are not shown here.

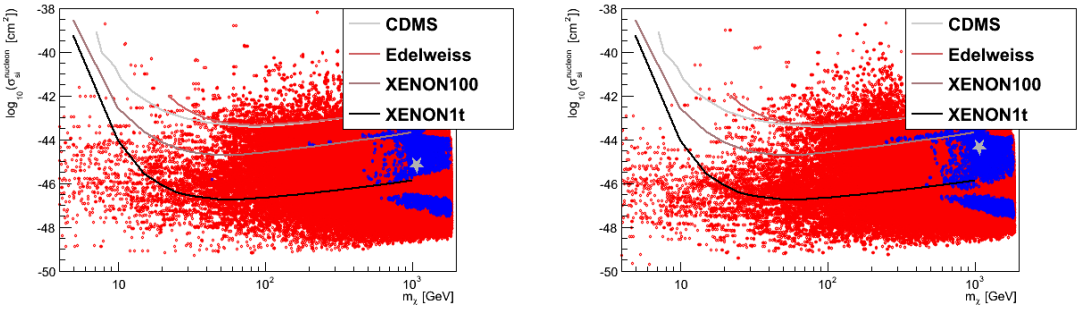

Figure 6.60: "Best-fit" model (gray asterisk) of NUHM1 (left) and NUHM2 (right) with respect to direct dark matter detection observables $\sigma_{\mathrm{SI}}^{\mathrm{nucleon}}$ vs. m_χ and the given limits by XENON 100, CDMS, EDELWEISS as well as the predicted sensitivity of XENON 1T. Colors: blue: $122 < m_h < 128$ GeV and $0.09 < \Omega h^2 < 0.13$, red: all other models.

NUGM:
In this paragraph, the χ^2 analysis is applied to the scenario with non-universal gaugino masses (NUGM). To calculate the χ^2, the parameter space of NUGM was scanned in the following parameter ranges

$$\begin{aligned} m_0 &\in [0, 8]\ \text{TeV}, \\ m_{1/2} &\in [0, 4]\ \text{TeV}, \\ A_0 &\in [-3, 3]\ \text{TeV}, \\ \tan\beta &\in [2, 60]\ \text{TeV}, \\ \theta_1 &\in [-45, 135]\ \text{degree}, \\ \theta_{24} &\in [-45, 135]\ \text{degree}, \\ \theta_{75} &\in [-45, 135]\ \text{degree}, \\ \theta_{200} &\in [-45, 135]\ \text{degree}, \\ \mathrm{sgn}(\mu) &= +1. \end{aligned} \tag{6.9}$$

The total χ^2 distribution of all models in the NUGM scenario is shown in Figure 6.61. In Appendix A.5 the χ^2 distributions of the individual observables in NUGM are shown. Compared to cMSSM, the tail decreases much faster, indicating a better agreement between predictions for the particular observables (see Table 6.4) and their measurements. Nevertheless, improvements are weaker compared to NUHM scenarios.

The smallest χ^2 value in the NUGM scenario is $\chi^2_{\mathrm{min}} = 18.2$. This corresponds to a p-value of 11%. Consequently, predictions and measurements of the particular observables are compatible within 1.59σ. Compared to NUHM and the cMSSM, the "best-fit" model shows the best agreement of all investigated scenarios, caused by a slightly better agreement for

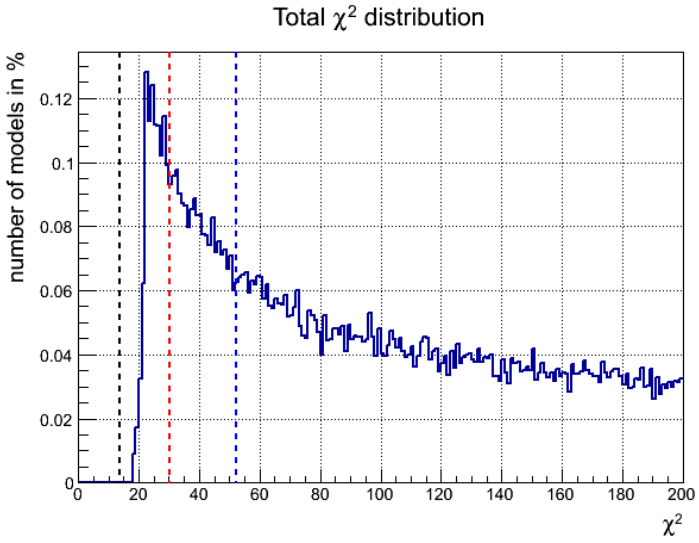

Figure 6.61: χ^2 distribution in the NUGM, calculated according to Equation 6.6, and normalized to the total number of models used for the χ^2 calculation. Black line: $\chi^2 = 13.8 \mathrel{\hat{=}}$ p-value of 1σ; red line: $\chi^2 = 30.1 \mathrel{\hat{=}}$ p-value of 3σ, blue line: $\chi^2 = 52.2 \mathrel{\hat{=}}$ p-value of 5σ.

flavor observables compared to cMSSM and NUHM. In Figure 6.62, the bar chart including the χ^2 values of the individual observables is shown.

Due to the high dimensionality of the scenario's parameter space, it is difficult to identifiy clear regions favoured by measurements. In Figure 6.63, the χ^2 distributions in the different parameter space planes are shown. Extended regions, that are excluded at the 5σ level ($\mathrel{\hat{=}} \chi^2 > 52.2$) were found for m_0, $m_{1/2}$ as well as for non-singlet mixing angles θ_{24}, θ_{75}, θ_{200}. They are listed in Table 6.5. In the case of the singlet mixing angle, θ_1, no continuous region was found to constrain θ_1.

Excluded regions (5σ level)
$m_{1/2} < 0.7$ TeV and $m_{1/2} > 2.5$ TeV for $m_0 \in [0, 8]$ TeV
$0.05 < \theta_{24}/\pi < 0.25$ for $m_0 \in [0, 8]$ TeV $0.1 \lesssim \theta_{24}/\pi < 0.75$ for $m_0 < 3$ TeV
$-0.25 < \theta_{75}/\pi < -0.05$ for $m_0 < 2$ TeV
$-0.25 < \theta_{200}/\pi < 0.05$ for $m_0 < 3.5$ TeV

Table 6.5: Parameter regions excluded at the 5σ level in the NUGM scenario. No continuous region for the singlet mixing angle, θ_1, was found.

Like in the previous scenarios, flavor observables shift χ^2_{total} to values above ~ 18, which

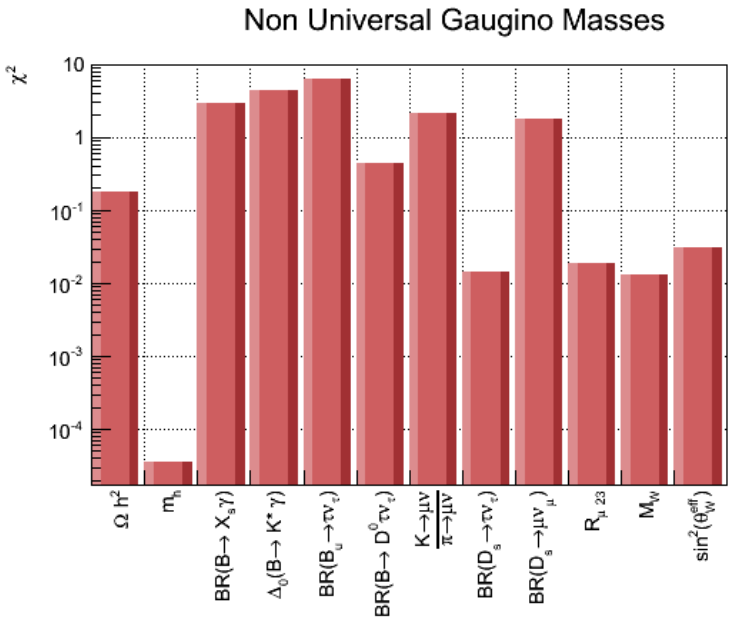

Figure 6.62: χ^2 values of the different observables for the "best-fit" model in the NUGM.

corresponds to a p-value of 0.02% (see Figure 6.64). Thus, the incompatibility between prediction and experiment is mostly driven by constraints coming from flavor physics. Neglecting flavor observables reduces the overall χ^2 values. Consequently, the minimal χ^2 is $\chi^2_{\text{min}} = 0.11$, which corresponds to a p-value of 99.86%. More models are compatible with measurements within 1σ, 3σ and 5σ. Corresponding plots are shown in Appendix A.6 (Figure A.30 and Figure A.39).

Like in the previous scenarios, none of the current indirect and direct detection experiments is able to exclude the model with χ^2_{min} (see Appendix A.5, Figure A.29). The future XENON 1T experiment will be able to test the "best-fit" model at 90% C.L. (Figure 6.65).

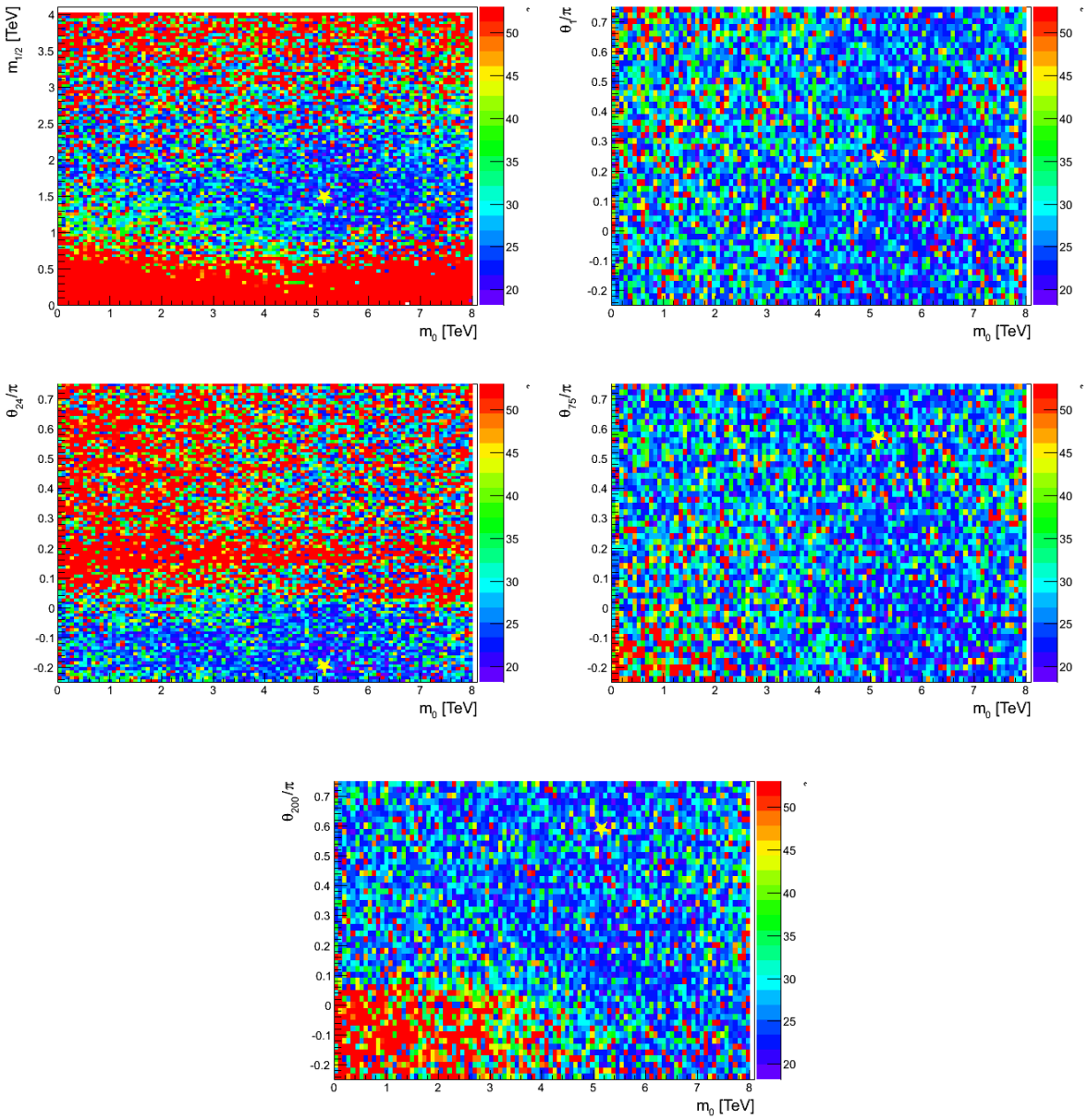

Figure 6.63: χ^2 distribution in the m_0-$m_{1/2}$ plane (top left), m_0-θ_1 plane (top right), m_0-θ_{24} plane (middle left), m_0-θ_{75} plane (middle right) and m_0-θ_{200} plane (bottom central). χ^2 values are color coded. Models colored in red have a total χ^2 value bigger than 53, and thus, are excluded. The yellow asterisks correspond to the "best-fit" model.

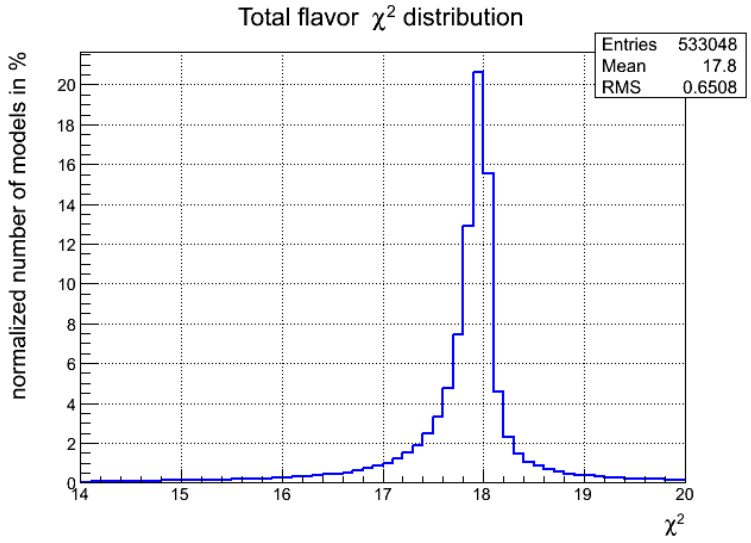

Figure 6.64: χ^2 distribution of flavor observables in the NUGM scenario. The mean value of 17.8 leads to $\chi^2_{\text{total}} \geq 18.2$.

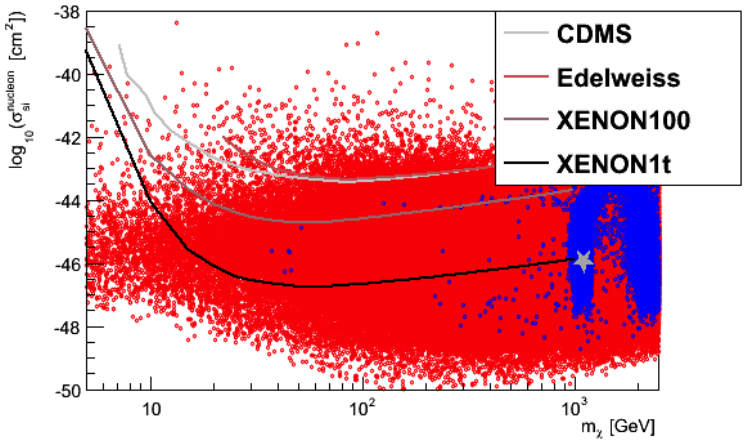

Figure 6.65: "Best-fit" model (gray asterisk) in NUGM with respect to direct dark matter detection observables $\sigma_{\text{SI}}^{\text{nucleon}}$ vs. m_χ and the given limits by XENON 100, CDMS, EDELWEISS as well as the predicted sensitivity of XENON 1T. Colors: blue: $122 < m_h < 128$ GeV and $0.09 < \Omega h^2 < 0.13$, red: all other models.

The χ^2- and corresponding p-values, the free parameters of the different scenarios, the individual χ^2-values of the particular observables, the indirect and direct detection observables as well as the SUSY particle spectra for the "best-fit" models of all SUSY scenarios are listed in detail in Appendix A.5.

6.7 Experimentally Favoured Regions for Indirect and Direct Dark Matter Search Observables

From the previous χ^2 analysis, favoured regions (by measurements of m_h, Ωh^2, m_W, $\sin(\theta_{\mathrm{W}}^{\mathrm{eff}})$, and flavor observables) for indirect and direct dark matter search observables were derived. Therefore, two dimensional histograms in the 'neutralino-mass'-'indirect/direct detection observable'-plane (e.g., the m_χ-$\log_{10}(\nu_\mu + \bar{\nu}_\mu$ flux $\mathrm{km}^{-2}\mathrm{yr}^{-1})$-plane) were generated. Such a histogram is exemplarily shown in Figure 6.66 for the NUHM2 scenario.

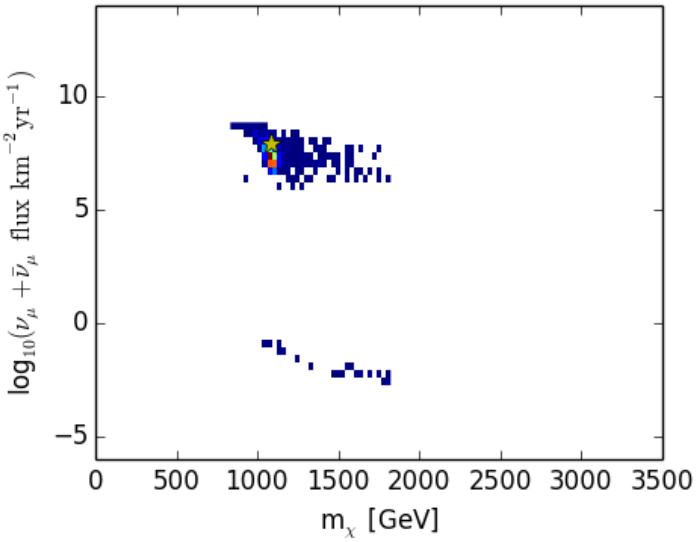

Figure 6.66: Two dimensional histogram in the m_χ-$\log_{10}(\nu_\mu + \bar{\nu}_\mu$ flux $\mathrm{km}^{-2}\mathrm{yr}^{-1})$-plane, for the NUHM2 scenario. Only models, where $\chi^2 < 21.35$ are plotted. Yellow asterisk: "best-fit" model.

Only models, where $\chi^2 < 21.35$ are plotted. Those models agree with experimental measurements of m_h, Ωh^2, m_W, $\sin(\theta_{\mathrm{W}}^{\mathrm{eff}})$, and flavor observables within 2σ. The yellow asterisk in Figure 6.66 represents the "best-fit" model. Bins, comprising the minimal number of entries (here, one), define the contour of models, compatible with measurements within 2σ. In this way, experimentally favoured regions for indirect and direct detection observables were derived and are shown in Figure 6.67.

Neither, limits on the spin-dependent WIMP-proton cross-section, nor on the muon-neutrino flux and the muon flux, given by indirect detection experiments, ANTARES and IceCube, are capable of excluding experimentally favoured models. In contrast, limits from direct dark matter detection experiments reach those models and exclude a small fraction of models in the NUHM2 scenario.

At the time, when this study was prepared, the LUX collaboration published their first results (Akerib et al. 2013). Their limit is shown in the bottom left panel of Figure 6.67

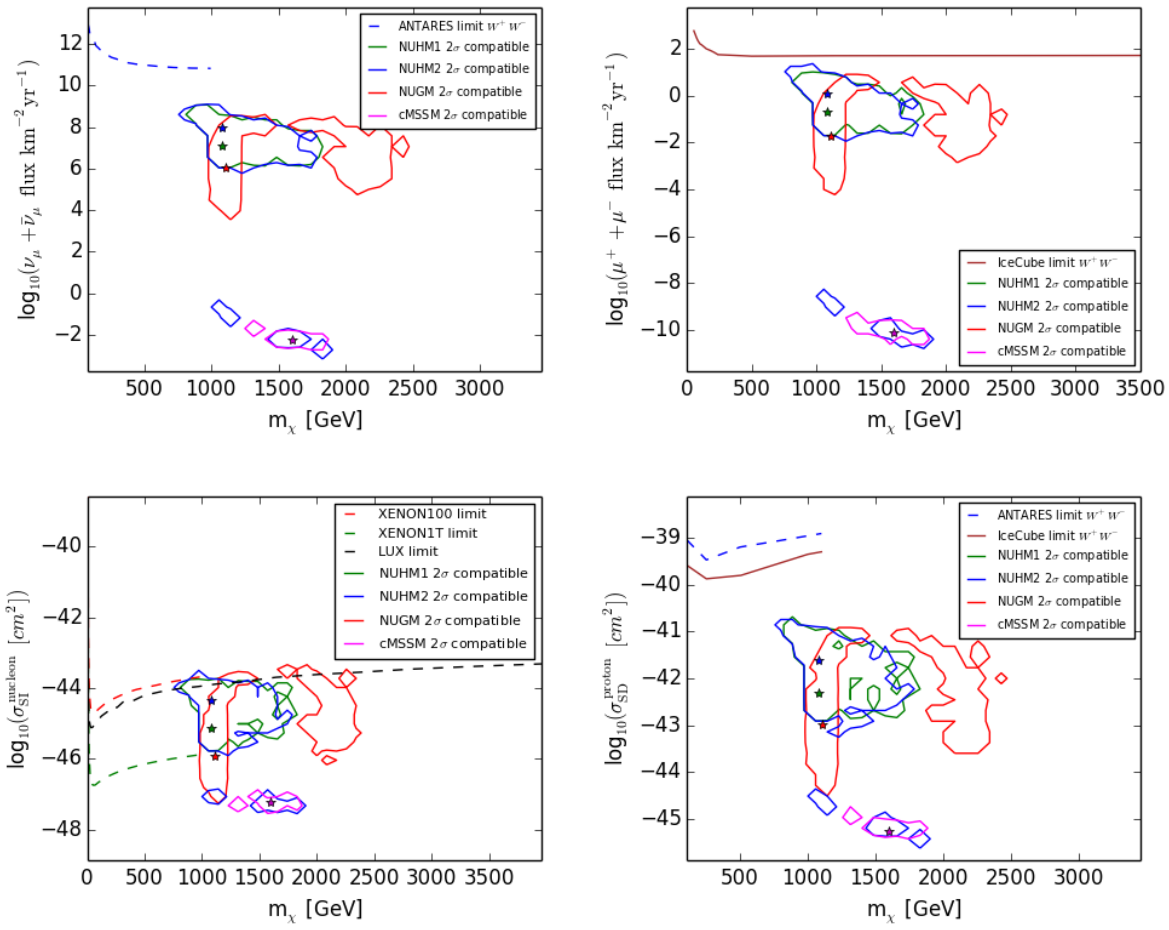

Figure 6.67: Experimentally favoured regions (compatible with measurements of Table 6.4 within 2σ) for the $\nu_\mu + \bar{\nu}_\mu$-flux (top left), the $\mu^+ + \mu^-$-flux (top right), $\sigma_{\mathrm{SI}}^{\mathrm{nucleon}}$ (bottom left) and $\sigma_{\mathrm{SD}}^{\mathrm{proton}}$ (bottom right). Also shown are the ANTARES (muon neutrino flux and $\sigma_{\mathrm{SD}}^{\mathrm{proton}}$) and IceCube limits (muon flux and $\sigma_{\mathrm{SD}}^{\mathrm{proton}}$) for annihilation channel W^+W^- as well as the XENON100 limit, the LUX limit, and expected XENON1T sensitivity for $\sigma_{\mathrm{SI}}^{\mathrm{nucleon}}$. Contours correspond to a 2σ compatibility region of the corresponding scenario (green: NUHM1, blue: NUHM2, red: NUGM, magenta: cMSSM). Asterisks represent the "best-fit" models of the corresponding scenario.

(black dashed line). Among current direct dark matter search experiments, this limit is most constraining for the spin-independent WIMP-nucleon cross-section, $\sigma_{\mathrm{SI}}^{\mathrm{nucleon}}$. A few models in NUHM1, NUHM2 and NUGM, that agree with measurements of e.g., m_h and Ωh^2, better than 2σ are already excluded by the LUX limit. Those models have $m_\chi > 700$ GeV and $\log_{10}(\sigma_{\mathrm{SI}}^{\mathrm{nucleon}}) \gtrsim -44$. Neither XENON100, nor LUX is able to exclude the "best-fit" models of any scenario. Nevertheless, the sensitivity of the future XENON1T experiment for $\sigma_{\mathrm{SI}}^{\mathrm{nucleon}}$ (assuming the given limit behaves like a smooth function, when continued to

higher neutralino masses) can test the complete favoured regions of both NUHM scenarios, as well as large parts of the NUGM scenario.

In case of the cMSSM, the "best-fit" model is too far away from any experimental sensitivity. Further, only a tiny fraction of all models agrees with measurements of the Higgs boson, the relic density, etc. within 2σ. This drastically shows, how strong the cMSSM is already constrained, leaving only a tiny window for being realized in nature.

Summarizing the above results: Indirect dark matter search experiments are not yet able to exclude any of the models, that agree with the included measurements within 2σ, in any of the considered scenarios. In contrast, XENON100 and LUX start exploring experimentally favoured regions for both NUHM scenarios (XENON100 and LUX) and the NUGM scenario (LUX). Taking the expected sensitivity of XENON1T into account, large parts of all investigated scenarios and models will be tested.

Neglecting flavor observables, extends experimentally favoured regions, so that relatively larger numbers of models in NUHM and NUGM scenarios are already excluded by XENON100 and LUX. Corresponding plots are shown in Appendix A.7 (Figure A.41).

7

Conclusion

In the first part of this work, improvements on the position calibration of the ANTARES detector were presented. An insufficient amount of data with alignment information ("missing alignment") was available in the database. Data where no alignment information is available have to be processed subsequently with the individual detector lines assumed to be exactly vertical (nominal detector) and the optical modules placed on the support cable. This leads to an unsatisfactory angular resolution.

Consequently, the existing alignment algorithm was improved to provide the track reconstruction software with an increased amount of alignment data. The modified algorithm provides up to $\sim 42\%$ more aligned data. Furthermore, a Gaussian error propagation for the x- and y-position as well as for pitch and roll was implemented and is available in the database for further processing by the reconstruction software.

In the second part of this work, supersymmetric scenarios with and without unified boundary conditions were investigated. Recently, experiments at the LHC claimed the observation of the Higgs boson. Its measured mass puts severe constraints on the most popular SUSY model with unified boundary conditions, the cMSSM.

Thus, this study was dedicated to finding scenarios agreeing better with experimental measurements without a loss of predictability. Two classes of models were identified. While in the cMSSM the theory's free parameters are assumed to be unified at the GUT scale, in these two classes a non-universal Higgs or non-universal gauge sector was introduced (NUHM or NUGM). The three scenarios cMSSM, NUHM and NUGM were confronted with measurements of the Higgs-boson mass, m_h, the dark matter relic density, Ωh^2, as well as measurements from direct and indirect dark matter search experiments. To identify well defined regions in the high dimensional parameter space, which meet the mentioned experimental constraints, in a first approach some of the scenarios' free parameters were fixed to reasonable values leaving free a parameter space with a reduced number of dimensions.

In the cMSSM only small regions, consistent with the mass of the Higgs boson ($122 < m_h < 128$ GeV) and the relic density ($0.09 < \Omega h^2 < 0.13$) were found. In contrast, NUHM scenarios yield more extended regions that agree with the requirements for m_h and Ωh^2. In NUGM, the relic density requirements had to be relaxed allowing for non-thermal dark matter production. Nevertheless, regions were found where constraints from the Higgs-boson

mass and the relic density (relaxed) were fulfilled in contrast to the cMSSM.

To complete the picture, experimental measurements from direct and indirect dark matter searches were included in this work, in contrast to standard studies, where focus was set on either particle physics and/or direct detection. Thus, in this study limits from direct and indirect dark matter search experiments were applied to regions of the scenarios' parameter spaces where requirements for m_h and Ωh^2 are fulfilled. Consequently, this study provides one of the most complete pictures of the investigated scenarios.

It was found, current limits from indirect (IceCube) and direct (XENON100) detection experiments are equally capable of constraining the scenarios' parameter spaces. In the cMSSM, the focus-point region is excluded at 90% C.L. and only models in the $\tilde{\tau}$-coannihilation region remain. Considering the NUHM scenario, parts of the A-funnel region are excluded, but still the $\tilde{\tau}$-coannihilation region is not accessible for current experiments. Overall, more models escape limits from current indirect and direct dark matter search experiments. However, the future XENON1T experiment will test huge parts of the NUHM parameter space. Likewise, larger regions in the parameter space of NUGM survive current limits of direct and indirect dark matter search experiments compared to the cMSSM. Like in NUHM, the future XENON1T experiment will test huge parts of the NUGM parameter space.

In order to derive a quantitative measure of agreement between models and experimental results, a χ^2 analysis was preformed with respect to the Higgs-boson mass, the mass of the W-boson, the weak mixing angle, the dark matter relic density as well as flavor observables. In contrast to the previous approach, the complete dimensionality of the parameter space of the corresponding scenario was used. It was found, in all scenarios the position of the "best-fit" model (the one with the smallest χ^2) in the parameter space is predominantly determined by the mass of the Higgs boson and the relic density. Whereas in some regions of the parameter space, m_h and Ωh^2 are well described, there are no regions where predictions and measurements of the combination of all flavor observables deviate less than 2σ. Thus, the overall compatibility of theory and experiment is weak (large χ^2). Consistent with previous results, predictions in NUHM and NUGM agree better with experimental measurements compared to the cMSSM.

For the first time, consequences of particle physics, flavor physics and relic density measurements for direct and indirect dark matter search observables in non-universal SUSY scenarios, were investigated. Regions in the parameter space of direct and indirect detection observables (e.g., spin-independent WIMP-nucleon cross-section, or muon neutrino flux) were identified, which are preferred by measurements of the Higgs-boson mass, the relic density and flavor observables. These regions escape experimental limits from current indirect and direct dark matter search experiments.

In conclusion, neither current existing dark matter search experiments, nor future extensions are able to exclude completely non-universal SUSY scenarios investigated in this study. Even if LHC experiments raise lower limits on squark and gluino masses up to 3 TeV, the NUGM scenario will not be excluded. In the case of NUHM scenarios, even more restrictive limits on squark and gluino masses (m_{squark}, $m_{\text{gluino}} > 5$ TeV) will not be able to exclude any of the NUHM scenarios. Nevertheless, the χ^2 analysis has shown, that input parameters and resulting SUSY mass spectra are pushed to higher and higher masses,

drifting away from the desired low-energy supersymmetry. In the future, the goal of SUSY model building must be the harmonization of the predictions and measurements in the flavor sector, as well as the particle physics sector and cosmology, especially the mass of the Higgs boson and the relic density.

Appendix A

Supplementary Plots of SUSY Analysis

A.1 Software Framework NUSUSY

For the sake of completeness, the flow chart for the new developed framework, NUSUSY, is shown in Figure A.1. It consists of the public package DarkSUSY (Gondolo et al. 2004), for the calculation of direct and indirect dark matter detection observables. Further, the public spectrum calculator SuSpect (Djouadi et al. 2007) is included in the framework. SuSpect was modified to perform the calculation of supersymmetric spectra for the non-universal SUSY scenarios, introduced in Section 5. The general structure of NUSUSY correlates to the structure of the modified SuperBayeS package, but the parameter space sampling method was replaced by an algorithm that generates random numbers according to an (user-) defined distribution (e.g. uniform, normal, χ^2 etc.) in user defined intervals. The complete procedure was described in Section 6.1 in detail.

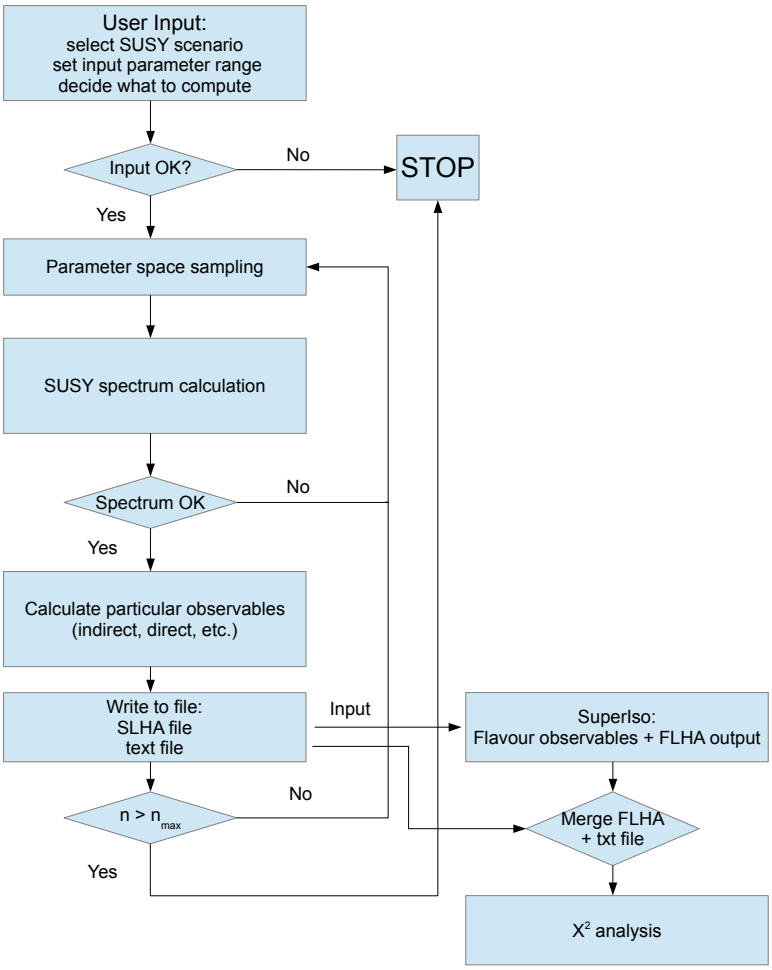

Figure A.1: Flow-chart of the simulation chain of NUSUSY. SuperIso is used to calculate flavor observables such as BR($B \to X_s\gamma$). Output files from SuperIso (FLHA files) are merged with output files from NUSUSY. The merged files are the base for a subsequent χ^2 analysis.

A.2 The Higgs Boson and Relic Density in NUGM

In this section supplementary plots for the NUGM scenario with independently varied mixing angles θ_1, θ_{24}, θ_{75} and θ_{200} are shown. Consequently, more models achieve a Higgs boson with mass $122 < m_h < 128$ GeV.

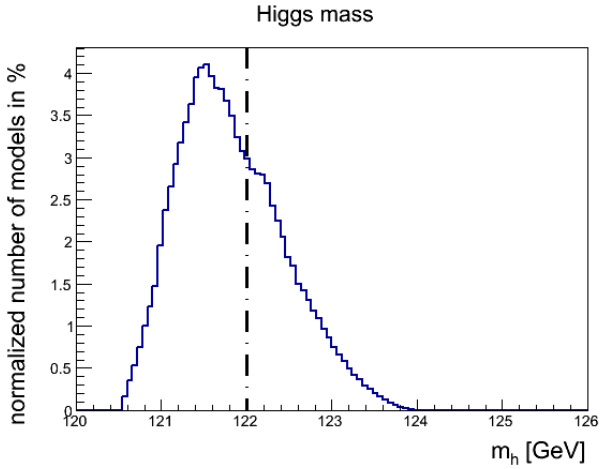

Figure A.2: Number of models with a calculated Higgs mass m_h, plotted on the y-axis for the NUGM scenario with independently varied mixing angles and $m_0 = 4$ TeV, $m_{1/2} = 600$ GeV, $A_0 = -m_{1/2}$ and tanβ =10, the corresponding Higgs mass is plotted on the x-axis; black dash-dotted line: lower limit of the theoretical uncertainty of ± 3 GeV, with respect to the measurements of The CMS Collaboration 2013 and The ATLAS Collaboration 2012a of $m_h \sim 125$ GeV. The number of models is normalized to the total number of simulated models.

Figure A.3 shows the number of models consistent with $122 < m_h < 128$ GeV, while Ωh^2 is smaller than 0.13 simultaneously, normalized to the total number of simulated models. The number of models is projected onto the corresponding mixing angle θ_i where i=1, 24, 75, 200. Like in Figure A.2, m_0 was fixed at 4 TeV, $m_{1/2} = 600$ GeV, $A_0 = -m_{1/2}$ and $\tan\beta = 10$.

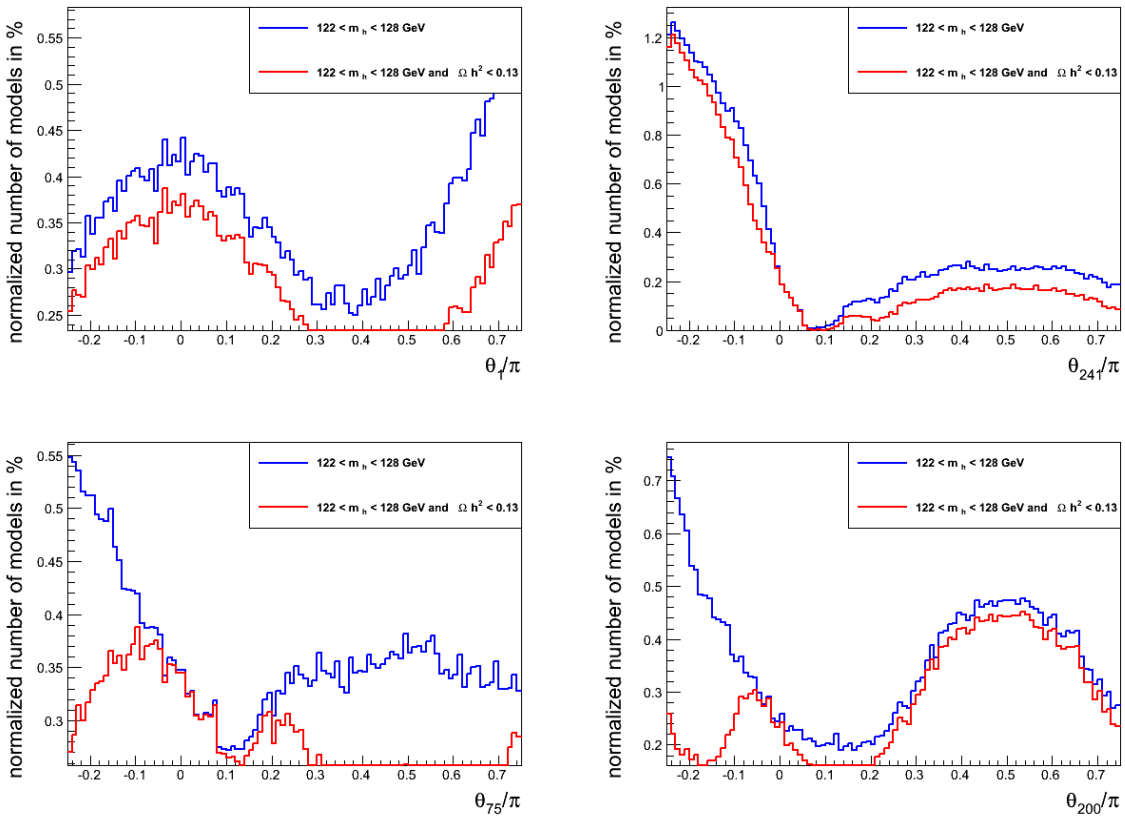

Figure A.3: Number of models with $122 < m_h < 128$ GeV (blue line) and $122 < m_h < 128$ GeV and Ωh^2 <0.13 (red line) of the four dimensional parameter space of mixing angels in the NUGM scenario. The number of models fulfilling the Higgs mass constraint and relic density requirements is plotted versus the singlet mixing angle θ_1 (top left), the 24-plet mixing angle θ_{24} (top right), the 75-plet mixing angle θ_{75} (bottom left) and the 200-plet mixing angle θ_{200} (bottom right). The number of models is normalized to the total number of simulated models

A.3 Indirect Detection - Spin Dependent WIMP Proton Cross-section

In this section, excluded regions in the m_0-$m_{1/2}$ plane of the cMSSM and the NUHM scenario are shown for the spin-dependent WIMP proton cross-section.

cMSSM:
In Figure A.4 regions are shown excluded by ANTARES, while Figure A.5 illustrates regions excluded by IceCube, for $\sigma_{\mathrm{SD}}^{\mathrm{proton}}$.

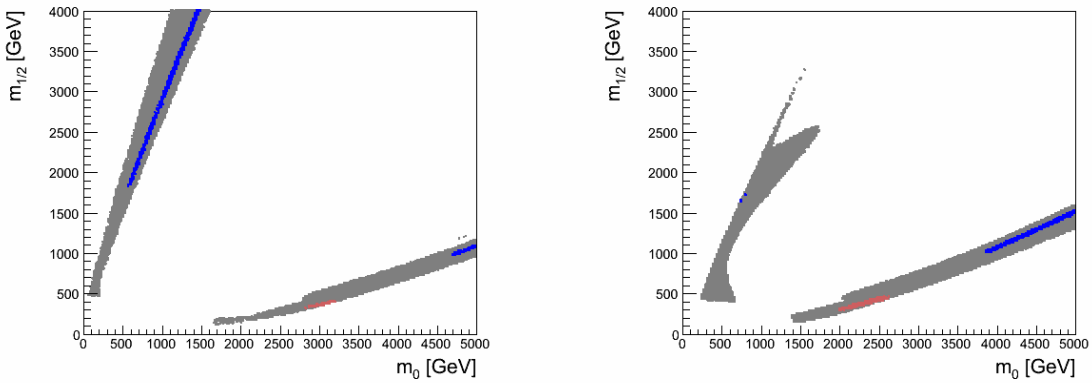

Figure A.4: ANTARES $\sigma_{\mathrm{SD}}^{\mathrm{proton}}$ excluded regions in the m_0-$m_{1/2}$ plane of cMSSM for $\tan\beta = 10$ (left) and $\tan\beta = 45$ (right); colors: gray: not excluded, faint brown: excluded at 90% C.L. for annihilation channel W^+W^- (Adrian-Martinez et al. 2012), blue: models with $122 < m_h < 128$ GeV and $0.09 < \Omega h^2 < 0.13$.

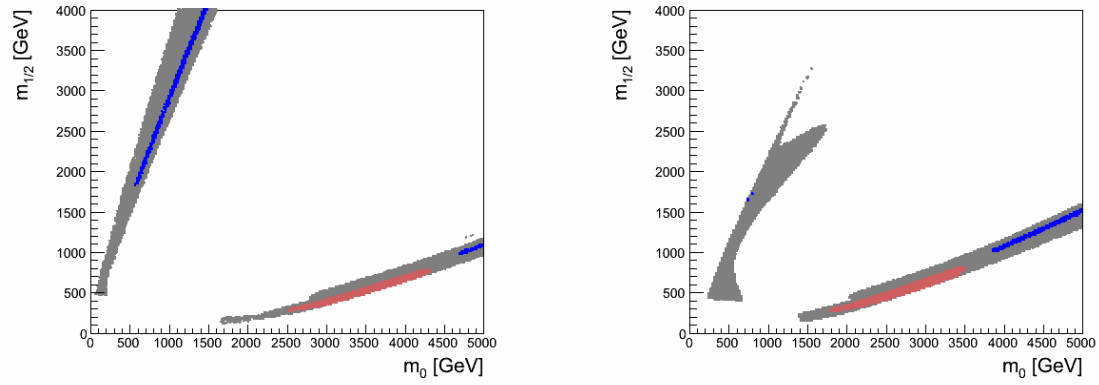

Figure A.5: IceCube $\sigma_{\mathrm{SD}}^{\mathrm{proton}}$ excluded regions in the m_0-$m_{1/2}$ plane of cMSSM for $\tan\beta = 10$ (left) and $\tan\beta = 45$ (right); colors: gray: not excluded, faint brown: excluded at 90% C.L. for annihilation channel W^+W^- (Aartsen et al. 2013), blue: models with $122 < m_h < 128$ GeV and $0.09 < \Omega h^2 < 0.13$.

NUHM:
First, IceCube excluded regions are shown in the NUHM1 scenario (Figure A.6) for annihilation channel W^+W^- and $\tan\beta = 10$ on the left and $\tan\beta = 45$ on the right hand side.

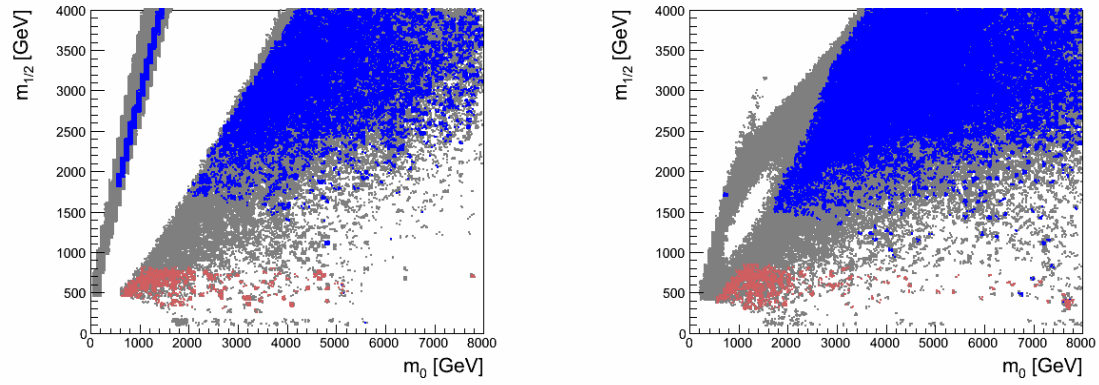

Figure A.6: IceCube $\sigma_{\mathrm{SD}}^{\mathrm{proton}}$ excluded regions in the m_0-$m_{1/2}$ plane of NUHM1 for $\tan\beta = 10$ (left) and $\tan\beta = 45$ (right); colors: gray: not excluded, faint brown: excluded at 90% C.L. for annihilation channel W^+W^- (Aartsen et al. 2013), blue: models with $122 < m_h < 128$ GeV and $0.09 < \Omega h^2 < 0.13$.

Only exclusion plots for the annihilation channel W^+W^- are shown, as the given limits channel $b\bar{b}$ can not exclude the kind of models investigated. Second, the corresponding IceCube exclusion plots for the NUHM2 scenario are shown (Figure A.7).

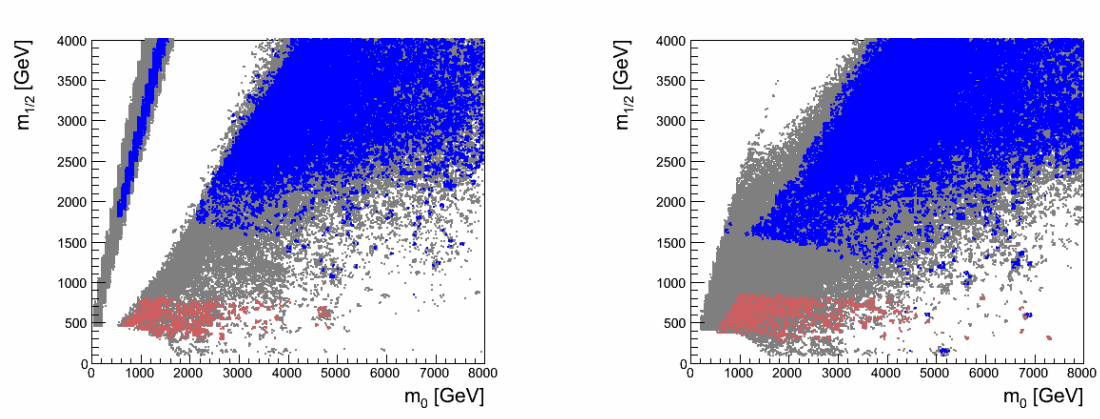

Figure A.7: IceCube $\sigma_{\mathrm{SD}}^{\mathrm{proton}}$ excluded regions in the m_0-$m_{1/2}$ plane of NUHM2 for $\tan\beta = 10$ (left) and $\tan\beta = 45$ (right); colors: gray: not excluded, faint brown: excluded at 90% C.L. for annihilation channel W^+W^- (Aartsen et al. 2013), blue: models with $122 < m_h < 128$ GeV and $0.09 < \Omega h^2 < 0.13$.

A.4 Direct Detection

For the sake of completeness, excluded/excludable regions for XENON 100/XENON 1T in the NUHM2 scenario are shown in Figure A.8/Figure A.9

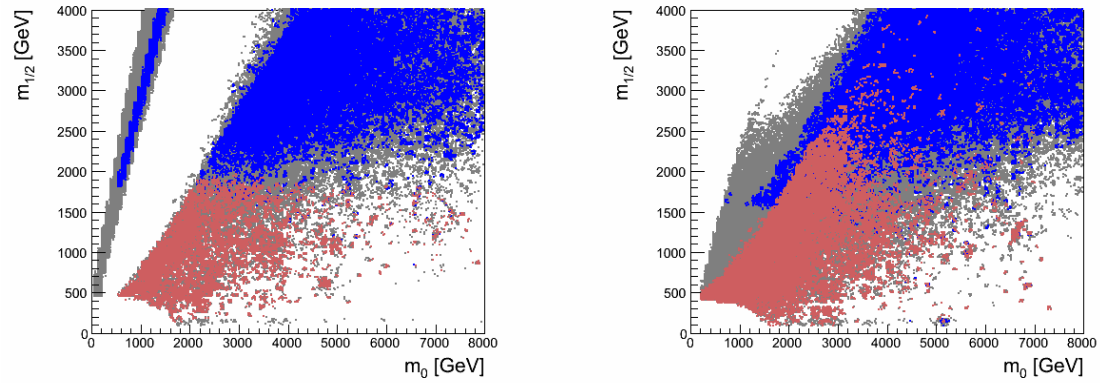

Figure A.8: $\sigma_{\mathrm{SI}}^{\mathrm{nucleon}}$ excluded regions (XENON 100) in the m_0-$m_{1/2}$ plane of NUHM2, for $\tan\beta = 10$ (left) and $\tan\beta = 45$ (right); colors: gray: not excluded, faint brown: excluded at 90% C.L. (April et al. 2012a), blue: models with $122 < m_h < 128$ GeV and $0.09 < \Omega h^2 < 0.13$.

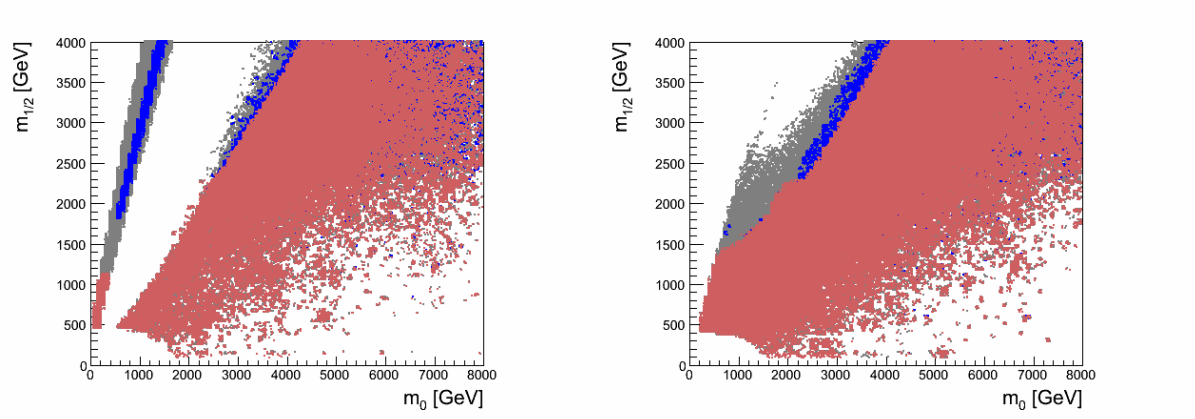

Figure A.9: $\sigma_{\mathrm{SI}}^{\mathrm{nucleon}}$ excludable regions (XENON 1T) in the m_0-$m_{1/2}$ plane of NUHM2, for $\tan\beta = 10$ (left) and $\tan\beta = 45$ (right); colors: gray: not excluded, faint brown: excludable at 90% C.L. (April et al. 2012b), blue: models with $122 < m_h < 128$ GeV and $0.09 < \Omega h^2 < 0.13$.

A.5 χ^2 Analysis

In this chapter, supplementary plots and tables of the χ^2 analysis for all scenarios are presented. First, the free parameters of the corresponding scenario are listed in Table A.1, for the model that achieves the best compatibility ("best-fit" model) with the measured values of the individual observables from Table 6.4. The minimal χ^2, the corresponding p-value and the $n\sigma$ compatibility with respect to included observables in Table 6.4 are listed in Table A.2. In Table A.3 the χ^2 values of the particular observables are shown, that lead to χ^2_{min}. The indirect and direct detection observables are shown in Table A.4. Last but not least, the supersymmetric mass spectrum of the corresponding SUSY scenario is listed in Table A.5.

Scenario / Input Params	cMSSM	NUGM	NUHM1	NUHM2
m_0 [GeV]	1286	5154	6833	5338
$m_{1/2}$ [GeV]	3533	1489	3360	2720
A_0 [GeV]	-2643	-2590	2694	-1510
$\tan\beta$	7.62	48.77	49.28	40.33
sgn(μ)	+1	+1	+1	+1
δ_{H_u}	–	–	0.07	0.27
δ_{H_d}	–	–	0.07	-0.42
θ_1 [rad]	–	0.77	–	–
θ_{24} [rad]	–	-0.62	–	–
θ_{75} [rad]	–	1.79	–	–
θ_{200} [rad]	–	1.85	–	–

Table A.1: Scenario dependent input parameters for the "best-fit" models.

Scenario / probabilities	cMSSM	NUGM	NUHM1	NUHM2
χ^2_{min}	20.3	18.2	18.8	18.4
p-value	0.062	0.11	0.093	0.10
$n\sigma$	1.87	1.59	1.68	1.64

Table A.2: χ^2, p-value and $n\sigma$ compatibility for the "best-fit" models of the cMSSM, NUGM, NUHM1 and NUHM2 scenario.

Scenario / χ^2(Observable)	cMSSM	NUGM	NUHM1	NUHM2
Ωh^2	$1.02 \cdot 10^{-2}$	0.18	$2.83 \cdot 10^{-2}$	$3.78 \cdot 10^{-2}$
m_h	$3.99 \cdot 10^{-2}$	$3.54 \cdot 10^{-5}$	$1.28 \cdot 10^{-2}$	$5.20 \cdot 10^{-2}$
BR($B \to X_s\gamma$)	2.84	2.88	2.73	1.93
$\Delta_0(B \to K^*\gamma)$	4.43	4.40	4.38	4.22
BR($B_u \to \tau\nu_\tau$)	6.08	6.27	6.27	6.48
BR($B \to D^0\tau\nu_\tau$)	0.46	0.43	0.48	0.49
$\frac{\text{BR}(K\to\mu\nu)}{\text{BR}(\pi\to\mu\nu)}$	2.00	2.15	2.24	2.52
$R_{\mu 23}$	$2.03 \cdot 10^{-2}$	$1.86 \cdot 10^{-2}$	$1.75 \cdot 10^{-2}$	$1.47 \cdot 10^{-2}$
BR($D_s \to \tau\nu_\tau$)	0.75	$1.44 \cdot 10^{-2}$	0.76	0.76
BR($D_s \to \mu\nu_\mu$)	1.78	1.79	1.79	1.79
M_W	1.16	$1.31 \cdot 10^{-2}$	0.10	$3.69 \cdot 10^{-2}$
$\sin^2\theta^W_{eff}$	0.71	$3.06 \cdot 10^{-2}$	$1.59 \cdot 10^{-2}$	$5.29 \cdot 10^{-2}$

Table A.3: χ^2 values of the individual observables for the "best-fit" model in the investigated scenarios cMSSM, NUGM, NUHM1 and NUHM2.

Scenario / ID/DD Observables	cMSSM	NUGM	NUHM1	NUHM2
$\log_{10}(\nu_\mu + \bar{\nu}_\mu$ flux km^{-2}yr^{-1})	-2.25	6.04	7.08	7.94
$\log_{10}(\mu^+ + \mu^-$ flux km^{-2}yr^{-1})	-10.14	-1.71	-0.69	0.11
$\log_{10}(\sigma^{\text{proton}}_{\text{SD}}$ [cm^2])	-45.26	-42.98	-42.32	-41.62
$\log_{10}(\sigma^{\text{nucleon}}_{\text{SI}}$ [cm^2])	-47.24	-45.92	-45.15	-44.36

Table A.4: Predicted indirect and direct detection observables for the "best-fit" models of the cMSSM, NUGM, NUHM1 and NUHM2.

Scenario / SUSY Mass Spectrum [GeV]		cMSSM	NUGM	NUHM1	NUHM2
h	(light Higgs boson)	125.2	125.3	125.2	125.4
H	(heavy Higgs boson)	4821.6	3367	2752	1530.5
A	(pseudoscalar Higgs boson)	4821.5	3367	2752	1530.5
$H^{\pm}$	(charged Higgs boson)	4822.4	3667.9	2753.3	1532.8
$\tilde{d}_L$	(down-squark)	6456.7	7304.5	9006.5	7197.5
$\tilde{d}_R$		6136.6	7443	8825.7	7035.5
$\tilde{u}_L$	(up-squark)	6456.3	7304.1	9006.2	7197.1
$\tilde{u}_R$		6173.9	8710.3	8845.9	7118.2
$\tilde{s}_L$	(strange-squark)	6456.7	7304.5	9006.5	7197.5
$\tilde{s}_R$		6136.6	7443	8825.7	7035.5
$\tilde{c}_L$	(charm-squark)	6456.3	7304.1	9006.2	7197.1
$\tilde{c}_R$		6173.9	8710.3	8845.9	7118.2
$\tilde{b}_1$	(bottom-squark)	5898.2	5579.2	7244.5	5910.5
$\tilde{b}_2$		6115.3	6335.9	7409.3	6338.7
$\tilde{t}_1$	(top-squark)	4844	5447.6	6499.3	4991
$\tilde{t}_2$		5888.5	6743.6	7213.9	5886
$\tilde{e}_L$	(electron-slepton)	2582.5	6749.6	7128.8	5632.4
$\tilde{e}_R$		1811.4	9468.2	6928.5	5331.6
$\tilde{\nu}_{eL}$	(electron-sneutrino)	2581.4	6749.2	7128.4	5631.9
$\tilde{\mu}_L$	(muon-slepton)	2582.5	6749.6	7128.8	5632.4
$\tilde{\mu}_R$		1811.4	9468.2	6928.5	5331.6
$\tilde{\nu}_{\mu L}$	(muon-sneutrino)	2581.4	6749.2	7128.4	5631.9
$\tilde{\tau}_1$	(tau-slepton)	1788.4	5904.7	5140.2	4585.9
$\tilde{\tau}_2$		2574.9	8272.6	6334.4	5297.3
$\tilde{\nu}_{\tau L}$	(tau-sneutrino)	2573.6	5904.2	6333.9	5296.6
$\tilde{g}$	(gluino)	7106.2	5995.7	7115.1	5835
χ_1^0	(neutralino)	1599.3	-1107.5	1082.5	1083.1
χ_2^0		2924.8	1110	-1087.6	-1094
χ_3^0		-4040.2	-2637.4	1534.3	1237.6
χ_4^0		4043.7	9998.1	2834.3	2288.3
$\chi_1^{\pm}$	(chargino)	2924.8	1108.3	1085.5	1091
$\chi_2^{\pm}$		4043.5	2637.5	2834.3	2288.3
W	(W-boson)	80.5	80.5	80.5	80.5

Table A.5: Supersymmetric mass spectra for the "best-fit" models of the cMSSM, NUGM, NUHM1 and NUHM2. Indices L and R label left and right handed sparticles (no sfermion mixing for 1st/2nd generation), indices 1,2 label mass eigenstates (squark and slepton mixing only in 3rd generation).

The χ^2 distributions of the individual observables for a given SUSY scenario will be shown in the following.

cMSSM:

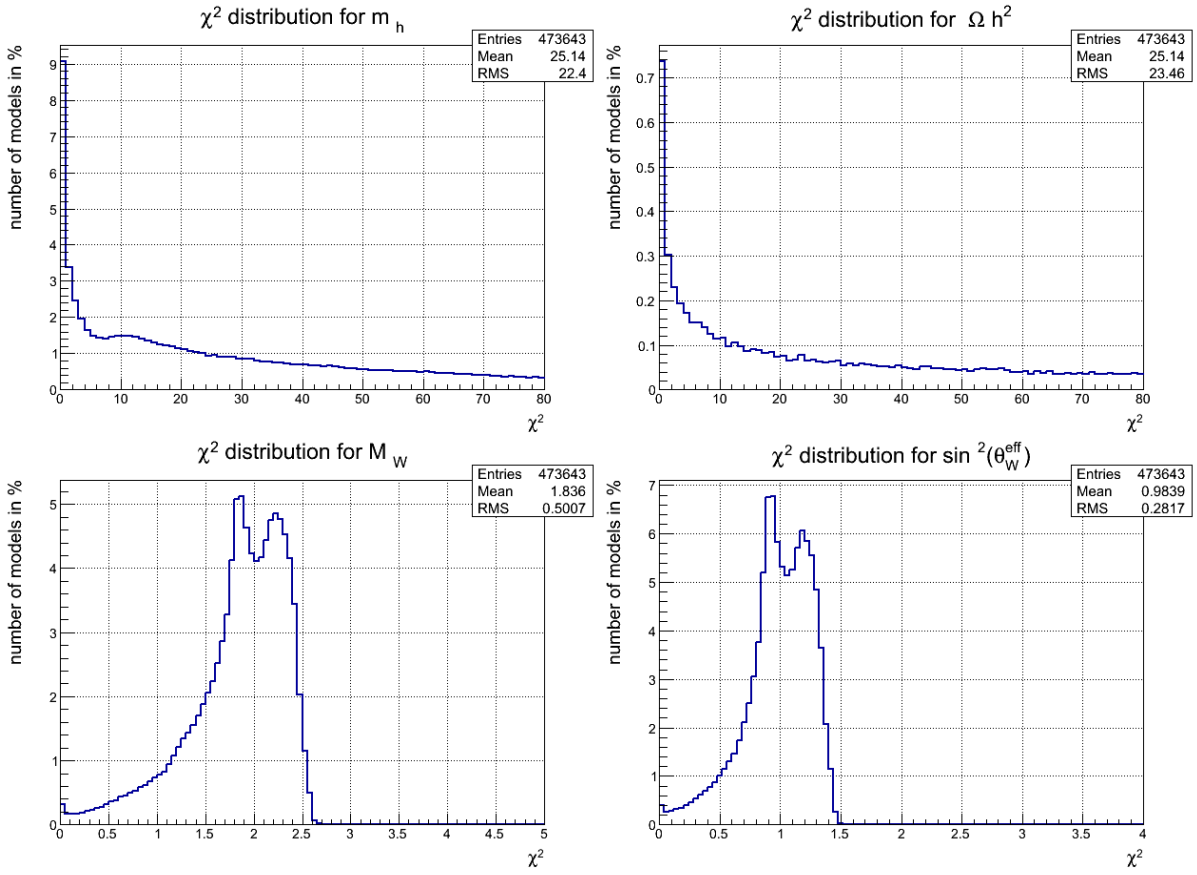

Figure A.10: χ^2 distributions for m_h (top left), Ωh^2 (top right), M_W (bottom left) and $\sin^2(\theta_W^{eff})$ (lower right) in the cMSSM scenario. The number of models is normalized to the total number of simulated models.

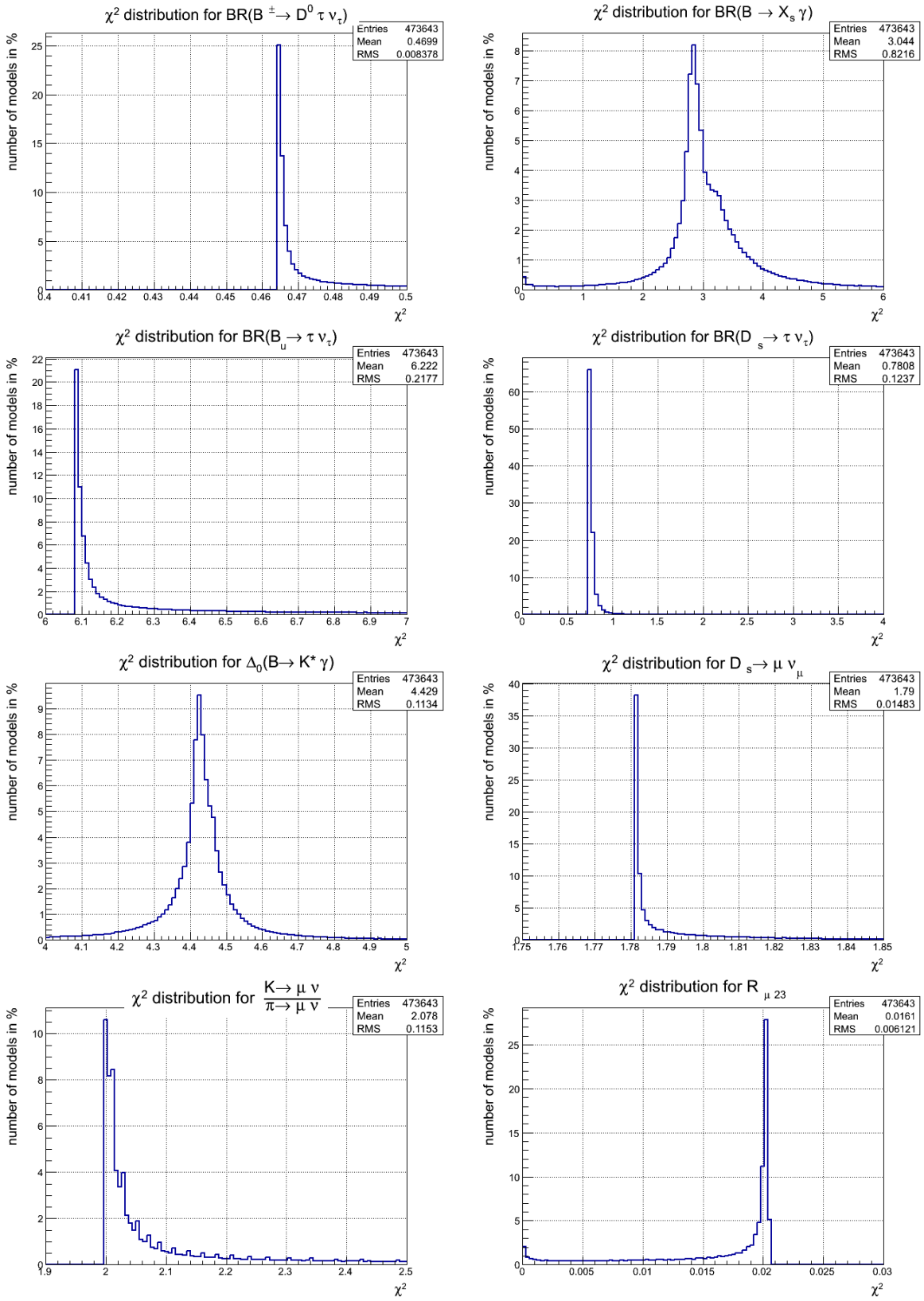

Figure A.11: χ^2 distributions for the flavor observables in the cMSSM scenario. The number of models is normalized to the total number of simulated models.

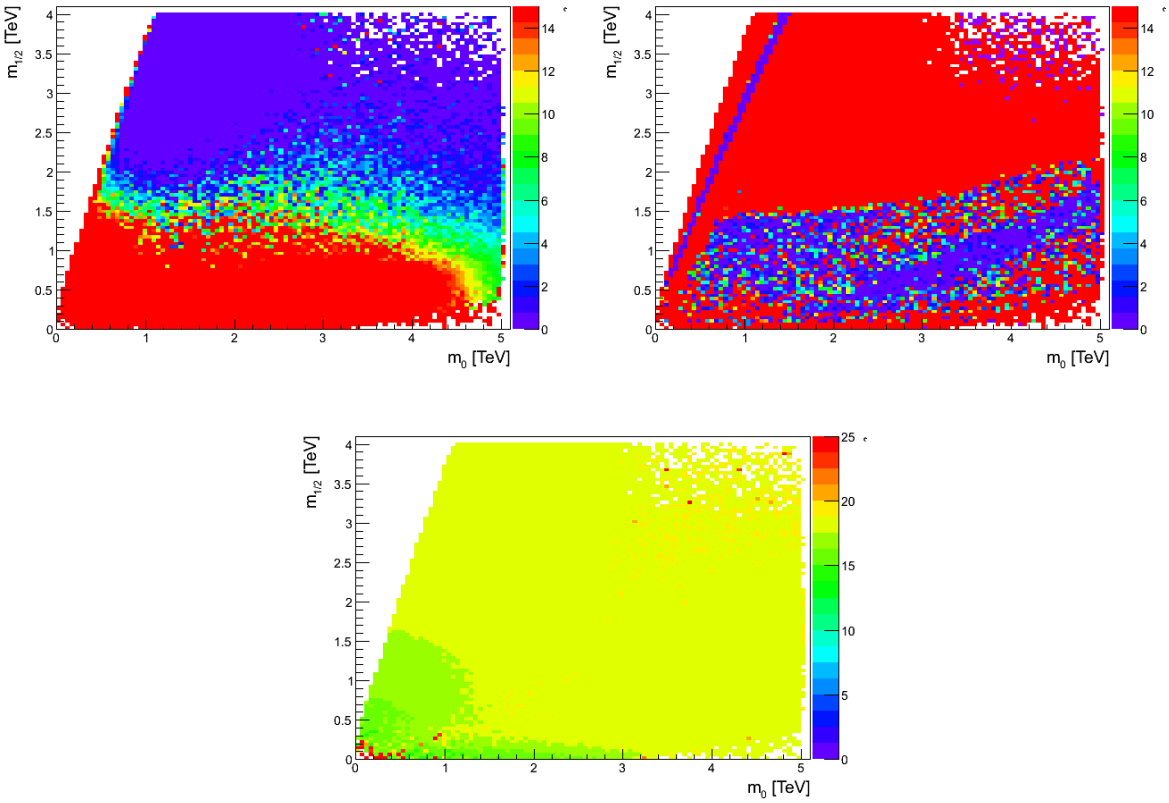

Figure A.12: χ^2 distributions of m_h (top left), Ωh^2 (top right) and $\sum \chi^2_{\text{flavor}}$ (bottom central) in the m_0-$m_{1/2}$ plane in the cMSSM scenario. χ^2 values are color coded. Red colored models have $\chi^2 \geq 15$ (≥ 25, bottom central).

NUHM1:

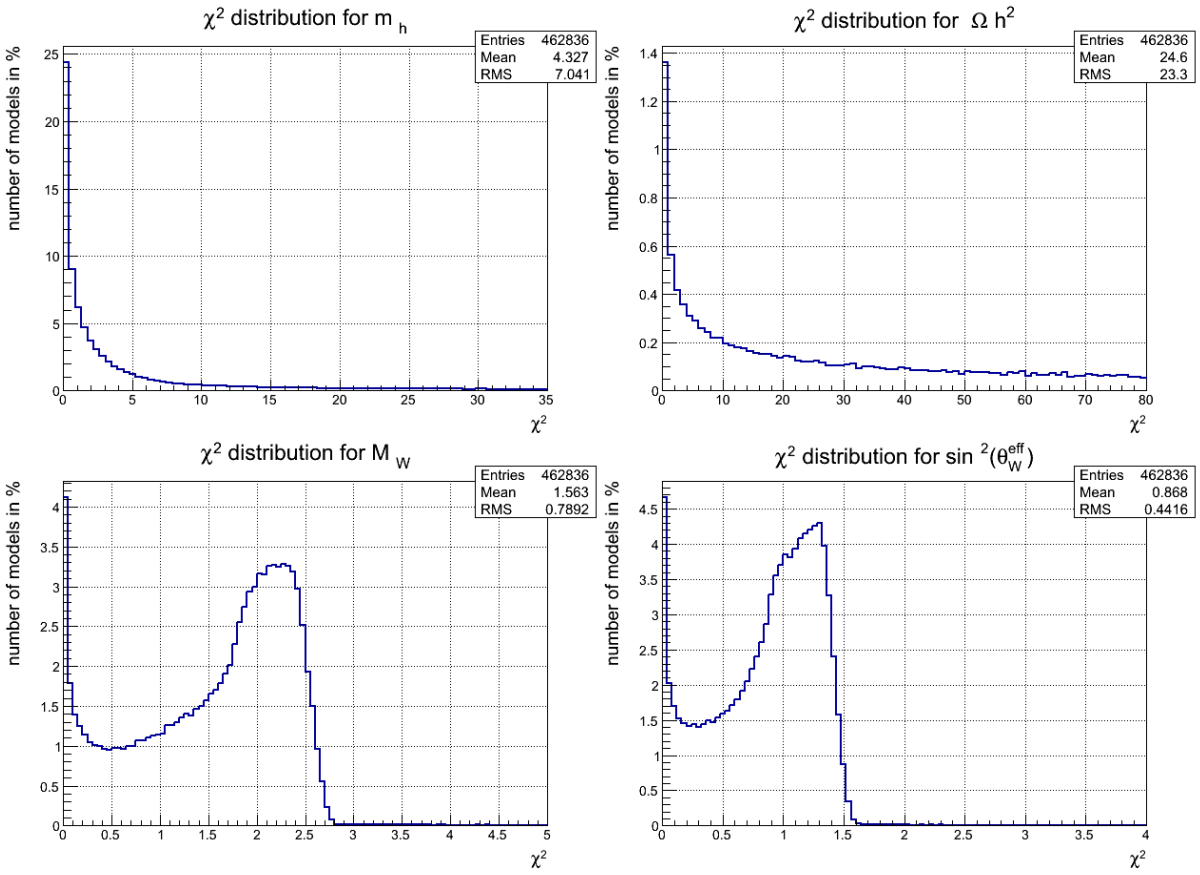

Figure A.13: χ^2 distributions for m_h (top left), Ωh^2 (top right), M_W (bottom left) and $\sin^2(\theta_W^{eff})$ (bottom right) in the NUHM1 scenario. The number of models is normalized to the total number of simulated models.

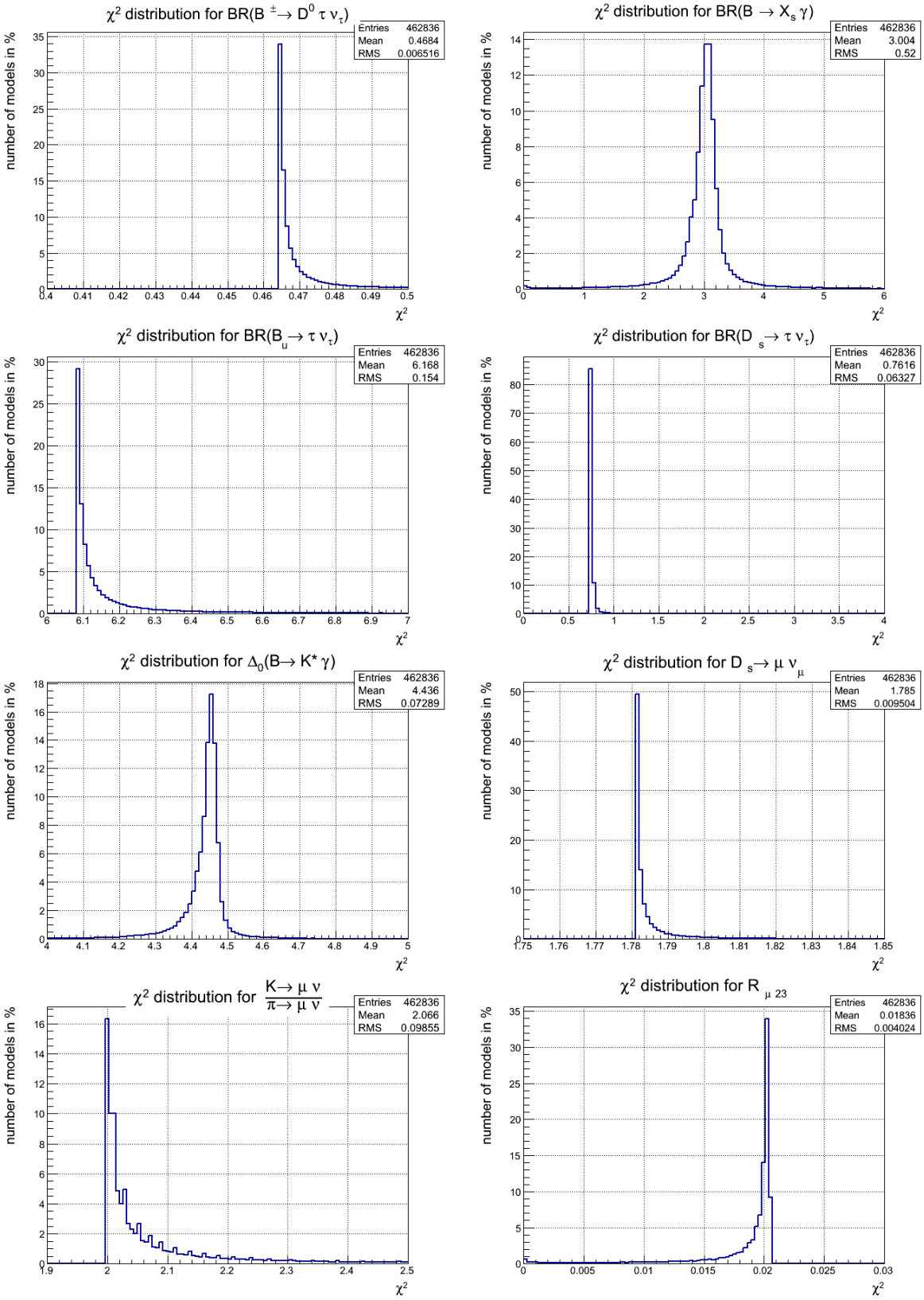

Figure A.14: χ^2 distributions for the flavor observables in the NUHM1 scenario. The number of models is normalized to the total number of simulated models.

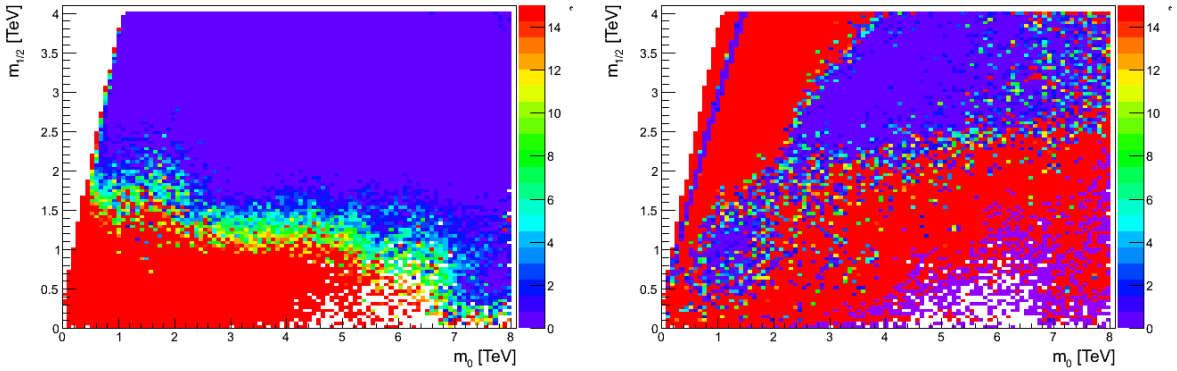

Figure A.15: χ^2 distributions of m_h (left) and Ωh^2 (right) in the m_0-$m_{1/2}$ plane of NUHM1. χ^2 values are color coded. Red colored models have $\chi^2 \geq 15$.

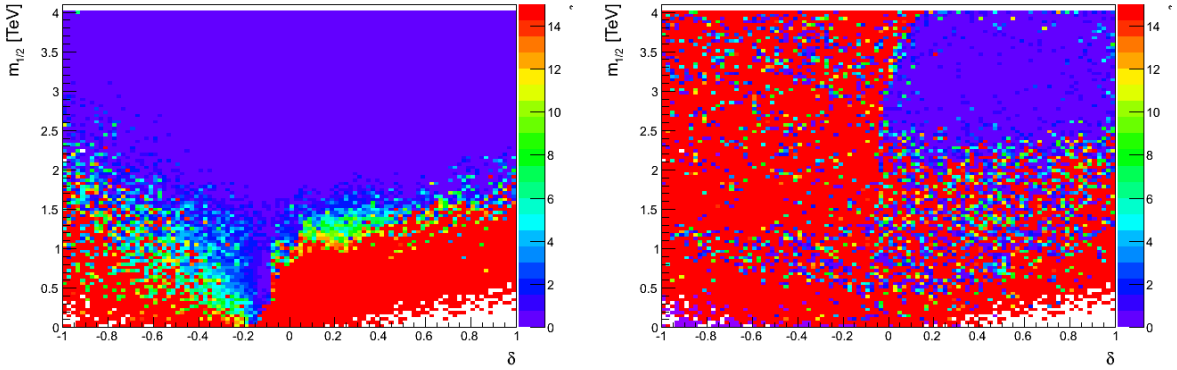

Figure A.16: χ^2 distributions of m_h (left) and Ωh^2 (right) in the δ-$m_{1/2}$ plane of NUHM1. χ^2 values are color coded. Red colored models have $\chi^2 \geq 15$.

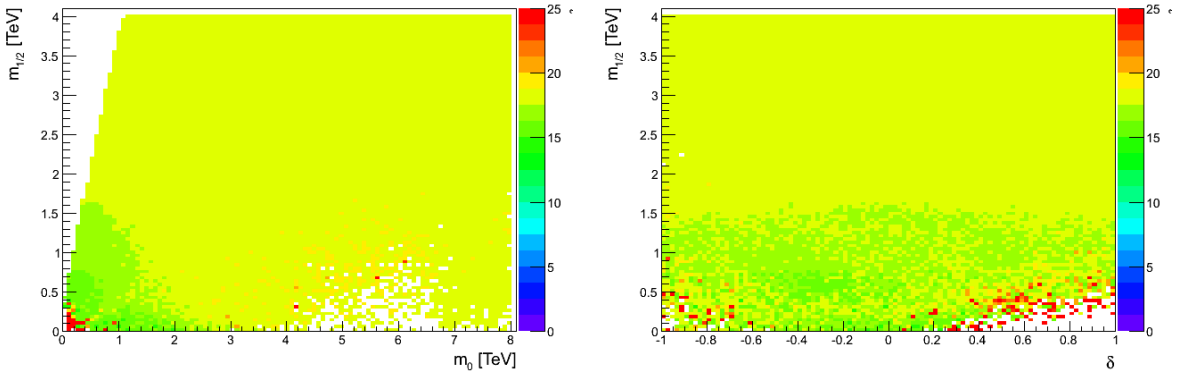

Figure A.17: χ^2 distributions of $\sum \chi^2_{\text{flavor}}$ in the m_0-$m_{1/2}$ plane (left) and δ-$m_{1/2}$ plane (right) of NUHM1. χ^2 values are color coded. Red colored models have $\chi^2 \geq 25$.

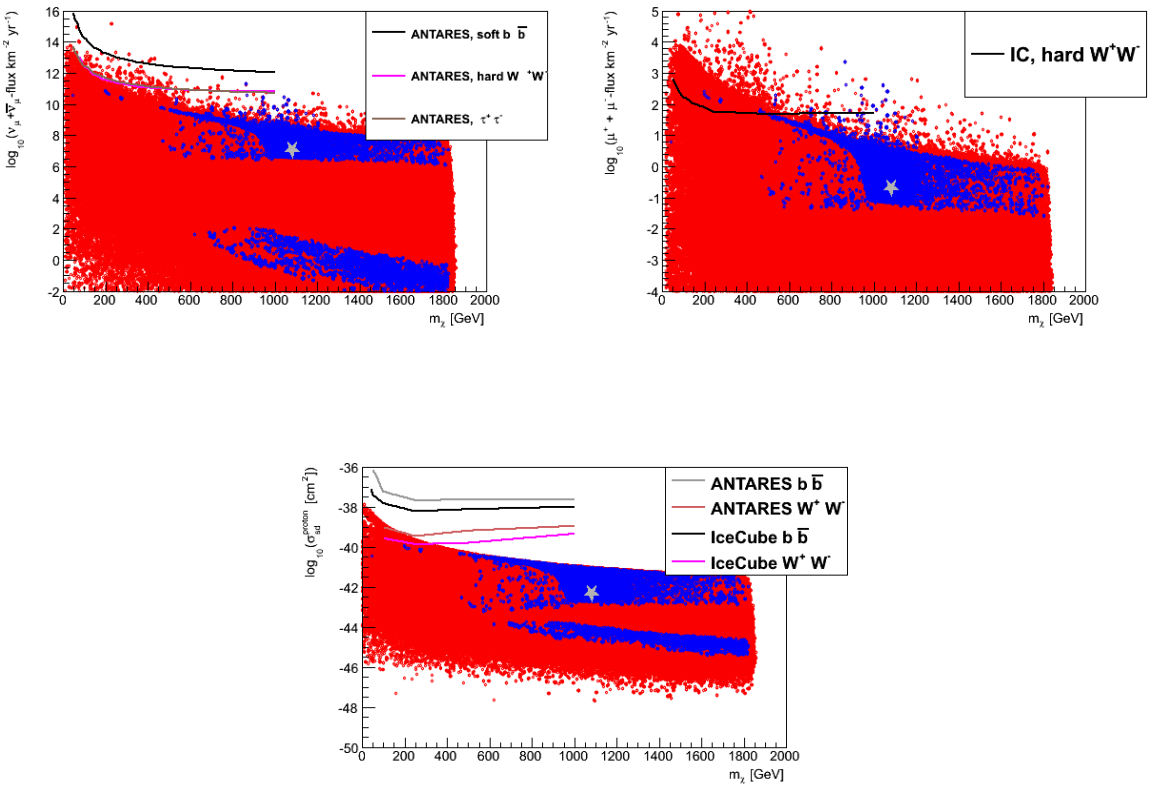

Figure A.18: "Best-fit" model (gray asterisk) of NUHM1 with respect to indirect dark matter detection observables, $\nu_\mu + \bar{\nu}_\mu$ flux (top left), $\mu^+ + \mu^{-2}$ flux (top right) and the spin-dependent WIMP proton cross-section (bottom central). Also shown are ANTARES and IceCube limits. Colors: blue: $122 < m_h < 128$ GeV and $0.09 < \Omega h^2 < 0.13$, red: all other models.

NUHM2:

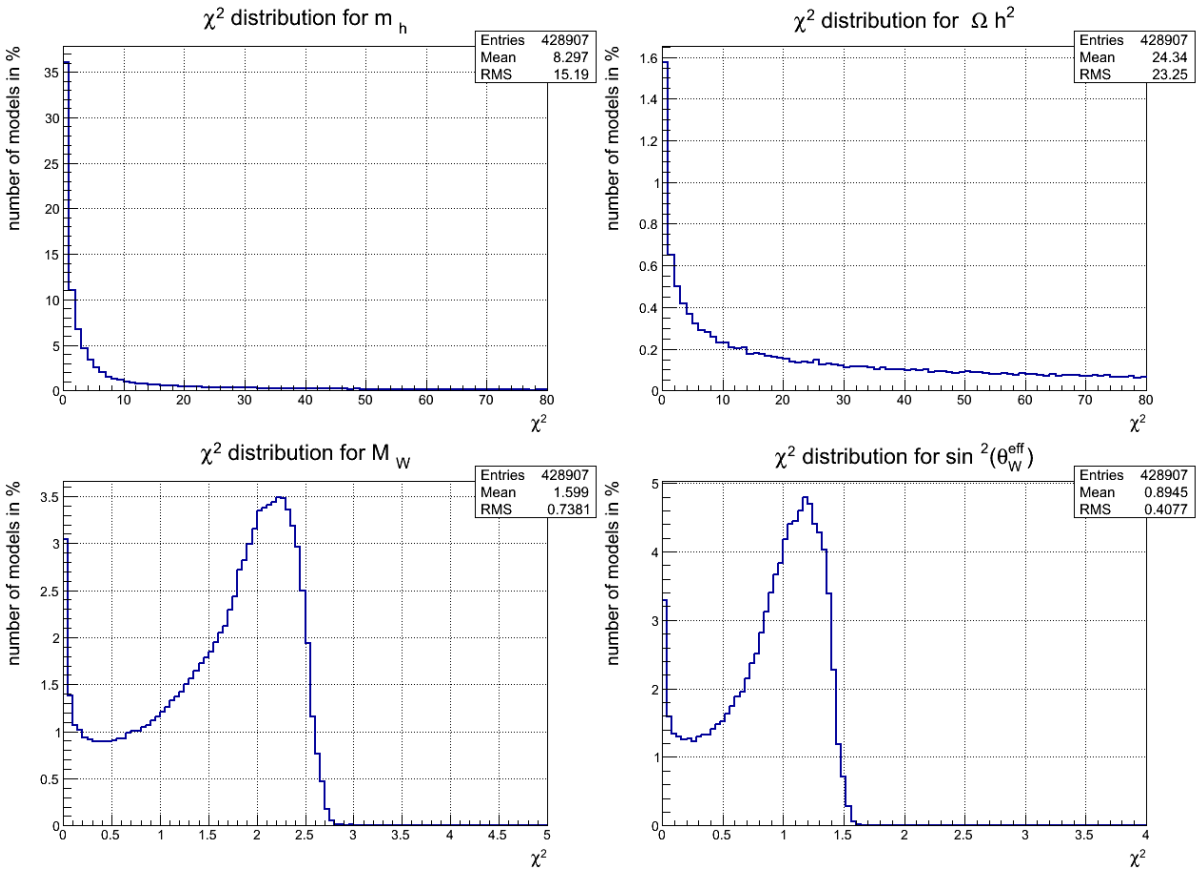

Figure A.19: χ^2 distributions for m_h (top left), Ωh^2 (top right), M_W (bottom left) and $\sin^2(\theta_W^{eff})$ (bottom right) in the NUHM2 scenario. The number of models is normalized to the total number of simulated models.

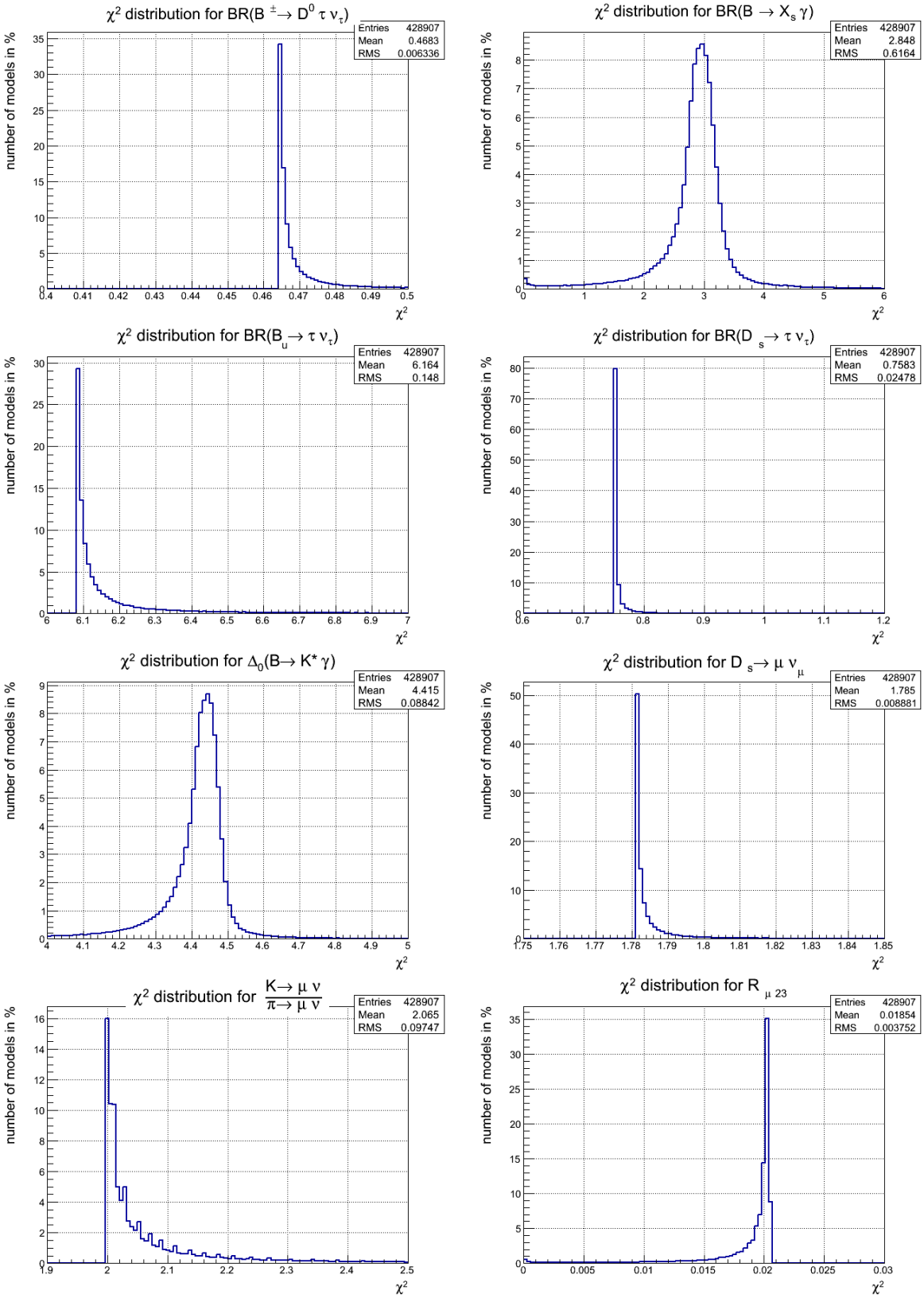

Figure A.20: χ^2 distributions for the flavor observables in the NUHM2 scenario. The number of models is normalized to the total number of simulated models.

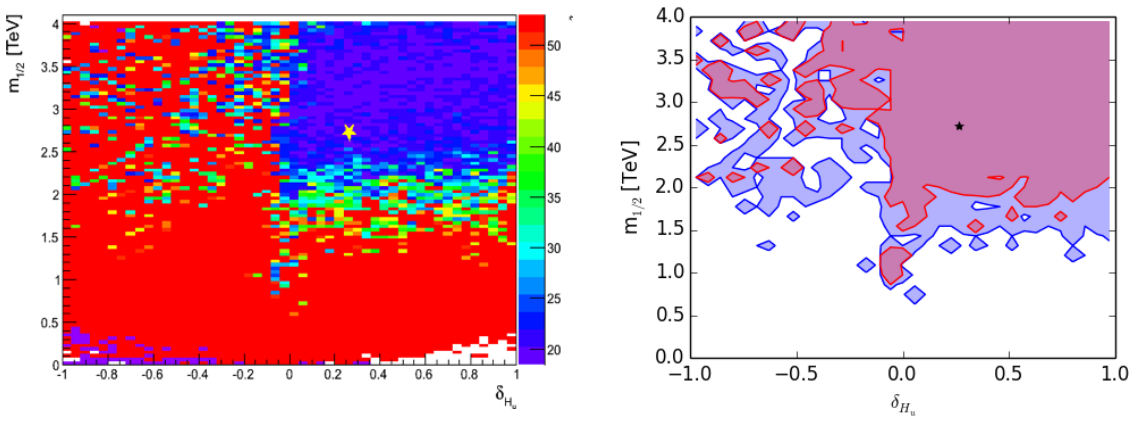

Figure A.21: χ^2 distribution (left) and compatibility regions within 3σ and 5σ (right) in the δ_{H_u}-$m_{1/2}$ plane of NUHM2. χ^2 values are color coded on the left hand side and red colored models have $\chi^2 \geq 53$. The red contour on the right hand side corresponds to deviation less than 3σ, the blue contour corresponds to deviation less than 5σ from experimental measurements. The yellow (left) and black asterisk (right) corresponds to the "best-fit" model. Models outside the blue contour deviate from measurements more than 5σ and are not shown here.

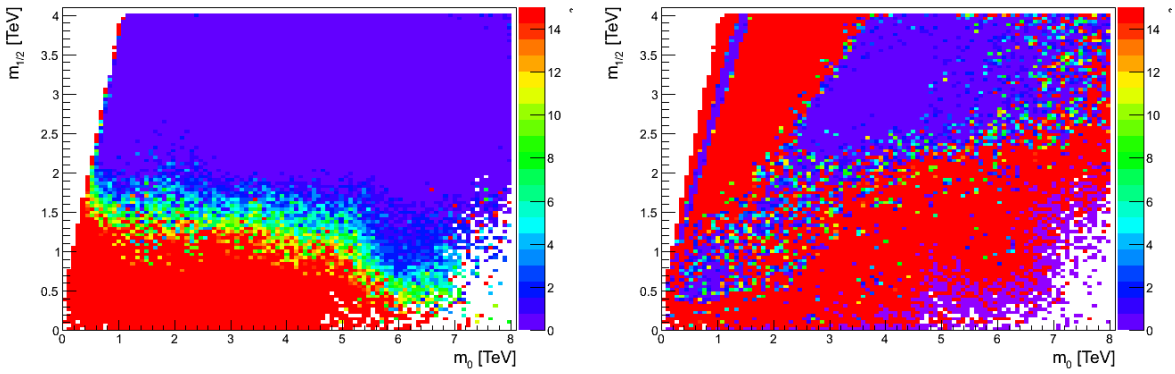

Figure A.22: χ^2 distributions of m_h (left) and Ωh^2 (right) in the m_0-$m_{1/2}$ plane of NUHM2. χ^2 values are color coded. Red colored models have $\chi^2 \geq 15$.

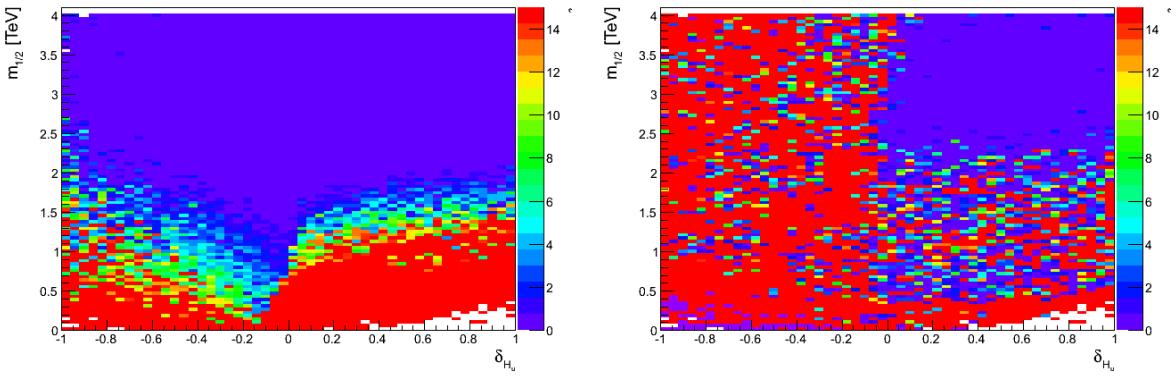

Figure A.23: χ^2 distributions of m_h (left) and Ωh^2 (right) in the δ_{H_u}-$m_{1/2}$ plane of NUHM2. χ^2 values are color coded. Red colored models have $\chi^2 \geq 15$.

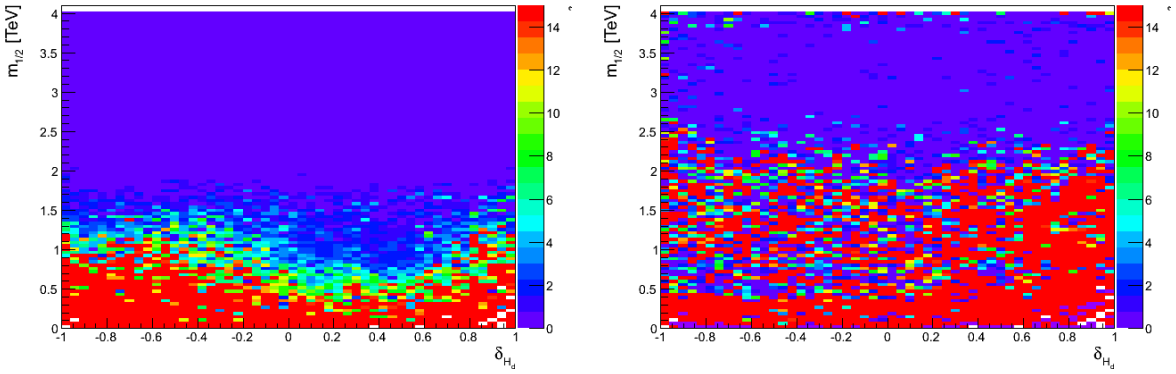

Figure A.24: χ^2 distributions of m_h (left) and Ωh^2 (right) in the δ_{H_d}-$m_{1/2}$ plane of NUHM2. χ^2 values are color coded. Red colored models have $\chi^2 \geq 15$.

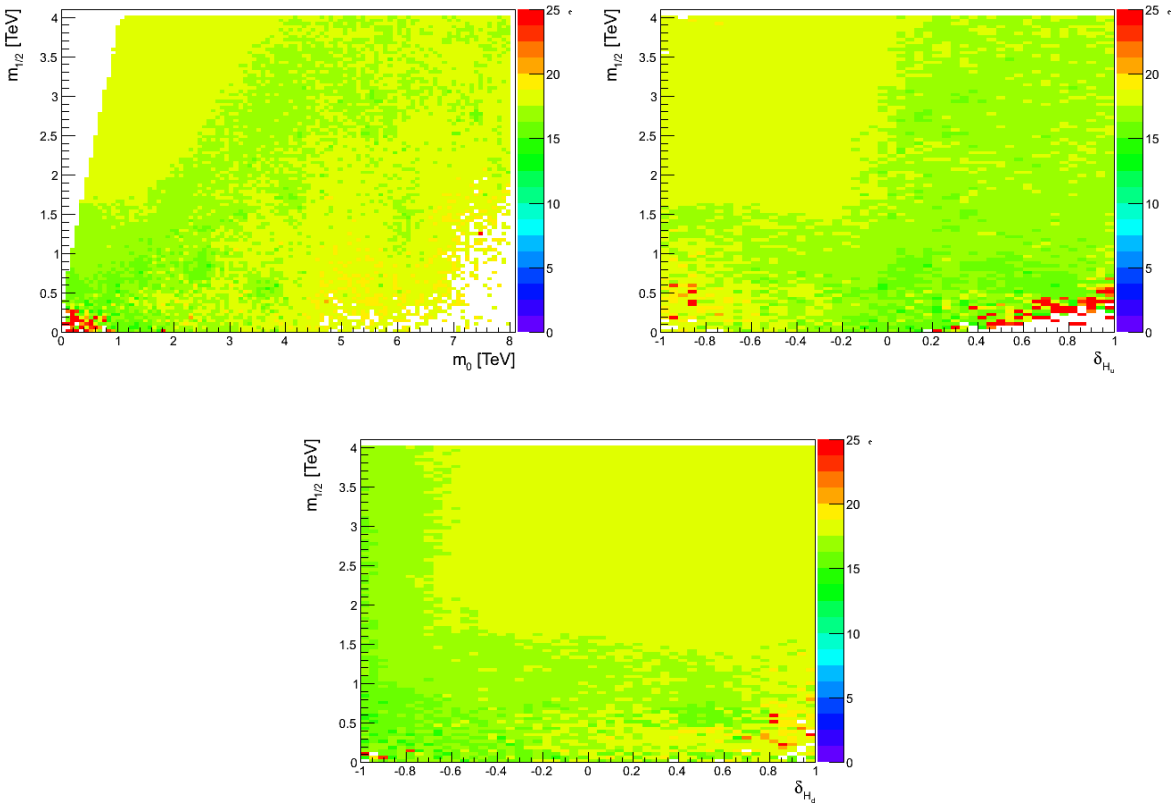

Figure A.25: $\sum \chi^2_{\text{flavor}}$ distribution in the m_0-$m_{1/2}$ plane (top left), the δ_{H_u}-$m_{1/2}$ plane (top right) and the δ_{H_d}-$m_{1/2}$ plane (bottom central) of NUHM2. χ^2 values are color coded. Red colored models have $\chi^2 \geq 25$.

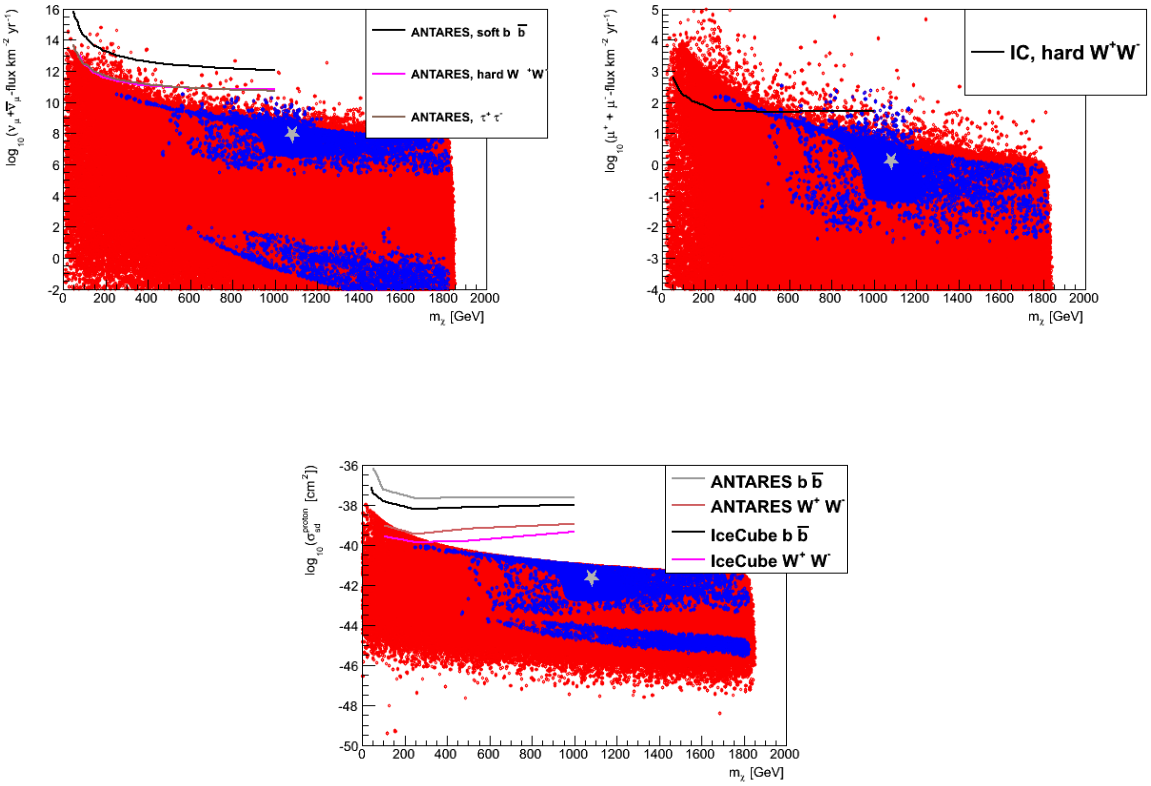

Figure A.26: "Best-fit" model (gray asterisk) of NUHM2 with respect to indirect dark matter detection observables, $\nu_\mu + \bar{\nu}_\mu$ flux (upper left), $\mu^+ + \mu^{-2}$ flux (upper right) and the spin-dependent WIMP proton cross-section (lower central). Also shown are ANTARES and IceCube limits. Colors: blue: $122 < m_h < 128$ GeV and $0.09 < \Omega h^2 < 0.13$, red: all other models.

NUGM:

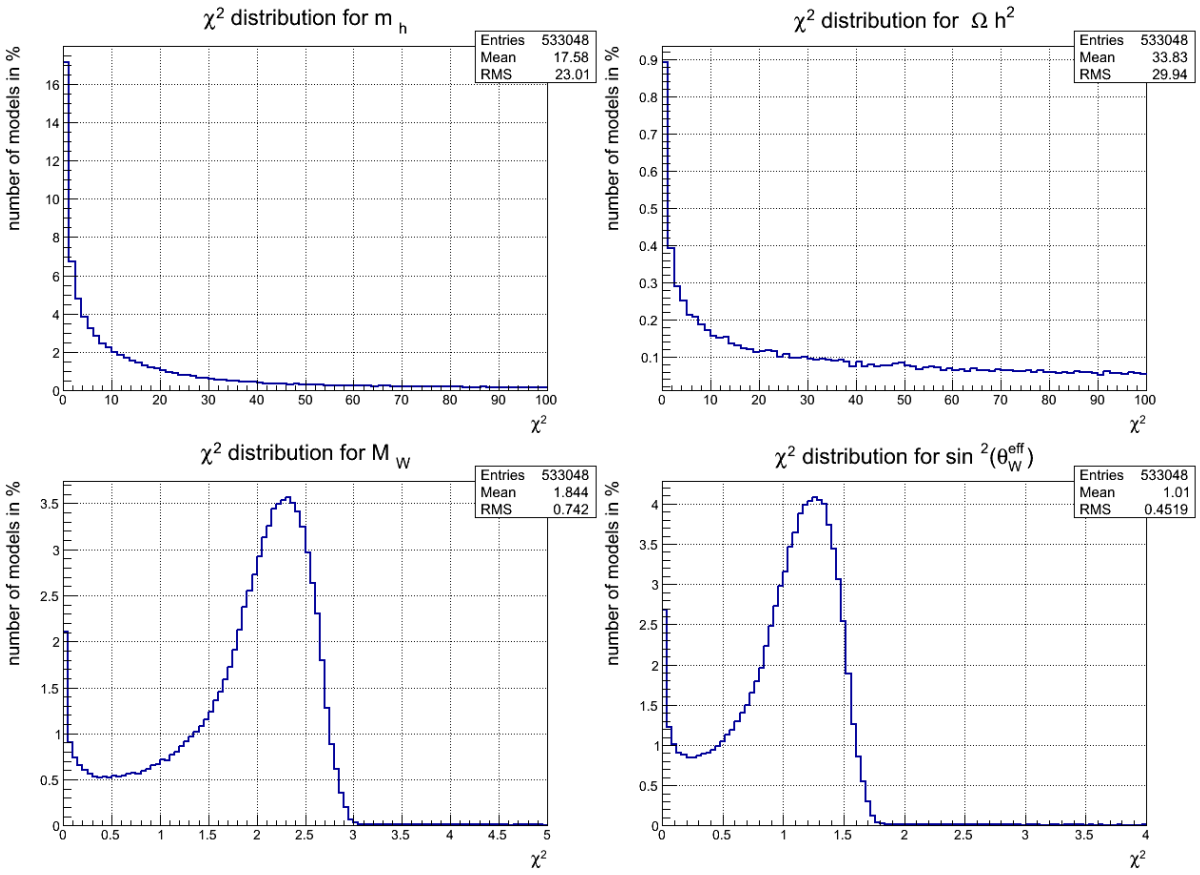

Figure A.27: χ^2 distributions for m_h (top left), Ωh^2 (top right), M_W (bottom left) and $\sin^2(\theta_W^{eff})$ (bottom right) in the NUGM scenario. The number of models is normalized to the total number of simulated models.

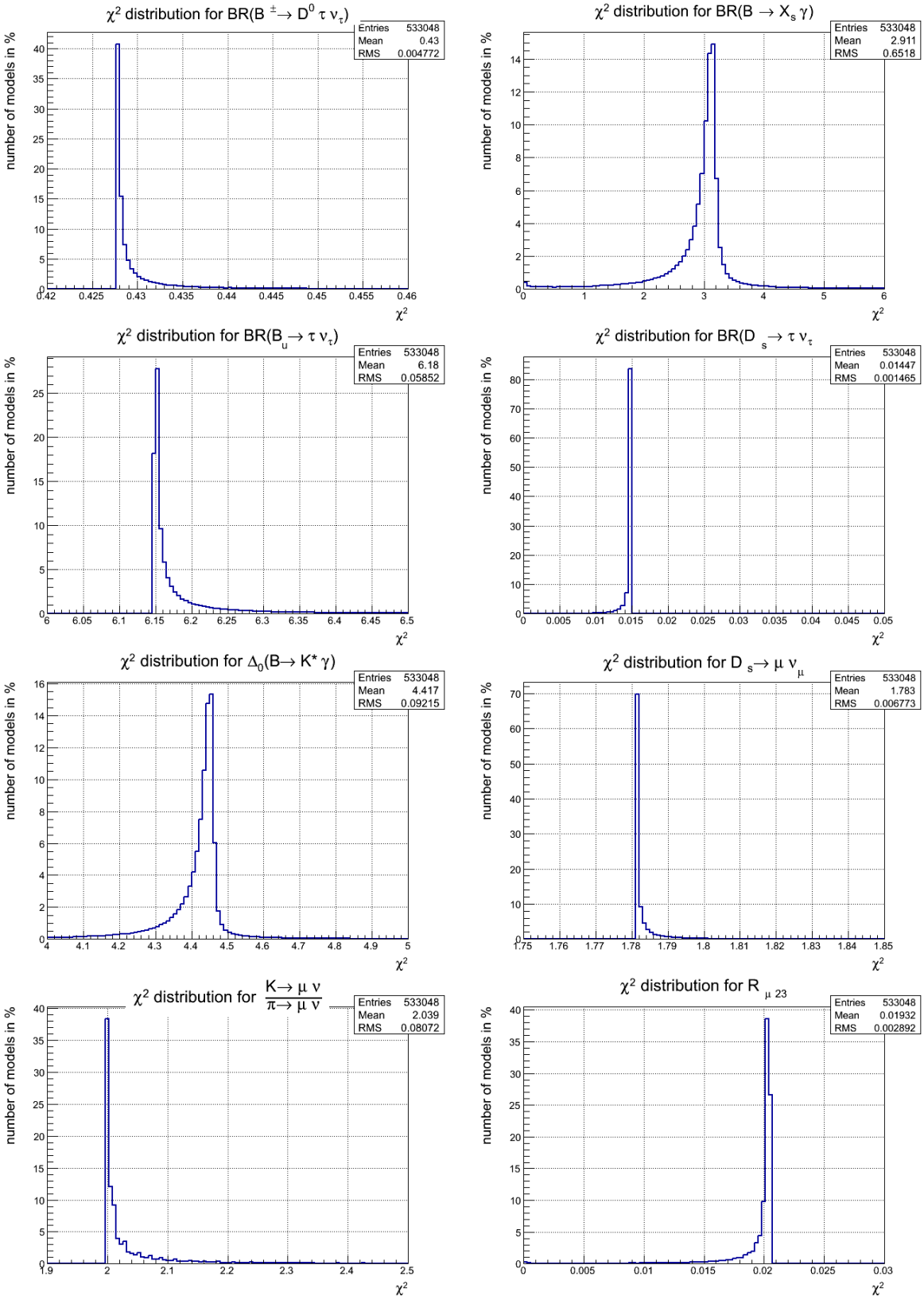

Figure A.28: χ^2 distributions for the flavor observables in the NUGM scenario. The number of models is normalized to the total number of simulated models.

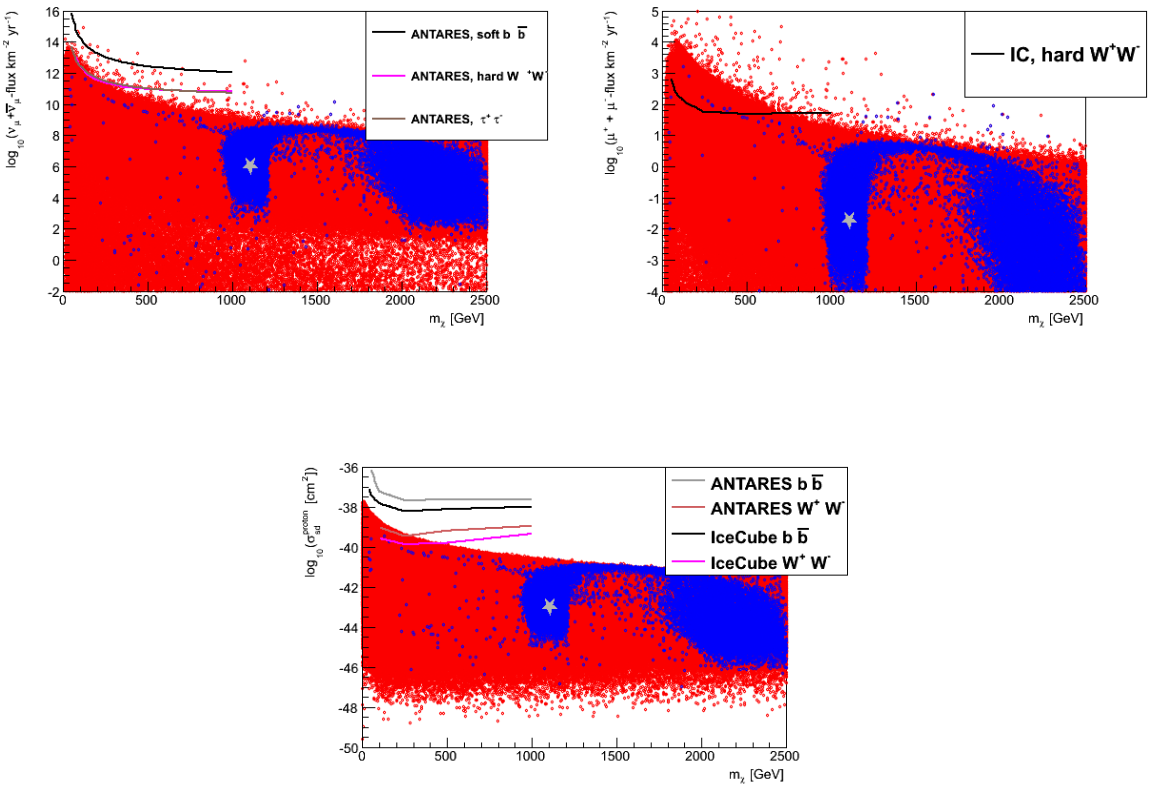

Figure A.29: "Best-fit" model (gray asterisk) of NUGM with respect to indirect dark matter detection observables, $\nu_\mu + \bar{\nu}_\mu$ flux (upper left), $\mu^+ + \mu^{-2}$ flux (upper right) and the spin-dependent WIMP proton cross-section (lower central). Also shown are ANTARES and IceCube limits. Colors: blue: $122 < m_h < 128$ GeV and $0.09 < \Omega h^2 < 0.13$, red: all other models.

A.6 χ^2 Analysis without Flavor Observables

The total χ^2 distributions are shown in Figure A.30 for the cMSSM (top left), NUHM1 (top right), NUHM2 (bottom left) and NUGM (bottom right). Flavor observables were not taken into account. In total, the χ^2 analysis has only four degrees of freedom, that are the measurement of the Higgs-boson mass m_h, the relic density Ωh^2, the mass of the W-boson of the standard model, M_W and the weak mixing angle $\sin(\theta^W_{\text{eff}})$ (used measured values of observables are listed in Table 6.4). The χ^2 distributions of the particular observables, i.e. $\chi^2(m_h)$, $\chi^2(\Omega h^2)$, $\chi^2(M_W)$ and $\chi^2(\sin(\theta^W_{\text{eff}}))$, of course don't change, as they were not fitted but calculated as described in Section 6.6.

cMSSM:
Neglecting flavor observables reduces the minimal χ^2 to $\chi^2_{\text{min}} = 1.92$, including four degrees of freedom. The p-value is 0.75, and predictions are compatible with measurements within 0.32σ for χ^2_{min}. The total χ^2 distribution in the cMSSM scenario is shown in Figure A.30 (top left panel). 0.09% of all simulated models deviate from measurements less than 1σ, 0.32% deviate less than 2σ, 0.6% are compatible within 3σ and 1.4% are compatible within 5σ. The spectrum of input parameters and supersymmetric particle masses is the same, that lead to χ^2_{min} including flavor observables. Thus, also the predicted observables for $\chi^2_{\text{min}}(\text{nDoF} = 4)$ remain unchanged. They are listed in Appendix A.5 (Tables A.1, A.3, A.4 and A.5).

NUHM:
The minimal χ^2 in the NUHM1 scenario (neglecting flavor observables) is given by $\chi^2_{\text{min}} = 3.7 \cdot 10^{-2}$ and a p-value of 99.98%. Thus, for χ^2_{min} the predicted observables deviate less than $2.1 \cdot 10^{-4}\sigma$ from experimental measurements. In total 1.1% of all simulated models are compatible within 1σ, 2.6% within 2σ, 3.8% within 3σ and 6.1% of the simulated models deviate less than 5σ from measurements. The total χ^2 distribution in the NUHM1 scenario is shown in Figure A.30 (top right panel). The input parameters of NUHM1, that lead to χ^2_{min} are listed in Table A.7. The predicted values of observables in NUHM1 that correspond to χ^2_{min} are listed in Table A.8. Indirect and direct detection observables for the "best-fit" model are presented in Table A.9. The resulting supersymmetric particle spectrum is listed in Table A.10.

The total χ^2 distribution in the NUHM2 scenario is shown in Figure A.30 (lower left panel). The minimal χ^2 value is given by $\chi^2_{\text{min}} = 1.7 \cdot 10^{-2}$ with a p-value of 99.9964%. Thus, the model with χ^2_{min} is compatible with measurements within $4.5 \cdot 10^{-5}\sigma$. In total, 1.3% of the simulated models deviate less than 1σ from measurements. 3% are compatible within 2σ, 4.5% within 3σ and 7% within 5σ. The input parameters of NUHM2, that lead to χ^2_{min} are listed in Table A.7. The predicted values in NUHM2 of the observables that correspond to χ^2_{min} are listed in Table A.8. Indirect and direct detection observables for the "best-fit" model are presented in Table A.9. The resulting supersymmetric particle spectrum is listed in Table A.10.

NUGM:
In the NUGM scenario a minimal χ^2 value of $\chi^2_{\text{min}} = 0.11$ is achieved neglecting flavor observables. The p-value is then given by 0.99. Predictions and experimental measurements in the NUGM scenario for χ^2_{min} are compatible within $1.7 \cdot 10^{-3}\sigma$. 0.22% of all simulated models deviate from measurements less than 1σ, 0.8% less than 2σ, 1.4% are compatible within 3σ and 2.8% of all models are compatible within 5σ. The total χ^2 distribution is shown in Figure A.30 (bottom right panel). Again, the input parameters of the NUGM scenario that lead to χ^2_{min} are listed in Table A.7. The observables are listed in Table A.8. Indirect/direct detection observables are listed in Table A.9 and the supersymmetric particle spectrum is listed in Table A.10.

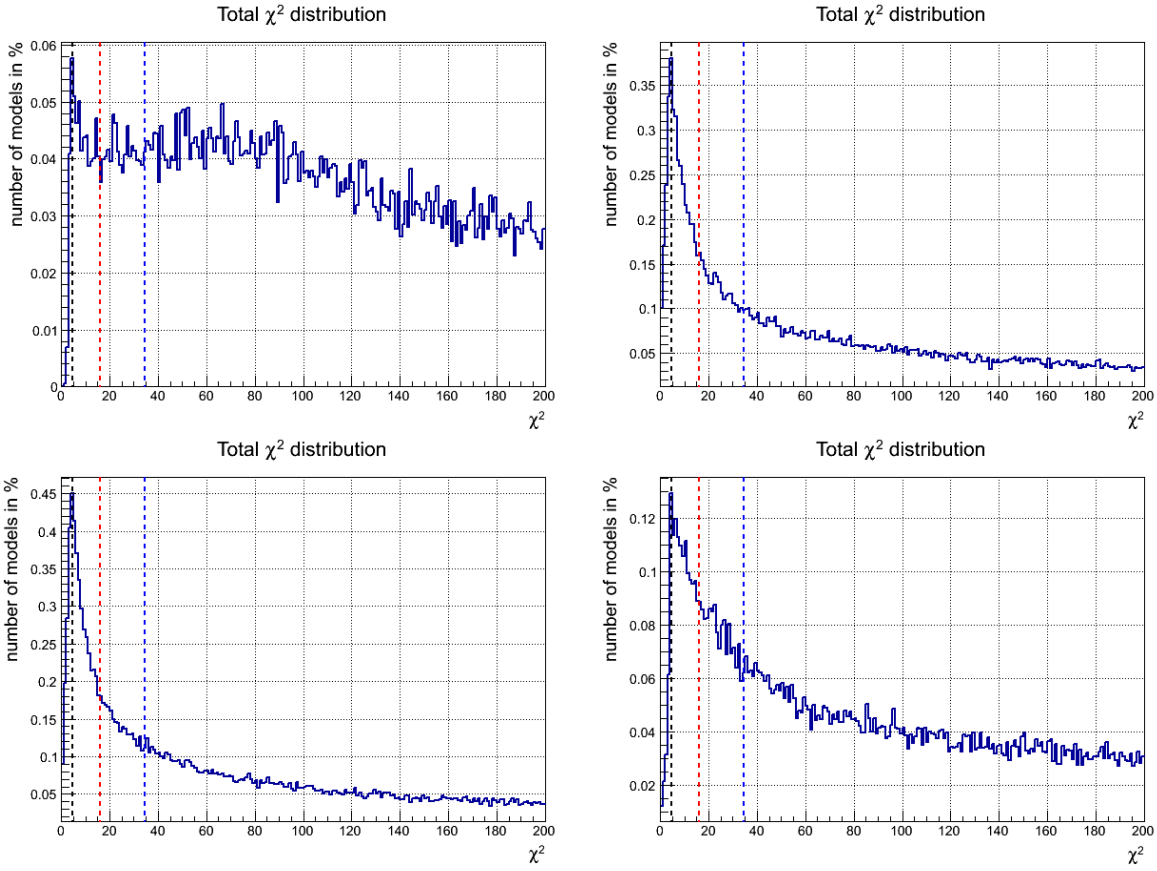

Figure A.30: χ^2 distributions for scenarios cMSSM (top left), NUHM1 (top right), NUHM2 (bottom left) and NUGM (bottom right). Flavor observables are not taken into account. Only observables m_h, Ωh^2, M_W and $\sin(\theta^W_{\text{eff}})$ were used. Colors: Black line: $\chi^2 = 4.72 \mathrel{\hat{=}}$ p-value of 1σ; red line: $\chi^2 = 16.25 \mathrel{\hat{=}}$ p-value of 3σ, blue line: $\chi^2 = 34.57 \mathrel{\hat{=}}$ p-value of 5σ.

The "best-fit" models and χ^2 distributions in different input parameter planes for the scenarios cMSSM, NUGM, NUHM1 and NUHM2 are shown in Figures A.31 - A.39. Also

shown are the regions where experiment and predictions are compatible within nσ, where n=1,3 and 5.

Scenario / probabilities	cMSSM	NUGM	NUHM1	NUHM2
χ^2_{min}	1.92	0.11	$3.7 \cdot 10^{-2}$	$1.7 \cdot 10^{-2}$
p-value	75%	99.86%	99.98%	99.9964%
$n\sigma$	0.32	$1.8 \cdot 10^{-3}$	$2.1 \cdot 10^{-4}$	$4.5 \cdot 10^{-5}$

Table A.6: χ^2, p-value and $n\sigma$ compatibility for the "best-fit" models of the cMSSM, NUGM, NUHM1 and NUHM2 scenario without taking flavor observables into account.

Scenario / Input Params	NUGM	NUHM1	NUHM2
m_0 [GeV]	2019	5446	4719
$m_{1/2}$ [GeV]	2061	2829	2850
A_0 [GeV]	1949	-899	-994
$\tan\beta$	55.2	43.38	44.06
sgn(μ)	+1	+1	+1
δ_{H_u}	–	0.21	0.35
δ_{H_d}	–	0.21	0.34
θ_1 [rad]	1.56	–	–
θ_{24} [rad]	-0.38	–	–
θ_{75} [rad]	-0.15	–	–
θ_{200} [rad]	1.25	–	–

Table A.7: Scenario dependend input parameters for the "best-fit" models without taking flavor observables into account.

Scenario / χ^2(Observable)	NUGM	NUHM1	NUHM2
Ωh^2	0.02	$5.5 \cdot 10^{-3}$	$7.0 \cdot 10^{-3}$
m_h	0.08	$8.9 \cdot 10^{-3}$	$5.4 \cdot 10^{-5}$
M_W	$2.6 \cdot 10^{-3}$	$3.6 \cdot 10^{-3}$	$9.0 \cdot 10^{-3}$
$\sin^2\theta^W_{eff}$	$3.3 \cdot 10^{-2}$	$1.9 \cdot 10^{-2}$	$8.8 \cdot 10^{-4}$

Table A.8: χ^2 values of the individual observables for the "best-fit" model in the investigated scenarios NUGM, NUHM1 and NUHM2 without taking flavor observables into account.

Scenario / ID/DD Observables	NUGM	NUHM1	NUHM2
$\log_{10}(\nu_\mu + \bar{\nu}_\mu$ flux km^{-2}yr$^{-1})$	5.70	7.58	7.56
$\log_{10}(\mu^+ + \mu^-$ flux km^{-2}yr$^{-1})$	-1.98	-0.19	-0.21
$\log_{10}(\sigma^{\text{proton}}_{\text{SD}}$ [cm^2])	-43.45	-41.84	-41.87
$\log_{10}(\sigma^{\text{nucleon}}_{\text{SI}}$ [cm^2])	-45.57	-44.71	-44.73

Table A.9: Predicted indirect and direct detection observables for the "best-fit" models of NUGM, NUHM1 and NUHM2 without taking flavor observables into account.

Scenario / SUSY Mass Spectrum [GeV]		NUGM	NUHM1	NUHM2
h	(light Higgs boson)	125.1	125.4	125.3
H	(heavy Higgs boson)	2168.5	3707.8	3325.8
A	(pseudoscalar Higgs boson)	2168.5	3707.8	3325.8
$H^{\pm}$	(charged Higgs boson)	2170.2	3708.8	3326.8
$\tilde{d}_L$	(down-squark)	6970.4	7411.7	6949
$\tilde{d}_R$		7073.7	7253.3	6773
$\tilde{u}_L$	(up-squark)	6970	7411.3	6948.5
$\tilde{u}_R$		7930.8	7270.8	6793.1
$\tilde{s}_L$	(strange-squark)	6970.4	7411.7	6949
$\tilde{s}_R$		7073.7	7253.3	6773
$\tilde{c}_L$	(charm-squark)	6970	7411.3	6948.5
$\tilde{c}_R$		7930.8	7270.8	6793.1
$\tilde{b}_1$	(bottom-squark)	5957.4	6010	5661
$\tilde{b}_2$		6352.5	6300	5869.8
$\tilde{t}_1$	(top-squark)	5924.8	5173.3	4874
$\tilde{t}_2$		6748	5984.4	5635.1
$\tilde{e}_L$	(electron-slepton)	4027.8	5712.5	5037
$\tilde{e}_R$		6611	5531.6	4821.7
$\tilde{\nu}_{eL}$	(electron-sneutrino)	4027.1	5712	5036.4
$\tilde{\mu}_L$	(muon-slepton)	4027.8	5712.5	5037
$\tilde{\mu}_R$		6611	5531.6	4821.7
$\tilde{\nu}_{\mu L}$	(muon-sneutrino)	4027.1	5712	5036.4
$\tilde{\tau}_1$	(tau-slepton)	3219.3	4441.3	3773.8
$\tilde{\tau}_2$		5673.6	5219.7	4573.1
$\tilde{\nu}_{\tau L}$	(tau-sneutrino)	3219.1	5219.1	4572.3
$\tilde{g}$	(gluino)	7735.6	6043.2	6031.8
χ_1^0	(neutralino)	2106.5	1062.7	1057
χ_2^0		-3243.2	-1071	-1065
χ_3^0		3245.1	1287	1292.9
χ_4^0		7909.4	2385.5	2394.7
$\chi_1^{\pm}$	(chargino)	2106.5	1068.25	1062.3
$\chi_2^{\pm}$		3245.8	2385.5	2394.7
W	(W-boson)	80.5	80.5	80.5

Table A.10: Supersymmetric mass spectra for the "best-fit" models of the NUGM, NUHM1 and NUHM2. Indices L and R label left and right handed sparticles (no sfermion mixing for 1st/2nd generation), indices 1,2 label mass eigenstates (squark and slepton mixing only in 3rd generation). Flavor observables were not taken into account.

cMSSM: χ^2 distributions and compatibility regions in the parameter space

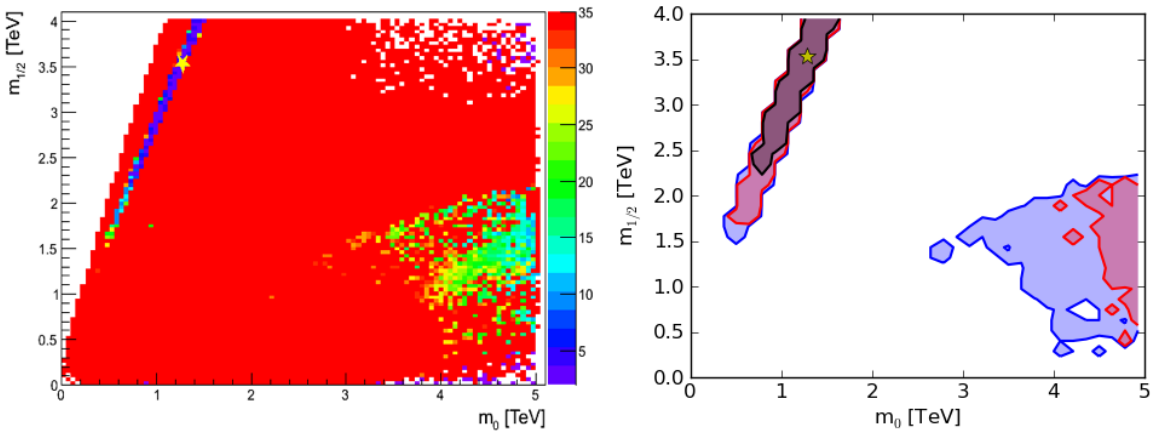

Figure A.31: The χ^2 values of the simulated models (color code, red colored models have $\chi^2 \geq 35$) in the cMSSM scenario in the m_0-$m_{1/2}$ plane (left) and models compatible within 1σ (black contour), 3σ (red contour) and 5σ (blue contour) (right). Flavor observables were neglected. Yellow asterisks represent the "best-fit" model. Models outside the blue contour deviate from measurements more than 5σ and are not shown here.

NUHM: χ^2 distributions and compatibility regions in the parameter space

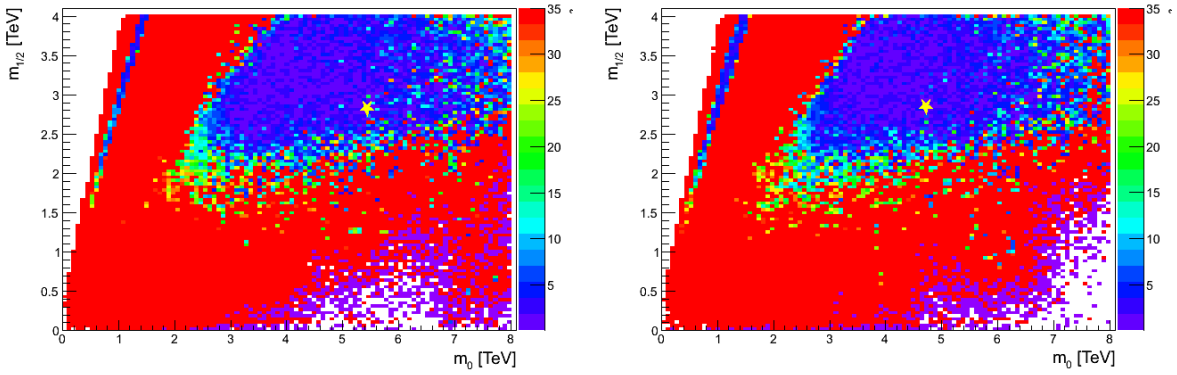

Figure A.32: χ^2 values of the individual models are color coded in the m_0-$m_{1/2}$ for NUHM1 (left) and NUHM2 (right). Red colored models have $\chi^2 \geq 35$. Flavor observables were neglected. Yellow asterisks correspond to the "best-fit" models.

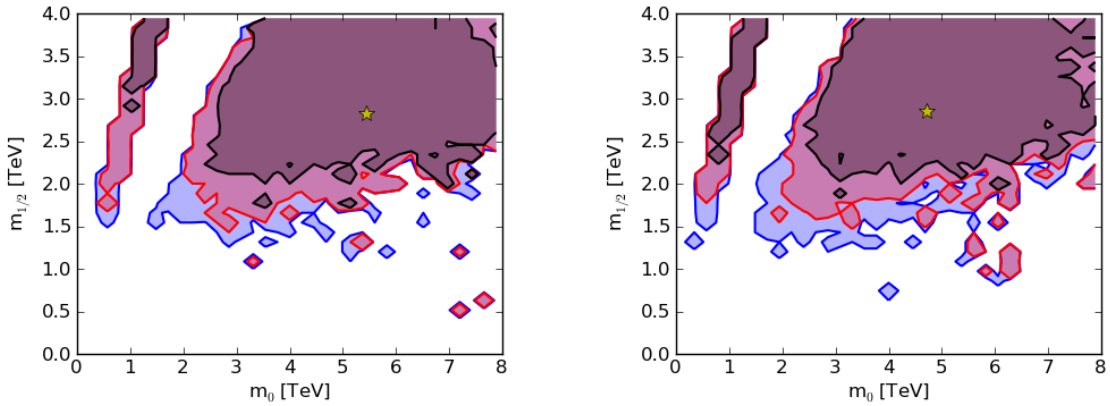

Figure A.33: Map of compatibility regions in the m_0-$m_{1/2}$ for NUHM1 (left) and NUHM2 (right). Flavor observables were neglected. Black contour: compatible within 1σ; red contour: compatible within 3σ; blue contour: compatible within 5σ. Yellow asterisks correspond to the "best-fit" models. Models outside the blue contour deviate from measurements more than 5σ and are not shown here.

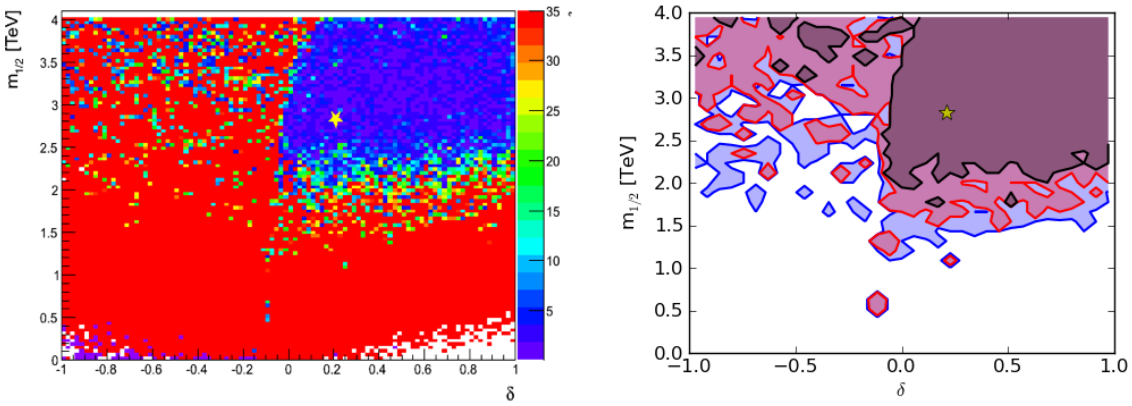

Figure A.34: χ^2 distribution (left) and compatibility regions within 1σ, 3σ and 5σ (right) in the δ-$m_{1/2}$ plane of NUHM1. χ^2 values are color coded on the left hand side, whereat red colored models have $\chi^2 \geq 35$. The black contour on the right hand side corresponds to a deviation within 1σ, the red contour corresponds to a deviation less than 3σ, the blue contour corresponds to a deviation within 5σ from experimental measurements. Yellow asterisks correspond to the "best-fit" model. Models outside the blue contour deviate from measurements more than 5σ and are not shown here.

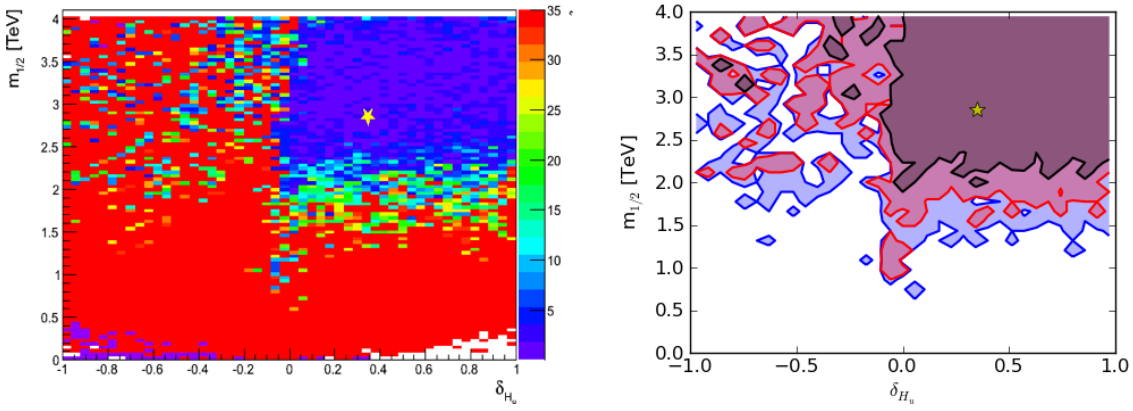

Figure A.35: χ^2 distribution (left) and compatibility regions within 1σ, 3σ and 5σ (right) in the δ_{H_u}-$m_{1/2}$ plane of NUHM2 neglecting flavor observables. χ^2 values are color coded on the left hand side, whereat models in red have $\chi^2 \geq 35$. The black contour on the right hand side corresponds to a deviation less than 1σ, the red contour to a deviation within 3σ and the blue contour corresponds to a deviation within 5σ from experimental measurements. Yellow asterisks correspond to the "best-fit" model. Models outside the blue contour deviate from measurements more than 5σ and are not shown here.

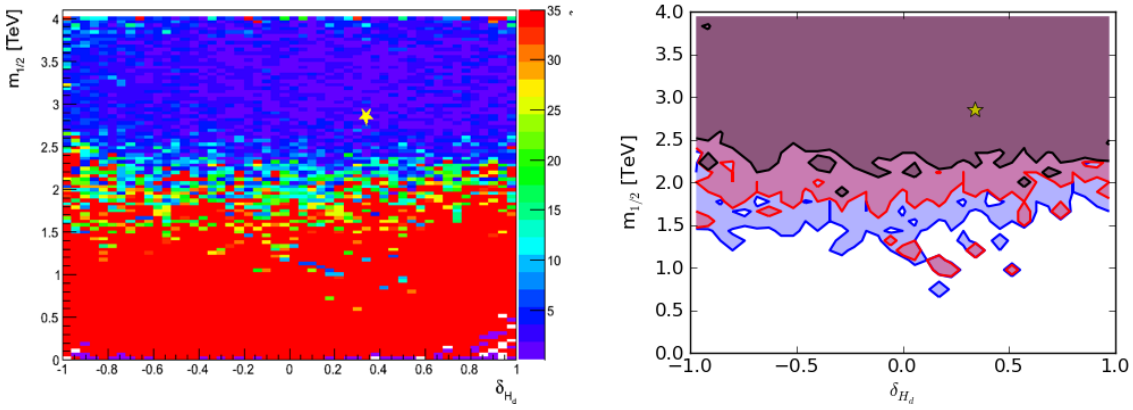

Figure A.36: χ^2 distribution (left) and compatibility regions within 1σ, 3σ and 5σ (right) in the δ_{H_d}-$m_{1/2}$ plane of NUHM2 neglecting flavor observables. χ^2 values are color coded on the left hand side, whereat models in red have $\chi^2 \geq 35$. The black contour on the right hand side corresponds to a deviation within 1σ, the red contour to a deviation within 3σ and the blue contour corresponds to a deviation less than 5σ from experimental measurements. Yellow asterisks correspond to the "best-fit" model. Models outside the blue contour deviate from measurements more than 5σ and are not shown here.

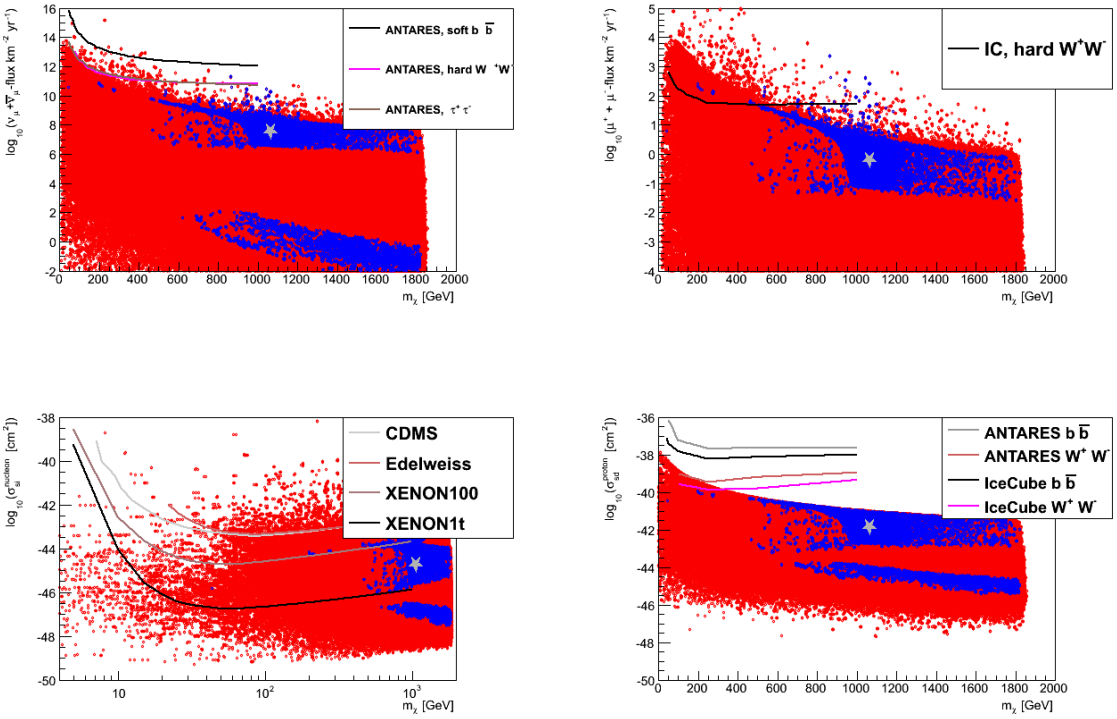

Figure A.37: "Best-fit" model (gray asterisk) of NUHM1 with respect to indirect dark matter detection observables, $\nu_\mu + \bar{\nu}_\mu$-flux (top left), $\mu^+ + \mu^-$-flux (top right), the spin-independent WIMP nucleon cross-section (bottom left) and the spin-dependent WIMP proton cross-section (bottom right). Also shown are ANTARES, IceCube, XENON, EDELWEISS and CDMS limits. Flavor observables were neglected. Colors: blue: $122 < m_h < 128$ GeV and $0.09 < \Omega h^2 < 0.13$, red: all other models.

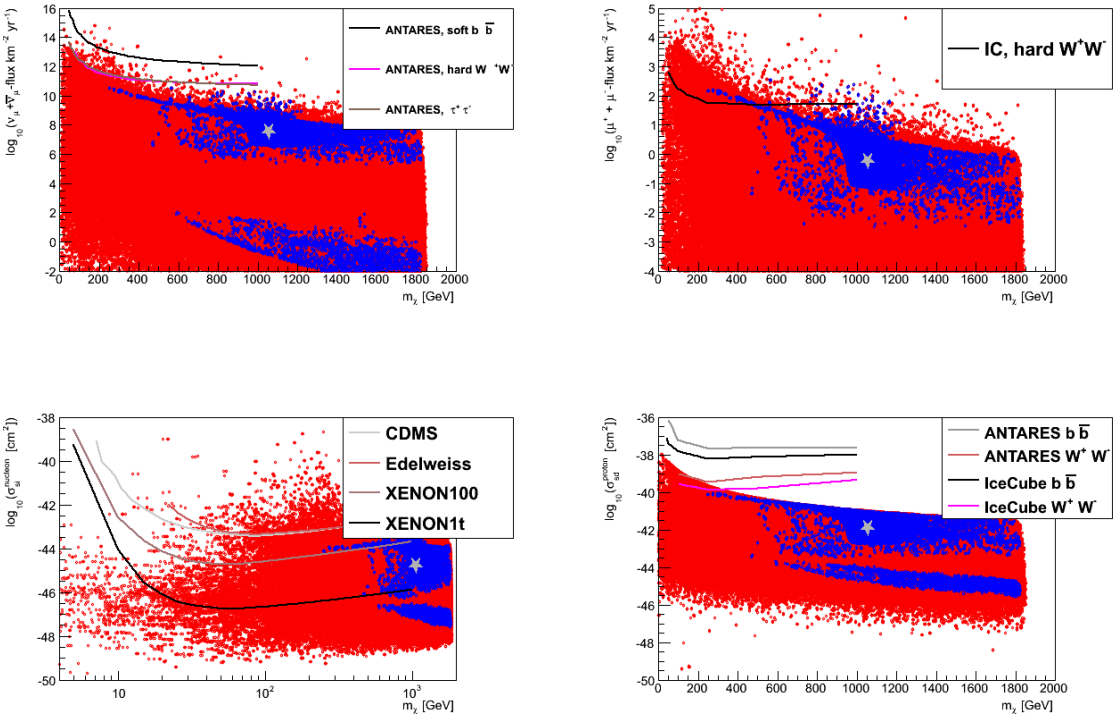

Figure A.38: "Best-fit" model (gray asterisk) of NUHM2 with respect to indirect dark matter detection observables, $\nu_\mu + \bar{\nu}_\mu$-flux (top left), $\mu^+ + \mu^-$-flux (top right), the spin-independent WIMP nucleon cross-section (bottom left) and the spin-dependent WIMP proton cross-section (bottom right). Also shown are ANTARES, IceCube, XENON, EDELWEISS and CDMS limits. Flavor observables were neglected. Colors: blue: $122 < m_h < 128$ GeV and $0.09 < \Omega h^2 < 0.13$, red: all other models.

NUGM: χ^2 distributions and compatibility regions in the parameter space

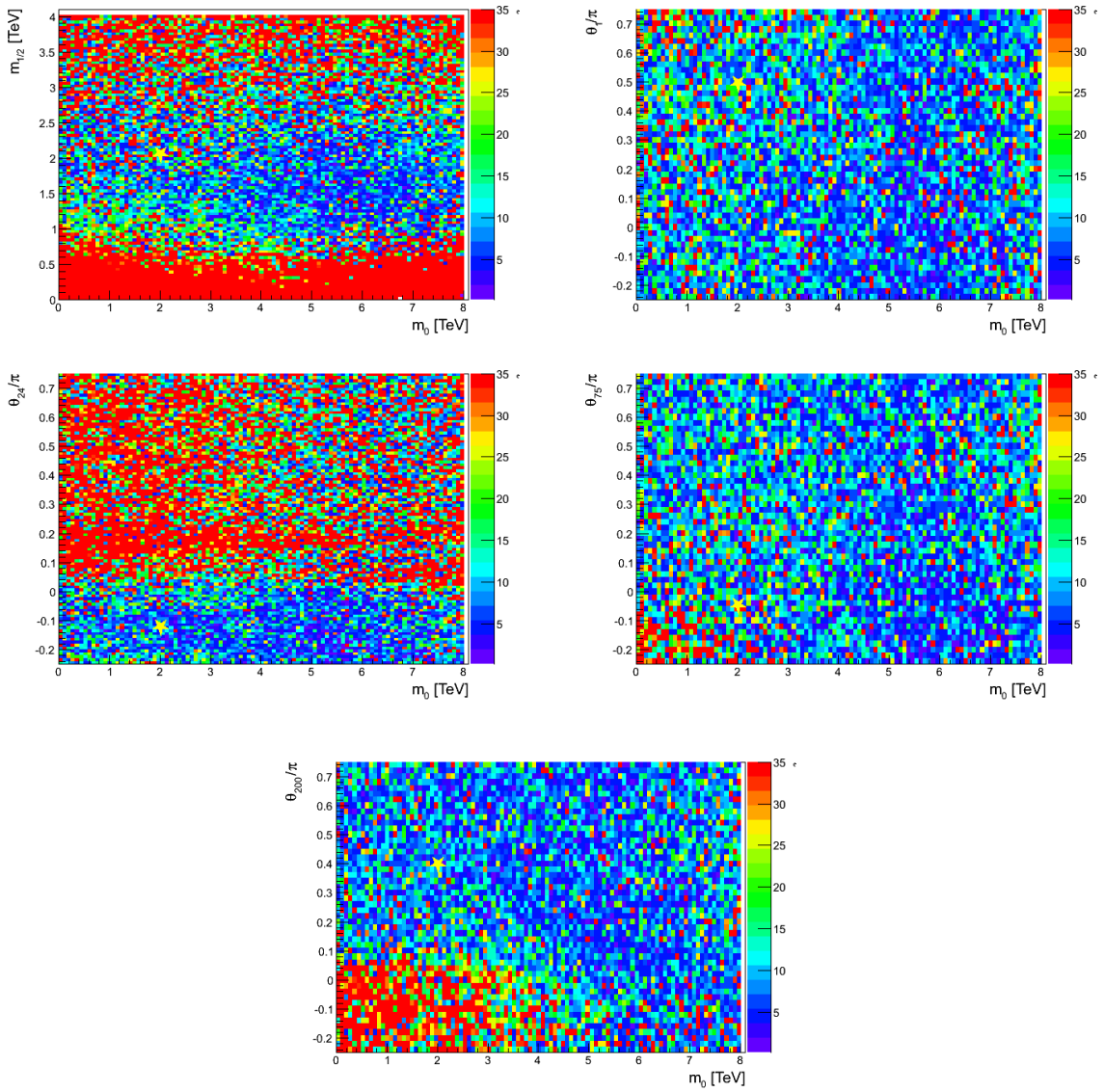

Figure A.39: χ^2 distribution in the m_0-$m_{1/2}$ plane (top left), m_0-θ_1 plane (top right), m_0-θ_{24} plane (middle left), m_0-θ_{75} plane (middle right) and m_0-θ_{200} plane (bottom central). χ^2 values are color coded. Models colored in red have $\chi^2_{\text{total}} > 35$, and are excluded. Flavor observables were neglected. Yellow asterisks represent the "best-fit" model.

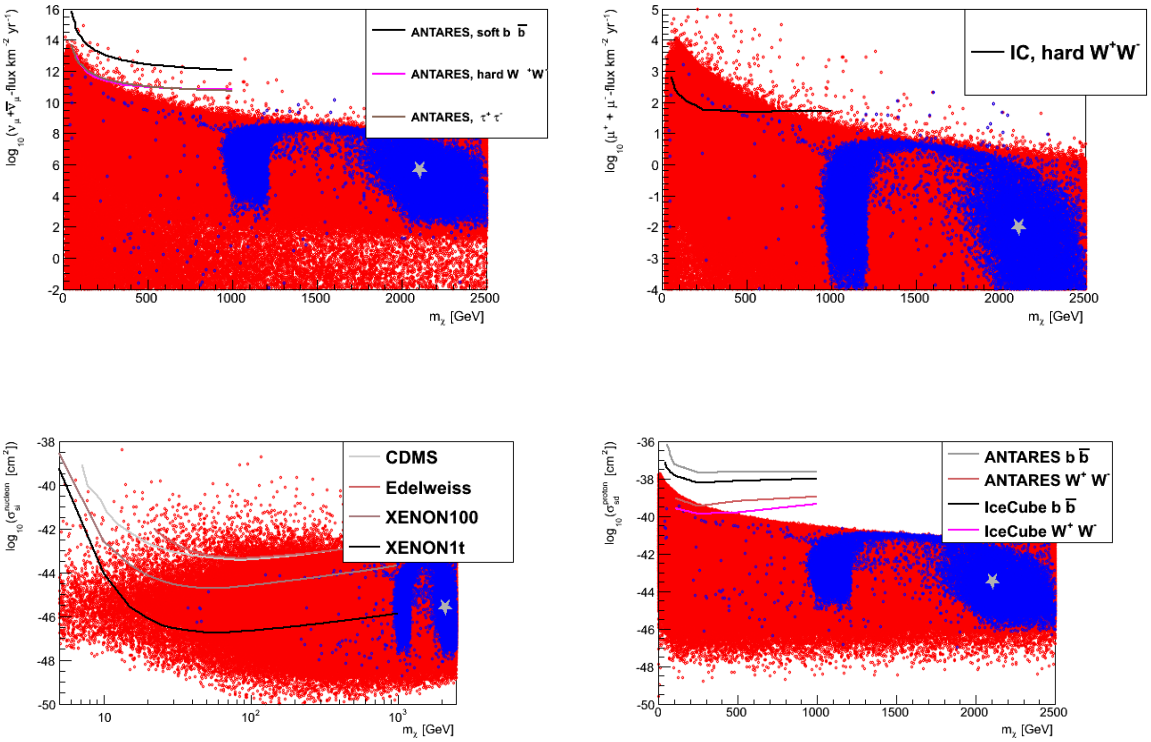

Figure A.40: "Best-fit" model (gray asterisk) of NUGM with respect to indirect dark matter detection observables, $\nu_\mu + \bar{\nu}_\mu$ flux (upper left), $\mu^+ + \mu^{-2}$ flux (upper right), the spin-independent WIMP nucleon cross-section (lower left) and the spin-dependent WIMP proton cross-section (lower right). Also shown are ANTARES, IceCube, XENON, EDELWEISS and CDMS limits. Flavor observables were neglected. Colors: blue: $122 < m_h < 128$ GeV and $0.09 < \Omega h^2 < 0.13$, red: all other models.

A.7 Experimentally Favoured Regions Neglecting Flavor Observables

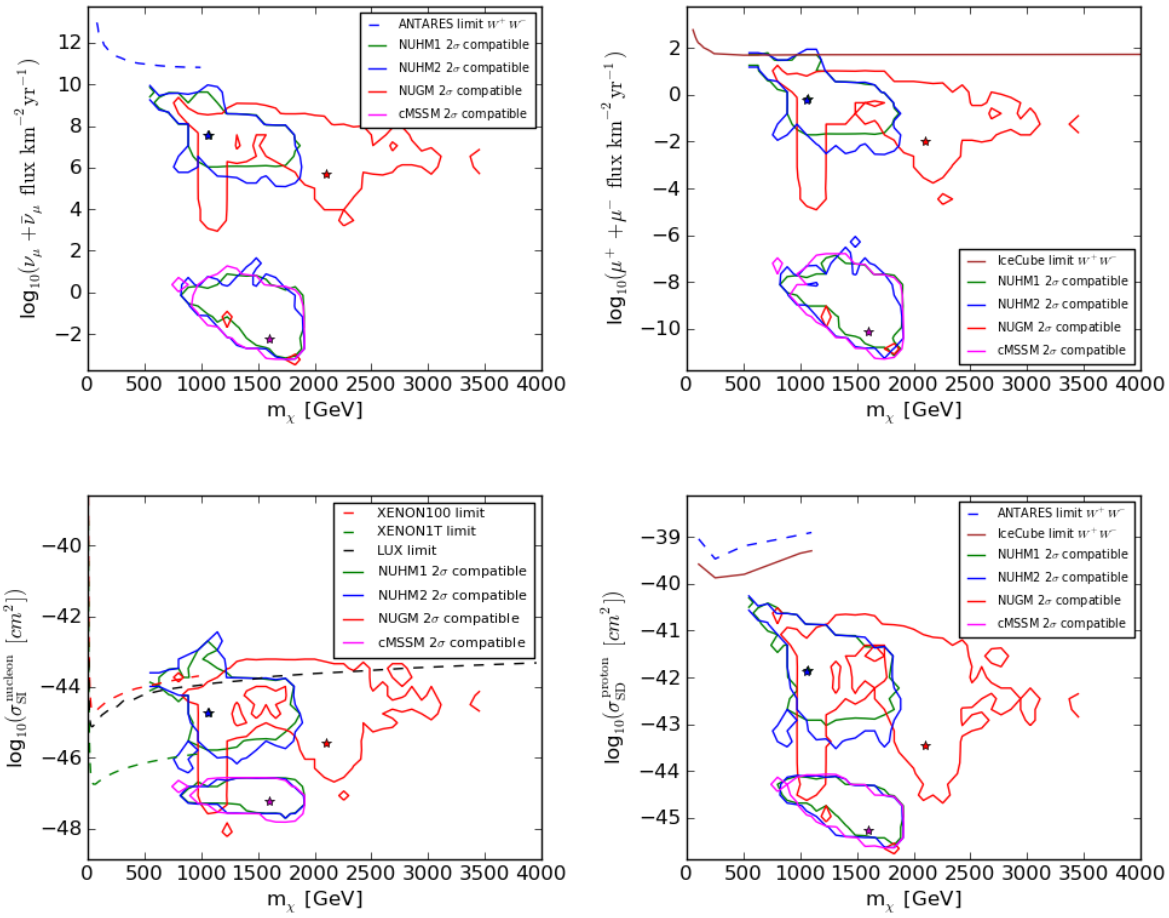

Figure A.41: Experimentally favoured regions (compatible with measurements within 2σ) for the $\nu_\mu + \bar{\nu}_\mu$-flux (top left), the $\mu^+ + \mu^-$-flux (top right), $\sigma_{\mathrm{SI}}^{\mathrm{nucleon}}$ (bottom left) and $\sigma_{\mathrm{SD}}^{\mathrm{proton}}$ (bottom right). Flavor observables were neglected. Also shown are the ANTARES (muon neutrino flux and $\sigma_{\mathrm{SD}}^{\mathrm{proton}}$) and IceCube limits (muon flux and $\sigma_{\mathrm{SD}}^{\mathrm{proton}}$) for annihilation channel W^+W^- and the XENON100 limit, the LUX limit, and expected XENON1T sensitivity for $\sigma_{\mathrm{SI}}^{\mathrm{nucleon}}$. Colors correspond to a 2σ compatibility region of the corresponding scenario (green: NUHM1, blue: NUHM2, red: NUGM, magenta: cMSSM). Asterisks represent the "best-fit" models of the corresponding scenario, (green: NUHM1, blue: NUHM2, red: NUGM, magenta: cMSSM).

A.8 Plots and Tables for NUHM Scenarios with Reduced Parameter Spaces

For a better comparability of results from the χ^2 analysis of the cMSSM and NUHM scenarios, NUHM1 and NUHM2 scenarios were also investigated for the following boundaries (same boundaries for m_0 as for the cMSSM scenario):

$$\begin{aligned} m_0 &\in [0, 5] \text{ TeV}, \\ m_{1/2} &\in [0, 4] \text{ TeV}, \\ A_0 &\in [-3, 3] \text{ TeV}, \\ \delta_{H_u} &\in [-1, 1], \\ \delta_{H_d} &\in [-1, 1], \\ \tan\beta &\in [2, 60], \\ \text{sgn}(\mu) &= +1. \end{aligned} \tag{A.1}$$

The total χ^2 distributions of NUHM1 and NUHM2 are shown in Figure A.42. Even with the reduced parameter range for m_0, the χ^2 distributions decrease much faster than in the cMSSM. This truly indicates a significant better agreement between predictions and experimental measurements of observables listed in Table 6.4.

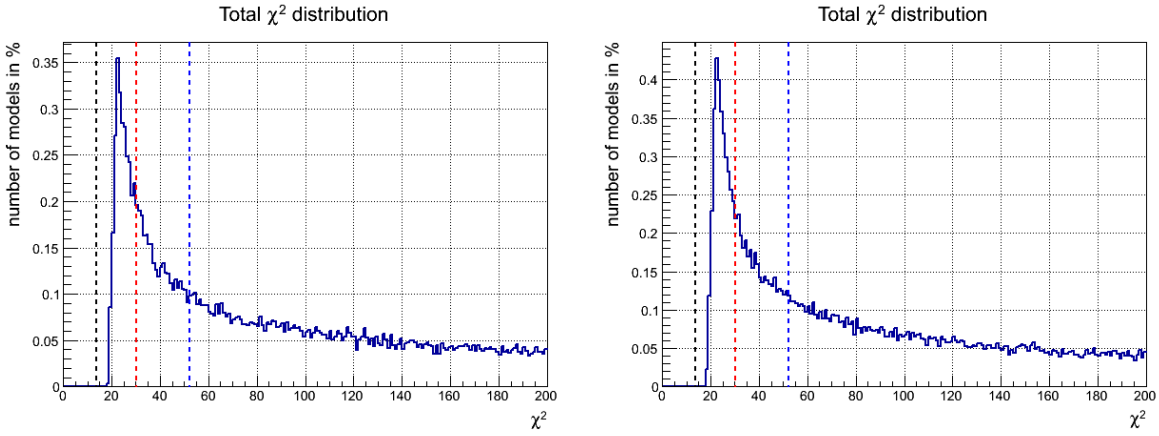

Figure A.42: χ^2 distributions in the NUHM1 (left) and NUHM2 scenario (right) normalized to the total number of simulated models. Parameter intervals for m_0 were reduced to the same intervals, that were used in the cMSSM. Black line: $\chi^2 = 13.8 \mathrel{\hat{=}}$ p-value of 1σ; red line: $\chi^2 = 30.1 \mathrel{\hat{=}}$ p-value of 3σ, blue line: $\chi^2 = 52.2 \mathrel{\hat{=}}$ p-value of 5σ.

In total, 2.7% of all simulated models in NUHM1 agree with measurements of Table 6.4 within 3σ and 5.7% are compatible within 5σ. The "best-fit" model in NUHM1 has a χ^2 value of 18.9 (compared to 18.8 for a larger interval for m_0.) and a p-value of 0.091. For NUHM2, 3.4% of all models deviate less than 3σ, whereas 6.8% deviate less than 5σ. These values are only slightly smaller, than values obtained for $m_0 \in [0, 8]$ TeV. The "best-fit"

model in NUHM1 has a χ^2 value of 18.4 (equal to χ^2_{min} for a larger interval for m_0.) and a p-value of 0.10. Consequently, predictions of the NUHM1 "best-fit" model are compatible with measurements within 1.69σ. Predictions in the NUHM2 "best-fit" model agree within 1.64σ.

Summary tables:
The obtained χ^2 values of the "best-fit" models for both scenarios agree within the per mill level with those obtained for larger parameter spaces. The minimal χ^2_{min}, the corresponding p-value and the $n\sigma$ compatibility with respect to the used observables from Table 6.4 are listed in Table A.11 for NUHM1 and NUHM2. For a better comparison, cMSSM values are also listed.

Scenario / probabilities	cMSSM	NUHM1	NUHM2
χ^2_{min}	20.3	18.9	18.4
p-value	0.062	0.091	0.10
$n\sigma$	1.87	1.69	1.64

Table A.11: χ^2, p-value and $n\sigma$ compatibility for the "best-fit" models of the cMSSM, NUHM1 and NUHM2 scenario. The boundary for m_0 was reduced to $0 < m_0 < 5$ TeV for scenarios NUHM1 and NUHM2.

As a consequence of smaller values of m_0, which were allowed, the set of input parameters, achieving the "best-fit" models, changes. Those parameters are listed in Table A.12.

Scenario / Input Params	NUHM1	NUHM2
m_0 [GeV]	4386	4561
$m_{1/2}$ [GeV]	3585	3509
A_0 [GeV]	2094	777
$\tan\beta$	46.1	44.5
$\text{sgn}(\mu)$	+1	+1
δ_{H_u}	0.51	0.53
δ_{H_d}	–	-0.13

Table A.12: Scenario dependent input parameters for the "best-fit" models.

Indirect and direct dark matter search observables have slightly smaller values. They are listed in Table A.13.

Scenario / ID/DD Observables	NUHM1	NUHM2
$\log_{10}(\nu_\mu + \bar{\nu}_\mu$ flux km^{-2}yr$^{-1})$	6.92	7.11
$\log_{10}(\mu^+ + \mu^-$ flux km^{-2}yr$^{-1})$	-0.83	-0.69
$\log_{10}(\sigma_{\text{SD}}^{\text{proton}}$ [cm^2])	-42.44	-42.39
$\log_{10}(\sigma_{\text{SI}}^{\text{nucleon}}$ [cm^2])	-45.28	-45.12

Table A.13: Predicted indirect and direct detection observables for the "best-fit" models in NUHM1 and NUHM2 for reduced parameter spaces.

The SUSY mass spectra for the "best-fit" models of NUHM1 and NUHM2 are listed in Table A.14

Parameter space plots:
For the sake of completeness, χ^2 distributions and compatibility regions in the parameter space planes of NUHM1 and NUHM2 are shown in this paragraph. Quantitatively and qualitatively, the same behavior for NUHM scenarios with a reduced interval of $0 < m_0 < 5$ TeV was found, compared to the case with $0 < m_0 < 8$ TeV (apart from the position of the "best-fit" models). Still, the position of the "best-fit" model is determined by the compatibility of predictions and measurements for the Higgs-boson mass and the neutralino relic density. Large χ^2 values are driven by the scenario's disability to describe flavor observables, agreeing sufficiently with their measurements.

The χ^2 distributions and compatibility regions are shown in Figure A.43 for NUHM1 (left hand side) and NUHM2 (right hand side). In Figure A.44, the δ-$m_{1/2}$-plane of NUHM1 is shown, for the χ^2 distribution (left) and compatibility regions (right). Last but not least, the $\delta_{H_u}/\delta_{H_d}$-$m_{1/2}$-plane of NUHM2 is shown in Figure A.45/Figure A.46, for the χ^2 distribution and regions compatible with measurements within 3σ and 5σ.

Experimentally favoured regions, translated to regions for indirect and direct detection observables, such as the muon neutrino flux, or spin-independent WIMP nucleon cross-section, have changed insignificantly. Thus, corresponding plots are omitted.

Scenario / SUSY Mass Spectrum [GeV]		NUHM1	NUHM2
h	(light Higgs boson)	125.1	125.38
H	(heavy Higgs boson)	3177	1637
A	(pseudoscalar Higgs boson)	3177	1637
$H^{\pm}$	(charged Higgs boson)	3178	1639
$\tilde{d}_L$	(down-squark)	7728	7716
$\tilde{d}_R$		7470	7462
$\tilde{u}_L$	(up-squark)	7727	7715
$\tilde{u}_R$		7499	7534
$\tilde{s}_L$	(strange-squark)	7728	7715
$\tilde{s}_R$		7470	7462
$\tilde{c}_L$	(charm-squark)	7727	7716
$\tilde{s}_R$		7499	7534
$\tilde{b}_1$	(bottom-squark)	6519	6517
$\tilde{b}_2$		6563	6676
$\tilde{t}_1$	(top-squark)	5744	5668
$\tilde{t}_2$		6494	6489
$\tilde{e}_L$	(electron-slepton)	4924	5091
$\tilde{e}_R$		4567	4656
$\tilde{\nu}_{eL}$	(electron-sneutrino)	4922	5090
$\tilde{\mu}_L$	(muon-slepton)	4924	5091
$\tilde{\mu}_R$		4567	4656
$\tilde{\nu}_{\mu L}$	(muon-sneutrino)	4923	5090
$\tilde{\tau}_1$	(tau-slepton)	3405	3768
$\tilde{\tau}_2$		4434	4713
$\tilde{\nu}_{\tau L}$	(tau-sneutrino)	4433	4712
$\tilde{g}$	(gluino)	7371	7250
χ_1^0	(neutralino)	1077	1098
χ_2^0		-1081	-1103
χ_3^0		1629	1595
χ_4^0		2998	2931
$\chi_1^{\pm}$	(chargino)	1079	1101
$\chi_2^{\pm}$		2998	2931
W	(W-boson)	80.5	80.5

Table A.14: Supersymmetric mass spectra for the "best-fit" models of NUHM1 and NUHM2 for reduced parameter spaces. Indices L and R label left and right handed sparticles (no sfermion mixing for 1st/2nd generation), indices 1,2 label mass eigenstates (squark and slepton mixing only in 3rd generation).

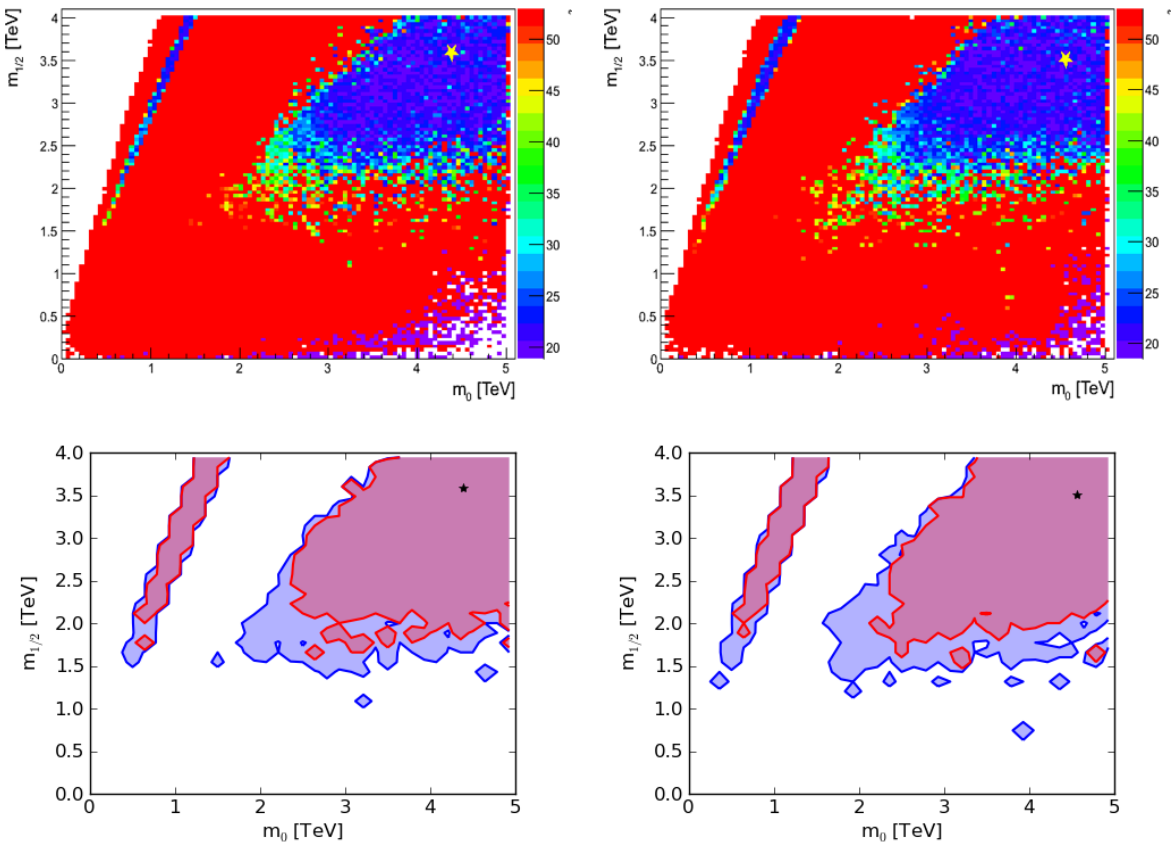

Figure A.43: χ^2 distributions for scenarios NUHM1 (top left) and NUHM2 (top right) in the m_0-$m_{1/2}$-plane. χ^2 values are color coded. Red colored models have $\chi^2 \geq 53$. Also shown are compatibility regions for a deviation less than 3σ (red contour) and less than 5σ (blue contour), for NUHM1 (bottom left) and NUHM2 (bottom right). The yellow (top panels) and black asterisks (bottom panels) correspond to the "best-fit" model. Model predictions outside the blue contour deviate more than 5σ from measurements and are not shown here.

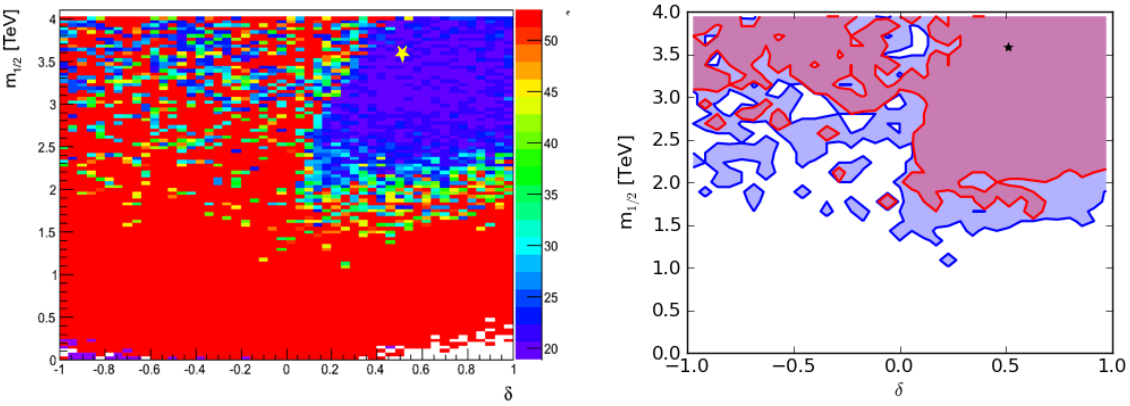

Figure A.44: δ-$m_{1/2}$-plane for the χ^2 distribution of NUHM1 on the left hand side and regions compatible with measurements within 3σ (red contour) and 5σ (blue contour) on the right hand side. χ^2 values are color coded. Red colored models have $\chi^2 \geq 53$. The yellow and black asterisk corresponds to the "best-fit" model. Model predictions outside the blue contour deviate more than 5σ from measurements and are not shown here.

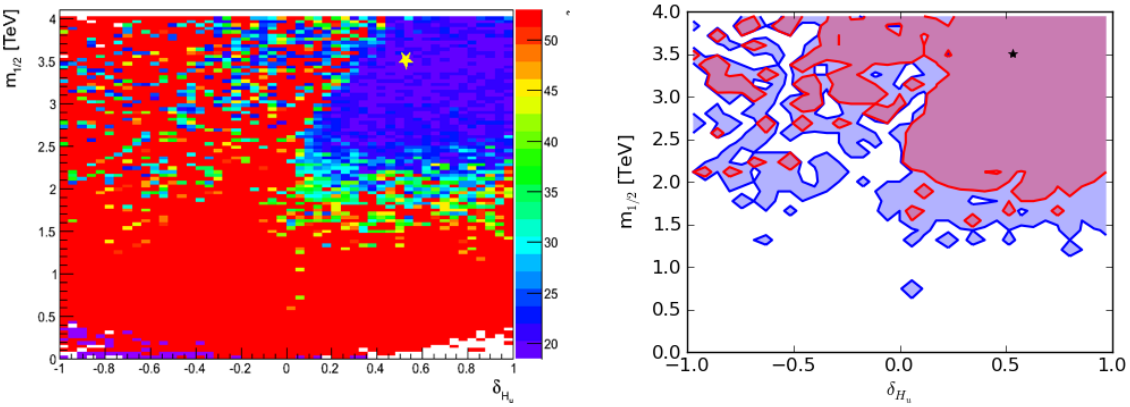

Figure A.45: δ_{H_u}-$m_{1/2}$-plane for χ^2 distribution for NUHM2 on the left hand side and regions compatible with measurements within 3σ (red contour) and 5σ (blue contour) on the right hand side. χ^2 values are color coded. Red colored models have $\chi^2 \geq 53$. The yellow and black asterisk corresponds to the "best-fit" model. Model predictions outside the blue contour deviate more than 5σ from measurements and are not shown here.

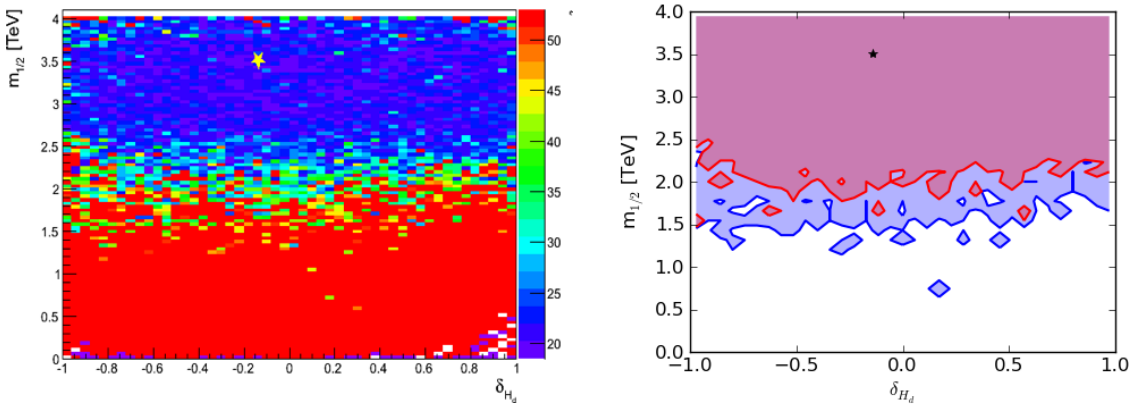

Figure A.46: δ_{H_d}-$m_{1/2}$-plane for χ^2 distribution for NUHM2 on the left hand side and regions compatible with measurements within 3σ (red contour) and 5σ (blue contour) on the right hand side. χ^2 values are color coded. Red colored models have $\chi^2 \geq 53$. The yellow and black asterisk corresponds to the "best-fit" model. Model predictions outside the blue contour deviate more than 5σ from measurements and are not shown here.

Bibliography

[Aslanidis et al. 1999] Aslanidis E et al., ANTARES Collaboration *A deep sea telescope for high energy neutrinos*, 1999 arXiv:astro-ph/9907432

[Adrian-Martinez et al. 2012] Adrian-Martinez S et al., ANTARES Collaboration *The Positioning System of the ANTARES Neutrino Telescope*, 2012 JINST 7 T08002

[Persic et al. 1996] Persic M, Salucci P and Stel F, *The universal rotation curve of spiral galaxies - I. The dark matter connection*, 1996 Mon. Not. R. Astron. Soc. 281, 27-47 (1996)

[Penzias & Wilson 1965] Penzias A A and Wilson R W, *A Measurment of Access Antenna Temperature at 4080 Mc/s.*, 1965 ApJ, vol. 142, p. 419-421

[Bertone et al. 2005] Bertone G, Hooper D and Silk J, *Particle dark matter: evidence, candidates and constraints*, 2005 Phys. Rep. 405 (2005) 279

[Challinor 2006] Challinor A, *The cosmic microwave background: a theorists perspective*, 2006 Cosmology, Galaxy Formation and Astroparticle Physics on the pathway to the SKA

[Hinshaw et al. 2012] Hinshaw G et al., *Nine-Year Wilkinson Microwave Anisotropy Probe (WMAP) Observations: Cosmological Parameter Results*, 2012 arXiv:1212.5226 [astro-ph.CO]

[The CMS Collaboration 2013] The CMS Collaboration, *Observation of a new boson with mass near 125 GeV in pp collisions at sqrt(s) = 7 and 8 TeV*, 2013 arXiv:1303.4571v1 [hep-ex]

[The ATLAS Collaboration 2012a] The ATLAS Collaboration, *Observation of a New Particle in the Search for the Standard Model Higgs Boson with the ATLAS Detector at the LHC*, 2012 Phys. Lett. B716 (2012) 1-29

[Weinberg 2005] Weinberg S, *The Quantum Theory of Fields Vol. 3 Supersymmetry*, 2005 Cambridge University Press

[Acciari et al. 1998] Acciari M et al., L3 Collaboration, *Measurement of the effective weak mixing angle by jet-charge asymmetry in hadronic decays of the Z boson*, 1998 Phys.Lett. B439 (1998) 225-236

[Farrar & Fayet 1978] Farrar G R and Fayet P, *Phenomenology of the production, decay, and detection of new hadronic states associated with supersymmetry*, 1978 Phys. Lett. B76 (1978) 575

[Nishino et al. 2009] , Nishino H et al. [Super-Kamiokande Collaboration], *Search for Proton Decay via $p \to e^+\pi^0$ and $p \to \mu^+\pi^0$ in a Large Water Cherenkov Detector*, 2009 Phys. Rev. Lett. 102 (2009) 141801

[Djouadi et al. 1999] Djouadi A, Rosiers-Lees S et al., *The Minimal Supersymmetric Standard Models: Group Summary Report*, 1999 arXiv:hep-ph/9901246

[Gunion et al. 1990] Gunion J F, Haber H E, Kane G and Dawson S, *The Higgs Hunters Guide*, 1990 Addison-Wesley (1990)

[Martin 2011] Martin S P, *A Supersymmetry Primer*, 2011 arXiv:hep-ph/9709356v6

[Djouadi et al. 2007] Djouadi A, Kneur J-L and Moultaka G, *SuSpect: a Fortran Code for the Supersymmetric and Higgs Particle Spectrum in the MSSM*, Comput. Phys. Commun. 176 (2007) 426 [arXiv:hep-ph/0211331]

[Edsjö 1997] Edsjö J, *Aspects of Neutrino Detection of Neutralino Dark Matter*, 1997 arXiv:hep-ph/9704384

[Griest & Seckel 1987] Griest K and Seckel D, *Cosmic asymmetry, neutrinos and the sun*, 1987 Nucl. Phys. B238 (1987) 651

[Gould 1987] Gould A, *Weakly Interacting Massive Particle Distribution in and Evaporation from the Sun*, 1987 Astrophys. J. 321 (1987) 560

[Gould 1991] Gould A, *Cosmological Density of WIMPS from Solar and Terrestrial Annihilations*, 1991 Astrophys. J. IASSNS-AST-91-34

[Saab 2012] Saab T, *An Introduction to Dark Matter Direct Detection Searches and Techniques*, 2012 arXiv:1203.2566 [physics.ins-det]

[Armengaud 2010] Armengaud E, *Gif Lectures on direct detection of Dark Matter*, 2010 arXiv:1003.2380 [hep-ex]

[Jungmann et al. 1996] Jungman G, Kamionkowski M and Griest K *Supersymmetric Dark Matter*, 1996 Phys. Rept. 267 (1996) 195-373

[Ahmed et al. 2010] Ahmed Z et al., CDMS Collaboration, *Dark Matter Search Results from the CDMS II Experiment*, 2010 Science 327 (2010) 1619-1621

[Armengaud et al. 2011] Armengaud E et al., EDELWEISS Collaboration, *Final results of the EDELWEISSII-WIMP search using a 4-kg array cryogenic germanium detectors with interleaved electrodes*, 2011 Physics Letters B 702 (2011) 329-335

[April et al. 2012a] April E et al., XENON 100 Collaboration, *Dark Matter Results from 225 Live Days of XENON100 Data*, 2012 arxiv:1207.5988 [astro-ph.CO]

[April et al. 2012b] April E et al., XENON 1T Collaboration, *The XENON 1T Dark Matter Search Experiment*, 2012 arxiv:1206.6288 [astro-ph.IM]

[Adrian-Martinez et al. 2012] Adrian-Martinez S et al., ANTARES Collaboration, *First Search for Dark Matter Annihilation in the Sun Using the ANTARES Neutrino Telescope*, 2012 arXiv:1302.6516 [astro-ph.HE]

[Aartsen et al. 2013] Aartsen M G et al., IceCube Collaboration, *Search for dark matter annihilations in the Sun with the 79-string IceCube detector*, 2013 Phys. Rev. Lett. 110, 131302 (2013)

[Boliev et al. 2013] Boliev M M et al., Baksan Collaboration, *Search for muon signal from dark matter annihilations in the Sun with the Baksan Underground Scintillator Telescope for 24.12 years*, 2013 arXiv:1301.1138 [astro-ph.HE]

[Behnke et al. 2012] Behnke E et al., COUPP Collaboration, *First dark matter search results from a 4-kg CF3I bubble chamber operated in a deep underground site*, 2012 Phys. Rev. D 86 (2012) 052001

[Felizardo et al. 2012] Felizardo M et al., SIMPLE Collaboration, *Final Analysis and Results of the Phase II SIMPLE Dark Matter Search*, Phys. Rev. Lett. 108 (2012) 201302

[Wikström & Edsjö 2009] Wikström G, Edsjö J, *Limits on the WIMP-nucleon scattering cross-section from neutrino telescopes*, JCAP 0904:009,2009

[The IceCube Collaboration 2011] IceCube Collaboration, *The IceCube Neutrino Observatory IV: Searches for Dark Matter and Exotic Particles*, 2011 arXiv:1111.2738 [astro-ph.HE]

[The ATLAS Collaboration 2013] The ATLAS Collaboration, *Search for dark matter candidates and large extra dimensions in events with a jet and missing transverse momentum with the ATLAS detector*, 2013 JHEP 1304 (2013) 075, arXiv:1210.4491 [hep-ex]

[Collins et al. 1989] Collins P D B, Martin A D, Squires E J, *Particle Physics and Cosmology*, 1989 Wiley and Sons

[Sanjeev & Weldon 1983] Sanjeev S K and Weldon A H, *Analysis of the Supersymmetry Breaking Induced by N=1 Supergravity Theories*, 1983 Phys. Lett. B 126 (1983) 215

[Kaplunovski & Louis 1993] Kaplunovski V S and Louis J, *Model-independent analysis of soft terms in effective supergravity and in string theory*, 1993 Phys. Lett. B 306 (1993) 269

[Choi et al. 1998] Choi K, Lee J S and Munoz C, *Supergravity Radiative Effects on Soft Terms and the μ Term*, 1998 Phys. Rev. Lett. 80 (1998) 3686

[Baer et al. 2005] Baer H, Mustafayev A, Profumo S, Belyaev A and Xerxes T, *Direct, Indirect and Collider Detection of Neutralino Dark Matter In SUSY Models with Non-universal Higgs Masses*, 2005 JHEP 0507:065,2005

[Spies & Anton 2013] Spies A and Anton G, *Confronting Recent Results from Selected Direct and Indirect Dark Matter Searches and the Higgs Boson with Supersymmetric Models with Non-universal Gaugino Masses*, 2013 JCAP 06 (2013) 022, arXiv:1306.1099 [hep-ph]

[Cremmer et al. 1982] Cremmer E, Julia B, Ferrara S, Girardello L and van Proeyen A, *Coupling Supersymmetric Yang-Mills Theories to Supergravity*, 1982 Phys. Lett. B116 (1982) 231

[Huitu et al. 2000] Huitu K, Kawamura Y, Kobayashi T and Puolamäki K, *Phenomenological Constraints on SUSY SU(5) GUTs with Non-universal Gaugino Masses*, 2000 Phys. Rev. D61 (2000) 035001 [arXiv:hep-ph/9903528]

[Ellis et al. 1985] Ellis J, Enqvist K, Nanopoulos D V and Tamavakis K, *Gaugino Masses And Grand Unification*, 1985 Phys. Lett. B155 (1985) 351

[Amundson et al. 1996] Amundson J et al, *Report of the supersymmetry theory subgroup*, 1996 arxiv:hep-ph/9609374

[Younkin & Martin 2012] Younkin J E and Martin S P, *Non-universal gaugino masses, the supersymmetric little hierarchy problem, and dark matter*, 2012 arXiv:1201.2989 [hep-ph]

[Strege et al. 2012] Strege C, Bertone G, Feroz F, Fornasa M, Ruiz de Austri R and Trotta R, *Global Fits of the cMSSM and NUHM including the LHC Higgs discovery and new XENON100 constraints*, 2012 arXiv:1212.2636 [hep-ph]

[Gogoladze et al. 2012] Gogoladze I, Nasir F and Shafi Q, *Non-Universal Gaugino Masses and Natural Supersymmetry*, 2012 arXiv:1212.2593 [hep-ph]

[Bhattacharya et al. 2011] Bhattacharya S, Biswas S, Mukhopadhyaya S and Nojiri M M, *Signatures of supersymmetry with non-universal Higgs mass at the Large Hadron Collider*, 2011 arXiv:1105.3097 [hep-ph]

[Allanach 2002] Allanach B C, *SOFTSUSY: a program for calculating supersymmetric spectra*, 2002 Comput. Phys. Commun. 143 (2002) 305 [arXiv:hep-ph/0104145].

[Gondolo et al. 2004] Gondolo P, Edsjo J, Ullio P, Bergstrom L and Schelke M, *DarkSUSY: Computing supersymmetric dark matter properties numerically*, 2004 JCAP 0407 (2004) 008 [arXiv:astro-ph/0406204]

[Heinemeyer et al. 2000] Heinemeyer S, Hollik W and Weiglein G, *FeynHiggs: a program for the calculation of the masses of the neutral CP-even Higgs bosons in the MSSM*, 2000 Comput. Phys. Commun. 124 (2000) 76 [arXiv:hep-ph/9812320]

[Roszkowski et al. 2007] Roszkowski L, Ruiz de Austri R and Trotta R, *Implications for the constrained MSSM from a new prediction for b –¿ s gamma*, 2007 JHEP 0707 (2007) 075, arXiv:0705.2012 [hep-ph]

[Skands et al. 2004] Skands P et al., *SUSY Les Houches Accord: Interfacing SUSY Spectrum Calculators, Decay Packages, Event Generators*, 2004 JHEP 0407 (2004) 036 [arXiv:hep-ph/0311123]

[Mahmoudi 2009] Mahmoudi F, *SuperIso v2.3: A Program for calculating flavor physics observables in Supersymmetry*, 2009 Comput.Phys.Commun.180 (2009) 1579, arXiv:0808.3144 [hep-ph]

[Mahmoudi 2012] Mahmoudi F, *Flavour Les Houches Accord: Interfacing flavour related Codes*, 2012 Comput. Phys. Commun. 183 (2012) 285, arXiv:1008.0762 [hep-ph]

[Allanach et al. 2004] Allanach B C, Djouadi A, Kneur J L, Porod W and Slavich P, *Precise determination of the neutral Higgs boson mass in the MSSM*, 2004 JHEP0409:044 [arXiv:hep-ph/0406166]

[Moroi & Randall 2000] Moroi T and Randall L, *Wino Cold Dark Matter from Anomaly-Mediated SUSY Breaking*, 2000 Nucl. Phys. B570 (2000) 455 [arXiv:hep-ph/9906527]

[Chung et al. 1999] Chung D J H, Kolb E W and Riotto A, *Production of massive particles during reheating*, 1999 Phys. Rev. D60 063504 [arXiv:hep-ph/9809453]

[Jeannerot et al. 1999] Jeannerot R, Zhang X and Brandenberger R, *Non-thermal Production of Neutralino Cold Dark Matter from Cosmic String Decays*, 1999 JHEP12(1999)003 [arXiv:hep-ph/9901357]

[Nakamura et al. 2011] Nakamura K et al. [Particle Data Group Collaboration], J. Phys. G 37, 075021 (2010) and 2011 partial update for the 2012 edition

[Ade et al. 2013] Ade P A R et al. [Planck Collaboration], *Planck 2013 results. XVI. Cosmological parameters*, 2013 arXiv:1303.5076

[Frere et al. 1983] Frere J M, Jones D R T and Raby S, *Fermion masses and induction of the weak scale by supergravity*, 1983 Nucl. Phys B222 (1983) 11

[Alvarez et al. 1983] Alvarez-Gaume L, Polchinski J and Wise M B, *Minimal low-energy supergravity*, 1983 Nucl. Phys. B221 (1983) 495

[Derendinger & Savoy 1984] Derendinger J P and Savoy C A, *Quantum effects and SU(2)×U(1) breaking in supergravity gauge theories*, 1984 Nucl. Phys. B237 (1984) 307

[Kounnas et al. 1984] Kounnas C, Lahanas A B, Nanopoulos D V and Quiros M, *Low-energy behaviour of realistic locally-supersymmetric grand unified theories*, 1984 Nucl. Phys. B236 (1984) 438

[The ATLAS Collaboration 2012b] The ATLAS Collaboration, *Search for squarks and gluinos with the ATLAS detector using final states with jets and missing transverse momentum at* $\sqrt{s} = 8$ *TeV*, 2012 ATLAS-CONF-2012-109, retrieved from http://cds.cern.ch/record/1472710/files/ATLAS-CONF-2012-109.pdf

[Bovy & Tremaine 2012] Bovy J and Tremaine S, *On the local dark matter density*, 2012 Astrophs. J. 756 (2012) 89

[Komatsu et al. 2010] Komatsu E et al., *Seven-year Wilkinson Microwave Anisotropy Probe Observations: Cosmological Interpretation*, 2010 arXiv:1001.4538 [astro-ph.CO]

[Murakami & Wells 2001] Murakami B and Wells J D, *Nucleon scattering with higgsino and wino cold dark matter*, 2001 Phys. Rev. D64 (2001) 015001 [arXiv:hep-ph/011082]

[Barberio et al. 2007] Barberio E et al. [Heavy Flavor Averaging Group (HFAG) Collaboration], *Averages of b-hadron and c-hadron Properties at the End of 2007*, 2007 arXiv:0808.1297 [hep-ex]

[Aubert et al. 2008a] Aubert B et al. [BABAR Collaboration], *Measurement of Branching Fractions and CP and Isospin Asymmetries in* $B \to K^*\gamma$, 2008 arXiv:0808.1915 [hep-ex]

[Nakao et al. 2004] Nakao N et al. [BELLE Collaboration], *Measurement of the* $B \to K^*\gamma$ *branching fractions and asymmetries*, 2004 Phys. Rev. D69, 112001 (2004) [hep-ex/0402042]

[Aubert et al. 2008b] Aubert B et al. [BABAR Collaboration], *Observation of the semileptonic decays* $B \to D^*\tau^-\bar{\nu}_\tau$ *and evidence for* $B \to D\tau^-\bar{\nu}_\tau$, 2008 Phys. Rev. Lett. 100, 021801 (2008) arXiv:0709.1698

[Antonelli et al. 2008] Antonelli M et al. [The FlaviaNet Kaon Working Group], *Precision tests of the Standard Model with leptonic and semileptonic kaon decays*, 2008 Nucl. Phys. Proc. Suppl. 181-182, 83 (2008)arXiv:0801.1817

[Antonelli et al. 2010] Antonelli M et al., *An evaluation of* $|V_{us}|$ *and precise tests of the Standard Model from world data on leptonic and semileptonic kaon decays*, 2010 Eur. Phys. J. C 69, 399 (2010) arXiv:1005.2323

[Akeroyd et al. 2009] Akeroyd A G and Mahmoudi F, *Constraints on charged Higgs bosons from* $D_s^\pm \to \mu^\pm\nu$ *and* $D_s^\pm \to \tau^\pm\nu$, 2009 JHEP 0904, 121 (2009) arXiv:0902.2393

[Akerib et al. 2013] Akerib D S et. al [The LUX Collaboration], *First results from the LUX dark matter experiment at the Sanford Underground Research Facility*, 2013 arXiv:1310.8214 [astro-ph.CO]